Crystal growth studied on a micrometer scale

Marco Plomp

1 μm

Crystal Growth studied on a micrometer scale

Marco Plomp

Crystal Growth studied on a micrometer scale

een wetenschappelijke proeve op het gebied van de
Natuurwetenschappen, Wiskunde en Informatica

Proefschrift

ter verkrijging van de graad van doctor
aan de Katholieke Universiteit Nijmegen,
volgens besluit van het College van Decanen
in het openbaar te verdedigen op
maandag 13 december 1999,
des namiddags om 3.30 uur precies
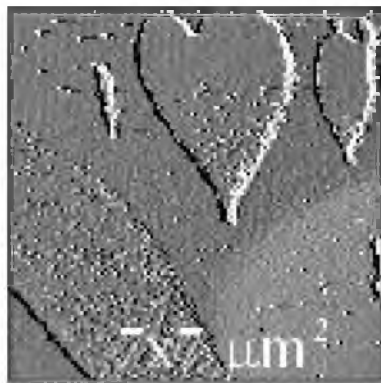
door

Marco Plomp

geboren op 24 mei 1969
te Doetinchem

Promotores: Prof. Dr. E. Vlieg
                     Prof. Dr. P. Bennema
Co-promotor: Dr. W.J.P. van Enckevort

Manuscriptcommissie: Prof. Dr. J.P.J.M. van den Eerden (UU)
                              Prof. Dr. J.W.M. Frenken (UL)
                              Prof. Dr. H. van Kempen

7x7 µm²

Voor Dorien

Voorwoord

Dan is het weer tijd voor het voorwoord, dat men het laatst schrijft en het eerst leest. Met daarin uiteraard het dankwoordgebeuren. Laat ik dan beginnen met de Vakgroep Vastestofchemie te bedanken. De relaxte sfeer en vrije omgangsvormen zorgen voor een fijn werkklimaat, wat niet zo vanzelfsprekend is als het vaak lijkt. Iedere Vastestofchemifysicus bedankt!

Voor hun bijdragen aan dit proefschrift wil ik al mijn co-auteurs bedanken, en wel in volgorde van opkomst: Koji, Willem, Piet, Koji, Willem, Ivan, Gertjan, Willem, Dirk, Jasper, Willem, Willem, Elias, Willem, Elias, Willem, Elias, Peter, Jacco, Willem, Peter, Willem, Frank, Jacco, Willem, Kenji en natuurlijk Willem. In het bijzonder wil ik Willem bedanken, voor zijn enthousiaste, deskundige, resultaatgerichte en altijd weer amusante begeleiding.

Nu dan de AFM-bedankjes: Jan bedank ik voor zijn regeltechische AFM-bijstand; Jasper voor zijn niet vernietigde data; Ivan voor zijn experimenten met lekkende condooms; Rob Kasman voor zijn memorabele scanner-reparatie-sessies en Elias voor de AFM verdrievoudiging. Onze vrienden bij InterSurface, MarTech en ThIS Scientific bedank ik voor hun nimmer aflatende pogingen om de AFM-vloot draaiende te houden.

Uiteraard wil ik het gebied Chemische Wetenschappen (CW), één van de zeven wetenschaps-gebieden van de Nederlandse Organisatie voor Wetenschappelijk Onderzoek (NWO) bedanken voor de financiële ondersteuning van mijn promotie-onderzoek.

Verder wil ik nog de programmeurs van WordPerfect en vooral CorelDraw bedanken. Zonder hen had dit proefschrift er niet zo uitgezien. Ook Mars B.V. uit Veghel heeft een Markante & Memorabele bijdrage geleverd.

Als laatste wil ik Dorien bedanken voor de morele ondersteuning, het soepele verloop van de werk- en vooral eetritme-verschuivingen en haar er zijn.

Marco,

Contents

Chapter 1:

Crystal growth on a micrometer scale monitored by atomic force microscopy

Chapter 1:

Crystal growth on a micrometer scale monitored by atomic force microscopy

Crystal growth is a phenomenon that is studied on various length scales. In general, there is a 'scale gap' between atomistic models describing the growth process on a atomistic scale and the observations on a macroscopic scale. One of the techniques that is able to bridge this gap is scanning probe microscopy (SPM). Since its development many scientific disciplines entered a new, 'nanoscopic' world, one of them being crystal growth. Thanks to SPM it is now feasable to image crystal surfaces on a micrometer and even a nanometer scale, both *in situ* and ex *situ*.
Direct observation of mono-atomic or mono-molecular steps, of growth spirals and stacking faults, which all are abundant in this thesis, give the possibility to study crystal growth surface phenomena in a much more detailed way as compared to optical microscopy or scanning electron microscopy. The opportunity to get molecular resolution on crystal faces with SPM gives even information about the surface lattice.

In this introductory chapter first the most important crystal growth features encountered on a micrometer scale are addressed. Then, the general technique and inherent problems of atomic force microscopy (AFM), which is the type of SPM applied throughout in this thesis, is briefly described together with some specific features about crystal growth. At the end, the organization of this thesis will be presented.

1.1 Processes at growing crystal surfaces

Most crystal growth theories are based on atomistic models of the crystal structure. From that point of view thermal and kinetic roughening, steps and growth spirals can be understood. Without the aim of giving a complete overview of crystal growth theory, some important aspects relevant for this thesis will be treated in this section.

Almost all of the observed crystal surfaces in this thesis can be regarded as molecularly flat. They consist of terraces up to millions of growth units wide, separated by mono- or multi-molecular steps. This means that the crystals are neither thermally nor kinetically roughened. Both types of roughening are
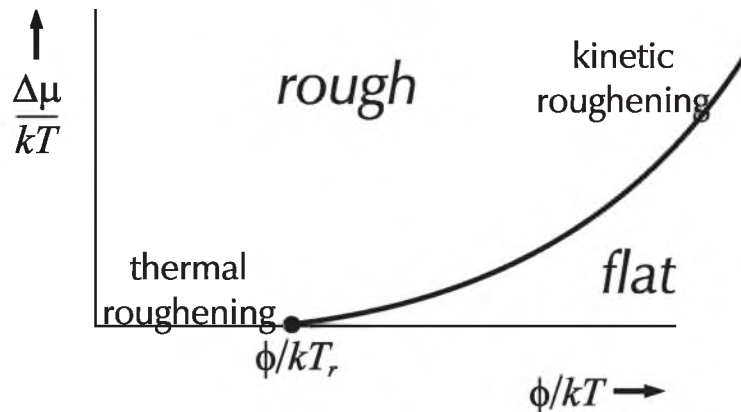
Figure 1.1 Kinetic and thermal roughening as a function of bond strength and supersaturation. The roughening transition at T_r is defined only for zero supersaturation.

depicted schematically in fig. 1.1. If the crystal bond energy, φ, between crystal units is high, it costs much energy to create a crystal surface covered by steps, and it will therefore be as flat as possible. Thermal roughening occurs if the kinetic energy kT of the crystal units roughly equals the bond energy φ. Then, the step free energy vanishes and new steps are created without energy barrier: Without a driving force for surface flattening the surface roughens (see e.g. [1]). The roughening transition occurs at a dimensionless temperature kT_r/φ , which can be calculated using different methods. The most important ones are Monte Carlo simulations for three-dimensional (3D) crystals and the application of statistical mechanics to two-dimensional (2D) Ising models. Often the Kossel model is used in which it is assumed that no overhangs can occur on a crystal surface (solid-on-solid condition). As an example, for a Kossel crystal the 3D and 2D roughening temperatures are kT_r/φ = 1.28 and kT_{crit}/φ = 1.14, respectively.

Kinetic roughening occurs when the driving force for crystallization, the supersaturation, which is defined as the dimensionless parameter μ/kT, is increased to a high extent. Here, μ is the change in chemical potential upon crystallisation. Below the roughening temperature and at low supersaturation, crystal surfaces grow, in the absence of linear or point defects and if not thermally roughened, by the formation of two-dimensional nuclei. If a circular nucleus with radius r grows, its free energy $G(r)$ decreases proportional to πr^2 μ by the incorporation of new particles but increases

proportional to $2\pi r\, \gamma_{step}$ because of the increasing step length (see fig. 1.2). Here, γ_{step} is the step energy. At small r, the step energy contribution dominates and the nucleus tends to shrink. At large r, the negative bulk contribution dominates the positive step contribution and the nucleus will expand further. Hence, a stable nucleus that keeps on growing will only form if it exceeds a certain critical size by statistical fluctuation. The critical nucleus radius r_c at which this will happen, can be calculated to be $r_c = \gamma_{step}/h_{step}\, \mu$, where is the volume of a growth unit and h_{step} the step height. If μ is continuously increased, at a certain moment r_c will decrease to the size of one growth unit, i.e. if just one unit lands on the crystal surface, it still grows out to form an island. If this happens, the surface roughens kinetically [2].

Within the scope of this thesis, we restrict ourselves to the growth regime of surfaces that are neither thermally nor kinetically roughened. As stated above, the general way in which a perfect crystal grows is via two-dimensional nucleation [3]. This process is often denoted as the *Birth and Spread* model. After the formation of a nucleus, growth proceeds by the addition of new growth units at the island edge. At low supersaturation, the critical radius r_c is so large

Figure 1.2 The bulk, step and total energy of a 2D nucleus as a function of its radius. The size of the critical nucleus r_c is defined by the maximum energy.

that new nuclei are hardly formed and crystal growth is supposed to stop. However, because most crystals are not perfect, another mode of growth, namely spiral growth [3, 4], takes over. The centre of a growth spiral is always formed by the outcrop of one or several screw dislocations, which impose a permanent step at the crystal surface. Growth now leads to a growth spiral, as can be seen in fig. 1.3. Spiral growth has proven to be the most important growth mechanism at low supersaturation. Other step sources present on the crystal surface may be stacking faults creating permanent partial steps [5], foreign particles acting as heterogeneous nuclei and 3D nuclei originating from the mother phase landing on the crystal surface.

The exact way how a growth unit transforms from a fluid particle in the mother phase into a solid

particle in the a crystal lattice should be determined in order to understand crystal growth kinetics. On flat surfaces, growth units are built in in the crystal at the kink sites of steps. The unit can arrive at a kink position directly from the mother phase, or first adsorb at a crystal surface terrace, then migrate to a step and finally adhere at a kink position. Arrived there, it can take some time to integrate in the crystal lattice. The stage in this growth process that takes most time is the *rate limiting step* and will determine the growth kinetics and growth velocity. Surface diffusion limited growth, which is described thoroughly by Burton, Cabrera and Frank in one of the most important papers on crystal growth [3], is often encountered for crystal growth from the gas phase, because here the mobility of the adsorbed species is large and the probability for desorption small. In the experiments described in this thesis, crystal
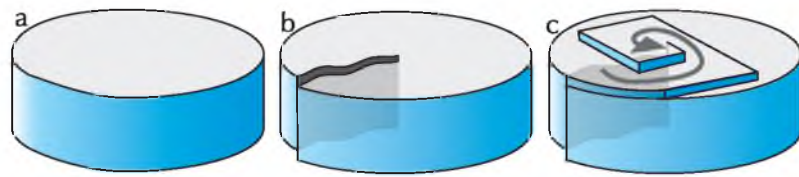
Figure 1.3 Spiral growth. (a) Perfect crystal. (b) Creation of a screw dislocation. (c) Spiral growth at the dislocation outcrop.

growth mostly takes place from solution. Then, in general, surface diffusion of adsorbed growth units is severely hindered by the solvent particles, and more growth units will integrate directly from the solution into the steps. Often, kink integration is the rate limiting step in this case. Then, the growth rate is dependent on the kink density, which is, at high φ/kT, strongly dependent on the orientation of the step: if the step is along a certain crystallographic direction it will contain far less kinks then if it is along an arbitrary orientation. Therefore, steps in arbitrary directions will grow much faster then "crystallographically" oriented steps, and the latter will determine the growth patterns. These will be highly polygonized and reflect the crystal symmetry. Examples of such polygonized patterns are given in figs. 9.3-5 in this thesis for the case of paraffin. For kink-integration limited growth adjacent steps do not interact with each other. However, if kink integration is fast and the supersaturation is high, volume diffusion can become rate-limiting, and if the diffusion fields of neighbouring steps overlap, their propagation velocities will decrease, similar to the case of surface diffusion.

Apart from the growth promoting processes described above, often there are also growth retarding mechanisms during experiments, of which the most important one is caused by the presence of impurities at the crystal surface. This can hinder or block the advancement of steps, as is shown in fig. 1.4. Both experiments (e.g. [6]) and Monte Carlo simulations indicate that impurities can have a large effect on crystal growth leading to a 'dead zone', which means a growth stop at low supersaturation, and to the promotion of step bunching at higher supersaturation.

There is a strong relation between the structure of a crystal and its macroscopic 3D morphology. The structure dictates in which directions crystal growth offers the largest energy gain. In these directions growth will be fastest. The eventual morphology will be comprised of the slowest growing directions. One of the earliest criteria to predict the morphological importance (MI) of crystal faces, which can be defined as being inversely proportional to the face's growth rate R, was based on the interplanar lattice distance d_{hkl}. The

Figure 1.4 Principle of step pinning. (a) Top view of a step approaching two impurities. (b) The step is pinned by the impurities. (c) Multiple step pinning.

larger d_{hkl}, the smaller the growth rate of the face *(hkl)* and the larger its MI. A more recent criterion for predicting crystal morphology is based on the Hartman-Perdok (HP) theory [7, 8]. In this theory, flat faces *(hkl)* are associated with 2D *connected nets* inside a slice of thickness d_{hkl}, consisting of interconnected *periodic bond chains* (*PBCs*). The total crystal energy E_{cryst} can be split up into the slice energy E_{slice} of all bonds that are within such a connected net and the attachment energy E_{att} of bonds between neighbouring slices. The HP criterion is that the faces with the lowest E_{att} have the lowest growth speed and thus the highest MI.

Being normally applied to 3D morphology, the basis of the HP theory are the 1D PBCs, and therefore it should also apply to the step patterns observed on crystal faces. The observed steps are expected to be aligned preferably along the 'strongest' PBCs <uvw>, which is indeed often the case. An example of a truly 2D HP analysis, in which the predicted PBC directions are compared with the observed step patterns, is presented in chapter 11 of this thesis.

1.2 Atomic force microscopy

The era of scanning probe microscopy started with the invention of the scanning tunneling microscope (STM) in 1982 by Binnig and Rohrer [9]. In a STM, a sharp conducting tip is scanned over a conducting specimen surface. The tip is positively or negatively biased with respect to the sample. When the tip is brought in close proximity to the sample a tunneling current passes between them. This tunneling current, which is strongly dependent on the tip-sample distance, is kept constant by adjusting the tip height. In this way, the tip nicely follows the surface topography and

a height profile of the surface can be obtained. Crucial for the construction of this first SPM was the development of a scan system that could displace the scanning tip with atomic accuracy, and of a mechanical construction with such a high degree of vibrational isolation that this atomic accuracy was not blurred by air or building vibrations.

The application of STM resulted in beautiful atomically resolved images of surfaces of metals and semiconductors. A lot has been and is being learned about surface reconstructions, epitaxy and even about step and kink dynamics (e.g. [10]). However, as mentioned before, SPM is based on a tip-sample interaction by electron tunneling, and therefore needs conducting specimens. In order to investigate non-conducting materials, these must be doped by foreign atoms, or very thin layers of them have to be deposited on a conducting substrate. In practice, this limitation rules out many materials and experimental conditions.

Therefore, the invention of atomic force microscopy by Binnig, Quate and Gerber [11] was another breakthrough. This SPM is based on the same principle of scanning a very sharp probe across the specimen surface. The difference is the type of interaction, which in the case of AFM is the force between tip and sample. Several forces may act between tip and sample, such as Van der Waals force, electrostatic force and capillary force. The resulting force can be repelling or attractive depending on the type of sample and tip, the tip-sample distance and the type of AFM involved. The power of AFM is that, since forces are always present between tip and sample, in principle each kind of surface can be investigated in various experimental conditions like vacuum air, in fluids. The latter is very important to mimic natural environments in biology and in solution crystal growth. The possibility of imaging electrically insulating surfaces (in fact, all investigated crystals in this thesis are insulating) together with the possibilities of *in situ* imaging make AFM very suitable to record crystal growth.
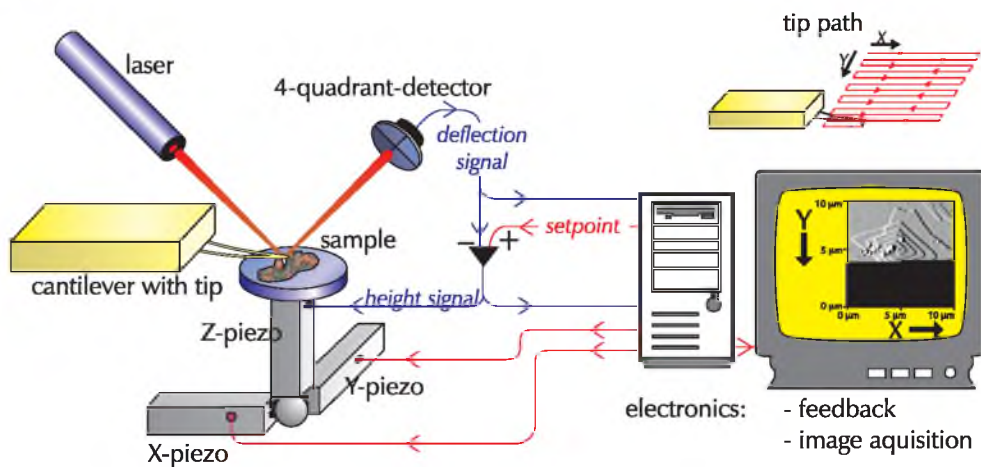
Figure 1.5 Schematic overview of a contact-mode AFM setup.

The principle of the first and most straightforward form of AFM, contact-mode atomic force microscopy (CM-AFM), is shown in fig. 1.5. The tip (often made of SiN_3) is attached to a SiN_3 cantilever, which is mounted on the AFM head. The tip or, as is depicted in fig. 1.5 the sample is scanned by a scanner made of piezo-ceramic material. Basically, by putting a voltage over this material, it expands or contracts in a very controllable way. The types of scanners used for AFM are the piezo tube and the tripod scanner (which is depicted in fig. 1.5). A piezo tube is controlled by four electrodes attached at the outside of the tube and one central electrode at the inner side. The tube is bended in the X,Y plane when a voltage is applied over opposing electrodes; and movement in the Z direction is accomplished by applying a voltage over the inner electrode relative to all outer electrodes. In case of a tripod scanner, the three scan directions X,Y and Z are controlled by three independent piezo stacks.

When the cantilever contacts the sample, it will deflect because of its very low spring constant (mostly between 0.01 - 1 N/m). This deflection is generally gauged by means of a laser beam focused on the cantilever. The reflected beam hits a 2- or 4-quadrant photodiode detector. When the scanning tip encounters a height difference on the sample, the cantilever deflection will change and with it the beam position on the detector. For small deviations the detector signal varies linearly with the cantilever deflection and with the tip-sample force. This detector signal is fed to a feedback loop, that tries to maintain a constant force by keeping the deflection signal equal to the deflection setpoint value. To achieve this, the feedback loop changes the tip-sample distance via the Z piezo element. If the force gets higher, e.g. at an ascending step, the feedback loop will retract the tip (or the sample) in order to diminish the force untill the original setpoint value is reached. The Z piezo voltage needed for this is recorded and used to generate a *topographical image* or *height image* of the specimen surface. For a perfect feedback loop the deflection signal would always be exactly equal to the setpoint deflection. However, because the feedback needs some time to adapt, at sudden height changes (e.g. steps) the deflection signal will show short pulses before it returns to the setpoint value. From recording the deflection signal or error signal the *deflection image* can be generated. This image often shows a much more detailed view of the surface morphology then the corresponding topographical image and is therefore often shown in this thesis.

A disadvantage of CM-AFM is that it introduces relatively high lateral forces. This can lead to damage to the surface, especially at steps. These forces can be reduced by using vibrating cantilevers. Depending on the AFM brand this mode is called non-contact AFM (NC-AFM), tapping mode (TM-AFM), or intermittent mode AFM (IM-AFM). During one oscillation cycle, the tip is only shortly (if at all) in contact with the sample. This interaction is predominantly in the Z direction, diminishing the lateral force. This makes TM-AFM more suitable for soft samples. The feedback loop input is now the oscillation amplitude, which is dependent on the tip-sample distance as well.

1.3 What you see is not always what it is

The ability to image crystal surface step patterns on a scale ranging from 100 μm to sub-μm without preparation, to measure step heights with ngström resolution and to image the surface lattice, all of which can be done in different environments, make AFM very well suited to study crystal growth. Despite this wonderful performance, there are a few aspects of AFM that lead to images that are not always *"what you see is what it is"*. The most important artefacts concerning crystal growth are:

1) lateral angle distortion

Due to the non-linear behaviour of the scanner piezo's, there is often some distortion of the images. An example is fig. 7.5, in which the angles of the etched pits should be 90 , but are distorted due to the piezo non-linearity. Systematic non-linearity can be corrected for by software, but a complete removal can only be accomplished by a feedback system that measures the actual displacement of the piezo's. Such a system is not incorporated in the AFMs used in this thesis. Thus, care has to be taken in measuring lateral angles for indexing of steps on the surface.
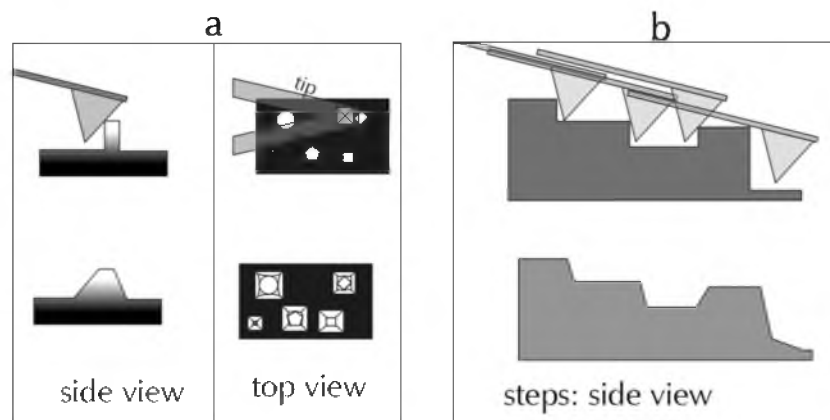
Figure 1.6 Tip convolution for small, steep particles (a) and for steep (macro) steps (b).

2) tip convolution

The actual AFM image is formed by a convolution of the surface morphology and the tip shape. For small-scale features (typically smaller than the tip radius), this becomes important because they adapt the tip shape (fig. 1.6a). A closely related phenomenon occurs at the measurement of step inclination. The observed angle of macrosteps or crystal side faces is limited by the tip shape (fig. 1.6b). For common pyramidalSiN$_3$ tips the maximum detectable inclination is about 40 .

3) non-zero acquisition time

In AFM, image acquisition is in a serial way, in contrast to optical microscopy, where all parts of the image are acquired parallel in a fraction of a second. Typical acquisition times are several minutes for large scan areas ($>$ 10 μm) and about one minute for smaller regions. In case of *ex situ* imaging, these scan rates requires only a patient researcher; in case of *in situ* crystal growth this puts serious limitations in recording fast propagating steps. Consider a step train that runs from the left to the right in the imaged area (fig. 1.7). Depending on its velocity, v_{step}, relative to the scan size, S_{scan}, and the time needed to record the image, T_{scan}, the image gets distorted as is shown in the figure. The original step velocity and direction can be reconstructed if the AFM scans alternatingly upwards and downwards for successive

$$V_{scan} = \infty V_{step} \qquad V_{scan} = 5\ V_{step} \qquad V_{scan} = V_{step} \qquad V_{scan} = 0.3\ V_{step} \qquad V_{scan} = -\ V_{step}$$
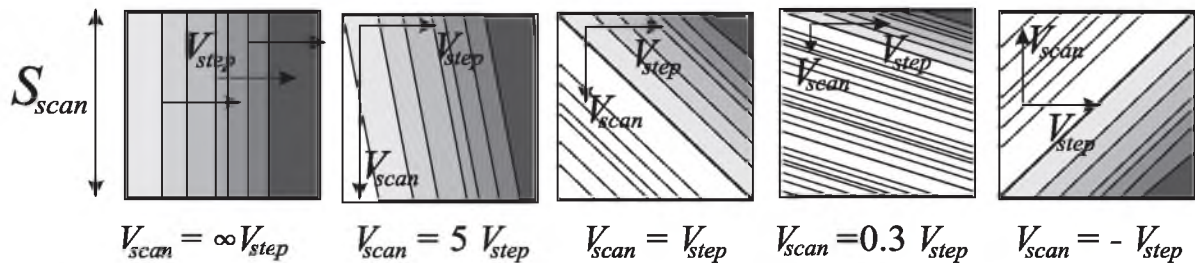
Figure 1.7 Apparent AFM images of a moving step train imaged with different scan speeds. This scan speed V_{scan} represents the rate at which linescans are made, and is defined as V_{scan} = S_{scan}/T_{scan}, with S_{scan} the scan size and T_{scan} the time needed to finish a complete scan. If V_{scan} is small compared to the step velocity V_{step} the image of the real step pattern (imaged for V_{scan}= V_{step}) will be highly distorted.

images. However, if the step velocity becomes several times larger the scan velocity S_{scan}/T_{scan}, the images cannot be interpreted anymore. Scanning faster helps, but *in situ* AFM remains limited to low step speeds and hence low supersaturations. In case of slowly growing crystals, such as proteins (chapter 12), growing steps can be easily followed, but in case of highly soluble ionic compounds whose solubility is often strongly temperature-dependent, problems arise. Unless a very stable temperature controller is incorporated in the *in situ* AFM, other measures have to be taken to control the growth/etch rate, such as the replacement of a high-solubility solvent by a low-solubility one (chapter 7).

4) tip-sample interaction

In general, *every* examination method interacts with the sample under investigation, thereby possibly damaging it. In case of crystal surfaces, frequently used observation methods are optical microscopy, which is mostly harmless, and scanning electron microscopy, which is potentially damaging because of the high energies involved. Often, crystals have to be covered with a thin gold layer to prevent charging in the electron microscope. AFM is in

general a non-destructive technique which requires no sample preparation. In AFM, the interaction takes place in the very small tip-sample contact area only. Despite the low applied forces (typically nN) in AFM, pressures at the tip can become so high that soft samples can be damaged. Especially with ex *situ* AFM, the thin water layer present on most crystals introduces extra capillary forces. The crystal surface molecules which are connected the most loosely to the body of the crystal, which are the molecules at steps and freely adsorbed molecules, will detach the easiest under influence of the interaction force. Therefore, 'step wear' is sometimes observed at crystal surfaces imaged with CM-AFM (fig. 10.1).

In case of TM-AFM, the tip-sample interaction is more complex and not governed by lateral forces anymore. For crystals with low melting points, the tip, which is heated somewhat by the deflection detection laser, can locally melt the surface, causing tip-induced crystal growth phenomena (chapter 10). Local differences on crystal surfaces can even provoke the switching between two different TM-AFM imaging modes, leading to an apparent surface topography not corresponding to reality (chapter 8).

1.4 About this thesis

The studies of this thesis are, by nature of the microscopic technique used, focused on the two-dimensional morphology of crystal surfaces on a micrometer scale. Given this confinement, the investigations cover a wide range of crystal growth topics .There are ex *situ* and in *situ* growth studies, and one ex *situ* study that turned into an in *situ* study (n-$C_{23}H_{48}$,ch. 10). Moreover, there is one etching examination, one cleavage study and one investigation about water layers on crystals in ambient air. Research has been carried out on ionic crystals (barium nitrate, silver bromide and potassium bichromate) as well as organic crystals (the n-paraffins n-$C_{23}H_{48}$ and n-$C_{40}H_{82}$, the fat crystals 16.16.16 and 16.18.16 and the protein insulin).

Apart from these differences, there are also important resemblances between the chapters. In all of them steps of monomolecular height are observed. Studying crystal growth, one of the basic questions is: where do these steps come from? Because of the small scales involved in AFM studies, it is often difficult to find the step sources. Sometimes they come from the crystal edge (AgBr, ch. 4), in other cases 2D nucleation is observed ($Ba(NO_3)_2$, ch. 2;fat, ch. 11; insulin, ch. 12). However, the most frequently encountered growth sources throughout this thesis are growth spirals, as is discussed in 7 of 11 chapters. This is partly explained by their clear morphology, which make them relatively easy to trace, and partly because they happen to be a dominant growth source in many systems.

Growth spirals can serve as excellent features to correlate preferential step directions with crystal structure, which is done in the chapters about fats (ch. 11) and insulin (ch. 12). The growth spirals that arise from different types of dislocations are studied for the case of $Ba(NO_3)_2$ (ch. 2). For these spirals, hollow cores that often appear at their centres are studied in detail (ch. 3). From the step observations, even movement of dislocations could be deduced for $Ba(NO_3)_2$ (ch. 2) and n-$C_{40}H_{82}$. Of course, the nicest spirals are the ones that can be seen growing *in situ*, as is observed for n-$C_{23}H_{48}$ (ch. 10) and insulin (ch. 12).

The crystal which is studied most intensively in this thesis is $K_2Cr_2O_7$. On this crystal, which has a long research tradition at the Nijmegen Solid State Chemistry group, four chapters are spent (chs. 5 - 8). In this part *in situ* and *ex situ* optical microscopy, scanning electron microscopy and *ex situ* and *in situ* AFM are applied to learn more about the growth, the etching and the cleavage behaviour of $K_2Cr_2O_7$, as well as the occurrence of a water layer on top of the crystals in ambient air. They are closely interrelated. The cleavage experiment (ch. 6) reveals the behaviour of the stable and the unstable layer *A* and *B* on the {001} faces. After cleavage, the unstable layer dissolves a little due to a water layer condensed from the ambient air. This water layer is detected and its thickness is estimated in ch. 7. The identification of the stable and unstable layers *A* and *B* with respect to the crystal structure could be accomplished thanks to the etching study in ch. 8. The subtleties of the double-layered structure may be responsible for the hypomorphism that is noticed in ch. 5.

References

[1]   J.P. van der Eerden, in: Handbook of Crystal Growth, vol 1a, ed. D.T.J. Hurle (Elsevier, Amsterdam, 1993), 377.

[2]   E. van Veenendaal, P.J.C.M. van Hoof, J. van Suchtelen, W.J.P. van Enckevort and P. Bennema, Surf. Science **417** (1998), 121.

[3]   W. Burton, N. Cabrera and C. Frank, Trans. Roy. Soc. A **243** (1951), 299.

[4]   I. Sunagawa and P. Bennema, in: Preparation and Properties of Solid State Materials, Vol. 7, ed. W.R. Wilcox (Dekker, New York, 1982), 1.

[5]   N.B. Ming and I. Sunagawa, J. Cryst. Growth **87** (1988), 13.

[6]   T.A. Land, T.L. Martin, S. Potapenko, G. Tayhas Palmore and J.J. De Yoreo, Nature **399** (1999), 442.

[7]   P. Hartman and W. Perdok, Acta Cryst. **8** (1955), 49; 521; 525.

[8]   P. Hartman and P. Bennema, J. Crystal Growth **49** (1980), 145.

[9]   G. Binnig, H. Rohrer, Ch. Gerber, E. Weibel, Phys. Rev. Lett. **49** (1982), 57.

[10]   M.S. Hoogeman, D.C. Schlosser, J.B. Sanders, L. Kuipers, J.W.M. Frenken, Phys. Rev. B **53** (1996), 13299.

[11]   G. Binnig, C.F. Quate, Ch. Gerber, Phys. Rev. Lett. **56** (1986), 930.

Chapter 2:

AFM observation of barium nitrate {111} and {100} faces: spiral growth and two-dimensional nucleation growth

Chapter 2:

AFM observation of barium nitrate {111} and {100} faces: spiral growth and two-dimensional nucleation growth[*]

K. Maiwa, M. Plomp, W. J. P. van Enckevort and P. Bennema

RIM laboratory of Solid State Chemistry, Faculty of Science, University of Nijmegen, Toernooiveld 1, 6525 ED Nijmegen, The Netherlands

Abstract

The growth mechanisms of the {111} and {100} faces of $Ba(NO_3)_2$ crystals growing from aqueous solutions were investigated by *ex situ* atomic force microscopy. Growth hillocks induced by dislocations and growth islands formed via 2D nucleation were observed on both faces. The thinnest steps observed on the {111} and {100} faces were, irrespective of step sources, d_{111} = 4.7 and d_{200} = 4.1 in height, respectively. These correspond to the elementary growth layers expected in Bravais-Friedel-Donnay-Harker (BFDH) and Hartman-Perdok (*i. e.* periodic bond chain) theories. The spiral hillocks on the {100} face consist of double elementary layers. On {111} faces, three kinds of spiral layers arising from single dislocations were discerned: single, double and triple elementary layers, which can be produced by dislocations with Burgers vectors b = 100 110 and 111, respectively. It was observed that the multiple spiral layers tend to split into elementary steps at the spiral centres, which can be explained by entropic repulsion. It was also found that several spiral centres are accompanied with hollow cores and that the diameters of these cores vary with the number of spiral arms connected with the central dislocation. The numerous 2D nuclei of elementary height found between the spiral arms were probably created in the short period of very high supersaturation during separation of the crystal from the solution.

2.1 Introduction

Recently, atomic force microscopy (AFM) has been increasingly applied to the study of crystal growth by observing the growth features on crystal surfaces with a spatial resolution of nanometer scale. For crystals growing from solution, many attempts of AFM observations were done particularly on organic crystals with large molecules [1]. Only a few were done on inorganic crystals, which generally have smaller molecules/ions [2-4]. In this work, we intend to employ ex *situ* AFM to observe the faces of $Ba(NO_3)_2$ crystals grown in an aqueous solution. As described below, these crystals are a good example for the study of the mechanisms of spiral growth and two-dimensional nucleation (2D) growth. From aqueous solution, $Ba(NO_3)_2$ crystals grow in shapes bounded by large {111}, moderate {100} and small {210} faces [5]. The growth features of the {111} and {100} faces were investigated both ex *situ* and in *situ* in large detail by the use of various observation methods [5-18]. The character of dislocations induced during growth in an aqueous solution was well studied in detail by X-ray topography [6-10] and stress birefringence microscopy [11, 12]. Combining these results and using kinetic measurements of the {111} faces with the help of a Michelson interferometer, the difference in growth rates of individual spiral hillocks was found to depend on the heights of the spiral steps and consequently on the type of the dislocation at their centres [14]. Shekunov et al. showed that, using the same technique, the growth rates oscillated as a result of a change in the dominant spiral centres on both faces [10, 13]. The change from spiral growth to 2D nucleation growth as a dominant growth mechanism was also observed on the {100} faces at the supersaturation = 4.3 %, whereas spiral growth persisted on the {111} faces at the same range of [15].

In this paper we report the various properties and behaviour of growth layers created by different dislocation sources and 2D nucleation on both {111} and {100} faces of $Ba(NO_3)_2$ grown in an aqueous solution as deduced from detailed AFM observations.

2.2 Experimental

Prior to experiments seed crystals were prepared from an aqueous solution and those with well developed {111} and {100} faces were selected. The specimen crystals were subsequently grown in an unstirred aqueous solution in a thermostated growth cell of 50 ml in volume, which is provided with an optical window to make in *situ* observation possible [19]. The saturation temperature of the solution was 23.0 C. Crystal growth was carried out under a growth temperature higher than 21.4

C, which corresponds with supersaturations less than 4 %.

Prior to AFM observation the faceted crystals were quickly removed from the growth cell and the solution remaining on crystal faces was immediately soaked up using highly water-absorbing paper, in order to preserve the as-grown surfaces as much as possible. Crystal faces were observed both *in situ* and *ex situ* using an optical differential interference contrast microscope (DICM) to compare the surface morphology in and out of the solution. In this way the consequences of the shut off effect can be estimated [19]. Polarized optical microscopy was applied to observe dislocations in the crystals [11, 12].

Ex situ AFM was used to study the details of the growth features on the surfaces. In AFM, a very sharp Si_3N_4 tip attached to a spring cantilever is scanned over the surface. The deflection of the cantilever, which is linear with the force between tip and sample, is measured and offered to a feedback loop, that maintains a constant force by adjustment of the tip-sample distance. Only at sudden height changes of the sample (*i. e.* at steps) a pulse in the deflection signal arises, because the feedback loop cannot compensate for this height difference immeadiately. When this deflection signal is imaged, it provides a more detailed image with more contrast, compared to the usual height image. Because of this, most of the depicted figures in this word are *force images*, made up of the deflection signal.

2.3 Observations

2.3.1 Spiral steps

{111} faces

Two different space groups, *Pa3* [20-23, 25] and $P2_13$ [24], have been reported in X-ray and neutron diffraction studies for $Ba(NO_3)_2$ and its isomorphous crystals. From surface morphological [6, 8] and kinetic studies [13] it was deduced that no centre of symmetry occurs, so the actual space group must be $P2_13$. This result was confirmed in the present study from the surface morphology of the {100} faces as will be discussed later. However, no distinct difference was detected in surface morphology between the {111} and the {1̄1̄1̄} faces. Therefore, in this report we shall treat both faces as having the same growth morphology.

Fig. 2.1 shows examples of spiral steps observed on {111} faces. At least three kinds of spiral layers induced by single dislocation outcrops were discerned: single (figs. 2.1a and b) double (fig. 2.1c) and triple spirals (fig. 2.1d). Concentric loops induced by a pair of spirals with opposite signs were also found (fig. 2.1b). The height of each step was determined to be 5 ± 1 , which can be taken as d_{111} (=4.7) within the experimental error. It was noticed that for the multiple spirals the steps are split
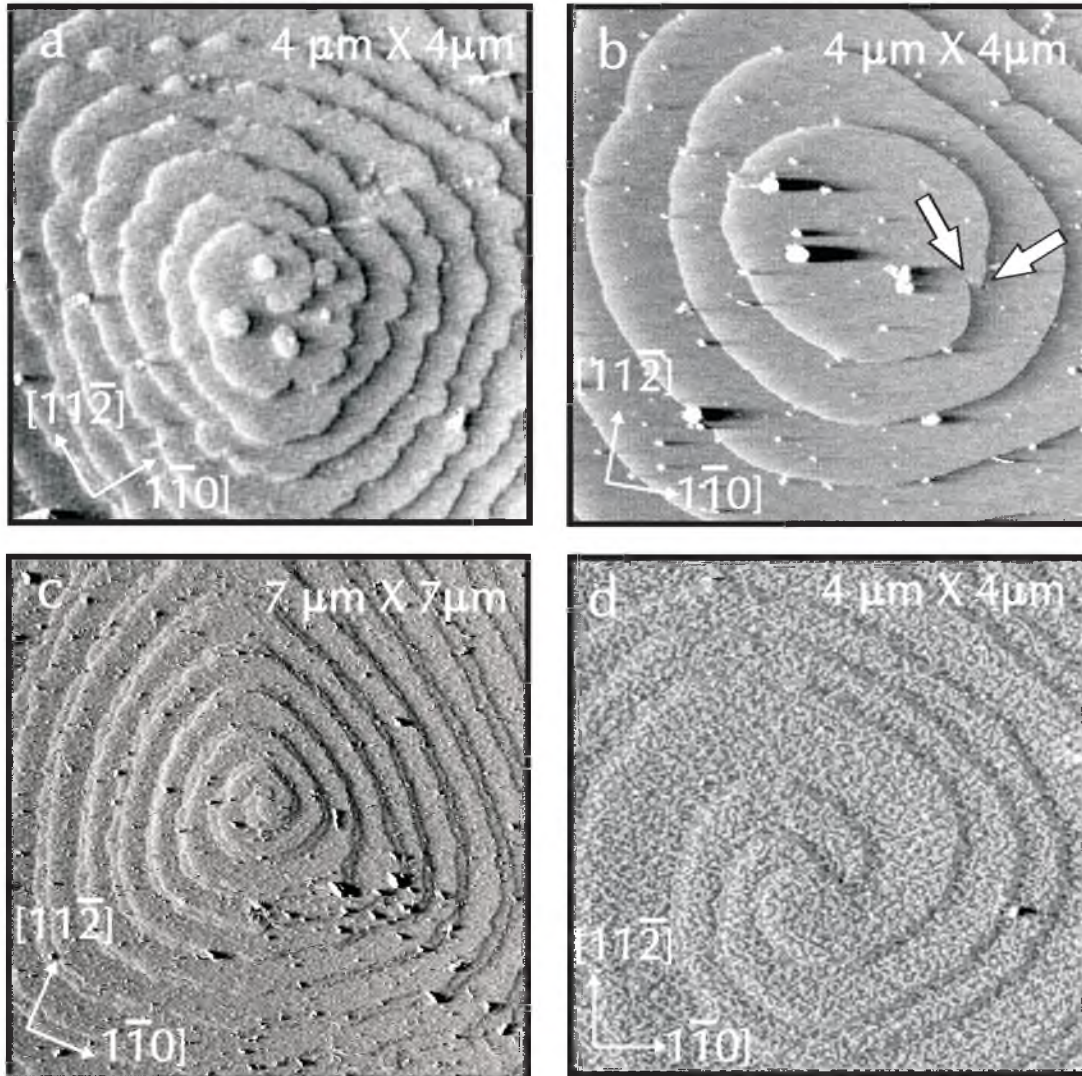
Figure 2.1 Force images of spiral steps observed on $Ba(NO_3)_2$ {111} faces. (a) Single spiral with a few 2D nuclei on top. (b) Concentric closed-loop steps produced by two single dislocations of opposite sign (indicated by arrows). (c) Double spiral with split steps. (d) Triple spiral with split steps and 2D network on top. In all cases the step height is equivalent to d_{111}.

into the unit-height steps d_{111} directly at the spiral centres and that this step separation becomes large far from the spiral centres. From their stress birefringence images, the dislocations corresponding to the double and triple spiral steps were identified as single ones of a mixed and a screw type withBurgers vectors $b = [110]$ and $[111]$, respectively [11, 12]. To avoid complexity, we give here only one representative Burgers vector; for example, $b = [101]$ and $[011]$ are equivalent to $[110]$. It was shown in a previous *in situ* observation of growth hillocks on $Ba(NO_3)_2$ {111} faces [14], that

the activities of growth centres varied depending on the types of corresponding dislocations and growth conditions. Under a high rate of solution flow, triple spirals dominated double ones and single spiral centres were not found. In contrast to the above mentioned investigation, during the present study single spiral layers were frequently observed on the crystals, which were now grown from an unstirred solution (figs. 2.1a and b).
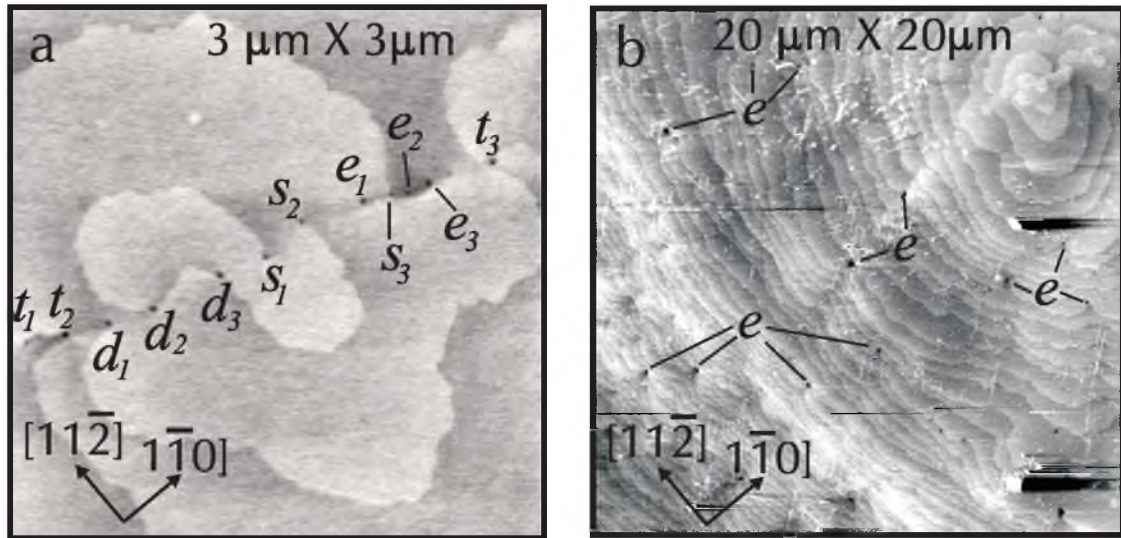
Figure 2.2 Array of dislocations on a {111} face. (a) Height image of single (s), double (d) and triple (t) steps in a growth hillock centre. Co-operative spiral-steps originate from clockwise (d_2, s_2 and t_3) and anti-clockwise (d_1, d_3, s_1 and s_3) dislocations, respectively; step segments between two emerging points of dislocations with opposite signs (t_1t_2, d_2d_3, d_2s_1 and d_3s_2) will develop closed patterns. (b) Lower magnification force image around the region in Fig. 2a, showing holes (e) that retard step propagation.

Often, several dislocation outcrops located closely in an array were observed (fig. 2.2a). Below these dislocations, inclusions of mother solution were correspondingly found; along the dislocation rows complex spiral centres developed (fig. 2.2a). Several characteristic features of spiral growth can be noticed in fig. 2.2a: *i)* single, double and triple steps (denoted by s, d and t, respectively) arising from individual dislocations, *ii)* co-operative spiral steps originating from dislocations with the same sign (d_2, s_2 and t_3 clockwise and d_1, d_3, s_1 and s_3 anti-clockwise), *iii)* step segments between two dislocations with opposite signs (t_1t_2, d_2d_3, d_2s_1 and d_3s_2) which will develop closed loops.

In addition to this, hollow cores were observed at the dislocations. The radii of these varied from 7 to 15 nm. It can be noted that the hollow cores that are accompanied with spiral steps increase in diameter with the number of spiral arms. Another type of hole, namely those that do not emit steps (denoted by e) was also observed. Such holes retard step propagation and cause weak step bunching (fig. 2.2b). Possibly these are hollow cores related to pure edge dislocations. The detailed observation

and the quantitative measurement of the hollow cores will be dealt with elsewhere [26].

{100} faces

Fig. 2.3a shows an example of spiral hillocks observed on an (100) face. The hillock shows an ellipsoidal shape elongated in the [01$\bar{2}$] direction and consists of double layers. The unit layers composing the double layers are 4 ± 1 in height, which is equivalent to d_{200} (= 4.1) within the experimental error. It was noted that step splitting is not so pronounced as on the {111} faces. The cavities with a depth of d_{200} on the terraces between spiral steps are characteristic for the {100} faces. Since besides the cavities also isolated 2D islands were observed on all crystals, these cavities were probably formed by the coalescence of 2D nuclei formed at the high supersaturation during the removal of the crystals from the solution. Hollow cores associated with spiral centres are also observed on this face (fig. 2.3a). The radii of hollow cores, ranging 30 - 50 nm in radius, were larger than those on the {111} faces.

On the {100} faces often another type of growth hillock was observed as shown in Fig. 3b. The hillocks had parallelogram shapes of which the long sides were parallel to [01$\bar{2}$] on an (100) face and, contrarily, parallel to [012] directions on an opposite ($\bar{1}$00) face. Here the indices of the faces and the crystallographic directions are assigned according to Refs. [8, 13]. The remarkable bunching of steps nearly parallel to the long sides of the hillocks is in agreement with the striations observed by Ribet and Authier [8] and is characteristic for an {100} face growing in a stagnant solution. This phenomena was clearly visible after removing the crystal from the solution. The different orientations of the growth hillocks on the opposite (100) and ($\bar{1}$00) faces indicates the
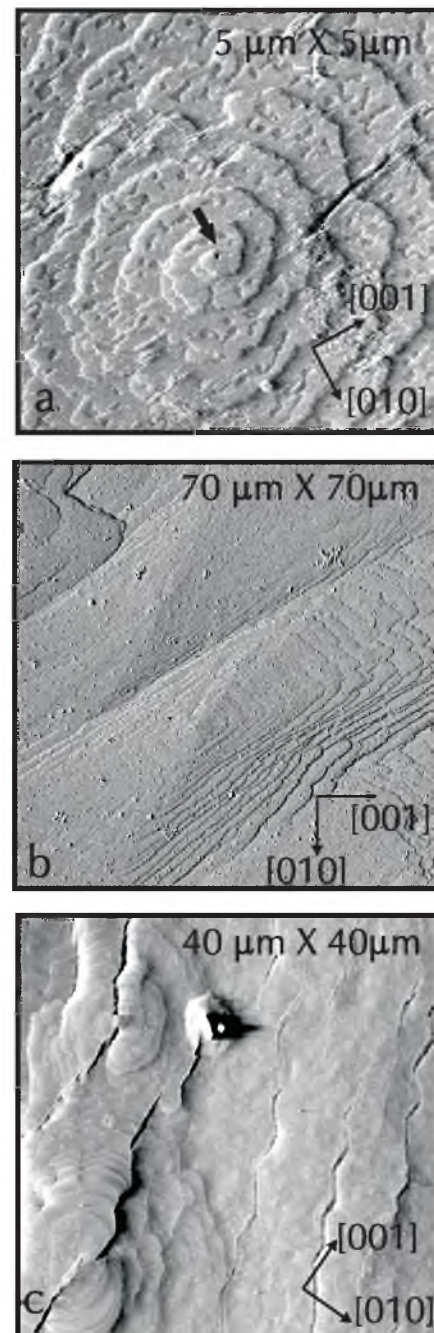
Figure 2.3. Force images of growth hillocks on the $Ba(NO_3)_2$ {100} faces. (a) Double spiral with unit-height cavities in the terraces. The hollow core at the centre of the spiral is indicated by the arrow. (b) Parallelogram-shaped hillock with bunched steps. (c) Growth hillocks intersected by 'cracks'.

absence of centrosymmetric symmetry. Therefore the space group symmetry of $Ba(NO_3)_2$ must be $P2_13$ instead of $Pa3$. The spiral nature of this type of growth hillocks could not be discerned because of the strong bunching.

The polygonized and anisotropic shapes of the growth hillocks on the {100} faces of fig. 2.3b are quite different from those observed during previous experiments in flowing solutions [15] and those shown in fig. 2.3a. A similar change of hillock shapes on the (100) faces of $Ba(NO_3)_2$ in relation with impurity content and supersaturation of a solution was reported by Shekunov et al. [10]. They observed that the shapes of growth hillocks were nearly circular in a purer solution. On the other hand, in a solution containing some amount of impurity, the growth hillocks were rectangular at low supersaturations and became rounded upon an increase in supersaturation.

An example of the most commonly observed type of hillock is shown in fig. 2.3c. The hillocks are intersected by deep 'cracks', which seem to have crystallographic directions. The two hillock sides near a crack often develop differently, which indicates that the crack was created before the hillock. Furthermore, the centres of these hillocks are very high, so that a spiral nature of these hillocks could not be discerned either. The cause of the cracks is not clear yet.

2.3.2 Two-dimensional nucleation

{100} faces

Fig. 2.4 shows growth islands formed by a two-dimensional (2D) nucleation mechanism on an (100) face. The isolated, small islands are elongated along approximately the [01$\bar{2}$] direction, which is the direction of the long side of the parallelogram shaped growth hillocks defined in the previous section. Each growth island has the same height as a unit layer of spiral steps, namely d_{200} = 4.1 . In fig. 2.4, at least four layers of different height level can be recognized: the birth and spread growth mechanism is clearly verified in this picture.

The growth islands covered the {100} faces of all crystals observed ex situ. A kinetic study of the $Ba(NO_3)_2$ (100) faces [15] showed that 2D nucleation takes place at supersaturations above = 0.4% on a surface free from dislocation outcrops. However, on crystal faces on
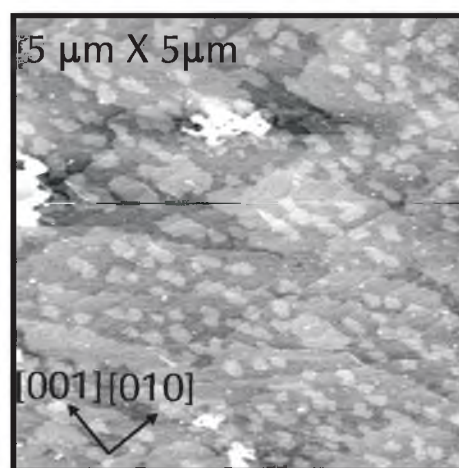
Figure 2.4 Height image of 2D nucleation islands with a height of d_{200} = 4.1 on top of a $Ba(NO_3)_2$ (100) face. The islands are slightly elongated along the [01$\bar{2}$] direction.

which screw or mixed type dislocations emerge, the spiral growth mechanism dominates the 2D nucleation growth up to = 5%. Since during the present study crystal growth was carried out at supersaturations below 4%, it can now be concluded that the 2D nuclei on the surfaces must have been formed during the period of removing the crystals from the growth cell, when 5%.

{111} faces

Fig. 2.5 shows 2D nuclei formed on an {111} face. The successive, parallel steps are spiral steps generated by a dislocation emerging somewhere else on the surface. The sharp bends of the successive steps coincide with the boundary of a droplet of solution that remained on the surface after soaking up the solution from the surface.

The height of 2D nuclei was determined to be 5 ± 1 , which agrees with the height d_{111} of single spiral steps. In contrast with an {100} face, 2D nuclei on an {111} face show nearly circular shapes. It is interesting to note that 2D nuclei were only seen on the relatively large terraces between the spiral steps. This suggests that the undulated fronts of the spiral are caused by a coalescence of the spiral steps and 2D nuclei. In the previous *in situ* observation study of the growth of {111} faces [14], it was found that spiral growth governed the growth of these faces and 2D nucleation was not observed in the experimental range of supersaturation up to 6 %. Therefore, the

Figure 2.5 Force image of 2D nuclei with a height of d_{111} = 4.7 on top of a Ba(NO$_3$)$_2$ {111} face. The successive steps originate from a dislocation elsewhere; the sharp bending of the steps at the centre of the picture corresponds to the boundary of a droplet of solution that remained on the surface after soaking up the solution from the surface.

2D nucleation observed on the {111} faces in this study probably occurred due to a very high supersaturation of at least 6 % during separation of the crystal from the solution at the end of the growth experiment.

2.4 Discussion

2.4.1 Properties and sources of steps

It was confirmed that d_{111} and d_{200} steps on {111} and {100} faces, respectively, were elementary steps in both 2D nucleation growth and spiral growth of $Ba(NO_3)_2$ crystals in an aqueous solution. This result agrees with the Bravais-Friedel-Donnay-Harker (BFDH) laws and the Hartman-Perdok (*i. e.* Periodic Bond Chain) theory [27], which implies that the thickness of a growth layer on a crystal surface is equal to the slice thickness d_{hkl} corrected for the systematic extinctions of the space group. By the studies on lattice defects of $Ba(NO_3)_2$ crystals grown from an aqueous solution [6-10], several types of dislocations have been found. From the fact that for spiral growth the total height of steps emitted by the dislocations must be equal to the component of the dislocation's Burgers vectors b perpendicular to the crystal surface, it follows that three kind of spiral layers are possible on (111) faces, namely *i)* single spiral layers produced by the mixed type dislocations with b = [100] and [$\bar{1}$11], *ii)* double spiral steps produced by the mixed type dislocations with b = [110] and *iii)* triple steps produced by the screw dislocations with b = [111]. Pure edge dislocations with b = [$\bar{1}$10] have also been reported [9] but no spiral step can be formed from such dislocations. The dislocations corresponding to the double and the triple spiral layers as well as the edge dislocations could be identified by polarized microscopy [11, 12].

It is interesting to compare the sizes of hollow cores and the types of spiral centres in relation to the dislocation properties. It has been shown theoretically that the radii of hollow cores at dislocation outcrops depend on, amongst others, the strains of dislocations and the supersaturation during crystal growth [28, 29]. For a given supersaturation, the radii of the hollow cores (if non-zero) are expected to increase with the strain energy of the dislocations which is proportional to the square of the Burgers vector, b^2. Although, unfortunately, the supersaturation at which the final surface morphology was formed is not well known because of a shut-off effect, it can be assumed that dislocation outcrops in a small region of a growing face are exposed to the same supersaturation. In fig. 2.2, as mentioned in section 3.1.1, the radii of the hollow cores increase with the number of spiral layers that are connected with the hollow cores. Of the two dislocations capable to form single spiral centres, namely [100] and [$\bar{1}$11], the first one has a three times lower strain energy. From this, and the fact that the single spirals show the smallest hollow cores, it follows that the dislocations with b = [100] are more likely to be sources of the single spiral steps than those with b = [$\bar{1}$11].

The dislocations with b = [100] were rarely found in the X-ray topographic study [9] and the corresponding single spiral hillocks were not found in the previous *in situ* investigation in a flowing solution [14]. Onuma *et al.* [18] showed that buoyancy driven convection plays a significant role in

the formation of hoppered morphology and liquid inclusions. As mentioned in section 3.1.1, such inclusions are obviously responsible for the high density of the dislocations in the crystal in the present experiment. From the above it is suggested here that the dislocations with b = [100] are formed due to lattice enclosure errors after formation of liquid inclusions.

On the other hand, for (100) faces, the dislocations capable to be spiral step sources are those with b = [100], [110] and [111]. The component of all theses dislocations' Burgers vectors normal to the (100) faces is d_{100} (i. e. two growth layers d_{200}). On the (100) faces, therefore, only the spiral hillocks composed of double elementary layers as shown in fig. 3 are created, regardless of the dislocations source.

2.4.2 Step splitting and activity of spiral hillocks

Step splitting was typically observed for multi-layered spiral steps on {111} faces. De Yoreo et al. [4] reported the same phenomenon on {101} faces of KDP crystals grown in aqueous solutions. The free enthalpy of step edges is expressed as $G = H - TS$, with H being the step enthalpy (which is very close to the step energy), T the growth temperature and S the entropy of the step. Assuming that step overhang does not occur at bunched steps, and assuming a relatively small step separation, the entropy term associated with the kink density increases with the separation between adjacent steps. As a consequence the free enthalpy decreases for increasing step separation and very close steps are not favorable from a thermodynamic point of view [30]. This was confirmed by a recent Monte Carlo simulation of a sequence of steps on the {001} surface of a Kossel crystal in the presence of surface diffusion [31]. At the centre of a spiral consisting of two or three layers the steps are very close to each other and tend to repel each other due to entropy repulsion. This explains the splitting of steps right from the beginning, when they are 'formed' at the spiral centres.

The splitting of spiral steps described above would give rise to the difference in growth rate of individual spiral hillocks as reported in Ref. [14]. Provided that m-layered spiral steps decomposed into elementary steps at the spiral centres, the interstep distance and of m-layered spiral would be $1/m$ of that of single spiral steps on the average and consequently the slope p of the former would be m times as large as that of the latter. From this and the fact that the growth rate R of spiral hillocks is given by $R = pv$ with v being the step velocity, the growth rate of m-layered spiral hillocks should be m times larger than that of single spiral hillock either when the interaction of the diffusion field around the successive steps is insignificant; i. e. the higher the total step height at the spiral centres, the larger the growth rate. On the {111} faces of $Ba(NO_3)_2$, therefore, the triple spiral centres are to be the strongest, the double ones in the second place and the single ones the weakest. This is partly confirmed by the experimental result in Ref. [14]. On the other hand, on {100} faces, such

variation in the growth rate of spiral centres due to the difference of the total step height is not expected because only the double layered steps are formed by dislocations on these faces as mentioned in section 2.4.1.

2.5 Conclusions

AFM is a very powerful method for the *ex-situ* examination of step patterns on the surfaces of crystals grown from solution. By this technique growth steps on monomolecular height on the {100} and the {111} faces of $Ba(NO_3)_2$ crystals grown from aqueous solutions have been imaged and analysed. From these investigations, amongst others, the following can be concluded:

1. Spiral growth and 2D nucleation growth were observed on both the {111} and the {100} faces. It was confirmed that the growth proceeds via the elementary steps that are expected from BFDH and PBC theory: d_{111} and d_{200} on the {111} and the {100} faces, respectively.

2. 2D nuclei observed in this study were probably formed during a period of very high supersaturation when the crystals were removed from the solution.

3. Single and multiple spiral layers arise from dislocation outcrops on the growing faces. Depending on the Burgers vectors of the central dislocation, spirals composed of single, double and triple layers on the {111} faces and double layers on the {100} faces are formed. The multiple steps tend to split into elementary steps, probably due to entropic repulsion.

4. Hollow cores, with radii of 7 - 15 nm on {111} and 30 - 50 nm on {100}, were observed at dislocation outcrops. These radii of hollow cores increase with the number of spiral steps associated with the dislocations.

Acknowledgments

References

[1]   For example, Yu.G. Kuznetsov, A.J. Malkin, W. Glantz and A. McPherson, J. Crystal Growth **168** (1996) 63 and its references.

[2]   A.J. Gratz, P.E. Hillner and P.K. Hansma, Geochem. Cosmochim. Acta **57** (1993) 491.

[3]   S. Manne, J. P. Cleveland, G.D. Stucky and P.K. Hansma, J. Crystal Growth 130 (1993) 333.

[4]   J.J. De Yoreo, T.A. Land and B. Dair, Phys. Rev. Lett. **73** (1994) 838.

[5]   K. Tsukamoto, K. Ohba and I. Sunagawa, J. Crystal Growth **63** (1983) 18.

[6]   M. Ribet, J.L. Ribet, F. Lefaucheux and M.C. Robert, J. Crystal Growth **49** (1980) 334.

[7]   M.C. Robert, F. Lefaucheux, M. Sauvage and M. Ribet, J. Crystal Growth **52** (1981) 976.

[8]   M. Ribet and A. Authier, J. Crystal Growth **57** (1982) 541.

[9]   K. Maiwa, K. Tsukamoto and I. Sunagawa, J Crystal Growth **82** (1987) 611.

[10]   B.Yu. Shekunov, L.N. Rashkovich and I.L. Smolskii, J. Crystal Growth **116** (1992) 340.

[11]   K. Maiwa, K. Tsukamoto, I. Sunagawa, C.-z. Ge and N.-b. Ming, J. Crystal Growth **98** (1989) 590.

[12]   C.-z. Ge, N.-b. Ming, K. Tsukamoto, K. Maiwa and I. Sunagawa, J. Appl. Phys. **69** (1991) 7556.

[13]   L.N. Rashkovich, B.Yu. Shekunov, V.N. Voitsekhovskii and M.V. Shvedova, Sov. Phys. Crystallogr. **34** (1989) 925.

[14]   K. Maiwa, I. Tsukamoto and I. Sunagawa, J. Crystal Growth **102** (1990) 43.

[15]   I. Sunagawa, I. Tsukamoto, K. Maiwa and K. Onuma, Prog. Crystal Growth and Charact. **30** (1995) 153.

[16]   K. Onuma, T. Kameyama and K. Tsukamoto, J. Crystal Growth **137** (1994) 61.

[17]   K. Onuma, K. Tsukamoto and I. Sunagawa, J. Crystal Growth **89** (1989) 177.

[18]   K. Onuma, K. Tsukamoto and I. Sunagawa, J. Crystal Growth **98** (1989) 384.

[19]   W.J.P. van Enckevort, Current topics in Crystal Growth Res. **2** (1995) 535.

[20]   L. Vegard, Z. Physik **9** (1922) 395.

[21]   F.M. Jäger and F.A. van Melle, Proc. Kon. Ned. Akad. Wetensch. **31** (1928) 651.

[22]   W. Hamilton, Acta Cryst. **10** (1957) 103.

[23]   G. Lütz, Z. Krist. **114** (1960) 232.

[24]   H. Nowotny and G. Heger, Acta Cryst. C **39** (1983) 952.

[25]   R. Birnstock, Z. Krist. **124** (1967) 310.

[26]   M. Plomp, K. Maiwa, and W.J.P. van Enckevort., J. Crystal growth **198/199** (1999), 246.

[27]   See, P. Bennema, in: D.T.J. Hurle (Ed.), Handbook of Crystal Growth, 1a. Thermodynamics and Kinetics, North-Holland, Amsterdam, 1993, p 477.

[28]   F.C. Frank, Acta Crystallogr. **4** (1951) 497.

[29]   B. Van der Hoek, J.P. Van der Eerden and P. Bennema, J. Crystal Growth **56** (1982) 621.

[30]   X.-S. Wang, J.L. Goldberg, N.C. Bartelt, T.L. Einstein and E.D. Williams, Phys. Rev. Lett. **65** (1990) 2430.

[31]   N.C. Bartelt, T.L. Einstein and E.D. Williams, Surf. Sci. 312 (1994) 411.

Chapter 3:

Atomic force microscopy observations of hollow cores on the {111} and {100} faces of barium nitrate

Chapter 3:

Atomic force microscopy observations of hollow cores on the {111} and {100} faces of barium nitrate[*]

M.Plomp, K. Maiwa and W.J.P. van Enckevort

RIM Laboratory of Solid State Chemistry, Faculty of Science, University of Nijmegen,
Toernooiveld 1, 6525 ED Nijmegen, the Netherlands

Abstract

The centers of several growth spirals on the dominant {111} and {100} faces of $Ba(NO_3)_2$ crystals grown from aqueous solutions were investigated using ex-*situ* atomic force microscopy. On both faces, often hollow cores were observed, at the outcrops of dislocations with Burgers vectors b = <100> on the {100} face, and b = <100>, <110> and <111> on the {111} face. The occurrence of the hollow cores depends on the supersaturation. For the {111} face, the dependence of the hollow core radius on the Burgers vector is measured. This observed dependence is less strong then the quadratic dependence expected from the Frank radius, which is explained by the influence of the supersaturation. Apart from that, recombination of two dislocations, leaving the hollow cores on the original positions has been observed.

PACS: 61.72Lk, 81.10Dn, 61.16Ch.

Keywords: hollow core, dislocation, barium nitrate, atomic force microscopy.

3.1 Introduction

In the 'scanning probe era', started with the invention of the scanning tunneling microscope and the atomic force microscope in 1982 respectively 1986, many solid state features previously only known in theory or characterized by mean values, could be revealed. One of these features is the empty space formed by the stress field of a dislocation, known as *nano tube* or *hollow core*. The possibility of the occurrence of hollow cores at dislocations with high Burgers vectors has been known for a long time. Frank estimated the size of hollow cores at equilibrium by the introduction of the Frank radius r_f [1], while Cabrera and Levine [2] introduced the strain field of a dislocation in the spiral theory of Burton, Cabrera and Frank [3], resulting in hollow cores. Van der Hoek et al. [4,5] derived the influence of supersaturation and the stress field on the occurrence and diameter of hollow cores. Hollow cores have been observed earlier optically at dislocations with very high Burgers vectors such as SiC [6,4,5]. But now, with AFM, they have been observed at dislocations with Burgers vectors equal to the unit cell length. These small hollow cores are noticed on several crystals, e.g. solution grown KH_2PO_4 [7] and canavalin [8], cleaved L-arginine phosphate monohydrate [9] and MOCVD-grown GaN [10]. We showed earlier the occurrence of these hollow cores on the {111} and the {100} faces of $Ba(NO_3)_2$ during a study of the growth mechanisms on these faces [11]. Here, we present detailed size measurements of these hollow cores in order to verify the predicted dependence of the hollow core radius on the Burgers vector.

3.2 Experimental

$Ba(NO_3)_2$ crystals were grown from seeds in an unstirred aquous solution with a saturation temperature of 23.0 °C at temperatures above 21.4 °C, which corresponds to supersaturations < 4%. Prior to AFM observation, the crystals were quickly removed from the solution and dried immediately with highly water-absorbing paper to preserve the as-grown faces as good as possible. The recorded AFM images are partly height images, partly force images, which can be regarded as the derivative of height images. Further details of the experimental procedure are given in [11].

3.3 Results

The height of the lowest observed steps on the {111} and {100} $Ba(NO_3)_2$ surfaces is 5 ± 1 resp. 4 ± 1 , which is conform the elementary step heights $d_{111} = 4.7$ and $d_{200} = 4.1$ as predicted by Bravais-Friedel-Donnay-Harker laws and the Hartman-Perdok theory.

As elaborated in [11], on the {111} faces three types of spiral layers belonging to dislocations with different Burgers vectors are possible, which follows from the rule that for growth spirals the total height of the emitted steps per turn has to match the component of the Burgers vector **b** perpendicular to the surface. These spiral types, which all have been observed [12], have *i)* three spiral arms, produced by screw dislocations with **b** = [111]; *ii)* two arms, originating from **b** = <110> mixed dislocations; and *iii)* a single spiral arm, created by mixed dislocations with **b** = <100>. Apart from that, pure edge dislocations with **b** = [110] are reported [12], not resulting in spiral steps. On the (100) face, all the dislocations being capable to form spiral steps (**b** = [100], **b** = [110] and **b** = [111]) have a screw component [100] and therefore will all form spirals with two d_{200} steps.
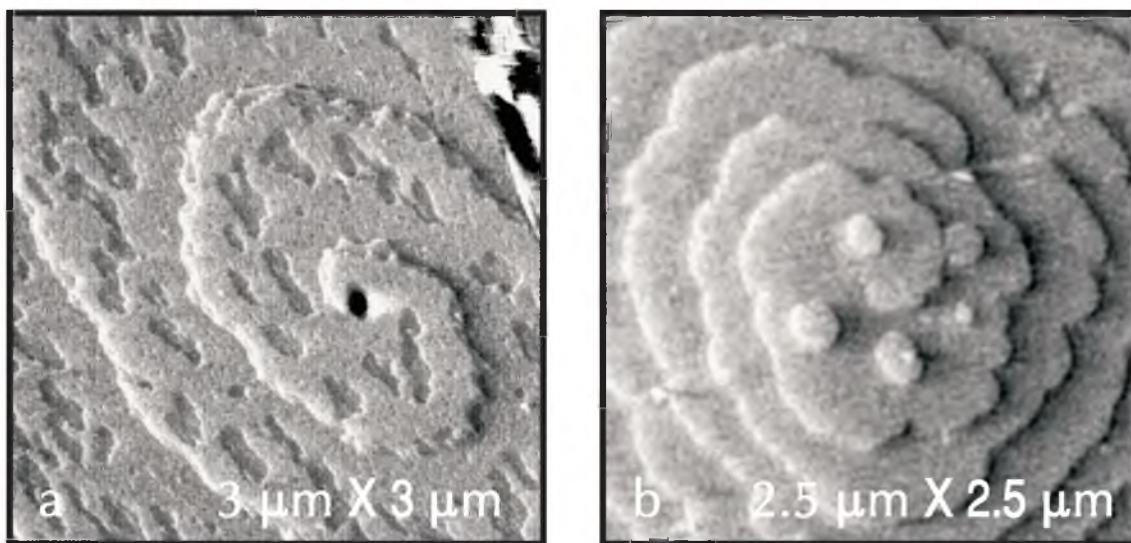
Figure 3.1 (a) Double-stepped spiral on the {100} face exhibiting a 0.15 μm wide hollow core. The upper spiral layer is partly eroded. (b) Single-stepped spiral on the {111} face without hollow core showing a few 2D nuclei on top.

All the spiral centers we observed on the {100} faces and of which we could determine the number of steps originating from the center, exposed two steps, and thus were all 'single Burgers vector' dislocations. On the {111} faces, all but one observed spiral centers exhibited one, two, or three steps and proved to be 'single' dislocations as well.

At about half of the observed spiral centers hollow cores were found. Examples of the presence of a hollow core at a double step dislocation on a {100} face and the absence of hollow core at the center of a on a single step spiral on a {111} face are given in fig. 3.1. If spirals are situated close to each other (*i.e.* typically within 100 micrometer), they exhibit the same hollow core behavior; if they are located in a different region of the crystal face (which is a few mm wide), they sometimes show differences in the presence or absence of a hollow core, while similar dislocations on different crystals do not correlate at all in having a hollow core. For this reason it is concluded that the presence/absence of a hollow core is governed mainly by the supersaturation, which has been different for all crystals during the short period of separation from the solution. Therefore, a good comparison of the hollow cores observed on different crystals cannot be made. The hollow cores observed within one AFM scan (max. 75 μm X 75 μm) however, can be compared with each other. Often the inspected dislocations are grouped together, one of the most favorable groupings being a dislocation row. This indicates that the dislocations originate from the same crystal defect. Indeed, repeatedly inclusions have been seen beneath the dislocation groups at the crystal surface, indicating again a common source for the dislocations.

The center of a composite spiral which is part of such a dislocation row on a {111} face is depicted in fig. 3.2a. It is formed by a higher density of dislocations then in the rest of the row. Fig. 3.2b shows the highest point of the spiral, revealing single, double and triple stepped dislocations, all exhibiting a hollow core. Of 14 of these hollow cores (8 <100>, 3 <110> and 3 <111> dislocations) the core radius r_{hc} was measured in order to verify the theoretical quadratic Burgers vector dependence as proposed by Frank [1].

Despite of the large visible contrast between the hollow cores and their surroundings, great care should be taken in interpreting the measured sizes as real hollow core widths, because of the combination of *i)* the trumpet-shaped hollow core outcrop described by Frank [1] and Srolovitz and Safran [13] and *ii)* the AFM tip radius of 50 nm limiting the size measurement to this crater region and the measured depth to 1 nm. Combined TEM and AFM hollow core measurements on GaN confirm the existence of such craters, and indicate that the actual hollow core radii are 2 to 10 times smaller than the measured ones [14]. Comparing the tip radius of 50 nm with the calculated Frank radii, and relating these with the calculated crater profiles of [1] and [13], it is expected that though the measured radii are indeed larger than the actual hollow core radii, the relative differences in the series of the actual hollow core sizes are still reflected in the series of measured radii.
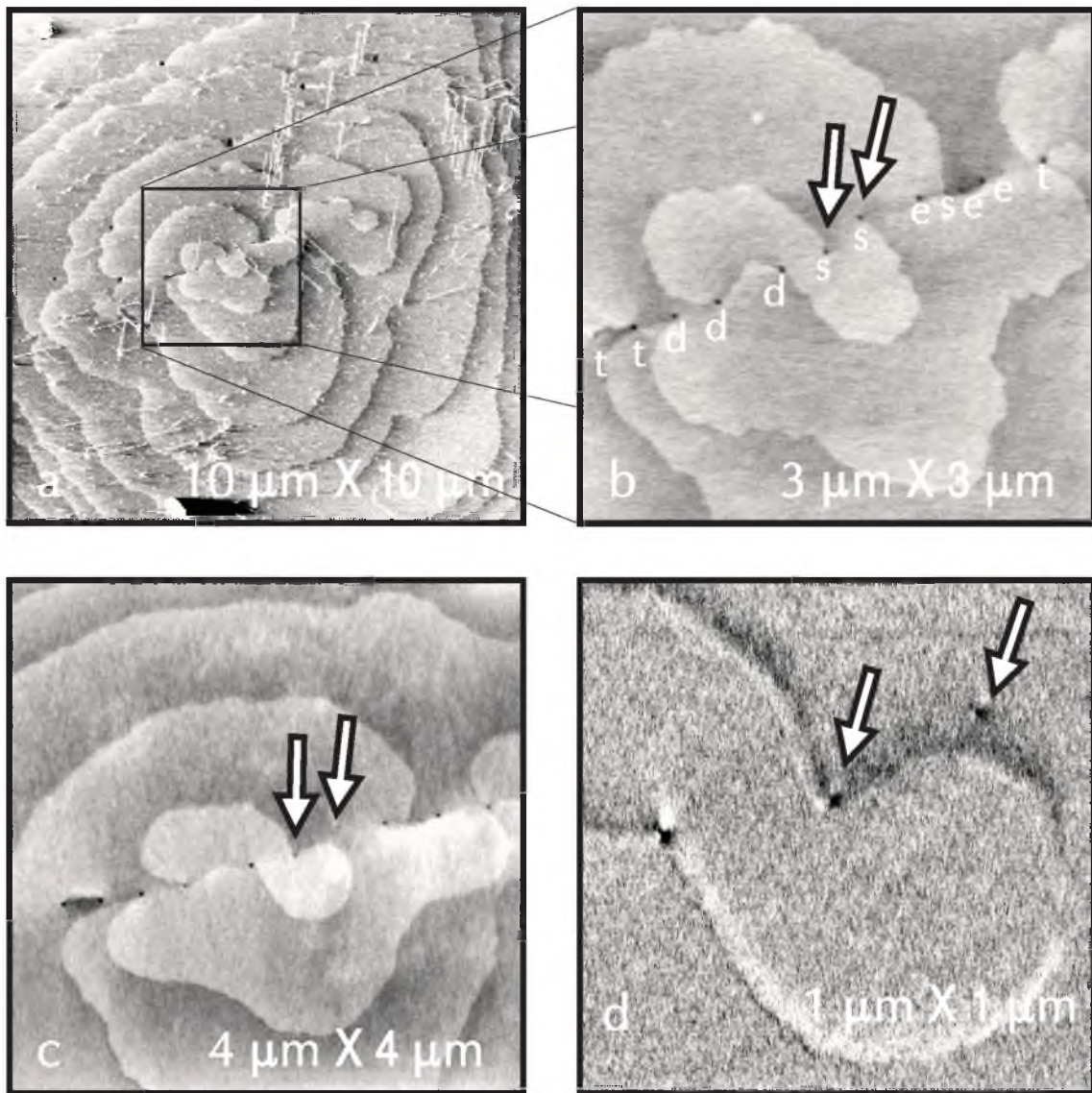
Figure 3.2 (a) Part of a dislocation row on the $Ba(NO_3)_2$ {111} face. (a) 10 μm image showing the center of one composite growth spiral along the row. (b) Enlarged image showing hollow cores at the dislocation centers. The type of dislocation is indicated with s (single-stepped), d (double-stepped), t (triple-stepped) and e (edge dislocation). (c) The same area imaged one month later, exhibiting step relaxation and dislocation recombination (indicated by arrows in (b) and (c)), which is more clearly shown in the enlarged image of (d).

The results of the measurements are depicted in fig. 3.3 on a double logarithmic scale together with a fit

$$r_{hc} \quad a(\frac{b}{\sqrt{K}})^{p} \tag{3.1}$$

in which r_{hc} is the measured hollow core radius, $b = |\boldsymbol{b}|$ is the length of the Burgers vector in units of d_{100}, K is a geometrical constant indicating the screw/edge character of the dislocation [4], and a and p are the fitting parameters. The results are dealt with in the discussion part of this paper.

Fig. 3.2c shows the same region after storing the crystal for one month in an exicator. What can be noticed directly is the relaxation of steps, leading to more rounded shapes which diminish the total step energy. Another interesting feature is the recombination of dislocations as shown in the detailed scan fig. 3.2d: Two single dislocations of opposite sign are merged together; leaving behind two 'empty' hollow cores and a step. One of the hollow cores now acts as a pinning point for the new step.
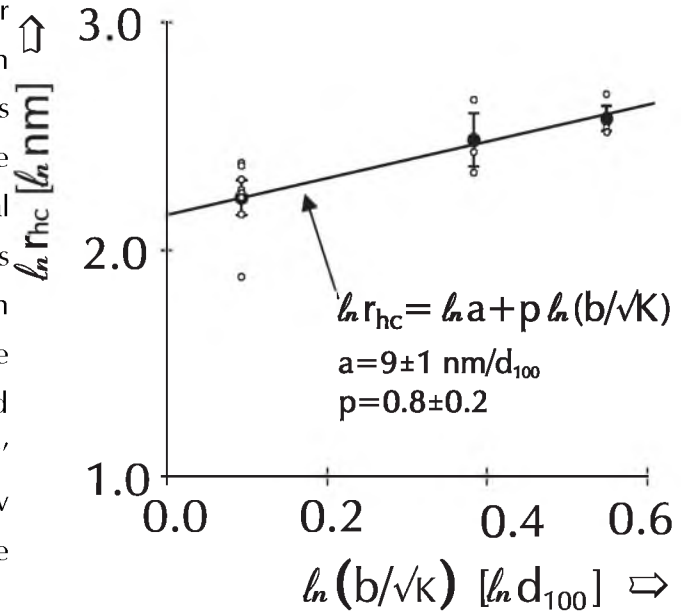
Figure 3.3 Hollow core radii of 14 hollow cores in the dislocation row of fig. 3.2 as a function of the length of the Burgers vector b for the three types of dislocations b_{100}, b_{110} and b_{111}. The constants a and p of the fit are calculated using the function $r_{hc} = a(b/K)^p$.

3.4 Discussion

A first estimate for the size of the hollow core is the Frank radius r_f, given by [1]

$$r_f = \frac{Gb^2}{8\pi^2 K\gamma} \ ,$$

(3.2)

where G is the shear modulus, γ is the edge free (expressed in energy per unit area), and K is the constant indicating the type of dislocation given by

$$\frac{1}{K} = \cos^2\psi + \frac{\sin^2\psi}{1-v} \ ,$$

(3.3)

in which ψ is the angle of b with the dislocation line direction and v is Poisson's ratio. $K=1$ for a pure screw dislocation and $K=1-v$ for a pure edge dislocation. ψ is calculated using the known angle α between and the surface normal n [12]. For the dislocations outcropping on the face {111} this results in $\psi=0$ for $b=<111>$, $\psi=19.0$ for $b=<110>$ and $\psi=33.7$ for $b=<100>$ For v a value

of $v = -S_{21}/S_{11} = 0.41$ is taken (S_{pq} are the elastic compliance constants closely related to the stiffness constants C_{ij}, see below), which results in $K=0.83$ ($b=<100>$), $K=0.93$ ($b=<110>$) and $K=1$ ($b=<111>$) for dislocation outcrops on the {111} face. The elastic constants v and G were obtained from the stiffness constants $C_{11}= 29.25$, $C_{12}=20.65$ and $C_{44}=12.77$ 10^9 N/m^2 [15]. For the anisotropic Ba(NO$_3$)$_2$ an average value for G is found with [16]

$$G \quad C_{44} \ 0.2H \quad C_{44} \ 0.2(2C_{44} \ [C_{11} \ C_{12}]) \quad 9.4 \ 10^9 \ N/m^2 \qquad (3.4)$$

where H is the 'anisotropy term'. Values for γ ($\gamma=24 \ 10^{-3}$ J/m^2 for the {111} face and $\gamma=6.6 \ 10^{-3}$ J/m^2 for {100}) are obtained from earlier experiments [17].

Table 3.1 Calculated Frank radii r_f compared with measured radii, r_{hc} and radii $r_{hc,calc}$ calculated according to (3.5).

Burgers vector b	outcrop face	calculated r_f [nm]	calculated $r_{hc,calc}$ [nm] acc. to (5)	measured r_{hc} [nm] (figs. 3.1,2)
<100>	{100}	11.9	9.3	
<110>	{100}	31.9	21.2	75 (fig. 1a)
<111>	{100}	52.0	30.5	
<100>	{111}	5.0	0	0 (fig. 1b)
<100>	{111}	5.0	2.3	9 (fig. 2)
<110>	{111}	8.0	3.1	12 (fig. 2)
<111>	{111}	9.8	3.7	13 (fig. 2)

The calculated values of r_f for the different dislocation types ending on the {111} and {100} faces as calculated with eqn. (3.2) are given in table 3.1 and are compared with the averaged values of the measured hollow core radii r_{hc} in fig. 3.4. As can be seen from this table, the order of magnitude of the measured radii resembles the calculated ones. Also, the trend of increasing hollow core radii for increasing Burgers vector lengths is clearly seen. However, the relation between r_{hc} and b appears not to be quadratic, as is shown by the logarithmic fit in fig. 3.3. This fit according to relation (3.1) gives $a=9\pm1$ nm and $p=0.8\pm0.2$ which means that r_{hc} increases linearly with b.

A better estimation can be made if a non-zero supersaturation and a non-elastic dislocation core is taken into account. This is done by van der Hoek et al. [4], resulting in

$$(\frac{r_{hc}}{r_c}-1) = \frac{r_f}{r_h^2}\frac{r_{hc}}{1-r_{hc}^2/r_h^2} , \qquad (3.5)$$

where r_h is the Hooke radius which indicates the boundary of elastic to non-elastic behavior in the core region, and r_c is the critical nucleus given by

$$r_c = \frac{\Omega\gamma}{\Delta\mu} \qquad (3.6)$$

Figure 3.4 Absolute (lower part) and scaled (upper part) sizes of the calculated $r_{f,calc}$ and $r_{hc,calc}$ and the measured r_{hc} for dislocations ending on the {111} face.

where Ω is the molecular volume and $\Delta\mu$ is the supersaturation. A rough estimation of r_h is $r_h = 3b$, which leads to $r_h = 2.4$ nm, 3.4 nm and 4.2 nm for the {111} face dislocations with $b = <100>$, $<110>$ and $<111>$, respectively. r_c is estimated from [2]

$$d_s = 19r_c , \qquad (3.7)$$

where d_s is the step distance between the spiral arms of single spiral. Because of the many interfering steps in fig. 3.4, the estimation of $r_c = 30 \pm 10$ nm is a rough one. The resulting values $r_{hc,calc}$ are given in table 3.1. The expected influence of a non-zero supersaturation is to diminish $r_{hc,calc}$ compared to r_f, resulting in lower absolute values than the measured ones. This can be explained easily by the 'trumpet effect' mentioned above. In order to compare the relative size of the hollow cores rather than the absolute size r_{hc}, r_f and $r_{hc,calc}$, in fig. 3.4 these values are scaled on r_{hc} for $b = <100>$. The supersaturation-corrected values resemble the measured values significantly better than the equilibrium r_f values.

The same procedure of calculating r_c with the help of equation (3.7) can be applied for the spiral of fig. 3.1b. The result is $r_c = 12$ nm. With the already calculated values for r_h and r_f, it follows from the phase diagram in [4] that no hollow core is possible for this large supersaturation. This is exactly what is observed in fig. 3.1b. The calculation of the hollow core diameter on the {100} face of fig. 3.1a gives, with $r_c = 45$ nm, a value of $r_{hc,calc} = 9$, 21 or 31 nm, depending on the (unknown) type of dislocation involved. Keeping the ratio of measured and calculated hollow core radii on the {111}

face in mind, it is concluded that the spiral of fig. 3.1a with $r_{hc}=75$ nm is probably caused by a <111> dislocation. The hollow core sizes of fig. 3.1 are also given in table 3.1.

The moved dislocation of fig. 3.2d proves that dislocations can move despite the stabilizing force of the hollow core. All the other, not moved dislocations of fig. 3.2c indicate however, that in the case of Ba(NO$_3$)$_2$ this is not a likely process, even if the dislocations are closely spaced.

3.5 Conclusions

The size of hollow cores on the {100} and {111} faces of Ba(NO$_3$)$_2$ is strongly dependent on the Burgers vector and the supersaturation, and can be estimated reasonably well by the Frank radius r_f. For a better estimate of the relative hollow core size of dislocations with different Burgers vectors the method of van der Hoek [4] et al. should be applied.

References

[1]   F.C. Frank, Acta Cryst. **4** (1951), 497.

[2]   N. Cabrera and M.M. Levine, Phil. Mag. **1** (1956), 450.

[3]   W.K. Burton, N. Cabrera and F.C. Frank, Phil. Trans. Roy. Soc. London **A243** (1951), 299.

[4]   B. van der Hoek, J.P. van der Eerden and P. Bennema, J. Crystal Growth **56** (1982), 621.

[5]   B. van der Hoek, J.P. van der Eerden, P. Bennema and I. Sunagawa, J. Crystal Growth **58** (1982), 365.

[6]   I. Sunagawa and P. Bennema, J. Crystal Growth **53** (1981), 490.

[7]   T.A. Land, A.J. Malkin, Yu.G. Kuznetsov, A. McPherson and J.J. De Yoreo, Phys. Rev. Lett. **75** (1995), 2774.

[8a]   I. Smolski, J.J. De Yoreo, N.P. Zaitseva, J.D. Lee, T.A. Land and E.B. Rudneva, J. Crystal Growth **169** (1996), 741.

[8b]   J.J. De Yoreo. T.A. Land and J.D. Lee, Phys. Rev. Lett. **78** (1997), 4462.

[9]   K. Sangwal and F. Sanz, Cryst. Res. Technol. **32** (1997), 261.

[10]   F.K. de Theije, A.R.A. Zauner, P.R. Hageman, W.J.P. van Enckevort and P.K. Larsen, J. Crystal Growth **197** (1999), 37.

[11]   K. Maiwa, M. Plomp, W.J.P. van Enckevort and P. Bennema, J. Crystal Growth **186** (1998), 214.

[12]   K. Maiwa, K. Tsukamoto, I. Sunagawa, J. Crystal Growth **82** (1987), 611.

[13]   D.J. Srolovitz and S.A. Safran, Phil Magazine A, **52** (1985), 793

[14]   W. Qian, G.S. Rohrer, M. Skowronski, K. Doverspike, L.B. Rowland and D.K. Gaskill, Appl. Phys. Lett. **67** (1995), 2284.

[15]   S. Haussühl, Phys. Stat. Sol. **3** (1963), 1072.

[16]   J.P. Hirth and J. Lothe, *Theory of Dislocations* (second edition), Wiley, New York, 1982, p. 430.

[17]   K. Maiwa, I. Tsukamoto and I. Sunagawa, J. Crystal Growth **102** (1990), 43.

Chapter 4:

Atomic force microscopy studies on the surface morphology of {111} tabular AgBr crystals

Chapter 4:

Atomic force microscopy studies on the surface morphology of {111} tabular AgBr crystals*

M. Plomp, J.G. Buijnsters, G. Bögels, W.J.P. van Enckevort

RIM Laboratory of Solid State Chemistry, Faculty of Science, University of Nijmegen, Toernooiveld 1, 6525 ED Nijmegen, the Netherlands

D. Bollen

Agfa-Gevaert NV, Septestraat 27, B-2640, Mortsel, Belgium

Abstract

Both ex *situ* and *in situ* atomic force microscopy have been applied to study the {111} and {100} surfaces of tabular silver bromide crystals grown from dimethyl sulfoxide-water solutions. This resulted in observations of monosteps, macrosteps, etch pits, pinning of steps and nucleated crystals showing twin planes. These examinations indicate that the growth and dissolution of both the {100} and the polar {111} faces occur via steps in many configurations. The registered 40-nm distance between the parallel twin planes of the nucleated crystals agrees with transmission electron microscopy measurements done on tabular crystals grown by the industrial double-jet precipitation method.

4.1 Introduction

Because of their importance for the photographic industry, tabular silver bromide crystals have been studied intensively for the last four decades. Their tabular shape, and thus a relatively large surface, permits the use of less silver for the production of photographic emulsions compared to block-shaped crystals. Although the experimental conditions at which {111} tabular crystals are formed are well-known in industry, the preferential lateral growth of these crystals is thought to be understood only for a couple of years. An important step in the understanding of the AgBr growth mechanism was the possibility of growing large tabular crystals, up to centimetres in size, from dimethyl sulfoxide (DMSO) [1]. The side faces of these large tabular crystals could be studied in great detail [2] compared to the side faces of the μm-sized crystals grown by the industrial precipitation method. The relation between the crystals grown from DMSO and other crystallization techniques (industrial double-jet precipitation, vapour growth) was explained in another study [3].

The key factor in the development of tabular crystals is the occurrence of twin planes parallel to the {111} top and bottom faces, which are formed during precipitation. These twin planes confine a number of fast growing {100} and slowly growing {111} faces. The relatively fast growing {100} faces present between the twin planes cannot grow out of the crystal habit. Instead, these {100} planes enhance the growth of the neighbouring {111} side faces by supplying substeps to these neighbouring faces at the twin plane position. This will increase the growth rate of the whole crystal side and thus tabular crystals will be formed [2].

The elementary photographic process taking place in silver halide crystals is known to be influenced by the surface morphology [4]. Kinks in surface steps can play a role in the formation and expansion of the silver clusters forming the latent image centres. For this reason, studying the surface morphology of tabular crystals may lead to useful information about the photographic process. Because crystals grown from the double-jet precipitation method have a size of the order of micrometres, it is difficult to investigate their surface morphology by optical microscopy. Scanning electron microscopy is not the ideal tool to study steps on surfaces, unless elaborate and indirect decoration techniques are used [5]. Therefore, scanning probe microscopy (SPM) is the most suited tool to examine the AgBr crystal face morphology. Because AgBr is non-conducting, scanning tunnelling microscopy (STM) can only be applied for extremely thin AgBr films [6]. This leaves atomic force microscopy (AFM) as the most suited instrument to probe AgBr crystals.

On the surfaces of {100} and {111} thin films of AgBr, grown by vapour deposition on cleaved NaCl or mica substrates, atomic resolution could be obtained using AFM in air [7, 8]. Some measurements suggest unreconstructed surfaces [7], which is unexpected for the {111} surfaces, because this implies that these surfaces are terminated by layers consisting of predominantly one type of ion,

which is energetically not favourable. In these studies, steps and growth spirals are encountered on the {100} face. Other experiments indicate reconstructed {111} surfaces, with an upper layer consisting of rhombic or hexagonal patterns of one type of ion [8], which agrees with reconstruction models proposed earlier [9].

A number of AgBr surface investigations using AFM have been carried out for cubic, octahedral [10][8] and tabular [11] [12][8] microcrystals. All these crystals were grown from gelatine suspension, which was removed prior to the AFM studies. Often only roughness measurements could be carried out on these small crystals: apart from some hillocks [11], steps or other growth features normally could not be observed. This indicates that the observed faces are very flat without macrosteps or many growth hillocks. Another factor explaining the missing of steps in the AFM topographs could be the presence of some residual gelatine, which is indicated by infrared spectroscopy [11], leading to a surface roughening that hides any small scale surface structures. Atomic scale measurements show reconstructed {111} faces in air [8][12] and unreconstructed {111} faces in water [12].

In situ AFM [13] has been used to measure surface changes on small tabular AgBr crystals upon the addition of KI solution. These experiments showed rapid three-dimensional growth of (probably) AgI, mainly at the edges of the tabular crystals. On small scales, steps with a height varying from 2 to 30 nm were noticed. Another *in situ* AFM experiment involved the growth and dissolution of silver halides on top of an evaporated Ag layer in an electrochemical environment [14]. Several surface structures were reported, as well as atomic resolution images showing surface reconstruction.

At this moment the most suitable environment for the investigation of the solution growth of tabular AgBr crystals is the DMSO-H_2O-KBr-AgBr system [1], from which crystals up to 1000 times larger than in conventional systems can be obtained. However, despite the production of large crystals, the growth conditions in the DMSO system are not all quantitatively defined, because the thermodynamics and hence the supersaturation in this complex four-component system is not known. Moreover, effects due to evaporation or creeping of solution, sensitivity to light, formation of various AgBr complexes, secundary nucleation and blocking of growth by impurities worsen the situation even more. Therefore, in this study the supersaturation can only be defined in simple terms like 'large', 'small', 'near equilibrium' and 'negative'.

The aim of this work is to gather a qualitative understanding of the processes that take place on the surfaces of tabular AgBr crystals during growth, equilibrium and dissolution in the DMSO system. Since this system is used to get better understanding of the growth of AgBr crystallites from (gelatine) aqueous systems, this research also provides some insight in the growth of AgBr crystals in the photographic industry. The surface examinations are carried out by making use of atomic force microscopy. *Ex situ* AFM was applied to examine larger-scale features. Since the smallest features, e.g. mono-molecular steps, were obscured by artifacts produced during separation of the crystals

from solution, *in situ* AFM was applied for examining the smallest-scale patterns.

Most observations are carried out on the {111} top faces. The *ex situ* measurements reveal large step bunches. Apart from the observations on the {111} top faces, some{100} side faces of AgBr tabular crystals were imaged. For the imaging of atomic steps *in situ* AFM appears to be necessary. Finally, precipitation was observed *in situ*.

4.2 Experimental

Tabular AgBr crystals used for investigation by AFM were grown from DMSO solution. DMSO (in combination with KBr) is used because of its high solubility for AgBr. To a stirred solution of 0.2 M AgBr and 0.2 M KBr dissolved in DMSO, drops of a 3:1 DMSO:water mixture were added until a precipitate was formed. Then the stirring was stopped and the mixture was kept in the dark at room temperature. Owing to physical ripening only the crystals exhibiting preferential growth will grow out at the cost of the untwinned crystals. After one month the tabular crystals have reached diameters up to about one cm, while their aspect ratio is about 100. It is clear that the growth conditions were close to equilibrium, *i.e.* the supersaturation was low. At this stage, individual crystals were taken out of the vessel carefully, rinsed with pure DMSO for two minutes, gently placed on the AFM sample holder using double-sided tape and carefully dried with a paper tissue. After the rinsing and drying, which both were performed in order to minimize the shut-off effect caused by dissolved AgBr and KBr in the mother liquor, the *ex situ* AFM measurements were performed.

For the *in situ* measurements, a saturated solution with approximately the same concentration as that of the mother liquid from which the tabular crystals were grown was used. For the etching experiments a slightly undersaturated AgBr solution was obtained by adding a few droplets of 1.0 M KBr in DMSO to the mother solution. After the sample holder containing the crystal was placed in the AFM liquid cell, the solution was transported into this cell by a syringe and tubes. The liquid cell is connected with the AFM piezo scanner via a latex membrane, in order to keep the cell solution tight and still retain some freedom of lateral movement of the crystal, which is necessary to position the AFM tip above the crystal under investigation.

To image the side faces of AgBr crystals, several crystals with relatively low aspect ratios of about 4, grown from a solution of 1.0 M AgBr and 1.0 M KBr dissolved in DMSO, were used. These were fixed on the sample holder with synthetic clay instead of tape, in order to position one of their side faces horizontally, which is necessary for AFM observation.

The *in situ* investigations turned out to be quite difficult and many problems were encountered: *i)* The DMSO used to dissolve AgBr is a polar organic solvent, that appeared to penetrate slowly the

latex membranes closing the fluid cell; *ii)* The laser used for the AFM tip deflection measurement (λ = 670 nm) caused local latent image formation of the crystals, leading to visible local black spots in the crystals; *iii)* In the beginning of an *in situ* experiment, the AFM tip could not be kept in the feedback loop for more than several seconds. After one hour, this period was extended to about one minute, enabling AFM imaging. This effect may be caused by movements of the crystal, latent image formation, small particles flowing in the solution, and/or crystal growth effects on the AFM tip itself. The AFM used was part of a Topometrix TMX 2000 system. SiN cantilevers with a length of 200 μm and a force constant of about 0.03 N/m were applied. For the *in situ* measurements, an electrochemical fluid cell (without any electrodes) and coated cantilevers were used.

4.3 Results

4.3.1 *Ex situ* imaging of the {111} top face

The most striking step pattern present on the {111} top face of the planar AgBr crystals can already be observed with optical microscopy. It is the occurrence of large bunches or macrosteps, mostly moving from the crystal edges towards the centre of the surface. These macrosteps are always broken up into hexagonal faceted parts parallel to the <110> directions with a length of about 50 μm, as shown in fig. 4.1a. Moreover, successive macrosteps break up at the same positions, leading to narrow grooves between the hexagonal faceted parts. When AFM is used to examine these macrosteps, this leads to typical pictures as shown in fig. 4.1b. Here, the rows of faceted steps with the narrow grooves in between can be recognized immediately. The macrosteps are parallel to the <110> directions on the {111} faces. A height profile along the central step row is depicted in the inset. Fig. 4.1c shows that the step bunches often originate from the edge of the crystal. The angle of inclination of the observed bunches is typically 2 to 3 . Their height can go up to 200 nm, which is 600 times the interplanar distance of the {111} planes (0.334 nm). A whole range of smaller steps is observed as well. Steps of a few molecular heights could not be detected, but this is probably caused by the present surface roughness rather than by the absence of these steps.

This surface roughness is mainly caused by a rapid crystallization of the KBr present in the mother solution during separation of the crystal from that mother solution. The impact of this shut-off effect is best illustrated on a relatively flat part of a crystal, as is shown in fig 4.1d. Here, a network of KBr can be seen on the {111} AgBr top face. The KBr ions present in the thin layer of DMSO adhering to the crystal surface after separation from the solution, crystallize preferentially at existing steps upon evaporation of the DMSO layer. This leads to decoration of the existing AgBr step pattern by KBr ridges of about 30 nm high. In between the decorated steps, three-dimensional KBr nuclei of about

the same height are formed, as can be seen in fig. 4.1d. To obstruct the shut-off effect as much as possible, the ex *situ* samples are usually rinsed with pure DMSO before imaging. This results in the vanishing of the KBr decoration, but a AgBr shut-off effect is often still present.
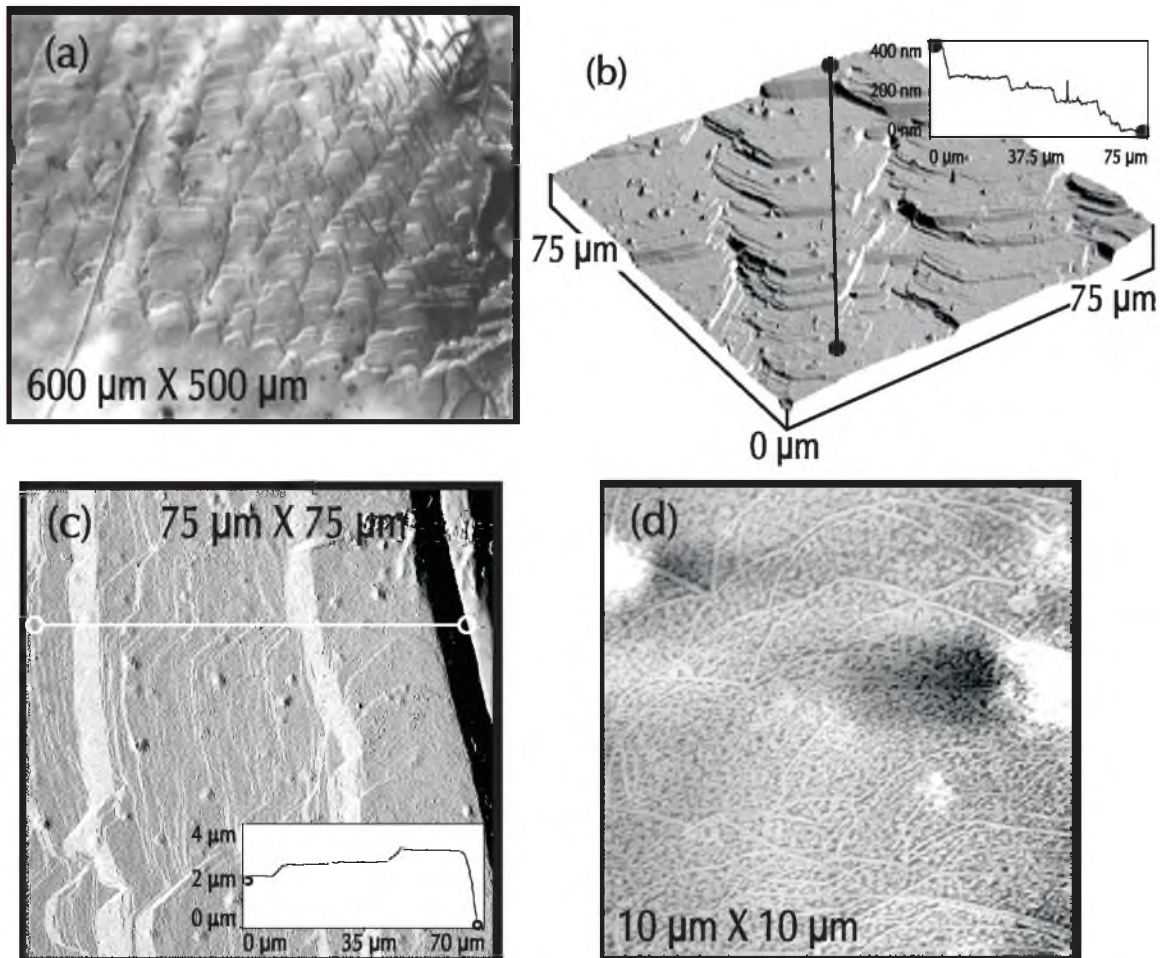
Figure 4.1 Faceted macrosteps on the {111} top face of tabular AgBr crystals observed *ex situ* using (a) optical microscopy and (b,c) AFM. (b) Rows of macrosteps with grooves inbetween. (c) Bunches growing from the edge (upper right) towards the centre of a crystal plate. Insets in (b,c) show height profiles along the lines indicated in the figures. (d) Decoration of lower AgBr steps with KBr at flat parts of a {111} crystal surface.

In order to observe the growth patterns on the {100} side faces, tabular crystals with the smaller aspect ratio of about 4 were used. These were placed in synthetic clay with the side face of interest in a horizontal position to enable AFM measurements. Fig. 4.2 shows a series of images depicting large bunches on a {100} side face. The large bunches have a height of about 250 nm, a smaller step in between has a height of 25 nm as can be concluded from the height profile of the inset in the

figure. The inclination angle of the large bunches is 6 ; the smaller step has an angle of 3 . The large bunches have, except for some pinned areas, <100> directions, while the smaller bunches are randomly oriented. Again, the lowest steps are obscured by the shut-off effect.

In order to be able to image monomolecular steps, *in situ* observations have been carried out.

4.3.2 *In situ* imaging of the {111} top face

As explained in the experimental section, the last preparation step before ex *situ* imaging consists of rinsing in DMSO, followed by careful drying, to prevent shut-off effects. When a thin film of DMSO containing AgBr is left on the surface, this leads to crystal growth during ex *situ* AFM imaging due to DMSO evaporation. An example of this 'semi *in situ*' AFM imaging is given in fig. 4.3. The three successive images of the same area are scanned with a time interval of four minutes. In the middle part of the area a very flat region develops occupied only by monosteps. At the left, right and upper parts of the image these monosteps seem blocked, leading to bunches of 10 to 20 nm high and a steepness of 2 to 3 . This blocking is quite irregular and goes together with the occurrence of holes with a diameter of typically 10 to 50 nm. The steps themselves have a height of 0.3 ± 0.1 nm, which corresponds to $d_{111} = 0.334$ nm. In the upward direction the steps form a more or less equidistant step train of parallel steps; while in the right direction the step shape and distance are quite irregular.

Figure 4.2 Series of four AFM topographs showing a {100} side face with large macrostep. The inset in (b) shows the height profile along the indicated line.

During the 'real' *in situ* growth measurements performed in the AFM liquid cell, monosteps are observed as well. However, at the beginning of an experiment it was often impossible to make successive scans or even to finish one single scan. For this reason, it turned out that the observation of actual change in growth patterns recorded during successive scans due to crystal growth was not feasible. However, repeated *in situ* observations were possible about two hours after the filling of the

in situ cell with the saturated solution. The observed growth patterns were stable at this time, indicating no or slight growth or etching. Examples of uncompleted scans showing monosteps are given in figs. 4.4a and b; a completed scan is depicted in c. In fig. 4.4b part of the monosteps is bunched in units of four or five single steps. In fig. 4.4c all steps are monosteps of 0.3 nm in height, except for one double step in the left part and one 10 nm high macrostep in the upper right part of the picture. Step distances vary from 500 nm in figs 4.4a and b to 50 nm in fig. 4.4c.

Fig. 4.4d shows a 7.5 μm wide AFM topograph made at a later stage of a growth experiment. At this stage (after about four hours) it was often possible to finish larger area scans. On this scale still monosteps, with a typical step distance of 300 nm, can be recognized. Besides that, bunching can be observed in this picture, often attended with holes of typically 30 nm in size. The surface morphology mostly observed at these later stages is a more or less brain-like structure of which an example is shown in fig. 4.4e. Large lobs, 300 nm wide, are alternated by 10 to 30 nm deep holes. These patterns, which were noticed on most crystals, turned out to be stable in time; so there was no growth anymore during scanning.

4.3.3 *In situ* etching of the {111} top face

As described above, etching experiments were carried out in a slightly undersaturated solution. A typical etch pit pattern observed a few minutes after immersion of the sample in the solution is given in fig. 4.5a. The triangular etch pits, which all have the same crystallographic orientation, vary in size from 70 to 200 nm and in depth from 3 to 6 nm. Their shape is 'point-
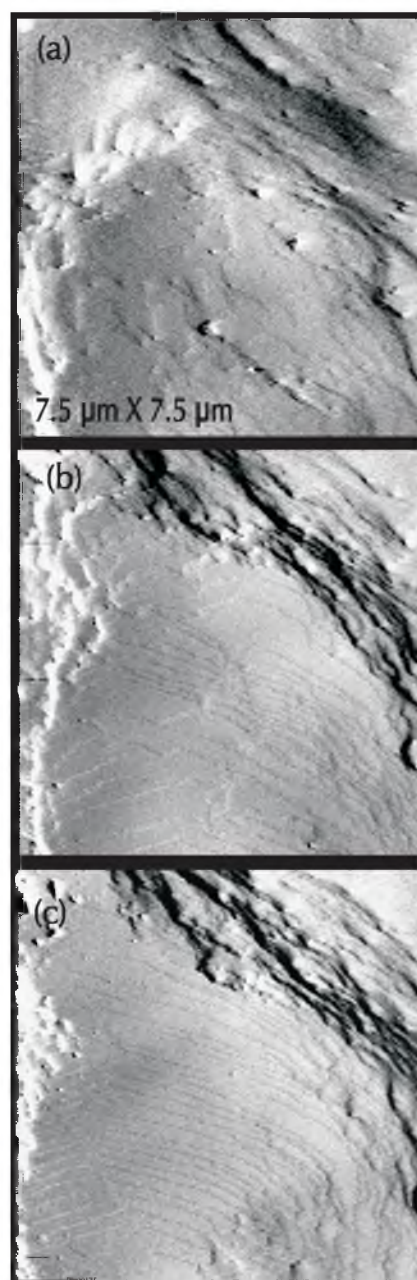
Figure 4.3 Time-series of AFM measurements of a DMSO wetted AgBr {111} face. In the middle part of each micrograph monosteps are present; at the left, right and upper edges step bunches are developing. At these bunches many small holes can be distinguished. The time interval between successive scans is 4 minutes.

bottomed' and their density is estimated $1 \cdot 10^{13}/m^2$. In the same experiment the flat-bottomed etch pit of fig. 4.5b was found. The shallow sides of this pit are formed by monosteps; the flat bottom has a width of 400 nm.
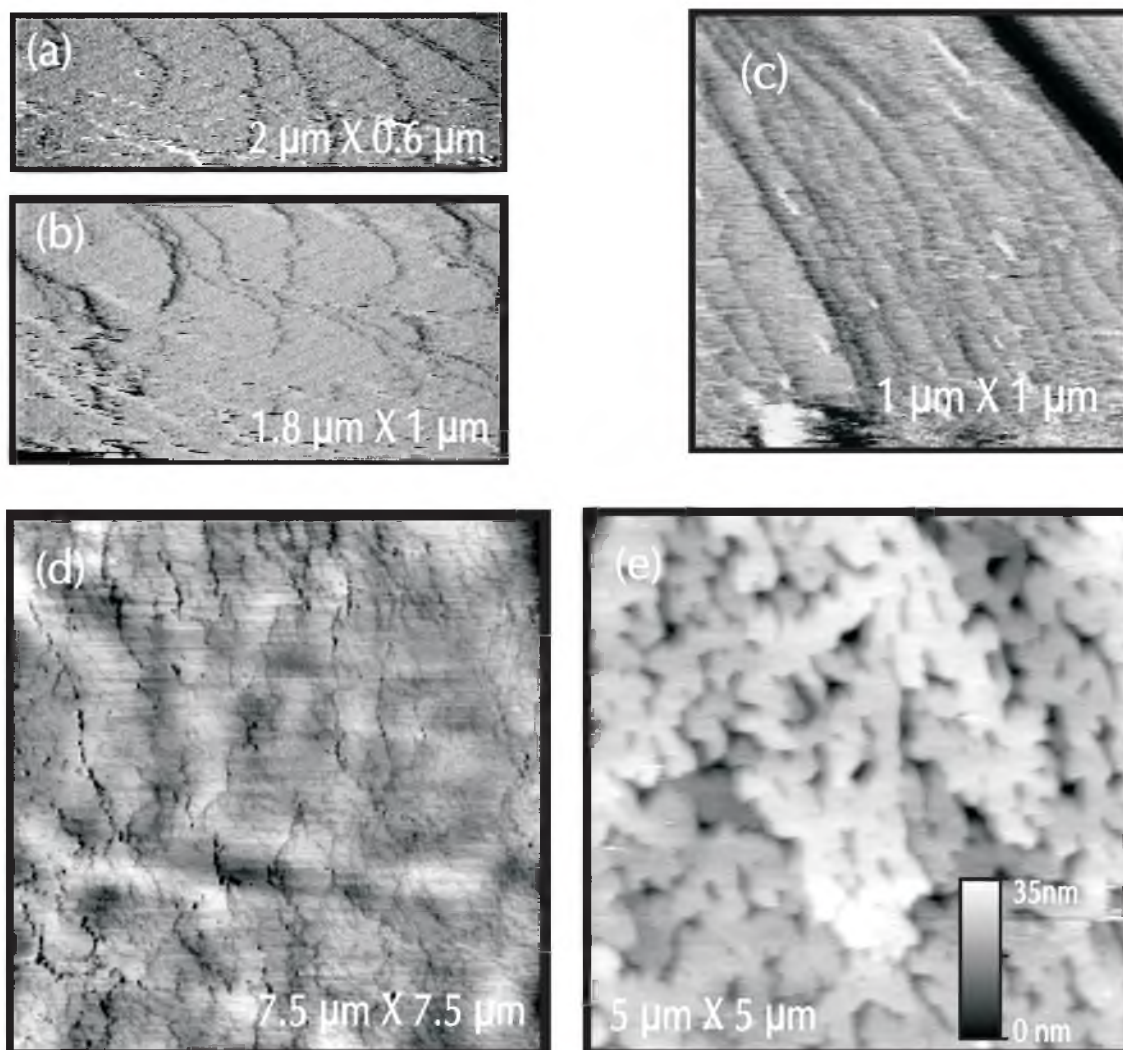
Figure 4.4 Monosteps on the AgBr {111} top face measured *in situ* by AFM. (a), (b) Uncompleted scans showing monosteps and bunched steps. (c) Completed scan showing monosteps, one double step and a 10 nm high macrostep. (d) Increasing step bunching and hole formation after four hours of immersion. (e) Brain-like structure observed at the same stage as (d) but at another surface area.

During the same etching experiment pinning of steps was encountered. In fig. 4.5c dissolving steps moving from the right to the left can be seen. These steps are blocked at the 50 nm high triangularly shaped structures, and thereby are forced to adopt a zig-zag pattern. Again, no difference between successive images could be noticed, indicating little or no etching at the time of imaging. The density

of the triangular structures was estimated to be $1.10^{12}/m^2$.
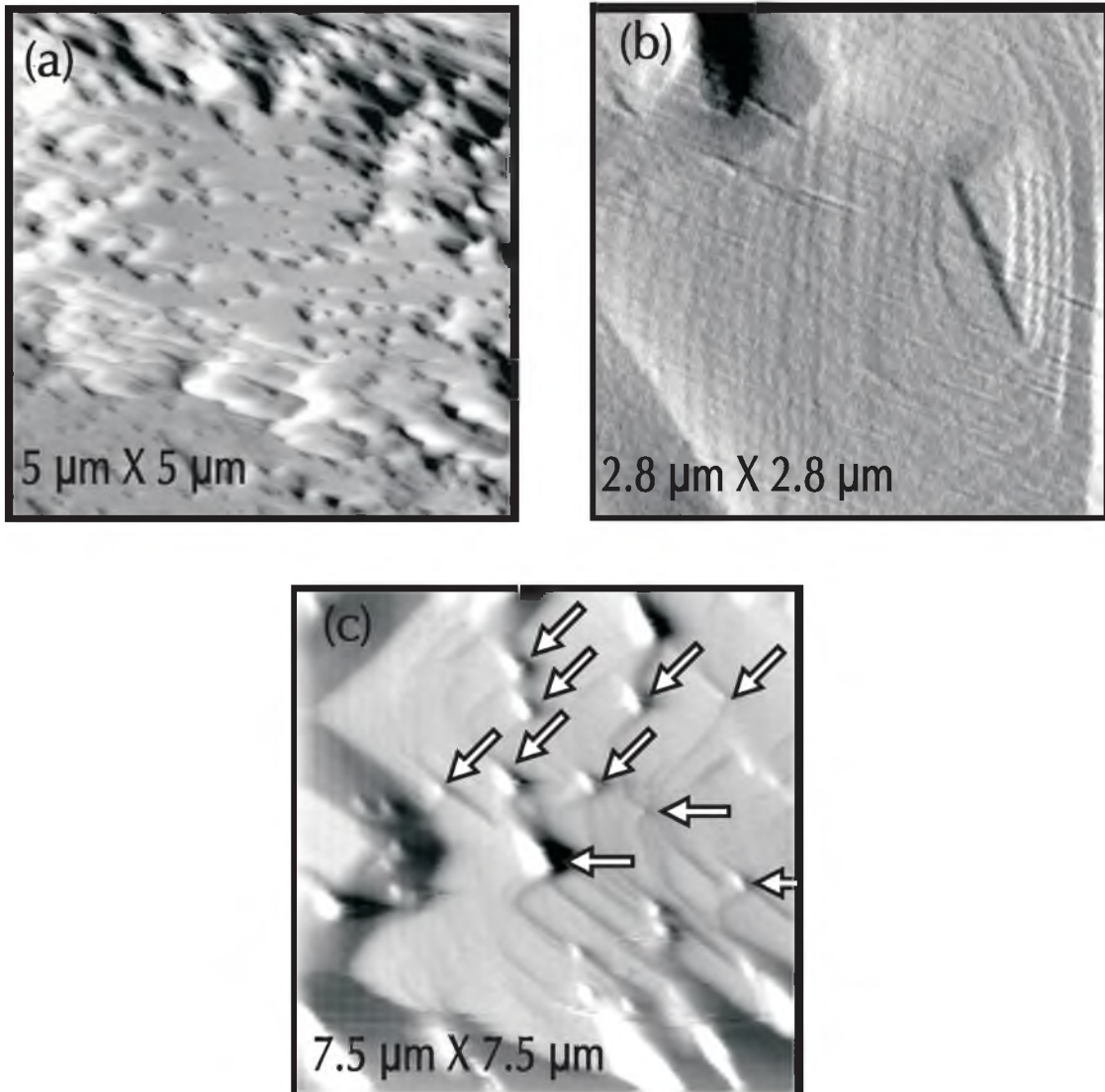
Figure 4.5 AFM topographs showing etch patterns on a AgBr {111} top face. Point-bottomed (a) and flat-bottomed (b) etch pits observed in a slightly undersaturated solution. (c) Pinning of dissoluting steps running from the right to the left (pinning indicated by arrows).

4.3.4 *In situ* observation of twinned AgBr crystals

When a somewhat higher supersaturated DMSO solution instead of a saturated or undersaturated solution is used, AgBr precipitation takes place inside the AFM *in situ* cell. Large parts of the {111} top faces of the tabular crystals become covered by a layer of small crystals varying in size from 0.3 to 0.8 μm, as is shown in fig. 4.6a, which is recorded 2½ hours after the onset of the experiment.

Higher magnification images of these small crystals, such as fig. 4.6b, reveal flat faces, part of which have a clearly hexagonal or rectangular shape and therefore can be indexed as {111} and {100} faces, respectively. Very high magnification images of the crystallite surfaces uncover parallel ridges and grooves composed by striplike facets of different orientations. An example is given in fig. 4.6c, which is a zoom-in of the central triangular crystal in fig. 4.6b. The top face resembles a slightly truncated hexagon, and the side faces are intersected by ridges which run parallel to the edges of the top face. Two ridges, however, intersect the top face itself and continue on one of the side faces.
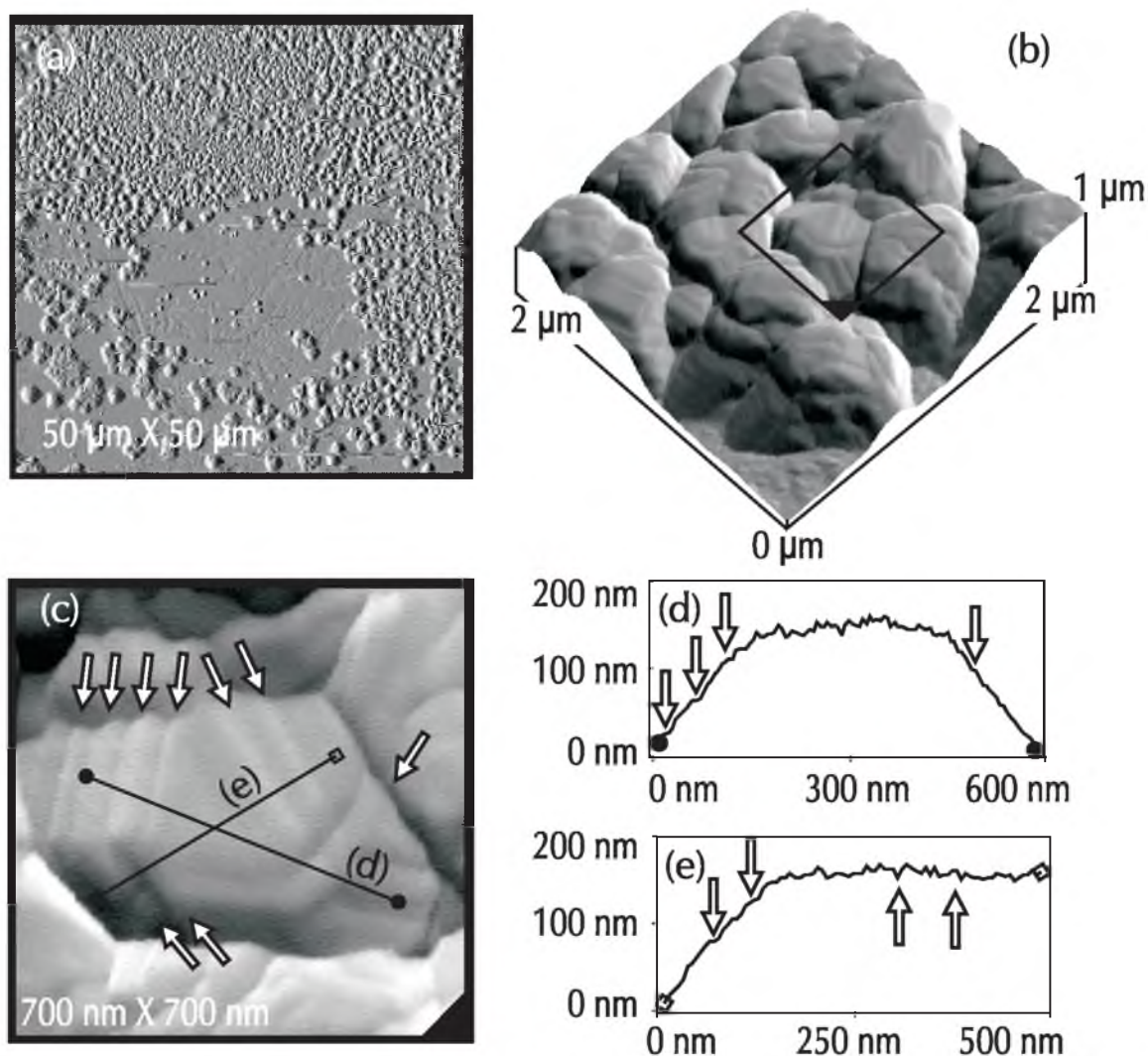
Figure 4.6 (a) Precipitated AgBr crystallites on a {111} AgBr top face. (b) Enlarged AFM image showing facets on the crystallites. (c) Zoom-in of the hexagonally shaped crystal at the centre of (b), revealing parallel ridges. (d,e) Height profiles along the lines indicated in (c), showing both the angles between the different faces and the parallel ridges indicated by arrows.

The distances between adjacent ridges varies between 30 and 70 nm. The angle between the 'top' and 'side' facets composing a ridge cannot be measured accurately because the radius of the AFM tip is about 50 nm, which is of the same order of magnitude as the ridge structures. Nevertheless, a minimum value of 35 can be estimated. For the angles between the different crystal faces only a minimum value can be estimated as well. This is caused by the pyramidal overall shape of the AFM tip, which makes the theoretically maximum measurable angle between 55 (along the tip pyramid edges) and 63 (along the pyramid faces). Experimentally measured angles of 45 and higher are therefore not reliable and should be taken as a minimum estimate of the real angle. The determined minimum values for the angles between the top and side faces of the crystallites varied between 39 and 49 . Fig. 4.6d and 4.6e are height profiles of the crystal depicted in fig. 4.6c, showing the angles between the faces and the occurrence of the ridges.

4.4 Discussion

4.4.1 Growth

The most striking observation of the growth patterns is the occurrence of large bunches on the {111} top faces (figs. 4.1 a-c) and the {100} side faces (fig. 4.2), which are even visible by optical microscopy. The bunches on the {111} top face, often starting from an edge, are very common. Series of bunches are almost always split up into faceted parts of roughly 50 μm and thus are intersected by grooves parallel to the growth direction. The angle of the bunches with respect to the top face is measured to be 3 , corresponding to a monostep separation of 6 nm. The occurrence of hopperlike bunch patterns near the crystal edges indicates morphological instability. Free convection, together with the somewhat increased viscosity of DMSO (1.98 mPas) compared to water (0.89 mPas) could give rise to solution flow over the {111} surface of the platelets, starting from the edges and advancing to the centre. This leads to depletion of the solution near the central region, which introduces hopper growth. Since the flow is parallel to the propagation direction of the steps, this could lead to bunching according to the model proposed by Chernov [15]. The supersaturation in the system is very low, which seems not to favour the mass transport explanation of the phenomenon. On the other hand, recently hollow needles of AgBr have been found with features typical for mass transport limited growth [16]. Other explanations of the hopper growth would be *i)* the occurrence of preferential nucleation of the growth layers at the edge on an atomic scale caused by electrostatic phenomena [17], or *ii)* the shielding of the crystal by the vessel walls or other crystals.

The minimum step height encountered on the {111} top face corresponds to the minimal slice

thickness d_{111} = 0.334 nm and was observed during many experiments involving 'semi *in situ*' growth (fig. 4.3), *in situ* growth (figs. 4.4a-d) and *in situ* etching (figs. 4.5b,c). The presence of monosteps means that the growth unit is of the order of one AgBr unit and that the surfaces being grown and etched were neither kinetically nor thermally roughened, as is expected for the strong bonds involved and the low under- and supersaturation applied. The actual growth unit of AgBr crystals grown from DMSO solution is unknown, but comparison with tabular crystals grown from the vapour phase, where the growth units are for the most part AgBr molecules [18][19], and grown from water, where the ions in solution are AgBr, $AgBr_2^-$, $AgBr_3^{-2}$ or $AgBr_4^{-3}$ depending on the Br^- concentration [20], indicates that the actual growth unit seems to influence neither the development of tabular crystals nor the occurrence of flat {111} faces on them.

The observation of monosteps and higher steps proves that the {111} face is a strong F-face. At first sight, this is in agreement with the results of a Periodic Bond Chain analysis [21], that predicts {111} to be a NaCl-type F-face for a crystal truncated in vacuum. However, due to the alternating positively and negatively charged ion layers perpendicular to the <111> direction, there are only repulsive bonds inside these ion layers, and the {111} face is polar, which make this F-face unstable. So, there should be an additional factor stabilizing this F-face.

In contrast to the vacuum surroundings assumed in the PBC analysis, at the experimental conditions the crystal surface is in contact with solvents (DMSO and/or H_2O). Stabilization of the charged surface layer by these polar solvents could be an explanation for the observed flat faces. However, in vapour phase growth experiments {111} faces have been found as well [22], indicating that there should be other mechanisms that can stabilize the {111} face.

Relaxation of the top ion layer can also explain the observed F-character. Suppose the {111} face is terminated by a Ag^+ layer. In this case these Ag^+ ions can be pulled somewhat downwards into the cavities between the Br^- ions of the underlying layer, due to the missing of a compensating pulling force of a Br^- layer above the top Ag^+ layer. This diminishes the repulsing forces between the ions of the same kind within one layer.

A third explanation for the occurrence of flat faces is the reconstruction of the upper layer of ions (Ag^+ or Br^-) as proposed by Hamilton and Brady [4] and observed in air by Hegenbart and Müssig [8], in which this upper layer contains half of the number of atoms of an unreconstructed layer, thereby again diminishing the repulsive forces. However, it is not sure that this reconstruction takes place in the polar DMSO as well, since Nozoye and Tarada observed reconstruction in air but not in water [12].

The commonly observed 'brain-like' structures of fig. 4.4e are likely formed by epitaxial three-dimensional nucleation at the very beginning of the growth experiment, followed by lateral growth and coalescence of these nuclei. Similar patterns have been observed for MOCVD grown GaN on

sapphire substrates [25]. The formation of these three-dimensional nuclei on top of a crystal surface of the same chemical compound, indicates that this surface is strongly hampered or even blocked in growth. If not, then the growth units would directly be incorporated into the crystal surface, and the surface supersaturation would be too low for the formations of 3D nuclei on top of it. This results from the fact that the activation barrier for 2D nuclei is by far lower than for the formation of 3D nuclei. Such a retardation of growth is a common phenomenon, which is induced by the adsorption of impurities. The question now raises whether the observed monostep patterns are positioned directly on the original mother crystal or on top of a smoothened 3D nucleation layer.

The 'semi in situ' growth series in a thin solution layer of fig. 4.3 shows monostep growth which is hindered by step pinning. This step pinning is induced by 10 - 50 nm sized holes, which could be hollow cores of edge dislocations (see e.g. [23] or [24] for observations of such hollow cores on the surfaces of respectively $Ba(NO_3)_2$ and. KH_2PO_4) or small etch pits caused by impurities. Because many holes in fig. 4.3a have disappeared on figs. 4.3b and c, and dislocations cannot vanish, impurities are more likely the source of the holes and thus of the observed pinning. The same mechanism of step pinning by impurities probably also holds for the in situ measurement of fig. 4.4d. It cannot be excluded that the holes are remnants of overgrown 'brain-like' structures.

4.4.2 Etching

The small, point-bottomed etch pits formed at small undersaturation (fig. 4.5a) can be caused by dislocations. If this is the case, then the dislocation density can be estimated to be 1. $10^{13}/m^2$. However, the etch pits may be caused by isolated or small impurity clusters as well, supposing that the undersaturation is sufficient for creating a pit, but not large enough for lateral expansion of the steps. This would lead to small, point bottomed pits as well.

The occurrence of pinning of monosteps at triangularly shaped structures during etching (fig. 4.5c) is a strong indication for the presence of impurity or defect clusters in the crystals. This type of imperfections, however, does not locally enhance the etching of the AgBr crystal, but is impeding it by remaining at the surface, leading to the triangular structures at the positions of the impurities. The types of impurities involved in both growth and etching are unknown.

4.4.3 Twinning of AgBr precipitates

The twinned crystallites observed on an AgBr surface in a slightly supersaturated solution exhibit facets which sometimes are clearly hexagonal or rectangular in shape, indicating {111} and {100} types of faces respectively. At high magnification parallel lines, which are actually ridges alternated with grooves, can be distinguished on these faces, as is depicted in fig. 4.6c. For several reasons, we conclude that these patterns mark the surface outcrops of {111} twin planes that may lead to tabular

crystals or needle-shaped crystals as described in the introduction part of this paper. The most important argument for this conclusion is the direction of these lines, which is always parallel to a facet edge, i.e. a <110> direction. Successive lines are always parallel to each other, which is expected as well for twin planes. As elaborated in the previous section, the angles between different faces and between the facet strips composing the ridged groove sequences could not be determined accurately. However, the estimated minimum value of 35 of the angle between the strips is an indication for the strips being facets rather than bunches, because the bunches observed in situ and ex situ on both the {111} top face and the {100} side face have an angle of only 2 to 3 relative to the top face. The observed distances between the twin planes of 30 to 70 nm correspond well to the values for {111} tabular crystals grown from by industrial double-jet precipitation method as determined earlier by transmission electron microscopy [26-29]. The crossing of the twin lines as observed in the upper part of the crystal depicted in fig. 4.6c indicates that this crystallite contains non-parallel twin planes, which would lead to a needle-shaped crystal rather than a tabular crystal, as elaborated in refs. [16, 30]. This observation confirms the hypothesis by Bögels [2] and by Jagannathan [31] that twinning of AgBr crystals occurs at the nucleation stage of their growth.

In similar in situ experiments using optical instead of atomic force microscopy, the nucleated crystals that grew out always were tabular or needle-shaped due to twinning. This common occurrence of twinning supports the above conclusions.

4.5 Conclusions

By using AFM, step patterns on tabular AgBr crystals grown from DMSO solutions have been investigated. A rich surface morphology, including monosteps, shallow faceted bunches growing from the crystal edges and precipitates was found on the {111} top face. In situ growth experiments of the {111} faces revealed monosteps of height d_{111} and pinning of these steps. Etching experiments uncovered small etch pits with a density of 1. $10^{13}/m^2$, and etch step pinning at particles having a density of 1. $10^{12}/m^2$. At higher supersaturations precipitated crystallites showing flat faces were observed. On these faces the outcrops of parallel twin planes were noted. A direct measurement of the twin plane separation resulted in an average distance of about 40 nm, which confirms earlier measurements by transmission electron microscopy.

Acknowledgements

References

[1]   A. Milan, P. Bennema, A. Verbeeck and D. Bollen, J. of Imaging Science and Techn. **42** (1998), 1.

[2]   G. Bögels, T.M. Pot, H. Meekes, P. Bennema and D. Bollen, Acta Cryst. **A53** (1997), 84.

[3]   G. Bögels, H. Meekes, P. Bennema, and D. Bollen, J. Crystal Growth, **191** (1998), 446.

[4]   J.F. Hamilton, Adv. In Physics **37** (1988), 359.

[5]   H. Haefke, E. Meyer and H.-J. Güntherodt, J. of Imaging Science and Techn. **35** (1991), 290.

[6]   M.G. Mason, J.C. Hansen, J. Vac. Sci. Technol. **A12** (1994), 2023.

[7]   H. Haefke, E. Meyer, L. Howald, U. Schwarz, Ultramicroscopy **42-44** (1992), 290.

[8]   G. Hegenbart and T. Müssig, J. of Imaging Science and Techn. **37** (1993), 551.

[9]   J.F. Hamilton and L.E. Brady, Surface Science **23** (1970), 389.

[10]   U.D. Schwarz, H. Haefke, H.-J. Güntherodt, J. Bohonek and R. Steiger, J. of Imaging Science and Techn. **37** (1993), 344.

[11]   U.D. Schwarz and H. Haefke, Appl. Phys. **A59** (1994), 33.

[12]   H. Nozoye and H. Takada, Jpn. J. of Appl. Phys. **33** (1994), 3764.

[13]   M.P. Keyes, E.C. Phillips and W.L. Gladfelter, J. of Imaging Science and Techn. **36** (1992), 268.

[14]   D. Sneddon and A. Gewirth, Surface Science **343** (1995), 185.

[15]   A.A. Chernov, J. Crystal Growth **118** (1992), 333.

[16]   G. Bögels, J.G. Buijnsters, S. Verhaegen, H. Meekes, P. Bennema and D. Bollen, accepted for publication in J. of Crystal Growth (1999).

[17]   L. Piela and J. Andzelm, Surface Science **84** (1979), 179.

[18]   H.M. Rosenstock, J.R. Walton and L.K. Brice, US At. Energy Comm. ORNL (1959), 2772.

[19]   A.V. Gusarov and L.N. Gorokhov, Chem. Abstr **58** (19963) 4005C.

[20]   E. Klein, Photogr. Korrespondenz **92** (1956), 139.

[21]   See e.g. P. Bennema, in: D.T.J. Hurle (Ed.), Handbook of Crystal Growth, 1a, Thermodynamics and Kinetics, North-Holland, Amsterdam, 1993, p. 477.

[22]   G. Bögels, H. Meekes, P. Bennema, D. Bollen, Phyl. Mag. **A79** (1998), 639.

[23]   K. Maiwa, M. Plomp, W.J.P. van Enckevort, J. Crystal Growth **186** (1998), 214.

[24]   J.J. De Yoreo, T.A. Land and J.D. Lee, Phys. Rev. Lett.**78** (1997), 4462.

[25]   F.K. de Theije, A.R.A. Zauner, P.R. Hageman, W.J.P. van Enckevort and P.K. Larsen, submitted for publication.

[26]   R.V. Metha, R. Jagannathan and J.A. Timmons, J. of Imaging Science and Techn. **37** (1993), 107.

[27]   Y. Hosoya, S. Urabe, Proc. 1997 Int. Symp. on silver halide imaging, Oct 27-30, Victoria (1997), 22.

[28]   J.F. Hamilton, L.E. Brady, J. Appl. Physics **35** (1964), 414.

[29]   C. Goessens, D. Schryvers, J. van Landuyt and R. de Keyzer, J. of Imaging Science and Techn. **41** (1997), 301.

[30]   C. Goessens, D. Schryvers, J. van Landuyt, A. Milan and R. de Keyzer, J. Crystal Growth **151** (1995), 335.

[31]   R. Jagannathan, J. of Imaging Science and Techn. **35** (1991), 104.

Chapter 5:

The structure of coarse crystal surfaces: the (00$\bar{1}$) face of $K_2Cr_2O_7$ crystals grown from aqueous solution as an example

Chapter 5:

The structure of coarse crystal surfaces: the (001) face of $K_2Cr_2O_7$ crystals grown from aqueous solution as an example[*]

M. Plomp, A.J. Nijdam, W.J.P. van Enckevort

Research Institute for Materials, Department of Solid State Chemistry, University of Nijmegen, Toernooiveld 1, 6525 ED Nijmegen, The Netherlands

Abstract

The surface structure of the coarse (001) face of Potassium bichromate ($K_2Cr_2O_7$) was studied *in situ* and *ex situ* with the help of optical microscopy, atomic force microscopy and scanning electron microscopy. A multitude of features, like unit cell height steps, bunches, macrosteps of which some are actually small facets, inclusions and spirals were observed. The observations lead to new ideas about the growth mechanisms of this face, in which the combined action of impurity adsorption and volume diffusion plays a key role. These mechanisms may be responsible for the coarse growth on other crystals as well.

Keywords: crystal defects, impurity blocking, inclusion, macrosteps, potassium bichromate, coarse growth.

5.1 Introduction

In crystal growth models, most attention is paid to flat crystal faces which are grown under well-defined conditions, because for these cases it is relatively simple to derive expressions describing the growth. Therefore, less experiments are done on coarse crystal faces exhibiting many defects, large macrosteps, misfits and inclusions. Because in industrial crystal growth compounds are not selected for their flat faces and the growth conditions are far from perfect, mechanisms leading to coarsening are worth studying.

Macrostep and subsequent inclusion formation are phenomena often encountered in crystal growth at larger supersaturation and are thought to originate from local supersaturation variations [1] or impurities [2]. Theoretical studies [3] and experiments with N-methyl urea [4] show that kinematic waves develop depending on the flow direction of the solution with respect to the direction of step propagation on the crystal interface. If the step flow and solution flow are directed in the same way, kinematic waves readily develop; if they are anti-parallel, the step patterns are much more stable. After further propagation the kinematic waves formed by the combined action of convection and diffusion on N-methyl urea transform to macrosteps and eventually to crystallographic facets, a process leading to inclusion formation as well [4]. Experiments on $NH_4H_2PO_4$ and KH_2PO_4 indicate that macrostep formation is most pronounced at the supersaturation where the elemental step velocity is most sensitive to variations in supersaturation and impurity concentration [5].

During the present investigation $K_2Cr_2O_7$ is studied: an ionic, orange compound of which large crystals can be grown from aqueous solutions. The morphological most important faces are the pair of {001} faces (Shubnikov's setting of axes [6] is used). The morphology of the opposite (001) and (00 $\bar{1}$) faces is quite different. The (001) face behaves like a 'normal', flat crystal face with D-shaped spirals as the main growth feature. The (00 $\bar{1}$) face however, looks roughened and has a metallic luster and a block-like structure [7, 8]. This roughened look is not caused by thermal or kinetic roughening [9] however, as can be concluded from the atomically flat surfaces that were observed with atomic force microscopy during the present study. Therefore, we will use the term 'coarse' instead of 'roughened' in this work to describe the (00 $\bar{1}$) face.

Remarkably, the clear difference of the opposite {001} faces of $K_2Cr_2O_7$ is not reflected in the symmetry of the crystal as determined by X-ray and other measurements. These suggest a P1 point group [10, 11], which, however, conflicts with the non-centrosymmetric overall shape of the crystals [12] and the difference in the surface morphology. The crystal growth features clearly indicate P1 symmetry. This controversy called hypomorphism was first formulated by Shubnikov [6].

Recently, Heide and Follner [13] have put forward an explanation for the hypomorphism, in which the coarse appearance of the (00 $\bar{1}$) face is ascribed to homoepitactic intergrowths, of which 10 %

are twins. These intergrowths are thought to originate from microscopic nuclei present in the solution, which contact and subsequently grow out on the mother crystal.

During the present investigation we used distinct surface topographic methods (optical microscopy, scanning electron microscopy, atomic force microscopy) to observe the growth features on the (001) face at high supersaturation, in order to improve the understanding of the growth process of this coarse face, rather than to explain the hypomorphism. The knowledge acquired by these observations may apply also to other substances which crystallize with coarse faces.

5.2 Experimental

5.2.1 *In situ* methods

The crystals used for the *in situ* observations were grown from seed crystals, which were obtained from an aqueous $K_2Cr_2O_7$ solution by slow solvent evaporation at room temperature. The seeds, about 10 mm^3 in size, were rinsed with a few droplets of demineralized water in order to remove possible surface contamination before they were placed in a growth cell. This temperature-controlled cell was filled with a supersaturated, aqueous solution and was provided with an optical window. During growth the crystal surfaces were observed by optical microscopy, using oblique illumination with the aperture diaphragm closed as much as possible and placed slightly eccentrically with respect to the optical axis, to provide an enhanced image contrast. The images were recorded on videotape with the help of a video camera connected with an analog differentiator and contrast enhancer. As elaborated in refs [14, 15] by this technique steps with heights down to a few nanometers can be revealed.

All crystals described in this paper were grown from a stirred solution with a saturation temperature of 25.0 C. A well defined relative supersaturation is obtained by lowering the temperature, and can be calculated from

$$\sigma = \frac{x - x_{eq}(T)}{x_{eq}(T)}, \qquad (5.1)$$

in which x is the actual mole fraction of $K_2Cr_2O_7$ in the aqueous solution, and x_{eq} is the equilibrium mole fraction in water at temperature T, which is given by the relations [16]:

$$x_{eq}(T) = 681.3e^{-2250/T} \; for \; T < 315 \; K \qquad (5.2a)$$
$$x_{eq}(T) = 138.4e^{-2847/T} \; for \; T > 315 \; K. \qquad (5.2b)$$

Most crystal surfaces were grown at a supersaturation higher then 5%, simply because at lower supersaturation there is little or no growth [8]. Due to inaccuracies in the preparation of the solutions and the measurement of the temperature the standard deviation in   is 0.2%.

5.2.2 *Ex situ* methods

For ex *situ* observations, crystals were isolated from the solution and, to reduce the shut-off effect [17] as much as possible, quickly dried with a paper tissue. In this way surface regions sufficiently clean for surface topography were obtained.

For the optical examination of the surface structures differential interference contrast reflection microcopy (DICM) was used [14]. In order to measure the sizes and the depths of liquid inclusions in a crystal underneath its surface, optical transmission microscopy was applied, by which quantitative values for the depths were obtained by focusing using a calibrated dial.

The smallest scale surface structures, such as unit cell height steps, were imaged by atomic force microscopy (AFM).The AFM measurements were carried out in the constant-force mode, which gives height information of the observed steps. During this topographic investigation besides the height signal often also the deflection signal, which is kept nearly constant by a feedback loop, is recorded and imaged. This deflection signal, which is also known as the 'error signal' [18], is roughly proportional to the derivative of the height signal, and is therefore pre-eminently suitable for imaging steps. In the deflection images obtained from the deflection signal large macrosteps and monosteps can be presented in the same picture, which is not possible for height images, due to the huge height difference of the steps. The scan size varied from 75 μm down to 10 μm and the vertical resolution was about 0.1 nanometer.

Three-dimensional structures on the crystal surfaces, such as "caves" in macrosteps were imaged by scanning electron microscopy (SEM). For SEM observation, the crystals were coated with a thin gold layer to prevent charging of the sample. This did not affect the surface structure visible by this electron microscopic technique.

5.3 Observations

In general, the morphology of the (001) face is that of a normal, flat face with spiral growth as the main growth mechanism. The monosteps of the D-shaped spirals bunch easily and accumulate to higher macrosteps (10 nm -1 μm) at larger distances from the growth centers. An example of this face covered by growth hillocks is shown in fig. 5.1a. In contrast to the more or less smooth (001) face, the coarse (001) face is covered with block-like structures and macrosteps behaving like small facets

and shows lots of inclusions below its surface. In the following, we shall focus attention to the (001) faces and the following aspects will be elaborated: 1) Low magnification surface topography and examinations of inclusions underneath the surface by ex *situ* optical microscopy; 2) Mini-facets and inclusions as observed by SEM; 3) Observation of the formation of inclusions by *in situ* optical microscopy; 4) Detailed surface topography by AFM.
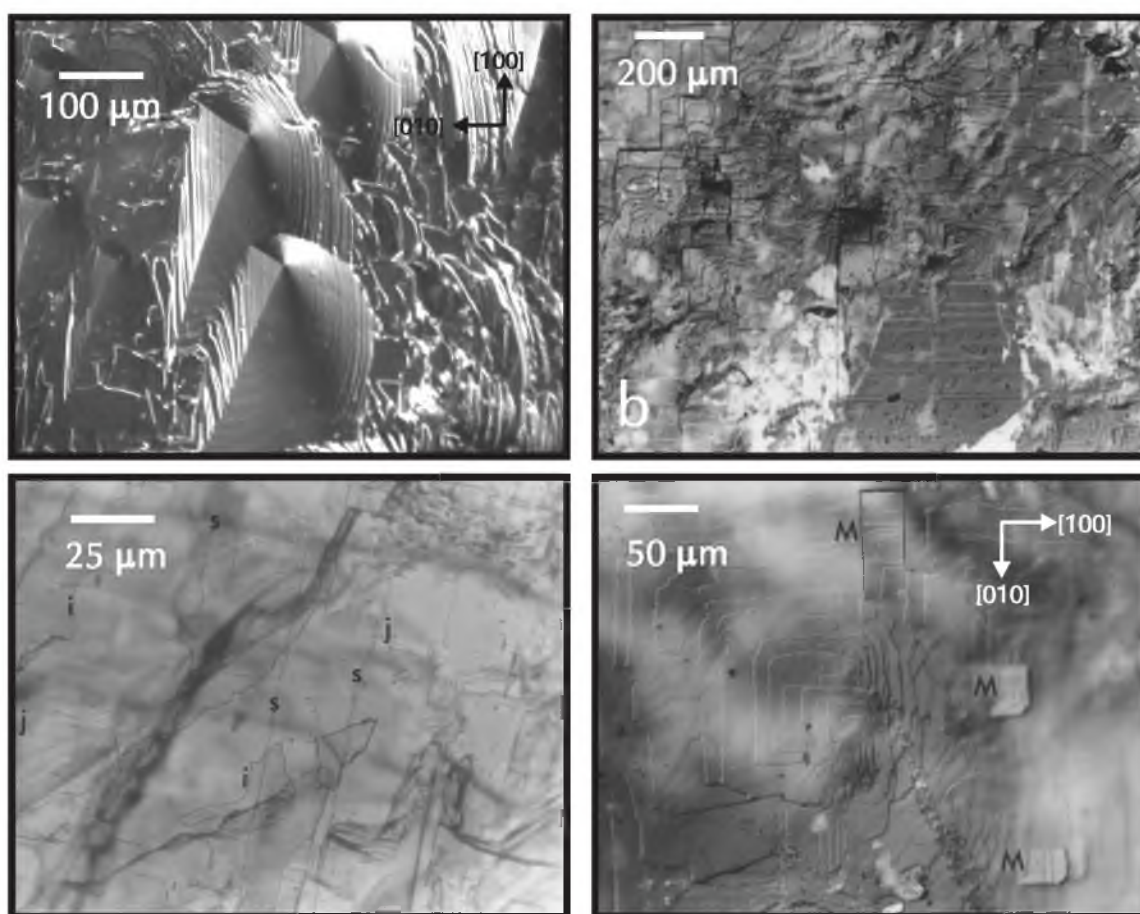
Figure 5.1 (a) Typical (001) face showing D-shaped spirals and no inclusions below. (b) Block-like structures on the (001) face of $K_2Cr_2O_7$. Bright areas represent inclusions (=20%). (c) Horizontal, planar inclusions at different depths beneath the (001) surface, showing their irregular shapes. Focussing is applied on an inclusion layer (indicated by **i**) at a depth of approximately 10 μm below the surface (steps on the surface indicated by **s**). Defocused inclusion layers with a depth of 20 μm are indicated by **j** (=7.8%). (d) Misfits observed by optical microscopy. Three misfits are denoted by **M**. The misfits have the same lateral crystallographic orientations as the mother crystal, only the upper face has a slightly different orientation (=20%).

5.3.1 Topography viewed using *ex situ* optical microscopy

A typical (OO̅1) face, showing most of the described features, is depicted in fig. 5.1b. The depicted area shows block-like growth from many different growth centers. The growth of these structures proceeds via large macrosteps of several hundreds of nanometers high. In this figure many inclusions can be discerned as bright areas. The presence of inclusions indicates that the macrosteps do not cover the underlaying layers completely.

In order to study the liquid inclusions in more detail, optical transmission microscopy was used. The shape of the inclusions is very flat with lateral dimensions of 10-100 μm at typical thicknesses of a few μm. In most cases the edges of the inclusions seem to have no particular preferential directions. Focusing was done on different depths at the same position of the (OO̅1) face. In this way, several layers of planar inclusions could be noticed. An example of these observations is given in fig. 5.1c, which reveals several layers of inclusion at different depths underneath the crystal surface. Inclusions could be observed down to a depth of 50 μm.

Another growth feature that could be observed was the occurrence of misfits, *i.e.* crystal parts on top of the (OO̅1) surface, which have a slightly different orientation than the main crystal matrix. Although in general the orientation of the crystal volume of the block-like structures bounded by most macrosteps is identical to that of the mother crystal, there are a few misfits in relation to [001]. Examples of such misoriented crystallites are shown in fig. 5.1d. The orientation of the upper (OO̅1) face of these misfits can differ up to a few degrees with respect to the (001) face of the mother crystal.
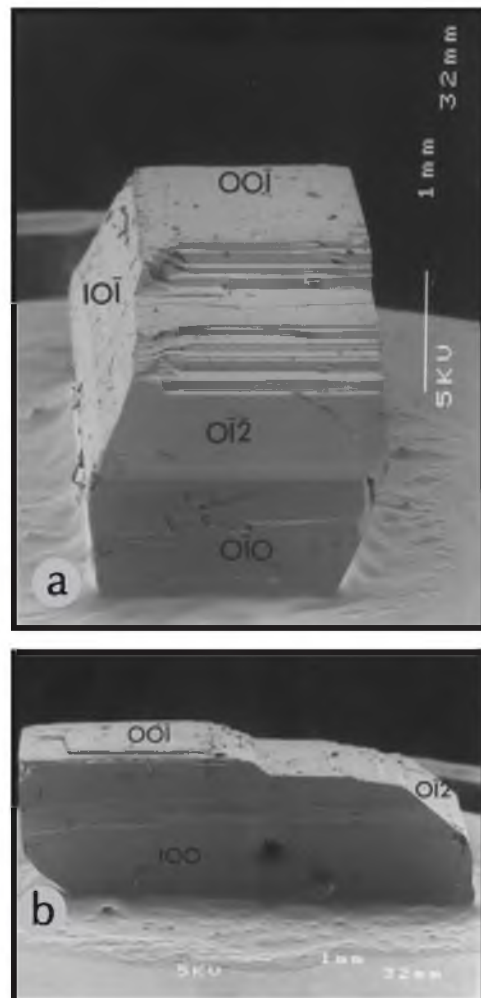
Figure 5.2 SEM survey photographs of a $K_2Cr_2O_7$ crystal: (a) Front view ,(b) side view. In both pictures the (OO̅1) face is on the top side. The mini-facets on the middle of the (OO̅1) face have the same orientation as the (O̅12) face (=12%).

5.3.2 Mini-facets and inclusions viewed using *ex situ* scanning electron microscopy

The SEM photographs in fig. 5.2 show a characteristic phenomenon of the $K_2Cr_2O_7$ (001) face, namely the occurrence of *mini-facets*. On the (001) face giant steps can be distinguished, whose appearance is that of a small facet rather then that of a macrostep. Their orientation was checked with an optical goniometer and coincides with the orientation of the (012) facet present on this crystal. This is one of the reasons that makes us denote this type of steps as mini-facets. They have been observed on the (001) faces of many $K_2Cr_2O_7$ crystals and have heights ranging from the order of 100 nm to 100 μm. Mini-facets were also observed on other faces of $K_2Cr_2O_7$. For instance, on the (100) and (100) surfaces (001) mini-facets could be seen, which, however, will not be shown here because they are beyond the scope of this paper.

A striking observation during the SEM examinations was the presence of inclusions. While in optical microscopy the inclusions look like a bright reflective layer frustrating the height contrast imaging of steps on the crystal surface, SEM reveals them as real cavities ending at mini-facets on the (001) face (provided that, of course, the inclusions were still being formed when the crystals were separated from the solution). Comparison of optical micrographs, on which several inclusions were found to terminate on macrosteps, with SEM topographs reveals outcropping cavities at the same positions, as is shown in fig. 5.3. In this picture, two (012) mini-facets enclosing a steeper mini-facet are depicted in SEM and optical micrographs. At the two boundaries of the different mini-facet types inclusions can be seen. In combination with the examinations by *in-* and *ex situ* optical microscopy the SEM observations give a good picture of the growth habit of mini-facets and inclusions. Fig. 5.4a shows a region of the (001) face containing a giant 'horizontal' inclusion with a height of approximately 50 μm. This inclusion, depicted enlarged
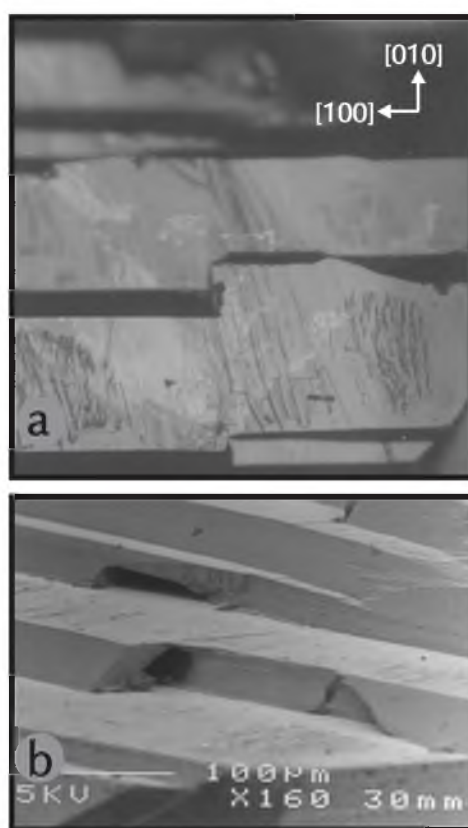
Figure 5.3 Optical micrograph of a 50 μm high step which is constructed of two (012) mini-facets on the left and right enclosing a steeper mini-facet. (b) SEM photograph of the same area, showing outcropping inclusions at the boundary of the (012) mini-facets and the central mini-facet. The curious local narrowing of the right mini-facets in (a) can easily be explained by the presence of the inclusion seen on the corresponding location in (b) (=12%).

in fig. 5.4b, is bounded by a (012) mini-facet at the' rear', a (001) topped crystal layer on top and a macrostep with an overall inclination slightly less than (012) at the front. The thickness of the front macrostep layer and the (001) top face layer is about 10 μm. These side faces grow fast and eventually may close the cavity, leading to the actual formation of an inclusion. As illustrated by figs. 5.4b and c, the formation of inclusions by macrostep overhangs is often encountered on different scales of magnitude. Fig. 5.4c depicts an enlarged view of the corner of the relatively small, double macrostep of 3 μm in height indicated in fig. 5.4a, and reveals a small inclusion in the upper step of about 0.5 μm in height. The size ratio between the two inclusions of figs. 5.4b and c is of the order of 1:100.

Apart from the horizontal inclusion type, where (001) and (001) facets act as top and bottom faces respectively, also a vertical type of inclusion was observed. At these inclusions (012) and (012) facets act as top and bottom faces. A part of a crystal where both inclusion types can be seen terminating at a mini-facet is depicted in fig. 5.5. In the lower part of the picture there is an extended horizontal inclusion, while the upper right part shows a series of (012) mini-facets alternated by rounded facets that are oriented more or less in the (001) direction. The upper left part shows several vertical inclusions, bounded by large (012) mini-facets. These mini-facets seem to grow thicker via (001) sub-mini-facets growing

Figure 5.4 SEM photographs of horizontal inclusions on the $K_2Cr_2O_7$ (001) face. (a) Survey of a region showing two mini-facets that are tens of μm heigh. The lower mini-facet shows a partly opened inclusion. (b) Enlarged image of (a), revealing steps on the 'rear' side of the inclusion. (c) Enlarged image of the area indicated by the arrow in (a), showing an inclusion at the corner of this step, which is roughly a hundred times smaller than the large inclusion of (a) (=12%).

upwards in the [021] direction and horizontally via (100) mini-facets. Apart from sub-mini-facets of the (012) facet of fig. 5.5, on many (012) mini-facets steps propagating in several directions were

observed. This proves that the mini-facets behave as real flat crystal faces rather than as step bunches.

5.3.3 Formation of inclusions as observed by *in situ* optical microscopy

In order to gain more insight in the formation of inclusions and mini-facets, *in situ* optical microscopy was applied. A seed crystal was placed in the growth cell with its (001) face on top. Then the growth process and the development of inclusions on this face were monitored *in situ* and recorded on videotape.

An example of these observations is the sequence of *in situ* micrographs given in fig. 5.6. Experiencing =7.8%, a large flat block-like structure grows from the lower part of fig. 5.6(a) upwards. At a given moment a step overhang is created and an inclusion is being formed as shown in (b). This inclusion, recognizable through its bright reflection, grows a few minutes (c) before the crystal 'closes' again, as can be seen in (d).

Figure 5.5 SEM photograph showing horizontal inclusions bounded by (001) top faces (lower part of picture, indicated by **h**, (01 2) facets (upper right part of picture, indicated by **f**) and vertical inclusions bounded by (012) faces (upper left part of picture, indicated by **v**). On the (01 2) minifacets (001) oriented sub-minifacets (indicated by **s**) can be distinguished (=12%).

An intriguing phenomenon which was always observed is the occurrence of a position dependent blocking of step propagation. The existence of a 'dead zone' in crystal growth is often reported [8, 19] and has been attributed to immobile impurities blocking the advancement of steps. As formulated by Cabrera and Vermilyea [2], to restart crystal growth, the supersaturation must be raised above a critical value *. Then the steps squeeze through the impurity fence and step propagation is no longer prohibited.

During the present *in situ* studies it was observed that the (001) $K_2Cr_2O_7$ face exhibits a similar dead supersaturation zone as the (001) faces, which have been studied in detail elsewhere [8, 20]. The (001) faces of $K_2Cr_2O_7$ exhibit 'local dead zones': while some structures steadily grow, in other regions on the same surface there is no growth at all. The growing structures finally overgrow the 'dead' parts of the crystal, which process is often accompanied by the formation of inclusions. This phenomenon is illustrated in the previously mentioned sequence of micrographs shown in fig. 5.6.

It can be seen that the steps in the left and upper region of the photographs do not propagate at all, while the structure coming from the lower part is overgrowing them forming inclusions. These local differences in the growth rate make it difficult to determine the critical supersaturation *, defining the dead zone width, with some accuracy. It was estimated to be in the range 2% < * < 8% depending on the position on the crystal face.

The nature of the observed growth centers on the (001) face could not be determined with certainty, but are related to largely defective crystal areas. Extended, regularly formed growth spirals, as observed on the (001) face, do not occur on this face. Here, the observed growth centers often generate rectangular macrosteps already close to their origin.

Finally, it was often observed that higher macrosteps advance faster than lower ones, especially at lower supersaturation.
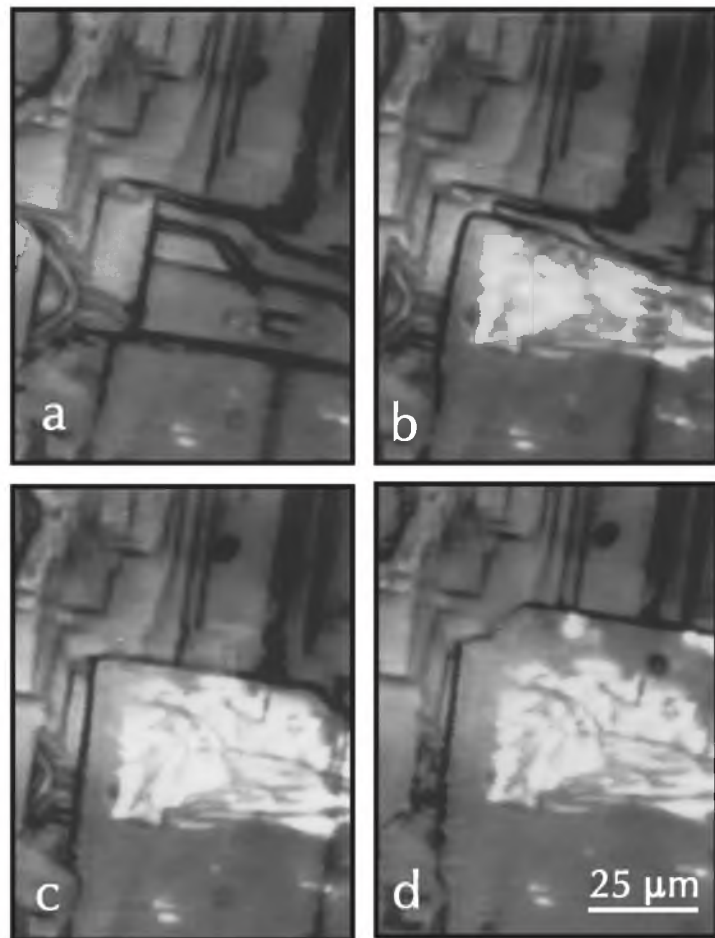
Figure 5.6 Sequence of *in situ* optical microscopy images of an inclusion forming on the (001) face: (a) the plateau at the bottom of the picture is growing upwards without inclusions, (b) suddenly, an inclusion has formed over almost the whole range of the step, (c) the inclusion is starting to close, (d) The inclusion has closed and two new, smaller, inclusions are being formed. The time interval between successive images is 60 s (=7.8%).

5.3.4 Macrosteps, spirals and misfits viewed with atomic force microscopy

To examine the growth of the K$_2$Cr$_2$O$_7$ (001) face on monostep scale, AFM has been used. The highest macrosteps that can be measured using AFM are in the order of a few μm in height; the lowest are monosteps of a few tenths of a nm in height.

Often, the observed macrosteps are oriented parallel to crystallographic directions, such as [100] and [010]. The higher the steps, the more straight and crystallographically oriented they become, the limiting cases being the mini-facets as observed with optical microscopy and SEM. Smaller steps (< 50 nm) are generally oriented more randomly.

An area with a large, local area misfit is depicted in fig. 5.7a. Here, a block-like structure in the upper
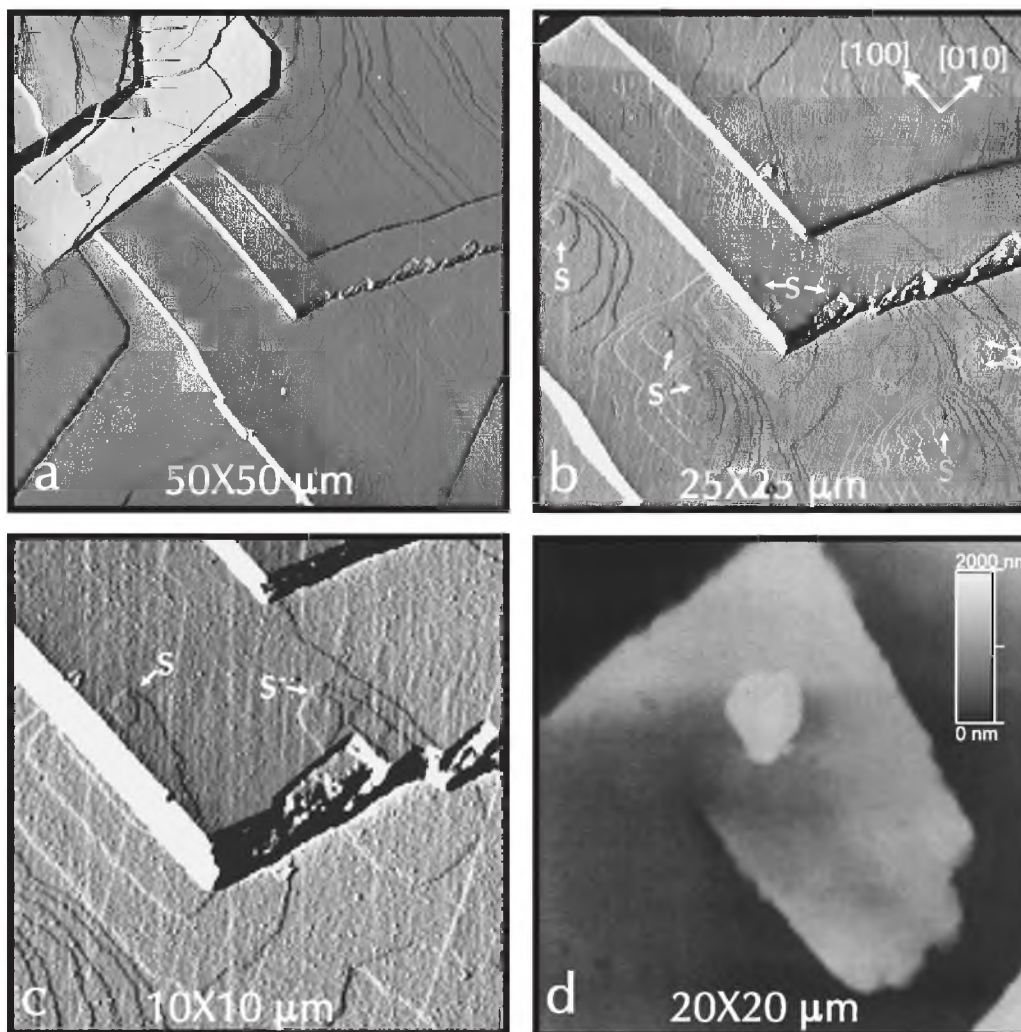
Figure 5.7 AFM images of growth spirals (=20%). (a). Deflection image of a region of a (001) face showing a misfit in the upper left part with a misorientation of 4 with respect to the flat face of the rest of the picture. (b) Enlarged image showing the central region of (a). Here, growth spirals (indicated by S) with monosteps originating from screw dislocations can be discerned. (c) Enlarged image showing the central region of (b), which shows that the spiral steps belonging to the screw dislocations have 'survived' the 0.3 μm high macrostep. Vertical and oblique lines in fig. 12(b)-(c) are due to a scan artefact. (d) Height image of a spiral-like structure with a step of 0.2 μm in height. This step probably originates from a bundle of dislocations (=12%).

left corner with a misfit angle of 3 is covering the macrosteps and the large terraces at the right part of the image. The height of the macrosteps separating these terraces is in the order of 0.25 μm, they have a steepness ranging from 16 to 40 with respect to the (001) plane. In the enlarged picture of fig. 5.7b growth spirals originating from single screw dislocations can be discerned. The steps of these spirals are 1.2 ± 0.2 nm high, which is identical to the length of the c-axis. This implies that the screw component of the Burgers vector perpendicular to the growth face is the unit length [001]. Furthermore, a substantial anisotropy in the step pattern can be noted. This anisotropy leads to more or less D-shaped spirals, which look similar to those on the opposite (001) face. This is suggestive for P1 symmetry on this small scale.

Despite their low height, the unit spirals 'survive' the ongoing μm-high macrosteps as can be seen in the close-up fig. 5.7c, in which one part of a unit spiral is on a lower and the other part is on the adjacent higher terrace. This agrees with the 'law of conservation of burgers vector' (e.g. [21]) and shows that the crystallographic orientation of the adjacent terraces is perfectly identical.

When the growth centers on the (001) face were studied in more detail, often spiral-like rectangular structures with macrosteps of about 20 nm were encountered. The steps were quite undulated and in many cases monosteps could not be detected, not even at the center of a growth hillock. Because no protruding particles were found in the middle of the growth centers, dislocations are still the most likely origins of the growth centers.

Another spiral-like feature is shown in fig. 5.7d. However, here the step originating from the center is not a monostep but a macrostep which is hundreds of nm high. This shows that not all of the frequently observed macrosteps on this face are formed by accumulation of monosteps, but that at least some of the them are formed directly at their source. This might be a large dislocation bundle outcrop introduced by large inclusions or misfits.

5.4 Discussion

5.4.1 Mini-facets and macrosteps

One of the most interesting findings of this investigation is the observation of macrosteps thus high and with such a precise crystallographic orientation that we named them mini-facets. The occurrence of steps on their surfaces (fig. 5.4b) confirms that they are facets rather than macrosteps. Most of the observed mini-facets on the (001) face have an orientation parallel to the (012) side face. Apart from mini-facets, also numerous monosteps and small macrosteps, which both are curved, as well as larger macrosteps, which are quite straight, have been seen.

As indicated already by McEwan et al. [4], there must be some kind of phase transition which

changes step bunches, via macrosteps, into mini-facets. To obtain mini-facets rather than step bunches there must be an attractive interaction between adjacent growth steps if their separation becomes very small. If the step distance is less than a few growth units, then due to meandering by entropy effects adjacent steps may contact each other locally. In this case additional bonds, not being part of the (001) growth slice, but belonging to the connected net parallel to the (012) plane may be formed. If the energy gain is larger than the effects due to entropy repulsion [22], than the multiple step becomes stable. In course of time all points of the adjacent steps that comprise the macrostep contact each other, and due to the formation of the extra bonds a stabilized (012) mini-facet with a minimal surface energy is eventually formed. This process explains the observed correlation between the height of a step and its specific crystallographic orientation and straightness. Prior to the formation of minifacets, macrosteps must develop. Four possible mechanisms for the formation and growth of macrosteps have been encountered during this study. *i)* Macrosteps are created at once at bundles of dislocations or misfits as illustrated in fig. 5.7d. *ii)* The 'classical' bunching mechanism induced by the Frank instability [23, 24], where closely separated steps advance faster than widely separated ones. In this case the narrowly spaced steps catch up more widely spaced ones in front and accumulate to bunches or macrosteps. The increased velocity of narrowly spaced steps is induced by time dependent impurity adsorption as has been investigated in detail for the opposite (001) surface of $K_2Cr_2O_7$ [20]. *iii)* Often macrosteps and mini-facets propagate slowly over 'dead' surface areas. Since the surface at the rear of these steps is 'cleaned' from impurities, lower steps from behind move faster, collide and heighten the macrostep. In addition, when the macrostep advances over a dead surface region, it will catch up the immobile steps ahead and will grow higher. This mechanism of renewed crystal growth preceded by macrosteps propagating over 'dead' crystal areas ,which actually is a special case of ii), has been observed on the (001) surface as well [8]. *iv)* The macrosteps and mini-facets themselves are not blocked by impurities on the (001) face, but their growth can be hindered by impurities on the mini-facets themselves. It is interesting to note here that the critical supersaturation * for blocking of step propagation by adsorbed impurities appears to be less for macrosteps and minifacets than for (lower) bunches and monosteps. This has been observed during the present study as well as during an earlier *in situ* investigation of step propagation on (001) KHPhthalate growing from aqueous solution [25]. The fact that macrosteps can propagate over dead surface areas is possibly due to the occurrence of a reentrant corner at the base of a step, which creates a surface region with a very large, negative curvature, and thus locally increases the effective supersaturation $_{eff}$ to such an extent that $_{eff} >$ *. Another condition is that the mini-facet surfaces (in this case (012)) are just less sensitive than the (001) face for blocking of the growth by impurities. A similar impurity-based difference between the critical supersaturation for different faces (in this case {100} and {101}) was found for KH_2PO_4 [26].

From the observation that large mini-facets propagate over non-growing (001) surfaces, it can be concluded that the lower steps advancing on the (012) mini-facets do not suffer from blocking of growth comparable to the (001) face. Or, putting this in a formula,

$$\sigma_{(0\overline{1}2)} < \sigma_{(00\overline{1})} .$$ (5.3)

5.4.2 Inclusions

The growth of mini-facets and large macrosteps often goes together with the development of planar inclusions having widths up to hundreds of μms and heights up to tens of μms. Mostly, they are bounded by (001) and (00$\overline{1}$) top and bottom faces and partly by mini-facets as 'front' faces. At positions where an inclusion is still 'open' the edges of the top face and mini-facets can be seen to consist of crystal layers with a thickness of a few μm with steps on them.

The origin of an inclusion is caused by impurity effects, which make the bottom part of a mini-facet or macrostep to advance slower or not at all over the contaminated, dead (00$\overline{1}$) surface. This is probably helped by volume diffusion effects, which make that, due to its higher interface supersaturation, the top of a macrostep or mini-facet captures more growth units than the bottom part. The top of the mini-facet grows fast, the lower part tends to grow slower and the bottom (00$\overline{1}$) face does not grow at all. When the lower part is hindered somewhere an inclusion can develop.
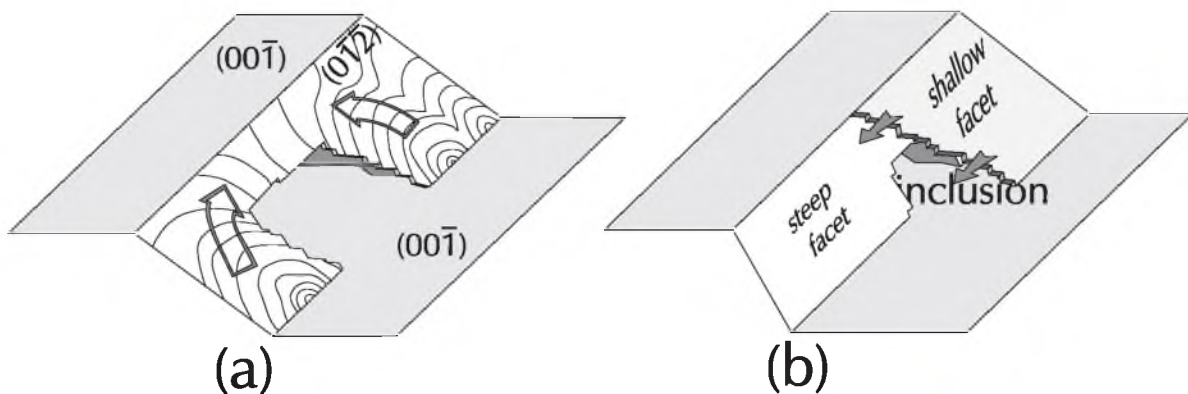
Figure 5.8 Schematic drawings of (a) inclusion formation by a combined action of step generation at the reentrant corner at the bottom of the mini-facet and volume diffusion effects, which cause an enhanced growth at the upper part of the mini-facet, and (b) inclusion being closed by a laterally expanding 'sliding door'.

A key problem in this simple model is the fact that two-dimensional nucleation of new growth layers at the top of the (012) mini-facets requires a very high supersaturation, which exceeds the applied supersaturation by far. Steps are much easier generated at the reentrant corner at the [001]

intersection line of the (01) mini-facets with the (001) surface, i.e. at the bottom of the mini-facets. Therefore it is more likely that at some favorable places of the mini-facets, for instance at local areas of increased supersaturation due to enhanced volume diffusion or at regions where the (001) surface is less contaminated, steps are nucleated at this reentrant corner and then spread laterally over the mini-facets. Since at the top of these minifacets these steps are expected to grow fast, inclusions are easily formed as shown in fig. 5.8a. Sideways expanding steps, macro-steps or sub-mini-facets have indeed commonly been observed at the front surface of the top layers of inclusions ending in a mini-facet.

Closure of the inclusion often proceeds by the formation and lateral propagation of a faster growing mini-facet with an orientation close to the (01) face but slightly inclined towards (001) in front of the inclusion. This 'sliding door' effect is schematized in fig. 5.8b and can be recognized from the SEM micrographs shown in figs 5.4 and 5.5.

The above shows that the formation of inclusions below the (001) $K_2Cr_2O_7$ surface is a complicated process involving impurity blocking, the development of mini-facets and probably volume diffusion. It is clear that the formation of inclusions in crystals can not always be described by simple models.

5.4.3 Mechanisms of coarsening

From the above it is clear that growth retardation or blocking by impurities and probably volume diffusion are the main causes of the development of large macrosteps on and inclusions below the $K_2Cr_2O_7$ (001) face. The presence of these macrosteps and inclusions can generate large dislocations, due to lattice enclosure errors occurring when the inclusions are closed at the last stage of their development. In their turn, these 'macro dislocations' are a source for new macrosteps, as shown in fig. 5.7d, which again leads to new inclusions and new defects. This self-amplifying effect eventually leads to the coarse (001) surface.

Heide and Follner ascribe the coarsening of the $K_2Cr_2O_7$ (001) face to the growth of layers expanding from crystal seeds precipitated on the (001) surface from the solution [13]. About 90% of these intergrowths have the same orientation as the mother crystal, but the others, having a twinned position relative to the mother crystal, cause cracks and dislocations in the layer, and are therefore held responsible for the coarse (001) surface. In this interpretation, all of the mini-facets that we have observed, would actually be facets of these plate-like intergrowths. Our observations indicate however, that these mini-facets can develop on the mother crystal itself as well, either via bunching of steps originating from dislocations or via immediate creation from 'macro dislocations' as shown in fig. 5.7d. In addition, the surviving spirals of fig. 5.7c indicates that the two plateaus separated by the mini-facet belong to the same crystal and are neither twinned nor misoriented with respect to each other. For these reasons, the mechanism as proposed by Heide and Follner seems not to be

the main cause of the coarsening of the (00) surface. However, the low number of misfits, as shown in figs. 5.1d and 5.7a, the seeds of which may originate from the solution, can also play a role in the generation of macrosteps and minifacets as suggested by Heide and Follner.

In contrast to the findings of McEwan et al. [4], who showed similar developments of steps into bunches and mini-facets, we conclude that in the present case the main cause for the macrostep formation is impurity blocking rather than volume diffusion.

5.5 Conclusions

The formation and propagation of large macrosteps, of which many are (012) mini-facets, is a very important growth mechanism of the (001) $K_2Cr_2O_7$ face. The development of these features predominantly results from the occurrence of time dependent adsorption of growth retarding impurities on the (00) surface. The mini-facets overgrow areas of the (00) face the growth of which is hindered or even blocked by adsorbed impurities. Due to this impurity blocking in combination with volume diffusion effects inclusions can develop, which eventually are closed by mini-facets growing sideways. The cyclic, self-amplifying process of the subsequent generation of macrosteps, inclusions, lattice defects, new macrosteps,... is an important cause of the observed coarseness of the (001) $K_2Cr_2O_7$ crystal surface.

The combined action of impurity retardation or blocking and volume diffusion, which leads to macrosteps, inclusions and macro defects, may be a general mechanism that can account for coarse growth on many other crystals as well.

References

[1]   T. Kuroda, J. Crystal Growth **71** (1985), 84.

[2]   N. Cabrera and D.A. Vermilyea, in: R.H. Doremus, B.W. Roberts and D. Turnbull (Eds.), *Growth and Perfection of Crystals*, Wiley, New York, 1958, 393.

[3]   A.A. Chernov, J. Crystal Growth **118** (1992), 333.

[4]   A. McEwan, R.I. Ristic, B. Yu. Shekunov and J.N. Sherwood, J. Crystal Growth **167** (1996), 701.

[5]   L.N. Rashkovich and B.Yu Shekunov, J. Crystal Growth **100** (1990), 133.

[6]   (a) A. Shubnikov, Z. Krist.**50** (1911), 19.

         (b) A. Shubnikov, Z. Krist. **76** (1931), 469.

[7]   M. Szurgot and K. Sangwal, J. Crystal Growth **79** (1986), 829.

[8]   A.J. Derksen, W.J.P. van Enckevort and M.S. Couto, J. Phys. D: Appl. Phys **27** (1994), 2580.

[9]   P. Bennema, in: D.T.J. Hurle (Ed.), *Handbook of Crystal Growth*, Vol. I, chapter 7, Elsevier, Amsterdam, 1993.

[10]   E.A. Kuz'min, V.V. Iljukhin, Yu.A. Khartinov and N.V. Belov, Krist. Und Techn. **4** (1969), 441.

[11]   J.K. Brandon and I.D. Brown, Can. J. Chem. **46** (1968), 933.

[12]   K. Sangwal and M. Szurgot, J. Crystal Growth **80** (1987), 351.

[13]   (a) G. Heide and H. Follner, Cryst. Res. Technol. **31** (1996), 171.

         (b) G. Heide and H. Follner, Cryst. Res. Technol. **31** (1996), 959.

[14]   W.J.P. van Enckevort, Current Topics in Cryst. Growth Res. **2** (1995), 535.

[15]   L.A.M.J. Jetten, B. van der Hoek and W.J.P. van Enckevort, J. Crystal Growth **62** (1983), 603.

[16]   J. Szewczyk, W. Sokolowski and K. Sangwal, J. Chem. Eng. Data **30** (1985), 243.

[17]   W.J.P. van Enckevort, Prog. Cryst. Growth Charact. **9** (1984), 1.

[18]   C.A.J. Putman, K.O. van der Werf, B.G. de Grooth, N.F. Van Hulst, J. Greve and P.K. Hansma, SPIE **1639** Scanning Probe Microscopies (1992), 547.

[19]   K. Sangwal, Prog. Crystal Growth Charact. **32** (1996), 3.

[20]   W.J.P. van Enckevort, A.C.J.F. van der Berg, K.B.G. Kreuwel and A.J. Derksen, J. Of Crystal Growth **166** (1996), 155.

[21]   A.M. Kosevich, in: F.R.N. Nabarro (Ed.), *Dislocations in Solids*, North Holland, Amsterdam, 1979, 40.

[22]   X.-S. Wang. J.L. Goldberg, N.C. Bartelt, T.L. Einstein and Ellen D. Williams, Phys. Rev. Lett. **65** (1990), 2430.

[23]   F.C. Frank, in: R.H. Doremus, B.W. Roberts and D. Turnbull (Eds.), *Growth and Perfection of Crystals*, Wiley, New York, 1958, 441.

[24]   D. Kandell and J.D. Weeks, Phys. Rev. B **49** (1994), 5554.

[25]   M.H.J. Hottenhuis and C.B. Lucasius, J. Crystal Growth **91** (1988), 623.

[26]   S.A. de Vries, P. Goedkindt, S.L. Bennet, W.J. Huisman, M.J. Zwanenburg, D.-M. Smilgies, J.J. De Yoreo, W.J.P. van Enckevort, P. Bennema and E. Vlieg, Phys. Rev. Lett. **80** (1998), 2229.

Chapter 6:

Cleavage asymmetry

of $K_2Cr_2O_7$ crystals

Chapter 6:

Cleavage asymmetry of $K_2Cr_2O_7$ crystals

M. Plomp, W.J.P. van Enckevort and E. Vlieg

RIM Laboratory of Solid State Chemistry, Faculty of Science, University of Nijmegen, Toernooiveld 1, 6525 ED Nijmegen, the Netherlands

Abstract

Potassium bichromate crystals were cleaved along the {001} plane. Both cleavage faces (001) and (00$\bar{1}$) were studied using tapping-mode atomic force microscopy. It was found that the lowest steps present on one cleavage face always had a height of a single unit cell d_{001}, while the other face exhibited steps of half this height, d_{002}, as well. Moreover, which of the two cleavage faces showed the d_{002} steps (either (001) or (00$\bar{1}$) turned out to be dependent on the cleavage direction ([100] or [$\bar{1}$00]). This means that the surface termination of the surfaces depends on the cleavage direction. It is shown that this dependency is caused by the combination of the double-layered crystal structure, the occurrence of an inversion point in each layer and the asymmetric cleavage with respect to the boundary plane between the two different layers. The recombination of the surface steps after cleavage is demonstrated to originate from a thin water layer condensing from the ambient air.

Keywords: cleavage, potassium bichromate, surface water layer, step recombination, AFM, atomic force microscopy.

6.1 Introduction

In the fields of surface science and crystal growth, cleavage of crystals is often used to obtain clean, molecularly flat crystal surfaces. By cleavage, possible poisoning effects of as-grown crystal surfaces by impurities are avoided. The process of cleavage is also very interesting in itself and is studied in materials science because it supplies information about the strength of the material involved. Both theoretical (e.g. [1-3] and references therein) and experimental [1, 4, 5] studies have been done on the development and propagation of cracks in a crystal being cleaved. For instance, the characteristic V-shaped step patterns often observed on the surfaces of cleaved crystals are attributed to an interaction between cleavage steps and slip steps from dislocations that are introduced by the cleavage process itself [4, 5]. Using AFM, cleavage steps, slip steps and hollow cores on L-arginine phosphate monohydrate [6], as well as the nature of multilayer steps on MgO {100} [7] were examined in great detail. While the morphology of cleavage steps has been investigated for a number of systems, here we focus on the relation between crystal structure and cleavage plane.

Upon cleavage, the crack propagates through the crystal in a way that it can absorb as much as possible strain energy of the material in front of it [1]. Moreover, when crystals with a multi-layered structure are cleaved, the cleavage plane is expected to develop between the same layers all the time in order to minimize the force needed. As will be elaborated in section 3 of this paper, the symmetry of the crystal structure is important regarding the choice of the cleavage plane. From this point of view, potassium bichromate crystals are interesting, not only because they exhibit a double-layered structure, but also because the inversion centre belonging to their P1symmetry is situated in the middle of the layers resulting in the occurrence of two distinct layers A and B with symmetrically equivalent boundary planes.

Another reason of interest for $K_2Cr_2O_7$ crystals is the occurrence of *hypomorphism* [8-10], *i.e.* a contradiction between the crystal structure and the crystal morphology. The $K_2Cr_2O_7$ (001) face is a 'normal' flat crystal face exhibiting large D-shaped growth spirals, while the opposite (001) face shows a block-like structure with a large amount of macrosteps, small facets and inclusions [11]. The surface morphology thus indicates P1 symmetry. Remarkably, this difference in opposite faces is not reflected in the structure of the crystal as determined by X-ray diffraction [12, 13], which shows P1 symmetry. All observations described in this study can be explained by considering P1symmetry and no assumptions about symmetry lowering were needed. Therefore the P1 X-ray structure will be assumed to be the correct one in this study.

The patterns observed in this study indicate movement of surface steps on the cleavage faces when kept in air. Similar ex *situ* growth and etching has been observed for ionic crystals like HgI_2 [14], $Ba(NO_3)_2$ [15], NaCl [4, 16], CaF_2 [17], $CaSO_4.2H_2O$ [18]. For instance, for cleaved ionic crystals

erosion of the top surface layer of CaF_2 {111} [17] as well as step splitting of d_{100} into d_{200} steps of $NaCl$ {100} has been observed [4]. The mobility of ions leading to this reorganization of the surface is generally attributed to the presence of an thin water layer on the crystal surface. Strong dependence of the step movement on the relative humidity (RH) was found in AFM studies of cleaved $NaCl$ {100} surfaces [16, 19]. Below 50% RH no step movement was observed, at 50 - 57% RH only curved steps moved and at 57 - 70% RH all steps moved [16]. Another AFM study showed preferential water adsorption at steps [19]. A third AFM investigation on 12 alkali halide and alkaline earth fluoride crystals showed that the presence of a water layer actually facilitated atomic resolution on these crystals [20].

6.2 Experimental

Potassium bichromate single crystals with sizes of about 5mm X 10 mm X 5 mm grown from aqueous solution were used. All crystals selected exhibited D-shaped growth spirals on their (001) faces, which were used for indexing the crystals. Cleavage, storage and AFM imaging were carried out in a room with a humidity of 32 - 36 % and a temperature of 23 C. During scanning, the temperature is locally increased a few degrees due to the focussed AFM laser beam, which is necessary for the detection of cantilever deflection [21]. Cleavage was accomplished using a sharp knife edge. After cleavage, the fastest possible AFM imaging could be done in 5 minutes. No change of this '5 minutes step pattern' could be detected during a following period of 24 h.

The Digital Dimension 3100 AFM was operated in tapping mode (see e.g. [22]). The tapping mode silicon cantilevers used had force constants and resonance frequencies of 42 N/m and about 260 kHz respectively. All images were recorded using frequencies somewhat below the resonance frequency, because
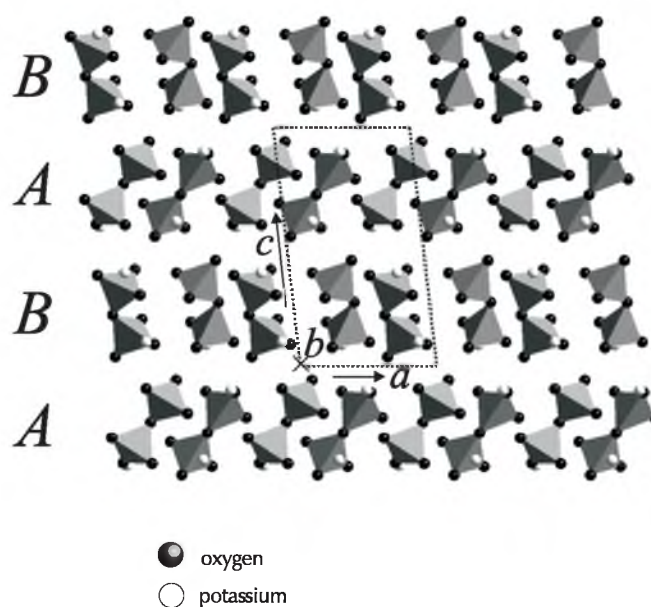
Figure 6.1 The double-layered structure of $K_2Cr_2O_7$ with different layers *A* and *B*. The unit-cell parameters are [13]: a = 7.445 , b = 7.376 , c = 13.367 , α = 97.96 , β = 96.21, γ = 90.75 .

this usually yields the best feedback [23]. Most images were acquired using a relatively low cantilever damping of about 10 to 25 % relative to the resonance amplitude in free air.
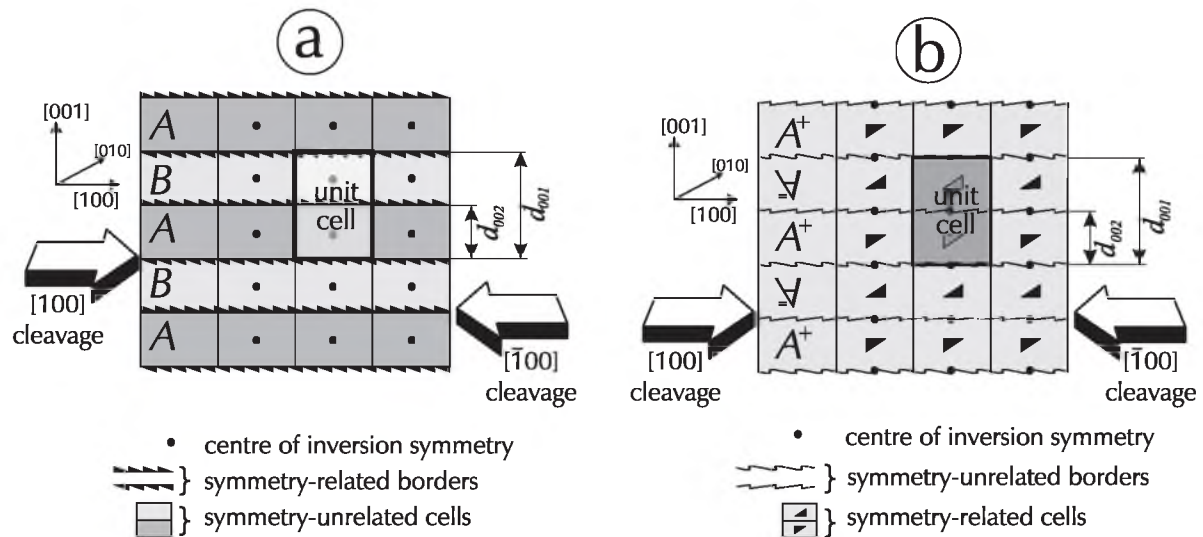
Figure 6.2 Schematic view of P1 double-layered structures with centres of symmetry situated in the layers (a) or between the layers (b). For $K_2Cr_2O_7$, the structure is of the (a)-type. In this case, the A- and B-layers are different and the boundaries between them are symmetry-related. In the (b)-case, the different layers A^+ and A^- are symmetry-related and their boundaries are not. The arrows indicating cleavage asymmetry are explained in the discussion section.

6.3 Crystal structure

The $K_2Cr_2O_7$ crystal structure as determined by X-ray diffraction measurements [13] is double-layered with respect to the {001} plane and exhibits P1symmetry (fig. 6.1). As shown schematically in fig. 6.2a, the centre of symmetry is situated in the middle of the {001} layers. The consequence of this is the occurrence of two different layers with spacing $d_{002} = 0.67$ nm which are not symmetry-related. From now on, these layers are called A and B according to [24]. In fact, these layers are related by pseudo-symmetry, namely if layer A is rotated 90 around [001], it looks almost similar to B by tetragonal pseudo-symmetry. In contrast to the layers, the boundary planes A-B and B-A are symmetry-related by the inversion point 1 For comparison, the case of a double-layered crystal with the P1inversion centre situated between the layers is schematized in fig. 6.2b. In this case, the layers instead of the boundary planes would be symmetry-related.

For $K_2Cr_2O_7$, it is highly unlikely that the layers A and B have the same surface energy. Therefore, in equilibrium the layer with the lowest surface energy will occur on top of a $K_2Cr_2O_7$ {001} face. From

now on, we will denote the layer with the lowest surface energy as A. From the current investigations, we do not know if this lowest energy layer A' really corresponds to the crystallographic layer A in fig. 6.1. However, by $K_2Cr_2O_7$ in situ AFM etching experiments it was confirmed that this is indeed the case [25]. During growth, etching and storage of crystals it is expected that the energetically most favourable layer, A, will always be on top of both the (001) and (00$\bar{1}$) surfaces. This results in 'double' BA surface steps of height $d_{001} = 1.34$ nm, which were indeed found during the $K_2Cr_2O_7$ etching study [25].

6.4 Results

Six {001} cleavages were carried out on different crystals using the two opposite cleavage directions [100] and [$\bar{1}$00]. Depending on the cleavage direction one of the {001} cleavage faces showed d_{002} steps, while the opposite one only revealed double d_{001} steps. This was checked on many different spots on the cleavage faces. In this section, first the step patterns on both types of faces will be discussed. After that, the dependency on the cleavage direction will be addressed.
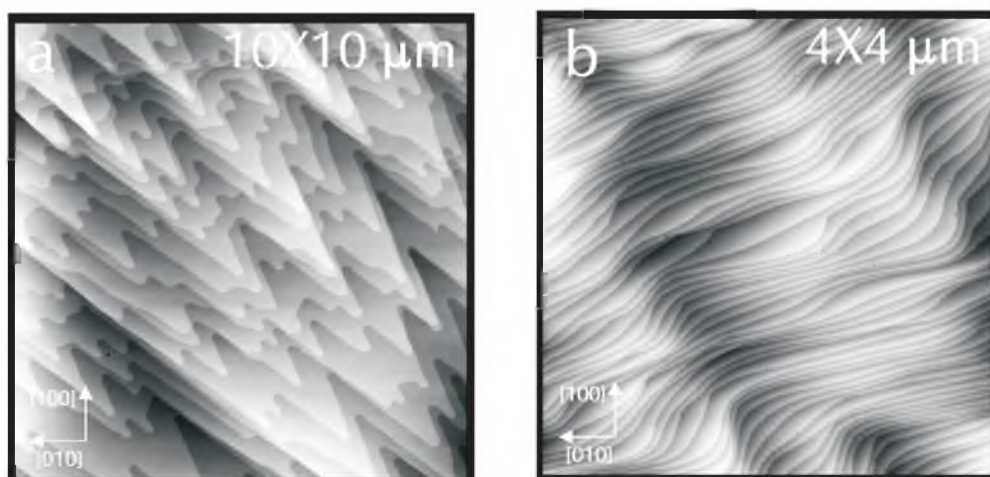
Figure 6.3 Step patterns on A-terminated cleavage surfaces without split steps. (a) Typical cleavage pattern on an (001) face cleaved from [$\bar{1}$00]. (b) Dense step train on an (001) face cleaved from [$\bar{1}$00]. All steps are BA, with height d_{100}.

6.4.1 Step patterns on cleavage faces without split steps

One of the two cleavage faces hardly ever shows d_{002} steps. The flat regions of these surfaces often exhibit the characteristic V-shaped cleavage patterns as shown in fig. 6.3a, which are known to occur on many ionic cleavage surfaces [4, 5, 17]. These features are composed of only d_{001} steps. On other

positions dense step trains as depicted in fig. 6.3b can be observed. The lack of step splitting and the lack of holes in the top layers both indicate that the top layer of these cleavage faces is the more stable type A and the steps are of type BA (*i.e.* d_{001} steps with the A layer on top). Usually, the steps on these faces are somewhat rounded, indicating some post-cleavage step movement under the influence of a water layer.
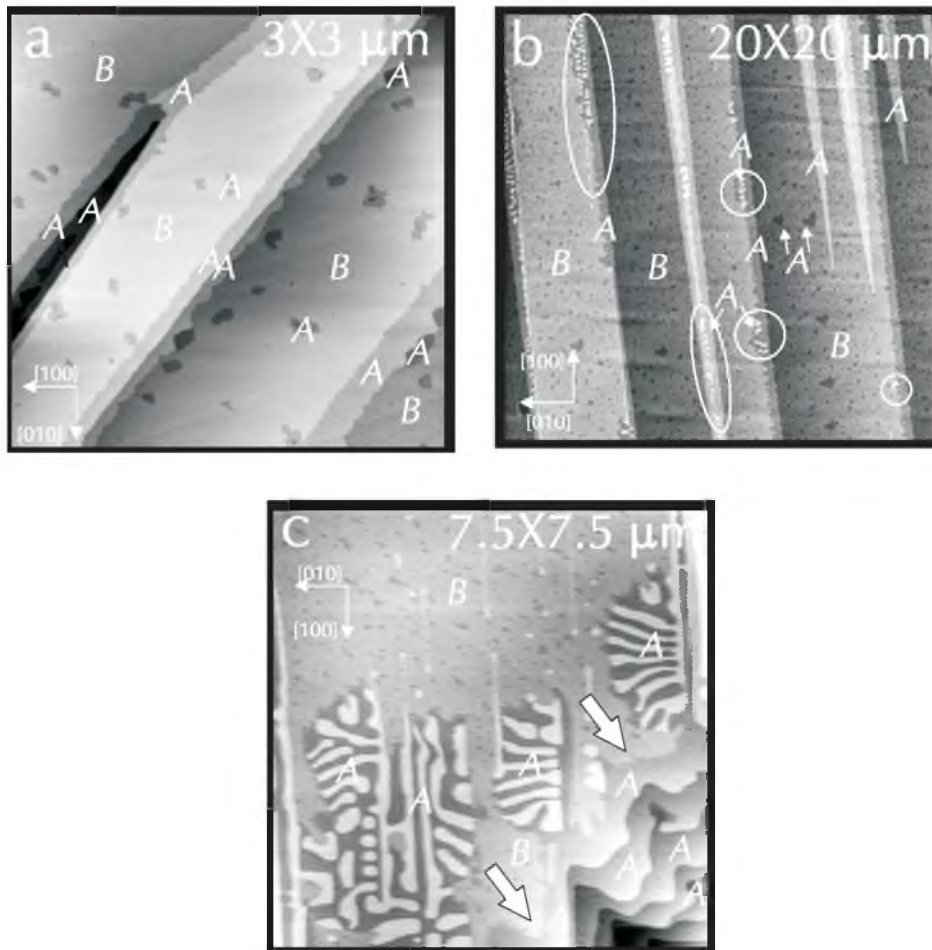
Figure 6.4 Split steps on B-terminated cleavage surfaces. (a) Split AB en $2AB$ steps together with holes of depth d_{002} on an (001) surface cleaved from [100]. Note that the AB steps have split into an A and a B step and that the $2AB$ step at the middle of the figure has split into a central BA step, an A step on the lower side and a B step on the high side. The type of top layer is indicated by A or B in the figure. (b) Cleavage pattern on an (001) face cleaved from [100], with split AB steps. The A step edges remain straight, while the B steps are capricious. Moreover, at the encircled regions new A layers have grown near step edges. (c) This region on an (001̄) face cleaved from [001̄] shows larger areas that have transformed from a B-terminated surface into a zebra-like A-topped surface. The densely stepped region in the bottom left part of the image has also recombined completely. The B step that forms the border between the large B terrace and the A-type step train is indicated by arrows.

6.4.2 Splitting of d_{001} into d_{002} steps

On the cleavage faces opposite to the ones described in section 6.4.1, many d_{002} steps are observed. Examples, both on (001) and (00$\bar{1}$) cleavage faces, are given in fig. 6.4. Fig. 6.4a shows that d_{002} steps occur in pairs, or in pairs with one d_{001} step in between. Apart from that, holes of depth d_{002} are present. This situation is once more illustrated in fig. 6.4b. All terrace edges are seen to consist of a pair of d_{002} steps. The lower ones are quite straight, while the upper ones are more capricious. Moreover, near the edges of the upper terraces some islands of height d_{002} are present. From these figures, it can be deduced that these cleavage faces originally consisted of B-terminated terraces, separated by an integer number of AB steps. Due to some post-cleavage etching these steps dissolved slightly. Because the B layers are the less stable ones, they etch more than the A layers, which caused both the etching of the holes with depth d_{002} and the step splitting in figs. 6.4ab. As indicated by fig. 6.4b, even recrystallization of dissolved $K_2Cr_2O_7$ took place in front of the B steps resulting in the formation of islands topped by stable A layers. This recrystallization effect is once more illustrated in fig. 6.4c, which shows a large B terrace with three regions of recombination. In these regions, both d_{002} holes and islands have evolved, leading to a complete A crystal surface with roughly the same amount of material as in the starting situation. In the lower right part of fig. 6.4c, the B terrace is bordered by one d_{002} step before a dense d_{001} step train sets on. At first sight, this seems odd because all d_{002} steps are suppose to originate from split AB steps and therefore should always occur in pairs as is shown in fig 6.4a. At second sight, the dense d_{001} step train consists of completely recombined BA steps (note: there are no holes in these terraces). The only way to create a transition between an original B cleavage face and a recombined A area is via a single d_{002} step.

6.4.3 Dependence on cleavage direction

To be sure that the recombination on the B-ended cleavage faces took place after cleavage, for several cleavage experiments exactly corresponding spots on both cleavage faces were located and imaged with AFM. This was done for cleavages both from the [100] and the [$\bar{1}$00] direction. An example of such corresponding regions on pairs of {001} faces for a cleavage from the [100] direction is shown in fig. 6.5. From this set of AFM topographs it can be concluded that i) the corresponding spots do not match exactly, which indicates that recombination indeed occurred after the cleavage, and ii) at the (001) face the B layer was on top and at the (00$\bar{1}$) face the A layer was on top. Fig. 6.6 shows similar corresponding surface areas after another cleavage at a different position of the same crystal as the one of fig. 6.5, but which now started from the [$\bar{1}$00] direction. It can be seen clearly that now the (001) face is A-terminated and the (00$\bar{1}$) face is B-terminated. These direction-dependent cleavage experiments were repeated for several crystals and the result, which is depicted schematically in fig. 6.7, was always the same.
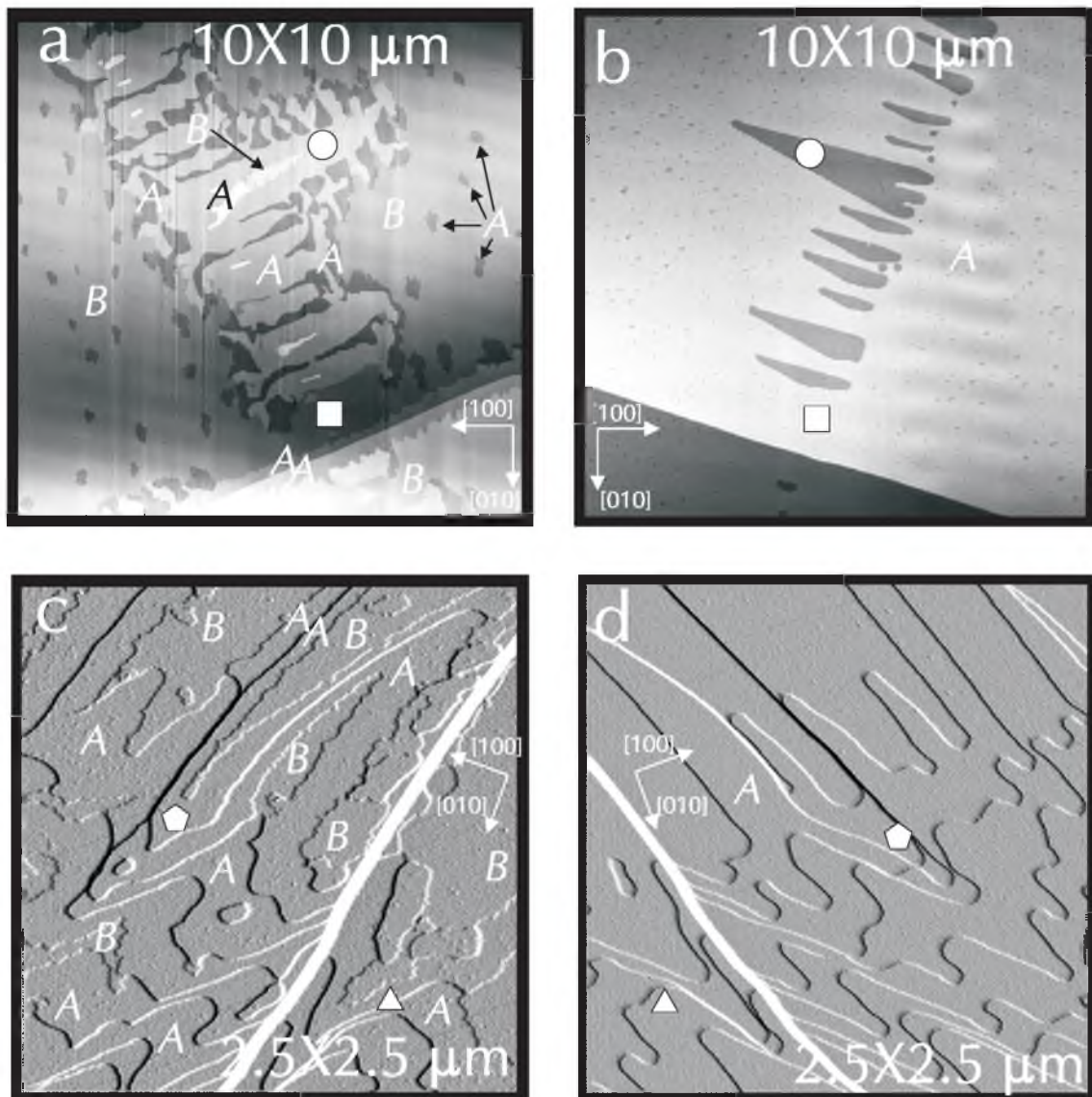
Figure 6.5 The topography of the two opposite {001} faces formed after cleavage from the [100] direction. (a,b) Topographic images of corresponding regions on {001}. (a) Originally *B*-terminated (001) surface showing recombination. The double step *ABAB* in the lower part of the image has split into one *BA* and two *B* steps. The central region with a row of *AB* islands has almost completely recombined into *A* domains which are d_{200} higher respectively lower than the surrounding *B*-terminated surface. (b) The corresponding region on the (00$\bar{1}$) face has no split steps, and the row of holes (corresponding to the row of islands on (001)) is relatively unchanged because of its *A*-termination. (c,d) Deflection images of another pair of corresponding areas on (c) the (001) and (d) the (00$\bar{1}$) cleavage face. Here, there is also recombination on (001) and not on (00$\bar{1}$). To help orientation, for both sets of images two pairs of corresponding surface spots have been indicated by white symbols.
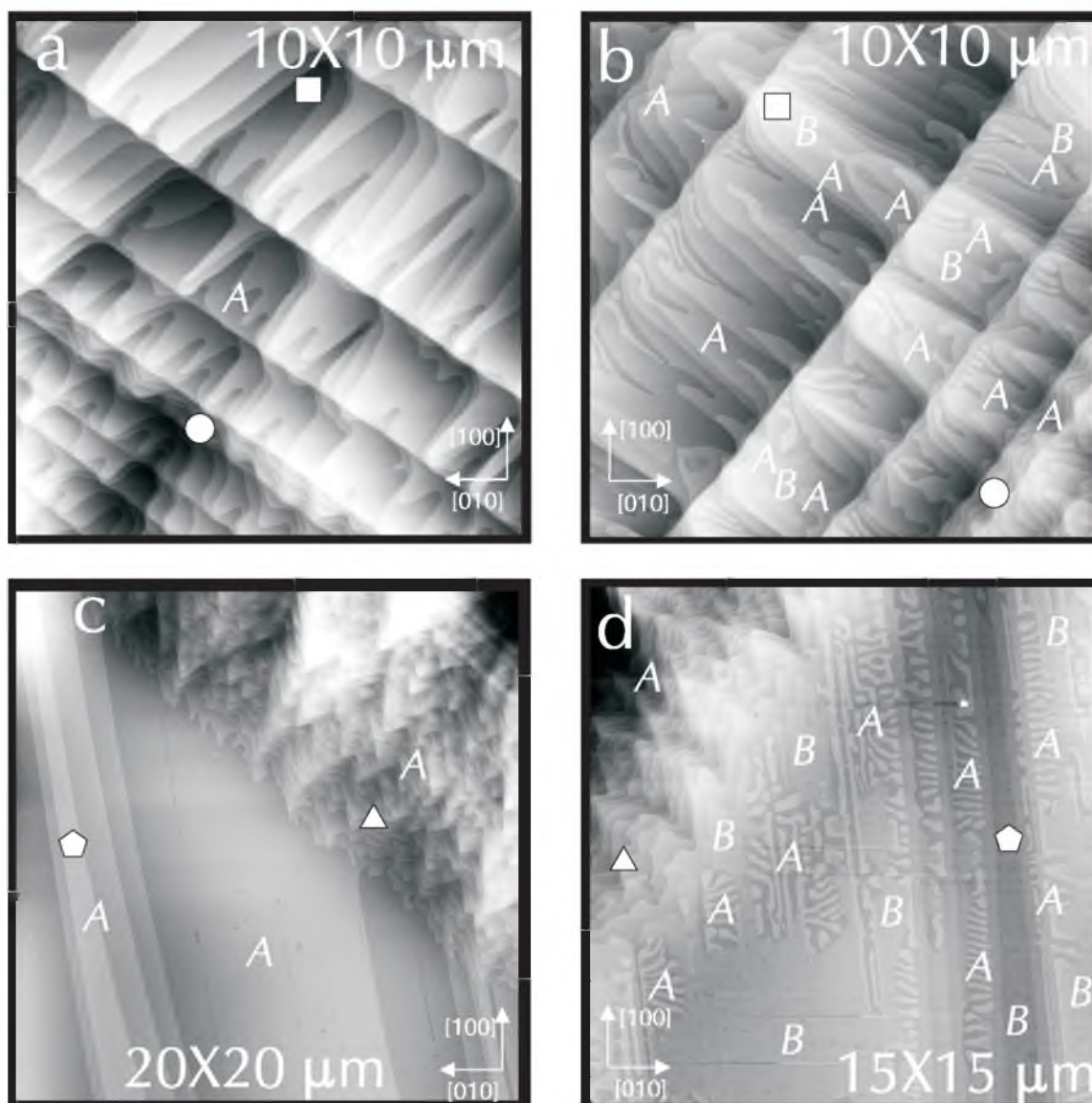
Figure 6.6 Topographic images of corresponding regions on (a,c) (001) and (b,d) (00$\bar{1}$) cleavage faces after a cleavage from the [00] direction. (a,c) For this type of cleavage, the (001) faces are A-terminated and hence do not show step splitting. (b,d) the corresponding regions on the (00$\bar{1}$) cleavage faces are B-terminated and show step splitting. In (b) the steps are so dense that most of the surface has transformed into A-coverage, in (d) the lower part is such flat that still large areas of B-coverage persist. Corresponding surface spots on the two opposite cleavage faces have been marked with white symbols.

6.4.4 Water layer present on the crystals

As stated above, the recombination of the step patterns observed on both the A- and B-terminated surfaces is thought to be facilitated by the presence of a thin water layer. The most likely source of this water is the ambient air. The only other possible water origin comes from opening dislocations
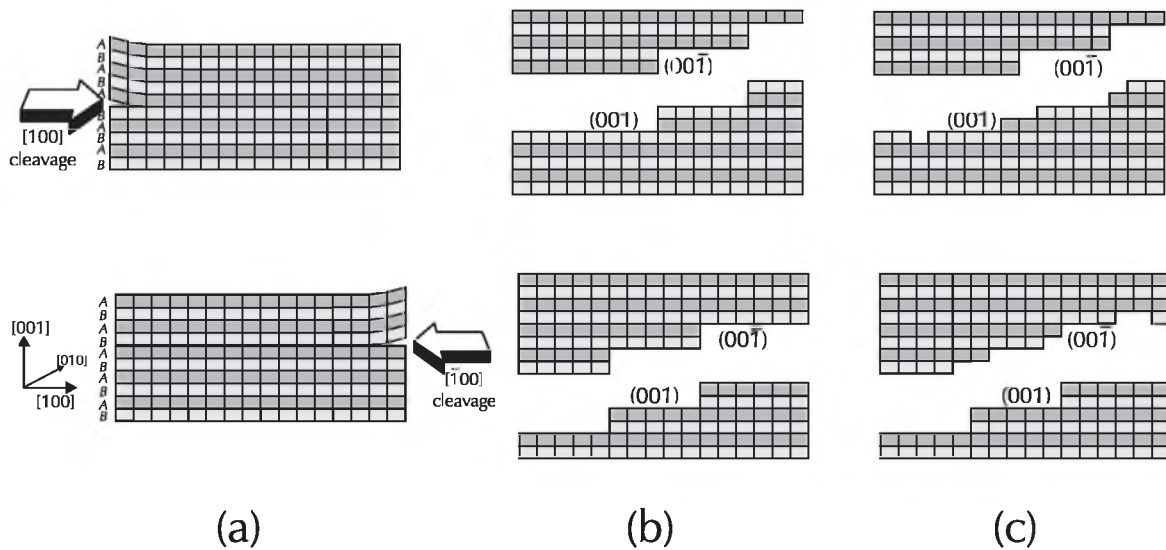
Figure 6.7 Schematic representation of the $K_2Cr_2O_7$ {001} cleavage process for cleavage from the [100] direction (top) and from the [$\overline{1}$00] direction (bottom). (a) Upon cleavage, the type of cleavage plane is determined by the cleavage direction as a result of force minimization. (b) This results in A-covered (00$\overline{1}$) faces and B-covered (001) faces for cleavage from the [100] direction and vice versa for [$\overline{1}$00] directed cleavage. (c) Due to condensed water the energetically less stable B layer partly dissolves and a fraction of that material recrystallizes in the form of A layers.

pouring solution on the cleavage surfaces, which have indeed been found in this study. However, their influence was limited to a region of less then $50\,\mu m^2$ in size. Relative humidity and temperature of the air were measured to be 32 - 36 % and 23 C respectively. In order to check any change of the step patterns on the cleavage faces, some regions were imaged over longer periods. The shortest possible time between cleavage and imaging was about 5 minutes. A few regions were studied over a period of two days. During this period, *no changes in the step patterns were observed*. This means that the noted recombination has occurred very quickly, within a few minutes after cleavage.

In order to unequivocally demonstrate the effect of a water layer present on the cleavage faces, the crystal specimens were placed in a closed vessel having a humidity of 100% for one hour. A typical result of this type of experiment is shown in fig. 6.8. Fig. 6.8a shows an originally B-terminated cleavage face before placement in the 100% humidity vessel. It can be seen that only 10% of the plateaus still has a B layer on top and the rest of the region has already transformed into A layers via capricious steps. Fig. 6.8b shows a region in the direct neighbourhood of that in fig. 6.8a after placing the crystal for one hour in the 100%-humidity vessel. From this image it can been concluded that the last 10% of B layers has been transformed into A-termination as well. The circular $K_2Cr_2O_7$ dots on this micrograph have been formed after the crystals were taken out of the vessel as a result of

crystallization due to a partial evaporation of the thicker water layer formed at 100% humidity. Presumably, the droplet areas denote the regions where B layers have been dissolved, although some parts of BA layers may have dissolved as well. Apart from the indirect evidence of a water layer given above, this layer is observable using tapping mode. This can be accomplished by varying the tapping-mode amplitude damping setpoint, which corresponds to the applied force. This work, which is presented in another study [26], showed the presence of water layers on both {001} cleavage faces.
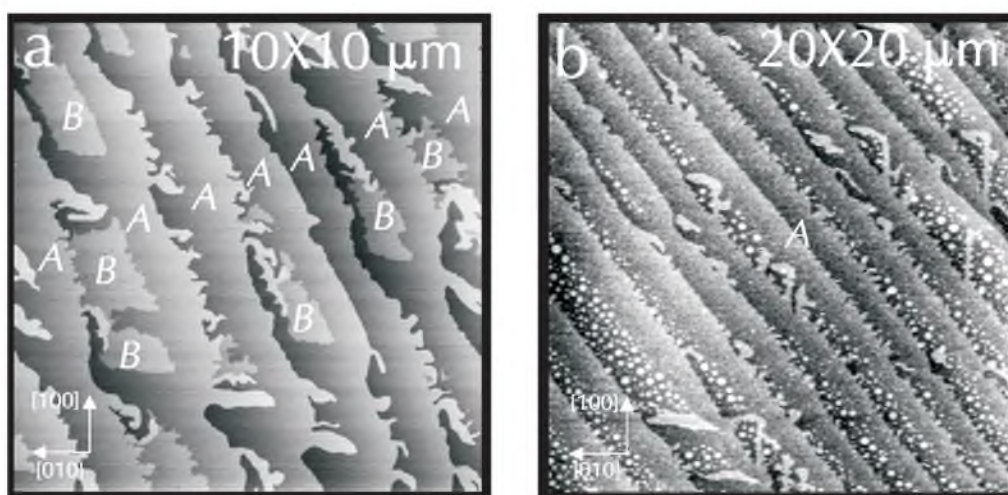
Figure 6.8 (a) An originally B-terminated (0 0 1̄) surface with about 10% B coverage left. (b) A similar surface after one hour exposure to air with 100% humidity. The complete top layer has turned into type A. Probably, the 'droplet regions' indicate former B-terminated areas.

6.5 Discussion

6.5.1 Cleavage asymmetry

The cleavage behaviour as depicted in fig. 6.7, can be understood completely from the crystal structure. In case of cleavage, for one of the cleavage faces the energetically unfavourable layer B is forced to be on top. Here, it is assumed that cleavage always takes place along the same boundary plane, otherwise both cleavage faces will show top B layers. If the cleavage process 'chooses' the same type of border plane (A-B or B-A) throughout the whole crystal, then the top layer is completely A for one cleavage face and completely B for the opposite one. This will result in steps of $d_{001} = 1.34$ nm, of type BA on one face and AB on the other face. In case of a double-layered P1 structure with the inversion centre in the layers, like $K_2Cr_2O_7$, the 'choice' for cleavage along the A-B or the B-A boundary must be dependent on the cleavage direction. If the crystal of fig 6.2a is cleaved from the left, which corresponds to the [100] direction, the cleavage knife, and thus the cleavage force, 'sees'

two different border layers A-B and B-A. The cleavage process will choose just one of them for separation of the two crystal halves, because of the smaller force necessary for this one. From the experiments, this border layer appeared to be B-A, as seen along [001], which is indicated by the left-hand arrow in fig. 6.2a. The same holds for cleavage from the right direction, i.e. [$\overline{1}$00], with the important difference that because of the $\overline{1}$ symmetry now the other border (A-B) should be the favorite choice, which is indicated by the right-hand 'cleavage arrow'. For comparison, the case of a crystal with symmetry centres situated on the layer borders is given in fig. 6.2b. Here, cleavage would occur along the same plane independently of the cleavage direction, as is illustrated in fig. 6.2b, because both border layers are different and one border layer is symmetry-related with itself. The cleavage behaviour of $K_2Cr_2O_7$ crystals is in exact conformity with the above predictions that were made from the $\overline{1}$ crystal structure. Apparently, the cleavage process is selective in such a way that always the most 'force-effective' cleavage plane is chosen for both cleavage directions.

6.5.2 Step recombination

After cleavage, the crystal surface wants to achieve a minimum free energy. In the case of A-terminated faces, this means that the sharp steps become somewhat rounded, minimizing the total step energy. In the case of B-terminated faces, this means step splitting by etching of the B-steps and the formation of d_{002} deep holes in the upper B layer. In case of dense step trains the AB steps fully recombine into BA steps. These processes lead to the development o f the energetically favourable A layer on top of the crystal surface. From fig. 6.4b it is clear that etching of the B top layer occurs on flat crystal parts as well as at steps. Moreover, at steps the dissolved B layer material is partially redeposited as A layers. This leads to the growth of domain-like A-topped patterns with a height of d_{100}, as shown in figs. 6.4c, 6.5a and 6.6d.

Pure etching of holes in the surface by the water layer is expected to stop if the solution is saturated. The recombination at step edges, where only a nett change of B into A coverage takes place, is expected to continue until the B coverage has completely disappeared. The observation that the recombination patterns do not change in time indicates that this recombination occurred in the first minutes after cleavage and does not, or undetectably slowly, continue. This cease of growth and etching may be caused by blocking of steps at low supersaturations, which is a well-known phenomenon for the growth of potassium bichromate crystals from bulk solutions [11, 27]. Indeed, when the cleaved crystals where etched in an ethanol/water mixture, it was observed that in general the top surface layer of the cleavage faces was not etched, unless the cleavage was carried out in ethanol and the cleavage faces were not exposed to air [25]. The occurrence of 20 nm sized grains, often observed in the study of water layers present on $K_2Cr_2O_7$ surfaces in ambient air [26], shows that the cleaved surfaces degrade upon exposure to ambient air, which may cause the blocking of

both growth and etching.

6.5.3 Water layer

The observed step recombination can only have occurred via an aqueous solution layer. Simply because there is no other fluid present and surface diffusion of ions on the bare crystal surface at room temperature over distances exceeding one micrometer is highly improbable because of the very high activation energies involved. Because no change in the step pattern was observed from 5 minutes to 2 days after cleavage, the recombination must have occurred within the first few minutes. The water needed for the recombination could have come from local liquid inclusions inside the crystal which are opened during cleavage, or from water condensed from the ambient air. The influence of opening inclusions was shown to be very local. This leaves the ambient air as the most likely source for the water. This is also suggested by the uniform behaviour and by the changes during the 100% humidity experiments (fig. 6.8).

When water vapour condenses to a layer on a freshly cleaved crystal face, some $K_2Cr_2O_7$ is expected to dissolve in this water layer. From the amount of dissolved material and the solubility of $K_2Cr_2O_7$ in water the thickness of the water layer can be calculated, assuming a saturated solution. In case of B-covered surfaces, for an estimate of the amount of dissolved $K_2Cr_2O_7$ the total surface of the holes present in the B top layer must be measured. In order to exclude any recrystallization effects from this calculation, the best areas to measure the dissolved top face fractions are the flat regions with only d_{002} deep dissolution holes and without steps where recrystallization occurred, as presented in fig. 6.4. The hole fraction of the flat areas in this region is measured to be 3%, 8% and 11% of the d_{002} layer for figs. 6.4a, b and c respectively. These fractions should be compared with the amount of dissolved $K_2Cr_2O_7$ calculated from bulk solubility. This solubility amounts to $0.08d_{002}$ per nm solution layer thickness at 23 C, as is calculated from experimental data [28]. Because in practice dissolution can only occur by full $1.0d_{002}$ layers for B-terminated surfaces, this means that one nm solution thickness corresponds to a dissolved fraction of 8% of the d_{002} top B layer. The dissolution fractions of 3%, 8% and 11% therefore correspond to 0.4, 1 and 1.4 nm solution thickness, respectively. This is identical to 1.5 to 5 monolayers of water. This agrees roughly with the detection of mono- and bilayers of water on NaCl {100} surfaces using different techniques [29-31]. On the A-terminated surfaces holes are rarely observed, which points to the higher stability of this A layer. Therefore, most dissolution of the surface should proceed via BA step edges. The generally rounded shape of these steps (see e.g. fig. 3) indicates that on this face there was some etching and maybe recrystallization as well. However, due to the lack of holes the dissolution fractions could not be estimated for these faces.

6.6 Conclusions

On $K_2Cr_2O_7$ crystals cleaved along the {001} plane, it was always found that the lowest steps present on one cleavage face had a height of d_{001}, while the other face exhibited steps of height d_{002} as well. The cleavage face showing the d_{002} steps (either (001) or (00$\bar{1}$)) is dependent of the cleavage direction ([100] or [$\bar{1}$00]). This asymmetry is caused by the $P\bar{1}$ double-layered crystal structure of $K_2Cr_2O_7$ with the centres of symmetry situated inside the layers, resulting in two different layers A and B.

The observed etching and recombination of the surface after cleavage is demonstrated to originate from a water layer condensed from the ambient air.

Acknowledgments

References

[1]   C. Day, Physics Today, feb. 1999, 17.
[2]   P. Gumbsch, S.J. Zhou and B.L. Holian, Phys. Rev. B **55** (1997), 3445.
[3]   S. Kohlhoff, P. Gumbsch and H.F. Fischmeister, Phil. Mag. A **64** (1991), 851.
[4]   L. Levi, Phil. Mag. **28** (1973), 427.
[5]   L.S. de Wainer and G.A. Basset, Phil. Mag. A **38** (1978), 707.
[6]   K. Sangwal, J. Torrent-Burgués, F. Sanz and J. Servat, Surf. Science **374** (1997), 387.
[7]   K. Sangwal, F. Sanz, J. Servat and P. Gorostiza, Surf. Science **383** (1997), 78.
[8]   O.G. Kozlova, Yu. A. Kharitonov and N.V. Belov, Sov. Phys. Dokl. **24** (1979), 509.
[9]   A. Shubnikov, Z. Krist. **50** (1911), 19.
[10]   A. Shubnikov, Z. Krist. **76** (1931), 469.
[11]   M. Plomp, A.J. Nijdam and W.J.P. van Enckevort, J. Cryst. Growth **193** (1998), 389.
[12]   E.A. Kuz'min, V.V. Iljukhin, Yu.A. Khartinov and N.V. Belov, Krist. Und Techn. **4** (1969), 441.
[13]   J.K. Brandon and I.D. Brown, Can. J. Chem. **46** (1968), 933.
[14]   H.P. Lang, A. Rossberg, M. Piechotka and E. Kaldis, J. Cryst. Growth **144** (1994), 371.
[15]   M. Plomp, K. Maiwa and W.J.P. van Enckevort, J. Cryst. Growth. **198/199** (1999), 246.
[16]   H. Shindo, M. Ohashi, K. Baba and A. Seo, Surf. Science **357-358** (1996), 111.
[17]   R.M. Overney, H. Haefke, E. Meyer and H.J. Güntherodt, Surf. Science **277** (1992), L29.

[18]   E. Finot, E. Lesniewska, J.-C. Mutin and J.-P. Goudonnet, Surf. Science **384** (1997), 201.

[19]   Q. Dai, J. Hu and M. Salmeron, J. Phys. Chem B **101** (1997), 1994.

[20]   A.L. Shluger, R. M. Wilson and R.T. Williams, Phys. Rev. B **49** (1994), 4915.

[21]   M. Plomp, P.J.C.M. van Hoof and W.J.P. van Enckevort, submitted for publication.

[22]   Q. Zong, D. Imniss, K. Kjoller, V.B. Elings, Surf. Sci. Lett. **290** (1993), L688.

[23]   Dimension 3100 Instruction manual v4.31re (1997), 8.17.

[24]   G. Heide and H. Follner, Cryst. Res. Technol. **31** (1996), 171.

[25]   M. Plomp, W.J.P. van Enckevort and E. Vlieg, to be published.

[26]   M. Plomp, W.J.P. van Enckevort and E. Vlieg, to be published.

[27]   A.J. Derksen, W.J.P. van Enckevort and M.S. Couto, J. Phys. D: Appl. Phys. **27** (1994), 2580.

[28]   Szewczyk, W. Sokolowski and K. Sangwal, J. Chem Eng. Data **30** (1985), 243.

[29]   R.A. Lad, Surf. Science **12** (1968), 37.

[30]   P.B. Barraclough and P.G. Hall, Surf. Science **46** (1974), 393.

[31]   P. Tepper, J.C. Zink, H. Schmelz, B. Wasserman, J. Reif and E. Matthias, J. Vac. Sci. Technol. B **7** (1989), 1212.

Chapter 7:

Etching of $K_2Cr_2O_7$ {001} faces observed by

in situ atomic force microscopy

Chapter 7:

Etching of $K_2Cr_2O_7$ {001} faces observed by *in situ* atomic force microscopy

M. Plomp, W.J.P. van Enckevort and E. Vlieg

RIM Laboratory of Solid State Chemistry, Faculty of Science, University of Nijmegen,
Toernooiveld 1, 6525 ED Nijmegen, the Netherlands

Abstract

In order to study the double-layered structure and the occurrence of hypomorphism of potassium bichromate crystals, these crystals were cleaved in air along {001}, and the opposite cleavage faces (001) and (00$\bar{1}$) were etched in ethanol or a water/ethanol mixture. The subsequent etching process was studied by *in situ* atomic force microscopy. It was found that the cleavage faces generally were not etched, in contrary to cleavage faces that were not exposed to air. This difference is attributed to surface poisoning that developed both in air as well as *in situ*. On the air-cleaved faces, only at some positions expanding etch pits developed, in which layer-by-layer etching took place at freshly etched parts on the flat bottom. Most etch steps are of height d_{001}, as expected for the double-layered structure of $K_2Cr_2O_7$. However, sometimes split steps of height d_{002} were encountered. 2D nucleation etch pits found on the (001) and (00$\bar{1}$) faces were similar, suggesting $\bar{1}$ symmetry and the absence of hypomorphy on this small scale. From the orientation of the d_{002} steps inside these pits the stable and the unstable {001} half layers A and B could be identified with respect to the crystal structure. During etching, A is nearly always on the outside of the crystal, proving that this is the most stable layer.

7.1 Introduction

$K_2Cr_2O_7$ crystals are of interest because of their double layered structure and the so-called *hypomorphism* observed on these crystals [1, 2]. The $K_2Cr_2O_7$ (001) face is a 'normal' flat crystal face exhibiting large D-shaped growth spirals, while the opposite (001̄) face shows a block-like structure with a large amount of macrosteps and mini-facets, and inclusions underneath. From previous experiments, we think that this coarse growth on (001̄) is primarily caused by the combined action of impurity adsorption and volume diffusion [3]. Remarkably, this clear difference between opposite crystal surfaces is not reflected in the structure of the crystals as determined by X-ray measurements [4, 5]. These suggest P1̄ symmetry, while the direct surface observations indicate P1. This phenomenon is called hypomorphism. Heide and Follner [6, 7] ascribe the coarse appearance of the (001̄) face to homoepitactic intergrowths, of which 10% are twins. These are thought to originate from microscopic nuclei present in the solution, which contact and subsequently grow out on the mother crystal. The 10% twins cause stresses in the growth layer which are responsible for the block-like structures. This explanation suggests that the hypomorphism is only present on macroscopic scale, and that on a much smaller scale the {001} faces would behave the same.

Etching of $K_2Cr_2O_7$ in water and other solvents has been studied intensively by optical microscopy before [8]. For the current experiments, $K_2Cr_2O_7$ crystals cleaved along {001} were used. The structure of $K_2Cr_2O_7$ consists of two different layers denoted as A and B (see fig. 6.1), which are only related by pseudo-symmetry based on a rotation of $\gamma = 90.75$ about [001] of one of the layers with respect to the other. We found that the cleavage plane depends on the cleavage direction [9], but this difference is not expected to influence the growth or the etching. During growth and etching the layer with the lowest surface energy, which is denoted A in accordance with [9], is expected to be on top of the d_{100} layers that occur on both {001} faces.

With the development of atomic force microscopy (AFM) crystal growth as well as etching can be investigated *in situ* on a very small scale. For both cases, however, the velocity of the process that can be monitored is limited by the slow, serial data collection which is inherent to AFM. Therefore, most *in situ* AFM studies so far are done on the surfaces of slowly growing/etching crystals, such as proteins [10-13], other organic compounds [14] and low-soluble ionic crystals [15, 16]. For highly soluble, fast growing, ionic compounds such as $K_2Cr_2O_7$, AFM observation of growing/etching step patterns is only possible by keeping the supersaturation very low, which can only be achieved by a very good control of the temperature, or by lowering the step velocity by e.g. adding growth-retarding additives [17] or using a specific solvent. In this study, the second method is applied by changing the solvent from pure water to ethanol with some water added.

7.2 Experimental

Potassium bichromate single crystals with sizes of about 5mm X 10 mm X 5 mm grown from aqueous solution were selected. All crystals exhibited D-shaped growth spirals on their (001) faces, which were used for indexing the crystals. These crystals were cleaved and imaged using tapping-mode AFM (TM-AFM) in order to investigate the cleavage patterns. This was done in a room with a humidity of 32 to 42 % and a temperature of 23 C. After 2½ hours to 7 days, the cleaved crystals were placed in a petri-dish containing pure ethanol. Etching of the crystals was accomplished by adding one or a few droplets of water to the ethanol before or after placing of the crystals in the liquid. Images were recorded at water concentrations of 0, 0.7 and 2.1 vol.% in ethanol. Some crystals were cleaved in ethanol to prevent air exposure of the cleavage surfaces.

In situ imaging was done by the AFM operating in contact mode (CM-AFM). The AFM employed was a Digital Dimension 3100. The contact mode silicon nitride cantilevers used had force constants of 42 N/m. Both topographic and deflection images were used to map height differences and step structures respectively. For detailed measurements of etch pit walls scanning electron microscopy (SEM) was applied. For this, a Jeol JSM-633 OF field-emission SEM was used.

7.3 Results

7.3.1 Etch pit formation on 'inert' cleavage faces

Cleaved crystals exposed to air at least two days did not change the morphology after immersion in ethanol, thus no etching occurs. This cleavage structure, which was described elsewhere [9], consists mainly of V-shaped cleavage patterns and rounded recombination steps, which were formed immediately after cleavage due to the condensation of a thin water layer on the faces. When water was added to a volume concentration of 0.7%, the imaged area started to deteriorate slowly, as can be seen in fig. 7.1 for both a (001) face in which a few images from a large time-series are shown. The top layer is very reluctant to etching, but when it is removed in certain areas, smooth layer-by-layer etching takes over. It can take 10 scans, corresponding to 50 minutes, to completely remove the top layer, and another 20 scans to flatten the rough surface induced by the irregular top layer etching. In the zoom-outs of this figure, it can be seen that the original cleavage face is still largely intact in those parts of the surface that were not previously imaged (fig 7.1d). From this, it can be concluded that the AFM imaging enhances the etching of the crystal.

This AFM-induced selective etching can be employed for lithography purposes, as is shown in fig.

7.2. In this figure, the result is shown of repetitive scanning at four areas of 2 μm X 65 nm. Four 'canyons' 90 nm wide and 5 nm deep were made. The very local etching indicates that the preferential removal of material is due to the tip-crystal surface interaction. After the removal of the top layer, some deeper etching occurs spontaneously.

Fig. 7.3 shows an etching series recorded for an ethanol solution with a higher water content of 2.1%. It can clearly be seen that the etch pits that start as d_{001} deep irregular holes, become deeper in course of time, become more and more faceted along the major crystallographic orientations
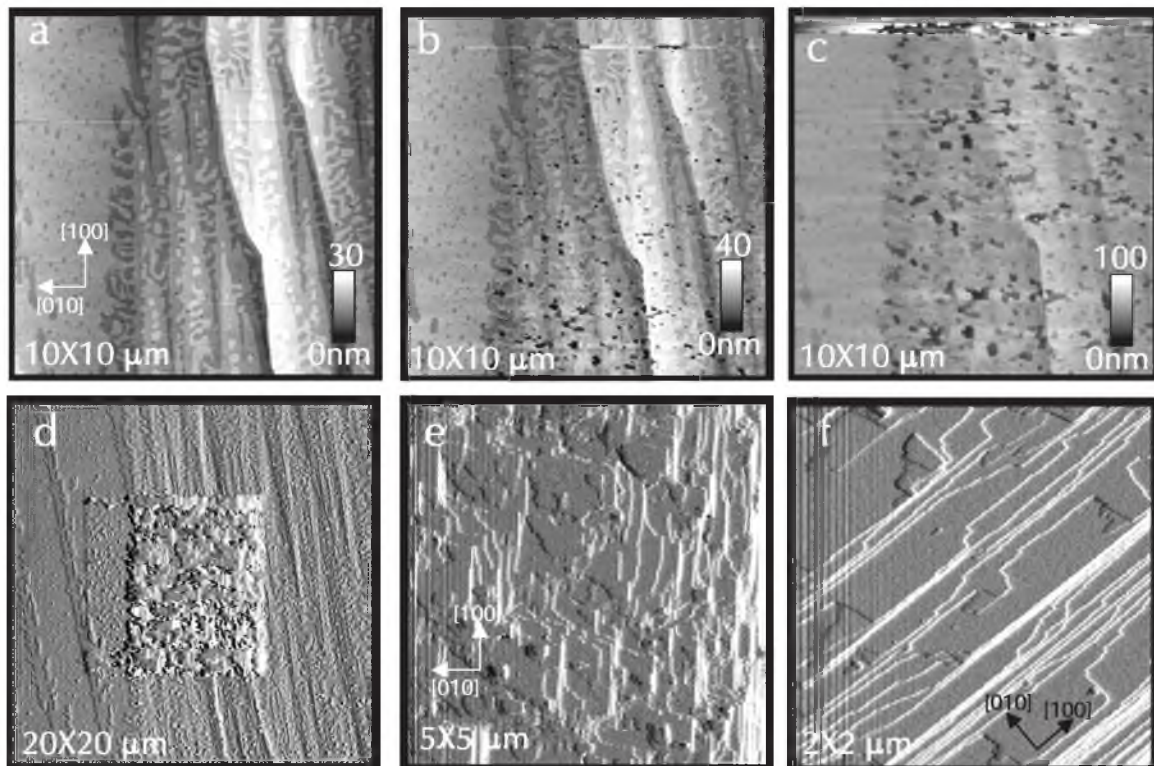
Figure 7.1 Deterioration of a (001) cleavage $K_2Cr_2O_7$ surface after repeated scanning in a 0.7% water/ethanol mixture. One week has elapsed between cleavage and immersion in the mixture. (a) Topographical image of the original cleavage pattern that is nearly intact after 50 minutes of immersion plus one scan. (b) 11 minutes and 2 scans later 15 nm deep holes start to appear, while large parts of the original surface remain unaltered. (c) 4 minutes and 1 scan later the amount and depth of the holes has increased. (d) Zoom-out deflection image recorded 13 minutes and 4 scans later as (c), showing that beyond the 8 times scanned 10x10 μm² area hardly any etching occurred. In the central region the depth has increased to 30 nm. In the course of time, the holes in the central region become wider and contact each other, which leads to the evolution of a flat surface, as is clearly visible in the 5x5 μm² zoom-in of (e), recorded 12 minutes and 14 scans after (d). (f) Zoomed-in and rotated image recorded 21 minutes and 35 scans after (e) showing layer-by-layer etching at the bottom of the etched square. Most steps are now along the [100] and [010] crystallographic directions.
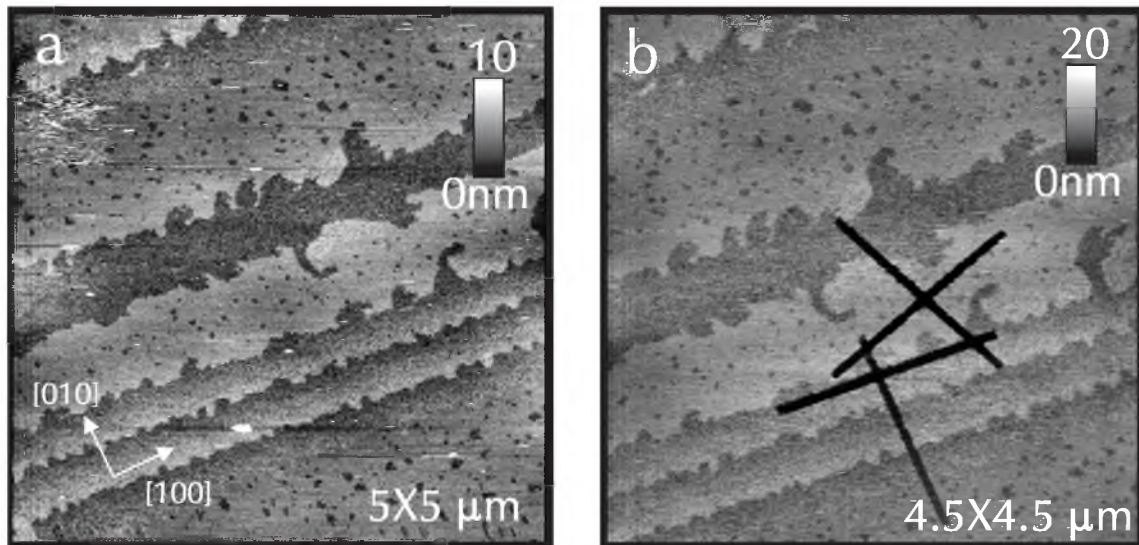
Figure 7.2 AFM *in situ* topographs of an area on a $K_2Cr_2O_7$ (001) cleavage face imaged in 0.7% water/ethanol before (a) and after (b) lithography. Four areas of 2 µm X 65 nm were scanned with 32 linescans per area, which resulted in canyons of 2 µm X 90 nm and 5 nm deep.

<100> and <010>. The bottoms of the pits consist of (multiples of) d_{001} steps. If two etch pits contact, the bottom of the shallowest one is etched quite fast until the bottom level of the deepest pit is reached.

In addition to the enhanced etching at surface positions that are repeatedly scanned by AFM at this water concentration, etch pit formation is also observed at previously non-imaged and even at never imaged areas as is shown by the optical photograph of fig. 7.3l, in which the AFM-imaged area of fig. 7.3h-k can be recognized as well. The depth/ width ratio development of two pits indicated in fig. 7.3 is depicted in fig. 7.4. This figure shows that in the first stage of the formation of a faceted etch pit, there is hardly any lateral or perpendicular etching. After the reluctant layer is removed, the etching is pure perpendicular for a while. Later on, the lateral etching becomes more important. The final depth/width ratio is 0.10 - 0.15 for most pits.

Fig. 7.5 shows another AFM topograph of a freshly scanned area with etch pits that are not scan-induced. In this figure both the original cleavage steps of height d_{100} parallel to [100] and the, mostly rectangular, etch pits can be distinguished. It was found that for all etch pits the centre of the bottom is somewhat higher than the region near the sides, from which it can be concluded that the etching starts near or at the side faces. Moreover, it can be noticed that the etch pit bottoms look somewhat rough. The AFM pictures suggest that the slope of the etch pit walls is about 45 . This corresponds to the maximum detectable inclination by AFM, because of the finite slope of the AFM tip itself.
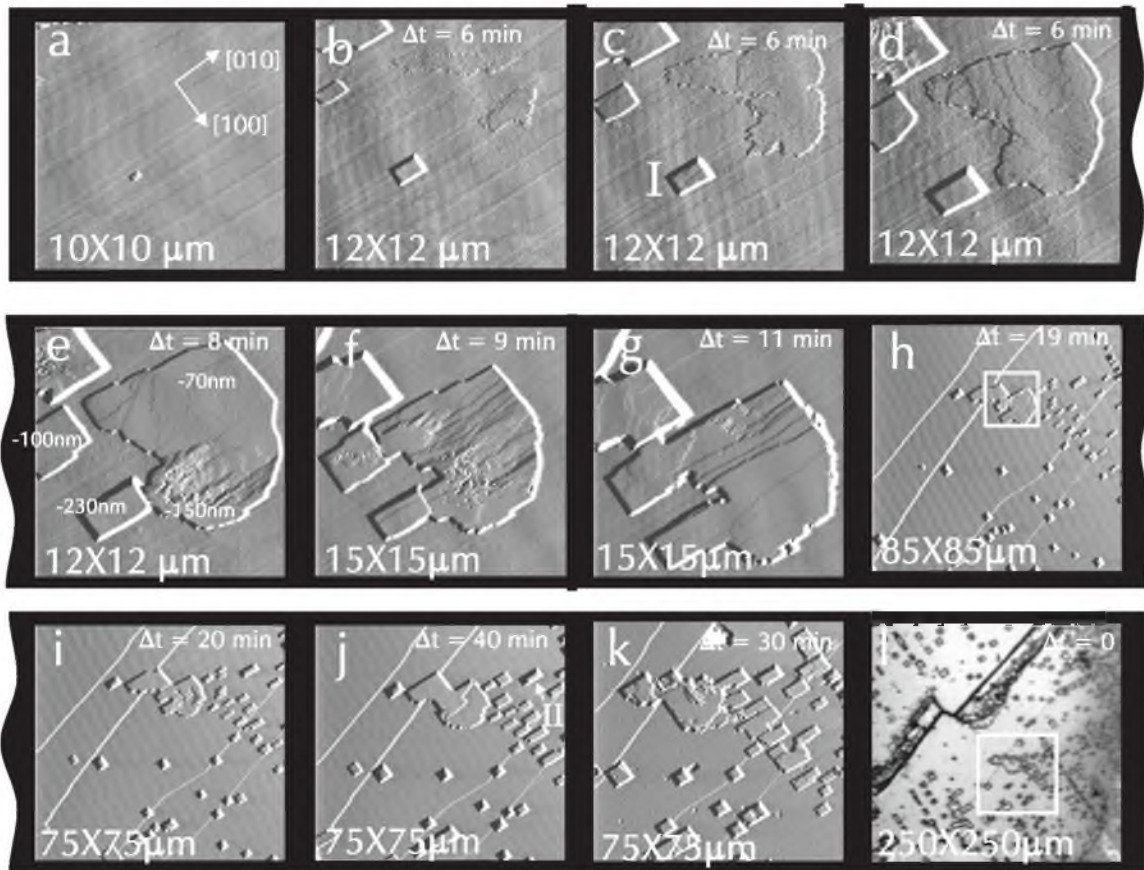
Figure 7.3 AFM deflection images showing the development of rectangular etch pits on a (001) K$_2$Cr$_2$O$_7$ surface immersed in a 2.1% water/ethanol mixture two days after cleavage. The elapsed time between the recording of the successive images shown is indicated in the figures. (a-k) The development of both deep, rectangular pits and large shallow, irregularly shaped depressions imaged on a scale varying from 10x10 μm^2 to 85x85 μm^2. In (e) the etch pit depths are indicated; in (k) the pit depths vary from 0.5 μm to 1.1 μm. (l) Optical image recorded after the etching experiment was stopped, showing that some etch pits are solitary, while others occur in rows, and that repeated scanning enhances the etching at the scanned regions, but is not the cause of etching. The white squares in (h) and (l) mark the regions imaged previously. The development of the pits marked I and II in figs. (c) and (j) is shown in fig. 7.4.
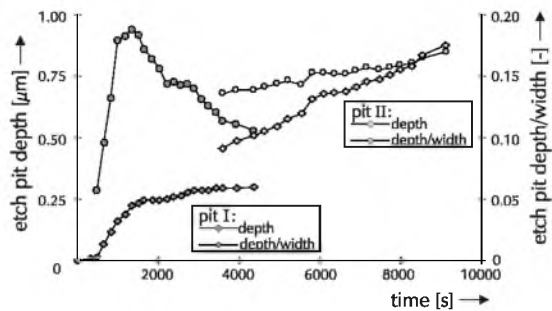
Figure 7.4 The development of the depth and depth/width ratio for the two etch pits I and II marked in fig. 7.3(c) and (j). For new pits, such as I, the depth/width ratio first increases rapidly, then decreases and finally becomes more stable. The final depth/width ratio is 0.1 - 0.2 for most pits.
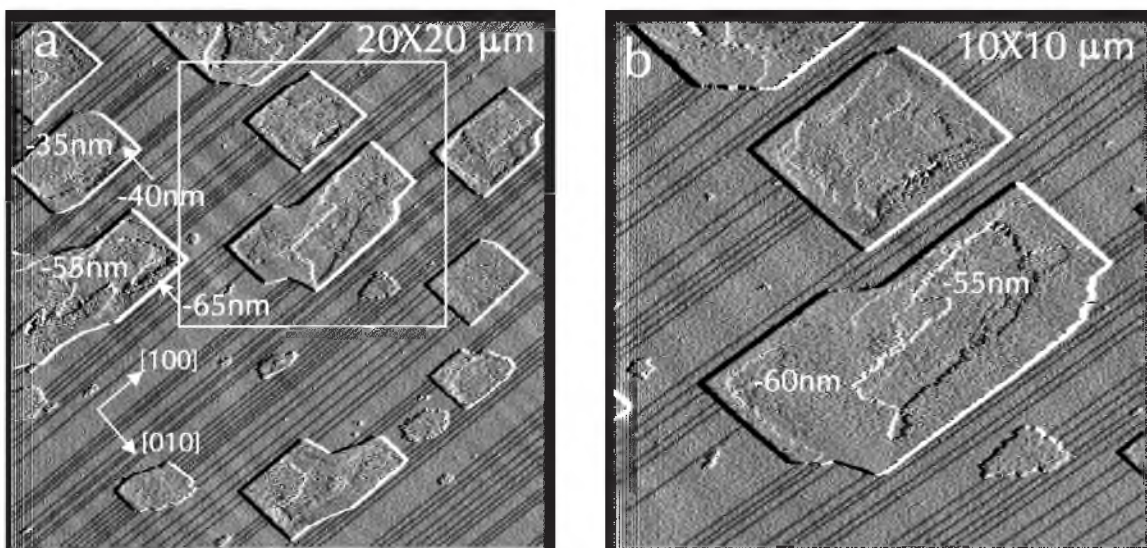
Figure 7.5 (a) Freshly scanned etch pits on still intact (001) cleavage surface immersed in ethanol/water one week after cleavage. (b) Zoom-in of the area marked by a white square in (a). Note that all pits have a somewhat roughened bottom, especially at the center, and that the etch pit bottoms are less deep at their centres than at their periphery. After scanning several times, the bottom turns flat. The depth of several pits is indicated in nm.

Therefore to get a reliable value of the pit side slope, scanning electron microscopy was applied after termination of the etching experiment (fig. 7.6). For several etch pits on {001} the inclinations of the side walls were determined to be close to or equal to 90 , *i.e.* the side faces are {100} and {010}

facets. The slope was thus indeed larger than detectable using AFM.

7.3.2 Layer-by-layer etching

When the resistant surface layer is removed, regular layer-by-layer etching takes place at the flat bottoms of the etch pits. If AFM is applied to small bottom areas of the etch pits (scan size   1 μm), this process can be followed in a detailed way. This is done both for (001) and (00$\overline{1}$) faces as shown in figs. 7.7 and 8, respectively. It is seen that lower layers are accessed by the formation of 2D nuclei. The large majority of the steps has height d_{100}. A comparison of the 2D etch pit morphology on both {001} faces will be made in section 7.4.4.
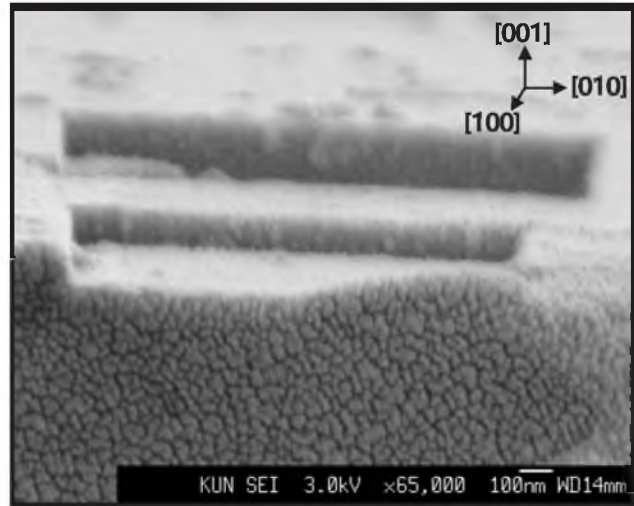
Figure 7.6 SEM image of two etch pits on the (001) face of a $K_2Cr_2O_7$ crystal. On the foreground a small part of the crystal's (100) side face, which is covered by gold particles, is visible. Because the front etch pit has grown such large that it contacts this (100) face, its side faces can be observed to make an angle of about 90 with respect to the (001) top face.

With respect to the double-layered nature of $K_2Cr_2O_7$, it is interesting to study the height of the steps at these new nuclei. From the $K_2Cr_2O_7$ structure it is expected that the most stable layer is preferably on top and all steps will be of d_{001} nature. In accordance with [9] the most stable layer is defined as A, from which it follows that the steps must be of type BA (*i.e.* a double step with the A layer on top). However, from 2D nucleation theory it is expected that new holes are formed layer by layer, *i.e.* both A and B type d_{002} steps are expected. From the images of figs. 7.7 and 8 it can be seen that d_{002} steps are indeed present at newly formed 2D nucleation pits or exist as more extended steps, although most steps are of BA d_{001} nature. The fast B d_{002} steps always catch up the slow A d_{002} steps ahead. This indicates that A termination is energetically more stable than B, but that it takes some time for the system to reach this stable configuration.
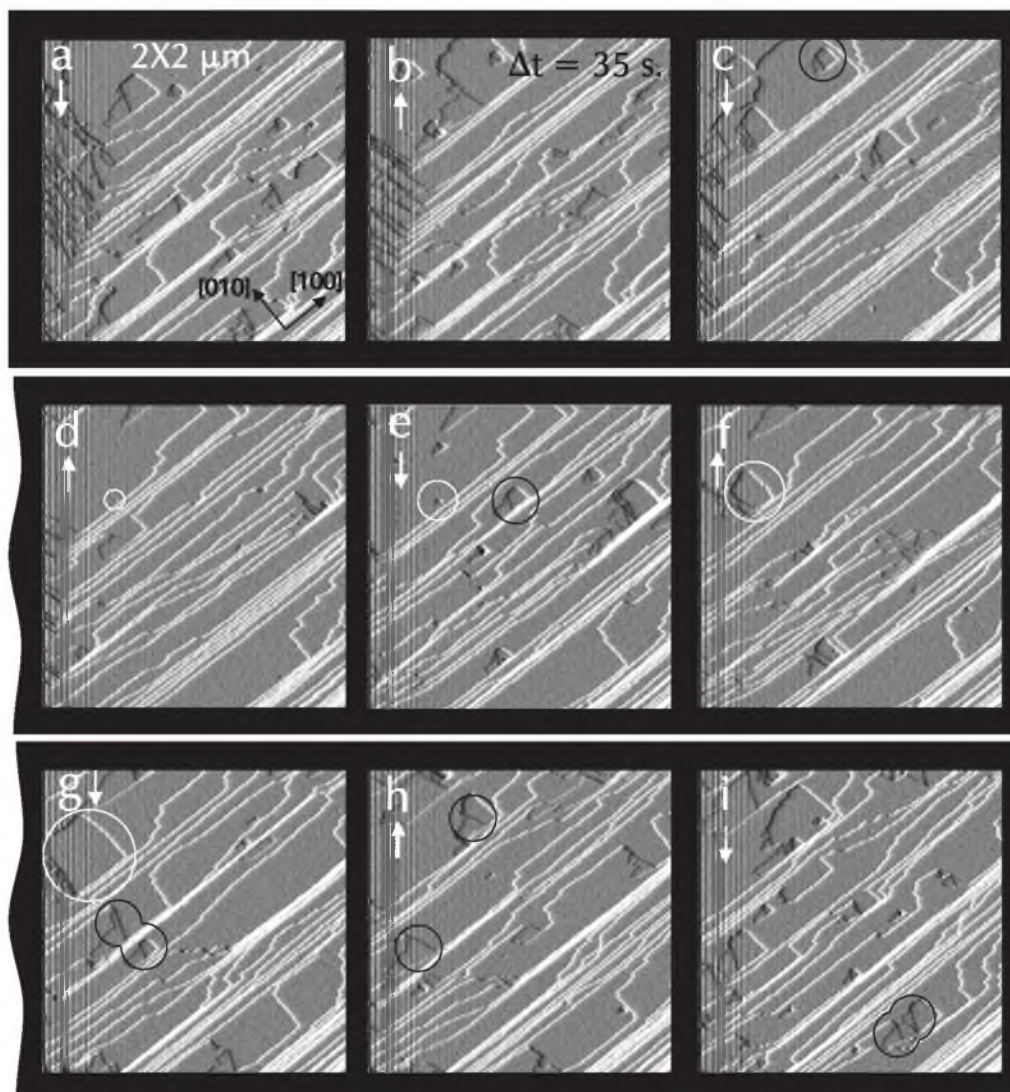
Figure 7.7 Time series of 2x2 μm^2 AFM deflection images showing the layer-by-layer etching of a $K_2Cr_2O_7$ (001) surface one week after cleavage and 2 hours after immersion in 0.7% water/ethanol. The images are recorded on the bottom of an etch pit; the time interval between successive images is 35 seconds. The slow scan direction goes from top to bottom or vice versa in an alternating way, as is indicated by the white arrows. Most d_{001} steps are along [100] and [010]. The development of one single 2D etch nucleus is indicated by white circles in (d-g). Step velocities vary between 3 nm/s for [0 10] to 11 nm/s for [100] directed steps. Besides the common d_{001} steps, a considerable number of d_{002} steps can be observed in all images. Some of these are marked by black circles in (c, e, g, h, i). These steps are always directed towards [1 00], but due to their large velocity as compared to the AFM slow scan axis (which is always the *y* axis in the figures) their apparent direction deflects somewhat to [010] for downward scans (see (g)) and to [0 1 0] for upward scans (see (h)). The propagation rate is measured to be 25 nm/s.
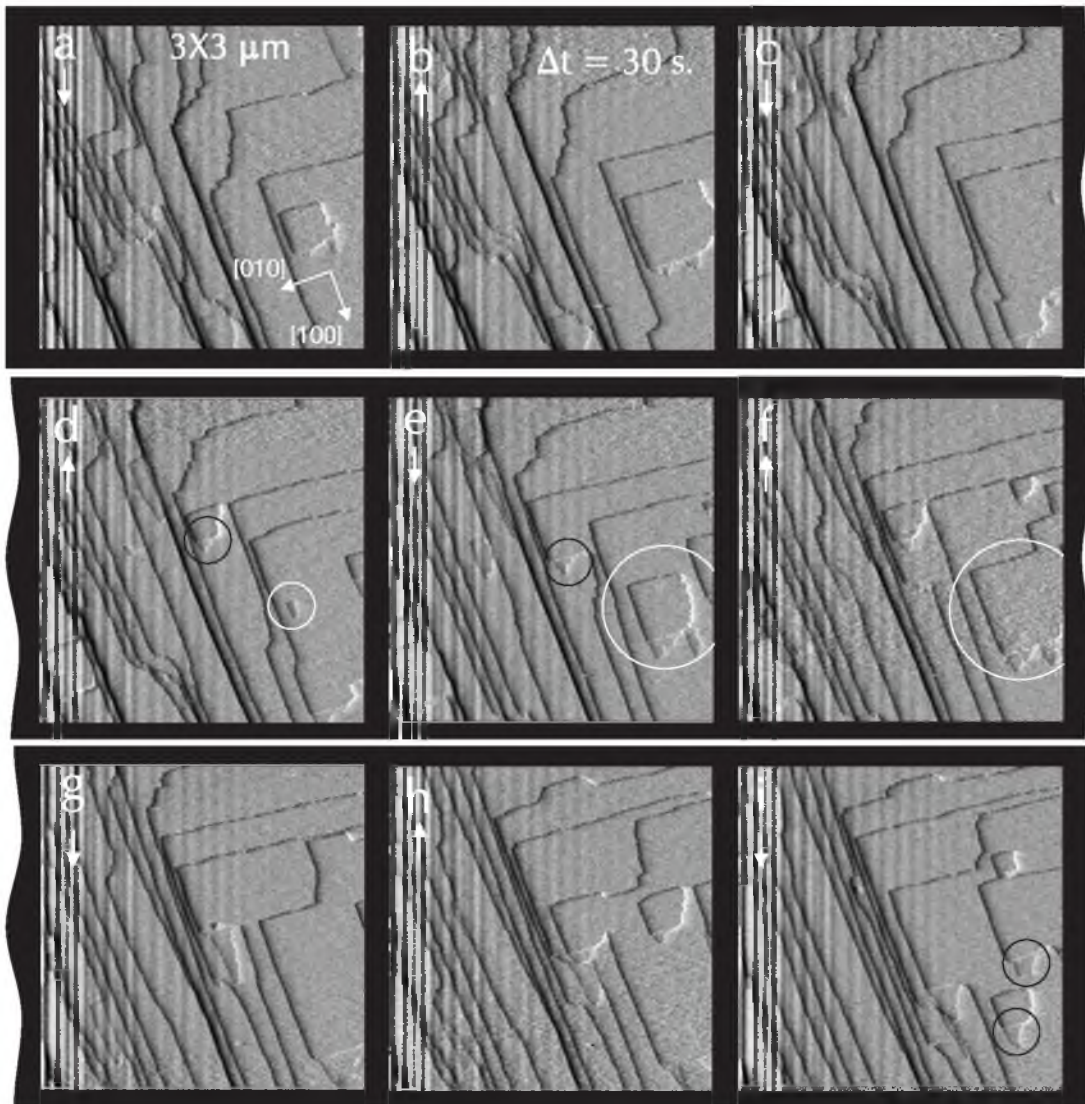
Figure 7.8 Time series of 3x3 μm^2 AFM deflection images of the layer-by-layer etching of a $K_2Cr_2O_7$ (00) surface, one week after cleavage and 2 hours after immersion in 0.7% water/ethanol. The images are recorded on the bottom of an etch pit; the time interval between successive images is 30 seconds, White arrows indicate the slow scan direction. The development of one single 2D etch nucleus is indicated by white circles in (d-f). Most d_{001} steps are along [100] and [010]. Their propagation velocity varies between 3nm/s for [010] to 15 nm/s for [0 10]. At the etch nuclei, [100] directed d_{002} steps are observed. Some of these are marked by black circles in (d, e, i). Their propagation rate is estimated 15 nm/s.

In successive images the direction of the trailing B steps is seen to change direction in an alternating way, in contrast to the BA d_{001} steps. This is caused by the combination of the alternating slow scan direction (upwards - downwards) in successive images and the fact that these trailing steps move relatively fast compared to this slow scan rate (see e.g. [11]). From the images and the known scan rate it was calculated that the BA d_{001} steps move with a velocity of 10 nm/s and the trailing B steps in the same series advance at a velocity of 25 nm/s. This difference is caused by the driving force for the energetically most stable surface. After making a zoom-out picture of the imaged layer-by-layer etching areas, it can be noted again that the etching is enhanced by the AFM imaging.
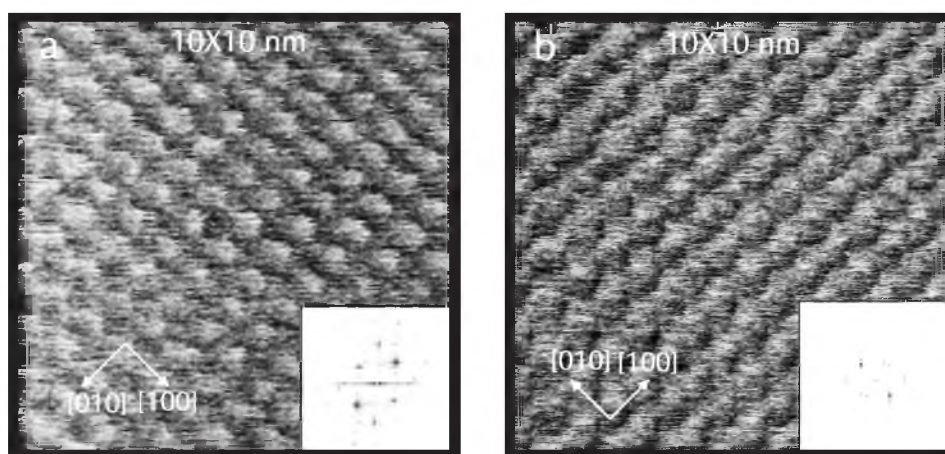
Figure 7.9 Unfiltered molecular resolution images, recorded in a 0.7% water/ethanol mixture, of the $K_2Cr_2O_7$ (a) (00$\bar{1}$) face and (b) the (001) face. The insets in both (a) and (b) show the corresponding fourier transformed images. The lattice parameters are within error the same for both faces.

7.3.3 Molecular resolution

After roughly 5 hours of immersion the etching slowed down, and molecular resolution images of both $K_2Cr_2O_7${001} faces could be made. This could only be done *in situ* at the bottom of the etch pits, which is illustrated in fig. 7.9 for both faces. The periodic structures shown are checked to be real molecular resolution images by zooming in and out and by rotating the images. The directions of the molecular rows coincide with the [100] and [010] crystallographic directions. The lattice parameters are within error the same for both faces and consistent with X-ray diffraction. This proves that in there is no reconstruction, at least not *in situ*. The spheres visible in these figures have roughly the size of the $K_2Cr_2O_7$ unit cell. Each unit cell consists of four $K_2Cr_2O_7$ units, organized in two d_{002} layers. In the upper d_{002} layer there are thus two $Cr_2O_7^{2-}$ ions in the two-dimensional unit cell ([100], [010]). Only one of them seems to be imaged by AFM. This is conform the structure determined by X-ray diffraction, which places one of the $Cr_2O_7^{2-}$ ions 10% of d_{002} higher than the other.

Ex situ molecular images could not be made, not even from freshly cleaved crystals. This is probably due to the dissolution/recrystallization effect caused by a water layer present on a surface exposed to ambient air, as demonstrated in [9].

For these cleaved surfaces molecular resolution could also not be achieved on the resistant top layer after immersion in ethanol and water. This indicates a change of the surface structure after cleavage, leading to some type of disordering.

7.3.4 Shorter exposure to ambient air

In order to verify the assumed development of an etch-protective layer on cleaved {001} $K_2Cr_2O_7$ surfaces in air, additional etch experiments were carried out for specimens that were exposed to air for a period less then the two to seven days mentioned above. For this, crystals exposed to air for 0 or 2½ hours prior to etching were used. Zero exposure was realized by cleavage and subsequent imaging in the ethanol, thus avoiding the cleavage face being in contact with the ambient air any moment.

Figure 7.10 Etching observed on $K_2Cr_2O_7${001} faces that were cleaved in ethanol and subsequently imaged without exposure to air. No protective layer is present. (a,b) Subsequent images of etching of cleavage macrosteps on (001) after ten minutes of cleavage. (c, d) Subsequent images of a flat part of the (001) face, showing isotropic 2D nucleation giving pits of both d_{100} and d_{200} depth, as indicated. Slow scan direction is indicated by white arrows. Similar pits were observed on (00Ī).

In this case of zero air exposure etching was slow, as is expected in pure alcohol, but steady. Moreover, the etching started directly at the cleavage steps, as is illustrated in figs. 7.10a, b. This proves the absence of an etch-protective layer. On flat parts of the crystal surface 2D nucleation etching is observed, as shown in figs. 7.10 b, c. Only after several hours the direct etching at the surface steps slowed down. Adding a few droplets of water caused acceleration of the surface etching and created deeper, faceted etch pits as well. The AFM scanning enhanced the etching, as in the case of crystals cleaved in air.

For the intermediate case of 2½ hours air exposure between cleavage and ethanol immersion, intermediate results were found (figs. 7.11, 12). The surface monosteps *did* etch, as was the case in

the non-air exposure experiments, but only a few layers (see figs. 7.11b, d) and during a period of less then 20 minutes. Most of the etching took place by the formation of deep pits, bounded by {010} and {100} side facets (figs. 7.11a, c), which are similar to those found for etching after days of air exposure (figs. 7.3, 5). Closer examination of these pits learns that they have bottoms with a roughened, somewhat higher central 'plateau', as compared to the atomically flat, peripheral regions of the pit bottoms (fig. 7.12). This was also observed for the experiments using crystals longer exposed to air (fig. 7.5). The flat parts are seen to originate from freshly etched side facets, whose lateral displacement leaves a 'clean' bottom area. In the course of time, these newly created flat parts are sensitive to roughening as well, as is illustrated in fig. 7.12. This roughening looks the same as the

Figure 7.11 The effect of 2½ hour exposure to ambient air between cleavage and immersion in pure ethanol. Imaged is a (001) face 45 min. (a, b) and 85 min. (c, d) after the start of etching. The topographic images (a, c) show the growth of pits with depths up to a few hundreds nm. The corresponding deflection images (b, d) show that the top surface did not change in this period. However, (b) clearly shows that some etching has occurred in the beginning of the ethanol exposure. Similar behaviour has been observed on the (001) face.

roughening of the top face. The results of the experiments with different air exposure times are summarized in table 7.1. The data in this table concerning the etching behaviour in air are extracted from the cleavage study published elsewhere [9].

Table 7.1 Etching behaviour of surface cleavage steps for different experiments

experiment	amount of etching	etch duration
air exposure only	10% of monolayer	< 5 min.
no air exposure; etching in ethanol	large, continuous etching	few hours
2½ h air exposure; etching in ethanol	<a few layers	< 20 min.
>2 days air exposure; etching in ethanol/0.7-2.7% water	no etching	-
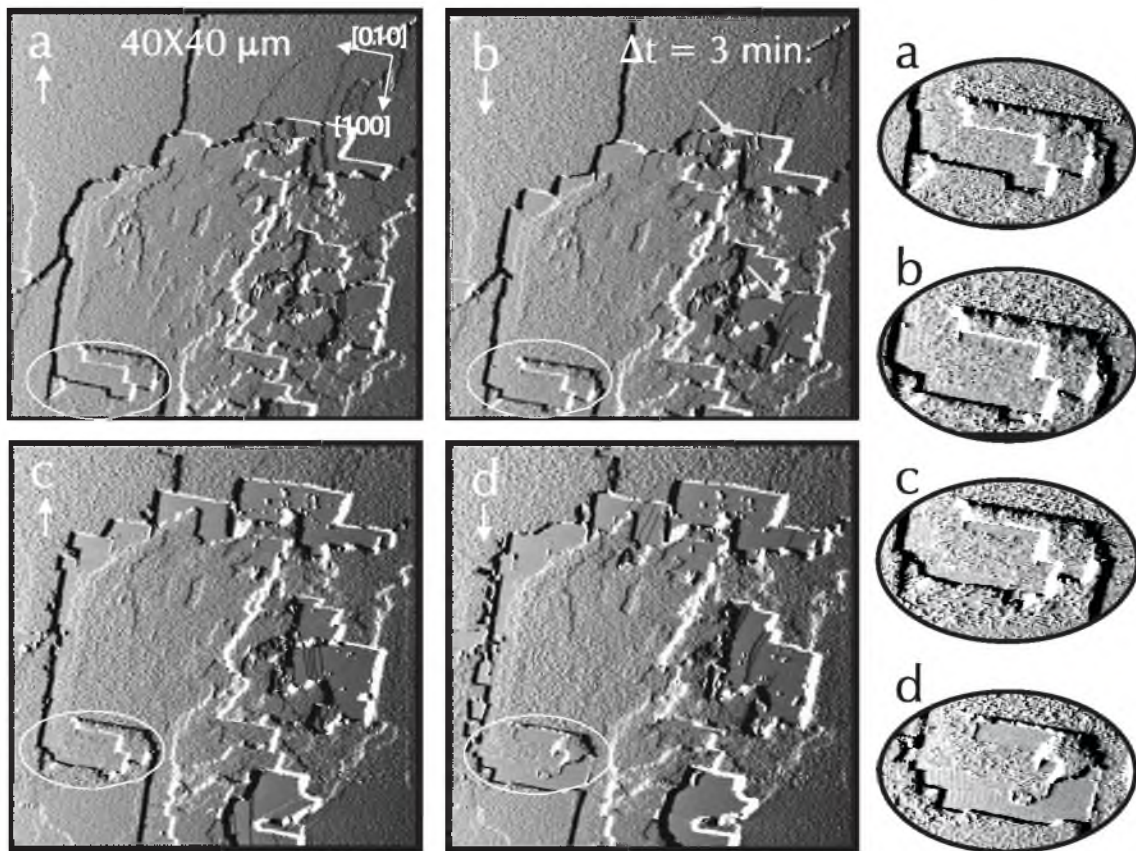
Figure 7.12 Time series of the development of the central pit of fig. 7.11 about 1 hour after immersion in ethanol. The pit only grows laterally by etching of the steep side facets. The pit's central region is as roughened as the top surface outside the pit. Only near the side facets the pit bottom is atomically flat, as is proven by the occurrence of moving molecular steps (indicated by grey arrows in (b)). The flat regions only occur at areas where the side facets just have etched away. In course of time these regions become roughened as well. This is illustrated for the encircled area. The flat surface in (a) becomes more and more roughened in (b-d), while the fresh bottom parts of (b-d) are still flat in (d).

7.4 Discussion

7.4.1 Surface poisoning

From the results summarized in table 7.1, it can be concluded that the top layer is very resistant to etching, and that this depends on the time of exposure to air between cleavage and immersion into the etching liquid. That the protective layer is formed in air follows from the experiment summarized in fig. 7.10, in which the cleavage surfaces of crystals cleaved in pure ethanol show immediate etching of surface cleavage steps, even without the addition of water. The longer the air exposure, the stronger the resistance to etching. After an air exposure of two days, the surface steps do not etch

at all. From the ex *situ* study of the cleaved K$_2$Cr$_2$O$_7$ {001} faces in air [9], it is known that the etching and reorganization of the crystal surface due to the presence of a layer of water condensed from the ambient air already stops a few minutes after cleavage. Probably the formation of a protecting layer leading to the blocking of steps already sets in then.

From non-continuously imaged etch pits it was found that the bottoms of the pits often are somewhat roughened at the centre, and that the periphery of the pit bottoms is often lower and more flat (figs. 7.5, 12). In contrast to the flat peripheral regions the central, rough area neither showed etching nor steps. In fact the roughened pit area looks the same as the roughened top face (fig. 7.12) The atomically flat regions near the advancing side faces of the pits gradually become roughened as well after 10 - 30 minutes of their creation (fig. 7.12). From this, it can be concluded that in a thin surface layer on a K$_2$Cr$_2$O$_7$ {001}surface exposed to air a protective layer develops. After 2½ hours of air exposure this layer can be removed by pure ethanol, but it rapidly forms again. After two days of air exposure the layer is so thick or strong that it cannot be removed anymore, even with the help of small amount of added water. The only way in which etching is still possible is by a local break-through of the protective layer. This is then followed by an initially perpendicular etch, creating tiny, but deep holes (figs. 7.1, 3). After about 20 minutes the pits start to expand laterally (fig. 7.4) by etching of the <100> and <010> side facets. These perpendicular side faces apparently are less resistant to etching than the {001} faces. Both the vertical and the lateral growth of the etch pits are determined by the pit's side faces. A similar difference between a blocked {001} face and growing mini-facets of other orientations on this K$_2$Cr$_2$O$_7$ surface was found earlier for the case of growth of the (001) face [3]. The occurrence of layer-by-layer etching after removal of the poisoning layer and the possibility of molecular resolution imaging in that case both indicate that, by the combination of an undersaturated solution and a continuous 'stirring' and etching by the AFM tip, the re-formation of the protective layer can be prevented.

Several K$_2$Cr$_2$O$_7$ {001} growth studies [3, 18] report on the occurrence of a large 'dead zone' for the K$_2$Cr$_2$O$_7$ {001} faces at low supersaturations, which is probably caused by the adsorption of impurities on the surface. At low supersaturations, the only detectable growth on the (001) face is via the propagation of large mini-facets of different orientations, while low steps are stopped completely [3]. From the current and the cleavage face AFM investigations published elsewhere [9] it can be concluded that this surface poisoning effect can already be effective after a few minutes of exposure of cleaved crystals to air. This indicates that not all blocking of steps must be attributed to the presence of foreign impurities. Maybe other mechanisms are involved as well, such as a reaction or reorganization of the surface layer K$_2$Cr$_2$O$_7$ by interaction with water vapour or oxygen forming an ultrathin 'etch and growth protective' layer. Maybe the oxidizing character of the Cr$_2$O$_7^{2-}$ ions is involved. They may oxidize ethanol, but this still does not explain the step blocking behaviour

in air, in which no reducing species are present.

7.4.2 Etch pit formation

It is shown above that the lateral expansion of the pits does not take place via layer-by-layer etching at the top face, because of the poisoning of the top layer on {001}. Instead, they expand by the displacement of {010 and {100} side facets. Further etching of the pit bottoms is nucleated near the side facets at relatively high undersaturations (figs. 7.3, 5), or is blocked at low undersaturations (fig. 7.12).

The pits are not caused by screw or edge dislocations. This is clear from the fact that the downwards etching at the bottom of the pits proceeds from the side walls or by 2D nucleation at random positions. No spiral patterns indicative for screw dislocation outcrops were found. In fig. 7.5 for example, it is clearly seen that the number of d_{100} steps on the top face is the same at both sides of every etch pit, proving the absence of screw dislocation outcrops. Edge dislocations are unlikely as well, because permanent step sources and hollow cores were never observed in the pits and all pits became flat-bottomed in course of time. It was found that, on average, the sizes of the various pits are quite similar, which indicates that they were all nucleated at the same, early stage of dissolution. After some period of etching, nucleation of new pits was rarely observed. This suggests that the pits originate from existing weak points in the protective surface layer on the {001} surface.

7.4.3 Layer-by-layer etching

If an etch pit is scanned continuously, then its bottom turns and remains molecularly flat. This is probably caused by a combination of the increased solution mixing by the AFM cantilever as compared to the non-scanning case and the continuous 'surface cleaning' of the tip. Moreover, due to the continuous etching, the protective layer has no chance to build up. Besides etching starting from the pit's side faces, now 2D nucleation etching is observed as well, as is shown in figs. 7.7 and 8. The height of most steps is d_{100}, as is expected from the double-layered crystal structure with chemically different layers A and B [9]. The d_{200} steps which are often found in the etch pits (see black circles in figs. 7.7 and 8) are thus pairs of the relatively unstable B steps and the stable A steps. From the much higher velocity at which the trailing B steps catch up with their A colleagues, as shown in fig. 7.7,it can be concluded that the B steps, and the B layers in front of them, are energetically unfavourable. The B steps only exist because it takes some time to create a new A-bottomed pit after the creation of a B-bottomed 2D pit, i.e. the nucleation itself proceeds by successive removal of d_{200} layers.

As discussed in section 7.4.2, the origin of the 2D pits cannot be attributed to dislocations. Homogeneous 2D nucleation or heterogeneous nucleation from point defects and impurities are

therefore more credible candidates for the vertical etching process. Nucleation from point defects and impurities is most plausible of both, as can be concluded from the observation that in many cases 2D nuclei of two to four d_{100} layers deep instead of just one are formed. This is very unlikely in the case of homogeneous 2D nucleation.

7.4.4 Hypomorphism

The shape of the 2D pits on both {001} faces is very interesting as concerns the crystal symmetry. As mentioned in the introduction section, on macroscopic scale the opposite $K_2Cr_2O_7$ {001} faces are a clear case of hypomorphism, showing coarse structures on (001) [3] and large D-shaped growth spirals on (001), despite the fact that X-ray structure determinations indicate P̄1 symmetry. If the present experiments show a different surface morphology

Figure 7.13 The general shape of the 2D etch pits on both {001} faces formed after immersion in water/ethanol. The representation is such that the pit on the (00 1̄) face is 'placed upwards' by a rotation of 180 around [010]. In case of perfect 1̄ symmetry these pits should be exact mirror images. The minor deviations from this 1̄ symmetry, namely a somewhat more elongated shape of the pit and a slightly shifted position of the B d_{002} steps on the (00 1̄) face compared to (001), can be attributed to a small difference in the undersaturation and therefore do not necessarily indicate 1 symmetry. The white arrows with the origins at the pit centers schematically show the slow and fast etch step directions as measured from figs. 7. 7, 8. The slow etch directions correspond to the straight steps, the fast etch directions correspond to the rough steps.

for the opposite {001} faces even on μm-scale, this would indicate P1 symmetry, and it has to be concluded that the X-ray structure determinations are just not accurate enough to measure the minimal deviations from1 symmetry. If the {001} faces behave similar, then this *could* mean that the symmetry is indeed P̄1 and that the different morphology of the opposite {001} faces has another cause, as suggested by Heide and Follner [6, 7]. From this it is clear that the shape of the observed 2D etch pits on the opposite {001} faces can be used to elucidate the symmetry relation between these faces. From etch pits like the ones observed in figs. 7.7 and 8 it is concluded that the general shape of the pits on both faces is about the same, as is shown in fig. 7.13. Slight differences in pit shapes can be attributed to small differences in the undersaturation, which was verified by measuring the step velocities of both d_{100} and d_{200} steps. The general resemblance suggests that the

crystal symmetry indeed is 1, and that the morphology difference of the {001} faces has a macroscopic ground. Moreover, also the molecular resolution images suggest that the (001) and (00$\bar{1}$) faces are the same on molecular scale, and that both show no surface reconstruction. However, a definite proof has still to be given.

7.4.5 Identification of *A* and *B*

From the direction of the trailing *B* steps in the etch pits conclusions about the pseudo-symmetric relation between of *A* and *B* can be drawn, as is illustrated in fig. 7.14. It is known that this pseudo-symmetry relates both layers via a rotation of $\pm$ 90 around [001] (see e.g. [7]). From the comparison of both figures of fig. 7.14c with the observed [100] directed trailing *B* steps in the d_{100} etch pits (see fig. 7.13), it is concluded that the rotation of the *B* layer with respect to the *A* layer is +90 on (00$\bar{1}$), which corresponds to -90 around [001]. If this is compared with the crystallographic layers A^* and B^* in ref. [7], it is concluded that our definition of the layers *A* and *B* [9] corresponds to that in ref. [7]: $A = A^*$ and $B = B^*$.
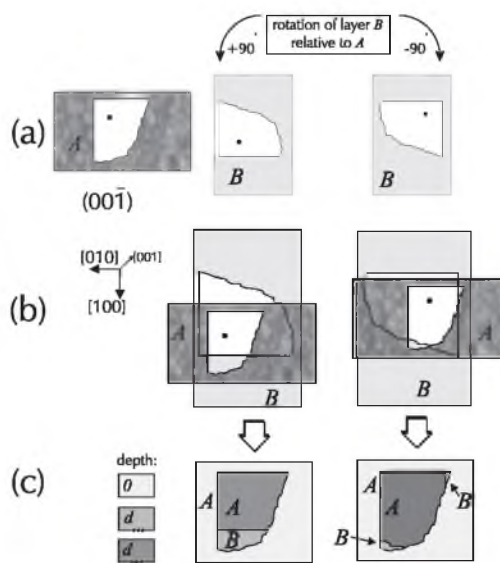
Figure 7.14 Prediction of the position of the d_{200} steps inside the 2D etch pits on the $K_2Cr_2O_7$ (00$\bar{1}$) face according to the crystal symmetry.(a) Shape of etch pits in d'_{200} layers. The shape of pits in the *A* layer is known from the experiments (see fig. 13). Because of pseudosymmetry the shape of an etch pit in a *B* layer is expected to be similar to that in an *A* layer, but rotated over an angle of $\pm$ 90 relative to the pit in *A*. The sign of the rotation depends on the relation of the *A* and *B* layers defined in this paper with the crystallographic layers A^* and B^* defined in ref. [7]. Both possibilities are shown in the figure. (b) When a new pit arises, first a pit in the *A* layer appears, which is very soon followed by a pit in the *B* layer. The development of the lower *B* pit is hindered by the slower advancement of the pit in the *A* layer. In order to predict the directions in which this hindering takes place, the pit shape of *A* is projected on top of that of *B* with the pit centers coinciding. Because of the higher etch speeds in the *B* layer, the *B* pit is larger in this projection. It can be seen that the *B* pit expansion is hindered in most directions for both rotations $\pm$ 90. The eventual shape of the *B* pit will be formed by the inner section of the A and the unhindered *B* pit, as shown in (c).

7.5 Conclusions

On the {001} surfaces of $K_2Cr_2O_7$ crystals obtained by cleavage in air a thin protecting surface layer rapidly develops that prevents layer-by-layer etching after immersion in a low-solubility solvent. After air exposure of a few hours, this layer can still be removed in the liquid, however after exposure of a few days to air this is not possible anymore. Instead of layer-by-layer etching, flat-bottomed etch pits bounded by {100} and {010} side walls develop at positions where the protective layer is removed, probably at weak points in this layer. In unstirred solutions both the lateral and the perpendicular etching of the pits proceeds via or from the side walls. Repeated scanning of the AFM tip causes local removal of the resistant top layer, eventually followed by layer-by-layer etching. This effect can be used for lithographic purposes. Repeated AFM scanning at the flat etch pit bottoms results in 2D nucleation etching. These nuclei are probably related to the surface positions of point defects. The equal shape of these 2D nuclei on both {001} faces indicates that these faces are indeed symmetry-related by1, as measured by X-ray diffraction. The expansion of the 2D nuclei mostly proceeds via unit cell height steps. In some cases the lower d_{200} steps, corresponding to one molecular layer, were found. From the patterns of the d_{200} steps inside these 2D pits the identification of the energetically stable A and unstable B layer with respect to the crystal structure can be made: 'Our' A and B are identical to the layers A^* and B^* in ref. [7], and A is nearly always on the outside. The symmetry of the 2D nuclei as well as molecular resolution images indicate that there is no hypomorphy at this small scale. The molecular resolution images on both faces show that there is no surface reconstruction in solution.

Acknowledgement

References

[1] O.G. Kozlova, Yu.A. Kharitonov and N.V. Belov, Sov. Phys. Dokl. **24** (1979), 509.

[2] a) A. Shubnikov, Z. Krist. **50** (1911) 19

b) A. Shubnikov, Z. Krist. **76** (1931) 469.

[3] M. Plomp, A.J. Nijdam and W.J.P. van Enckevort, J. Cryst. Growth **193** (1998), 389.

[4] E.A. Kuz'min, V.V. Iljukin, Yu.A. Khartinov, and N.V. Belov, Krist. und Techn. **4** (1969), 441.

[5] J.K. Brandon and I.D. Brown, Can. J. Chem. **46** (1968), 933.

[6] a) G. Heide, H. Follner, Cryst. Res. Technol. **31** (1996), 171.

[7] b) G. Heide, H. Follner, Cryst. Res. Technol. **31** (1996), 959.

[8] K. Sangwal and M. Szurgot, Cryst. Res. and Technol. **17** (1982), 49.

[9] M. Plomp, W.J.P. van Enckevort and E. Vlieg, submitted for publication.

[10] T.A. Land, A.J. Malkin, Yu.G. Kuznetsov, A. McPherson and J.J. de Yoreo, Phys. Rev. Lett. **75** (1995), 2774.

[11] T.A. Land, J.J. De Yoreo, J.D. Lee, Surf. Science **384** (1997), 136.

[12] A.J. Malkin, Yu.G. Kuznetsov and A. McPherson, J. Cryst. Growth **196** (1999), 471.

[13] T. Nakada, G. Sazaki, S. Miyashita, S.D. Durbin and H. Komatsu, J. Cryst. Growth **196** (1999), 503.

[14] P.A. Campbell, G.R. Ester and P.J. Halfpenny, J. Vac. Sci. Technol. B **14** (1996), 1373.

[15] H. Shindo, A. Seo, M. Itasaka, T. Odaki and K. Tanaka, J. Vac Sci. Technol. B **14** (1996), 1365.

[16] C.M. Pina, U. Becker, P. Risthaus, D. Bosbach and A. Putnis, Nature **395** (1998), 483.

[17] S. Kipp and R. Lacmann, J. Cryst. Growth **160** (1996), 320.

[18] A.J. Derksen, W.J.P. van Enckevort and M.S. Couto, J. Phys. D. **27** (1994), 2580.

Chapter 8:

Observation of a surface water layer on $K_2Cr_2O_7$ crystals by adhesive contrast in atomic force microscopy

Chapter 8:

Observation of a surface water layer on $K_2Cr_2O_7$ crystals by adhesive contrast in atomic force microscopy

M. Plomp, W.J.P. van Enckevort and E. Vlieg

RIM Laboratory of Solid State Chemistry, Faculty of Science, University of Nijmegen, Toernooiveld 1, 6525 ED Nijmegen, the Netherlands

Abstract

Under ambient conditions, many ionic crystals are known to be covered by an ultrathin water layer. Under appropriate conditions, we have been able to image this layer on the {001} faces of potassium bichromate crystals using atomic force microscopy. When tapping-mode atomic force microscopy was applied on {001} cleavage faces of potassium bichromate crystals, apart from the surface topography contrast, another contrast mechanism was encountered, leading to an apparent topography of a smooth layer with 2 - 4 nm holes in it, which superimposes on the surface topography. Under certain conditions the imaging switches between pure attractive and attractive-repulsive tapping-mode operation, which causes the observed contrast. The occurrence of this switching is influenced by the adhesive force of a thin water layer present on the crystal surfaces. Local changes in the adhesive force, corresponding to local differences in the water layer thickness, lead to the observed holes. The occurrence of adhesive contrast depends on the tip shape, on the tapping mode damping setpoint, the topography of the sample and local differences in the amount of adsorbed water.

Keywords: cleavage, potassium bichromate, surface water layer, AFM, atomic force microscopy.

8.1 Introduction

The presence of water layers on crystal surfaces in ambient air has been studied by many different methods for many years. This conformal water can cause dissolution and recrystallization of the crystal, especially for materials with high solubility. When AFM is applied to study crystal faces, this influence can be detected on a mesoscopic scale in the form of etching and growing of monomolecular steps [1-3]. By the use of force-distance curves the presence of water on surfaces in air can be detected via the pull-off force needed to release the tip from the surface [4]. Unfortunately, until recently it was not possible to image the water itself using AFM. This changed with the application of scanning polarization force microscopy (SPFM) [5], in which a biased metallized tip is used to polarize the water layer. The attractive force which evolves is used for the AFM feedback. With this technique water layers on mica, HOPG, gold and stainless steel in air could be detected [6-10]. On NaCl surfaces the preferential adsorption of water at steps was demonstrated in this manner [11].

In the current study, 'normal' tapping-mode AFM (TM-AFM) [12] is applied to detect a water layer. For this, a special contrast mechanism is used, which is caused by the complex TM-AFM tip-sample interaction. In TM-AFM, the tip oscillates at or near its resonance frequency with an amplitude of typically 10-100 nm. During one cycle, most of the time the tip hardly interacts with the sample. Only during the lowest part of its cycle, the tip-sample interaction is relatively strong. This interaction contains both short-range repulsive forces (Born repulsion) associated with tip-sample contact, as well as 'long'-range attractive forces (e.g. capillary force, attractive part of vanderWaals force). The attractive capillary forces are much stronger during the retraction of the tip then during its approach, leading to a high degree of non-linearity in the cantilever response. The competition between attractive and repulsive forces is known to enable two different imaging modes, which involve pure attractive and both attractive and repulsive forces, respectively (e.g. [13, 14]). This bimodal behaviour follows from simulations ([13, 14, 15]) and has been observed as well [16, 17]. It has been proven experimentally that changing attractive forces influence the switching between the modes [15].

In the present investigations, the presence of a water layer with varying thickness on the cleavage faces of $K_2Cr_2O_7$ crystals is demonstrated by means of the contrast introduced by the varying capillary force exerted by the layer. This is mapped with the help of tapping-mode AFM. Under certain conditions, the tapping mode will switch between pure attractive and attractive/repulsive mode. This mechanism is applied to detect local differences in the surface water layer.

8.2 Experimental

Potassium bichromate single crystals with sizes of about 5mm X 10 mm X 5 mm grown from aqueous solution were used. These were cleaved along {001}. Cleavage, storage and AFM imaging were carried out in ambient air with a humidity of 34 to 44% and a temperature of 23 C. During scanning, the temperature is locally increased a few degrees by the focussed AFM laser used for the detection of the cantilever deflection [18].

For the experiments a Digital Dimension 3100 as well as a Digital Multimode AFM were used. Both were operated in tapping mode. The silicon cantilevers used had force constants and resonance frequencies of 42 N/m and about 260 kHz respectively. All images were recorded using frequencies slightly below the resonance frequency, because this usually yields the best feedback [19]. The images were acquired using different cantilever damping levels. The setpoint amplitude $A_{setpoint}$ and damping $D_{setpoint}$ are interrelated by

$$D_{setpoint} \quad A_{free\ oscill.} \quad A_{setpoint} \quad ,$$

or $$\frac{D_{setpoint}}{A_{free\ oscill.}} \times 100\% \quad 100\% \quad \frac{A_{setpoint}}{A_{free\ oscill.}} \times 100\% \quad , \tag{8.1}$$

where $A_{free\ oscill.}$ is de amplitude of the cantilever's free oscillation in air. In our measurements, $D_{setpoint}$ varied from 10 to 90 % of $A_{free\ oscill.}$. In the figures the topographic signal or the amplitude signal is depicted, depending on which signal gave the desired information. The amplitude signal ,which is similar to the deflection signal in contact-mode AFM, often reveals more details, while the topographical image shows a clear overall height survey.

8.3 Results

Cleavages were carried out on different crystals and the surface patterns were studied on the two opposite cleavage faces {001}. From the step patterns interesting conclusions about cleavage asymmetry were drawn as described elsewhere [20]. At large scale (> 5 μm), the {001} cleavage faces look like a regular cleavage face, with flat terraces and steps with heights d_{100} and d_{200} inbetween. Closer examination, however, reveals that after keeping the crystal in air for some time the cleavage terraces get roughened, and that, depending on AFM tapping conditions, a pattern
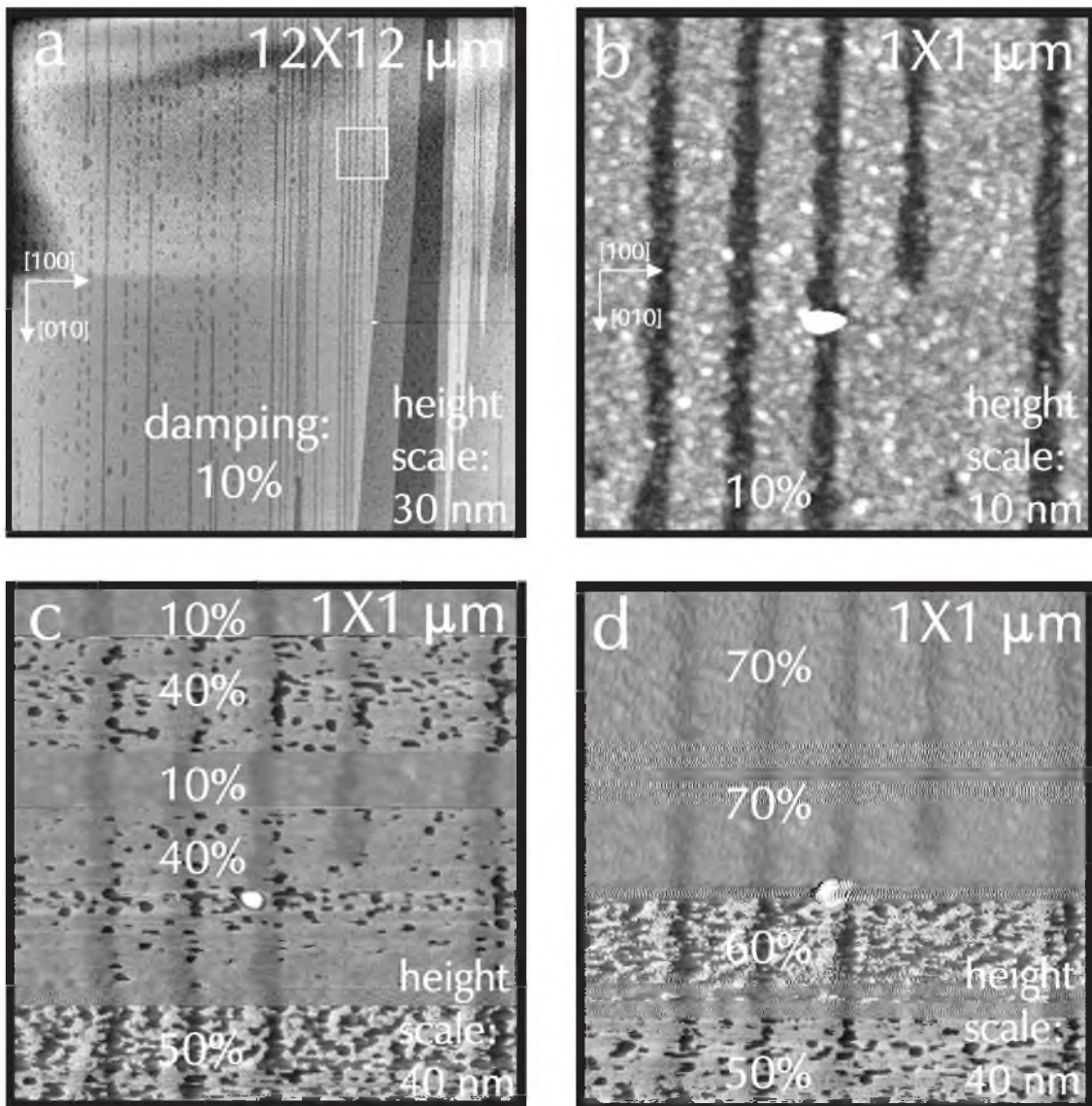
Figure 8.1 Switching between two different TM-AFM modes during imaging of a cleaved $K_2Cr_2O_7$ {001} surface at varying AFM tapping amplitude setpoints. (a) 12x12 μm^2 image of an (00l) cleavage face one week after cleavage, showing V-like patterns and long channels of depth d_{00l}. The area imaged in (b-d) is marked by a white square. (b) Part of region (a) imaged in the attractive mode using a low amplitude damping of 10% relative to the oscillation in free air. The surface shows some of the d_{001} deep channels. The plateaus inbetween them have degraded into a grainy surface. (c) The same region now imaged with various damping factors. At intermediate damping values of 40-50% the image shows a flat layer with holes in it. The holes correspond to the partly repulsive mode. The size of the holes increases for increasing damping setpoints. (d) The same region imaged with high damping setpoints of 50-70%. At highest setpoints the layer-with-holes pattern disappears and imaging is completely in the repulsive mode. In (d) oscillations start to appear because of the high damping. Note that even in the layer-with-holes regions the underlying crystal morphology is visible and that the height scale of (c,d) is larger to be able to correctly image the layer-with-holes pattern. The depth of the holes is approximately 4 nm. Relative humidity is 34%.

resembling a thin surface layer with holes appears. The origin of the roughening is discussed in another paper [21]. Here, the roughening is important in relation to the observed layer-with-holes pattern. The circumstances under which these patterns show up, are reported below.
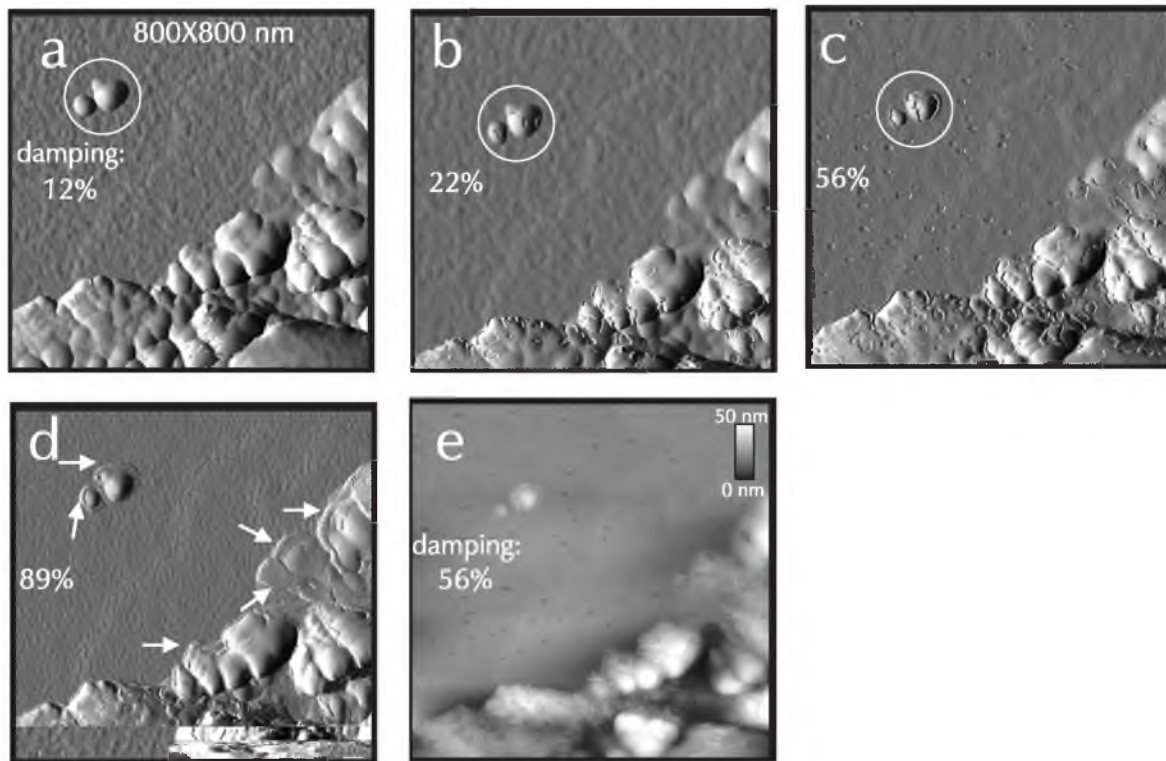
Figure 8.2 800X800 nm^2 area of a $K_2Cr_2O_7$ {001} cleavage face imaged with different amplitude setpoints at a relative humidity of 43%. The amplitude images show a somewhat grainy flat area, bounded by an area of about 50 nm high particles in the lower part of the image. The damping setpoint relative to the cantilever's free oscillation in air is indicated in the figure. At 12% damping, almost no holes are visible. When the damping is increased to 22%, holes of about 4 nm depth arise at the highest points of the particles. The flat part is still intact. When the damping is increased to 56% the holes are expanding. This is seen clearly at the encircled hills. Moreover, holes start to appear on the flat area. All the holes are highly reproducible from scan to scan. At a very high damping of 89% no holes are visible anymore. Instead, some remainders of the original layer can be seen around the particles, as indicated by arrows in (d). (e) shows the topography image corresponding to the amplitude image of (c), illustrating the character of the holes in the flat and high part once more.

8.3.1 Varying the damping

TM-AFM images with sizes down to a few μm wide show the typical cleavage patterns composed of unit cell height steps as shown in fig. 8.1a, which was recorded one week after cleavage. At low tapping-mode amplitude damping setpoints, such as the 10% applied in fig. 8.1b, true to nature zoom-ins of μm-scale can be made. In this figure, it can be seen that within this week of storage the molecular flat cleavage plane has deteriorated into a grainy surface. Relevant for this paper is the fact that the depicted morphology is that of the crystal surface. If now the amplitude damping setpoint, *i.e.* the force, is increased the AFM image looks completely different. Fig. 8.1c presents the same region imaged in (b) but now using various damping values ranging from 10 to 50%. Now, the main observed morphology shows a flat layer with 3 - 5 nm deep holes in it. The underlying crystal surface is still visible in the 40% damping parts of the image, but because of its lower height variations its contrast is not so manifest as that of the hole pattern. In fig. 8.1d the damping, and thus the tapping force, is increased to 60-70%, giving increased hole sizes and eventually 'clean' surface patterns for the highest damping. If time series of the same region are made with constant intermediate damping, most of the holes are reproduced, while others disappear or appear.

An even higher reproducibility of holes is found for fig. 8.2. Here, a partly flat, partly hilly area is imaged for different values of amplitude damping. Again, at low damping only the crystal surface is observed (fig. 8.2a). At higher damping (fig. 8.2b) sharply edged holes develop in the hilly areas, and eventually also in the flat part.(fig. 8.2c).The holes maintain their size upon repeated scanning with the same damping; and gradually increase with higher damping. At very high force, the holes have expanded into most of the image; only some remainders of the original layer are left (fig. 8.2d). The depth of the holes is measured to be 3 ± 0.3 nm.

8.3.2 Time series

When time series are recorded under constant circumstances and with the same scan settings, subsequent images are quite reproducible. Even when the damping is changed, holes appear on reproducible positions, as was shown above. Fig. 8.3 shows a series of an area in which a layer pattern builds up steadily. At first, the top level starts with a few lines (fig. 8.3b) and it ends up as an almost complete layer with a few reproducible holes at the positions of the protrusions of the original crystal surface (fig. 8.3i). Because the scan settings stay the same, the layer growth is associated with the actual formation of a water layer (see section 8.4.3). One snapshot from another time series is shown in fig. 8.4. Here, the switching from the repulsive to the attractive mode takes place only at the lower left part of the figure. In this case, there is no relation at all between the crystal surface morphology and the occurrence of the bimodal switching. The switching is therefore associated with local differences of the water layer thickness on μm scale (see section 8.4.3).
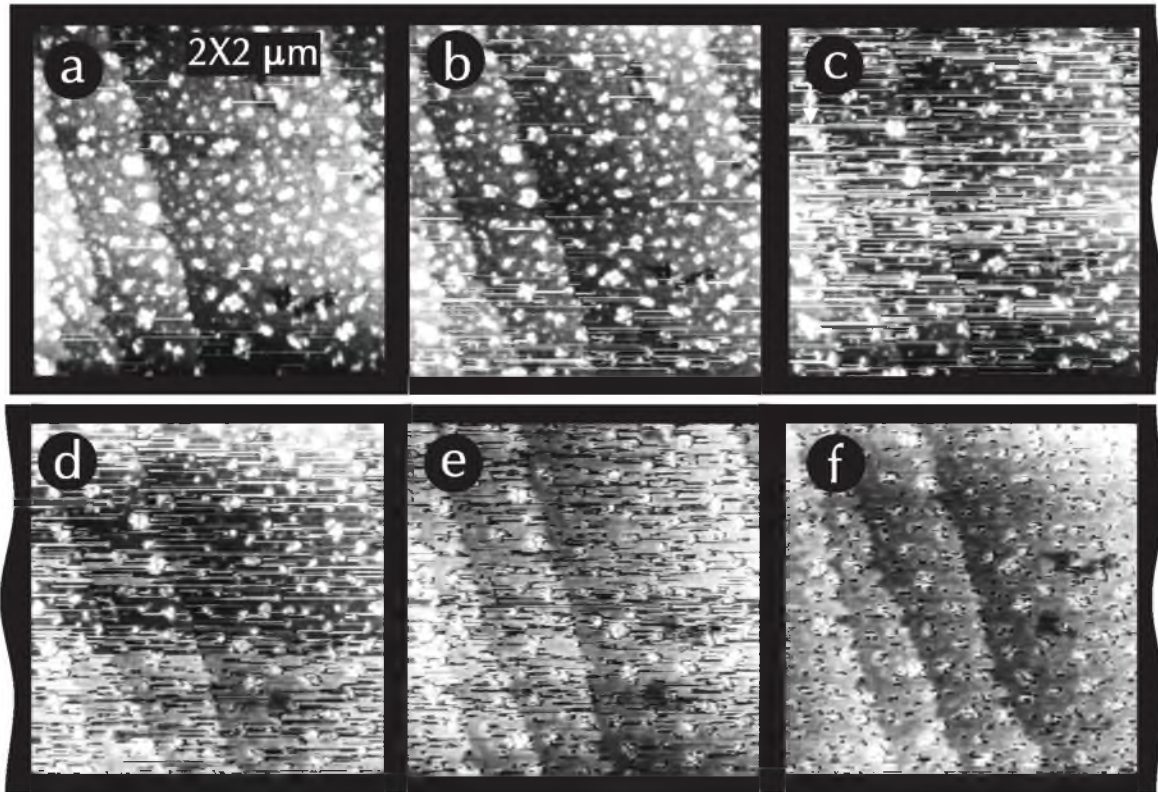
Figure 8.3 Series of TM-AFM topographical images of a $K_2Cr_2O_7$ {001} surfaces imaged at the same damping setpoint of 24%, showing steady growth of the layer structure. In (a) only a few lines with a height of 2 nm are present. Imaging is almost completely in the repulsive mode. (b,c) In course of time the lines increase in number, and (d) agglomerate in domains, before (e) they form an almost closed layer. (f) In the end, only the protruding crystal parts are left uncovered by the layer. Imaging is predominantly in the attractive mode.

8.3.3 Freshly cleaved crystals

When the experiments are repeated for freshly cleaved $K_2Cr_2O_7$ crystals, no hole patterns are found on the cleavage terraces, which are perfectly flat. The only areas where some patterns are found are the irregular holes that quickly evolve after cleavage due to etching caused by the thin water layer adsorbed on the crystals (fig. 8.5). This proves that for the detection of the hole patterns a somewhat roughened surface is needed.
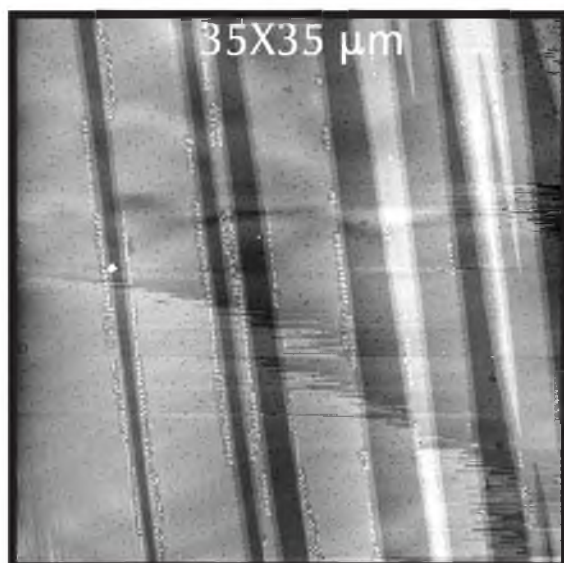
Figure 8.4 (001) cleavage face scanned at intermediate damping of 29% showing bimodal switching on a large scale. In the left bottom part of the figure the imaging is in the attractive mode, in the rest of the figure it is in the partly repulsive mode. The apparent layer thickness is 1.5 nm.
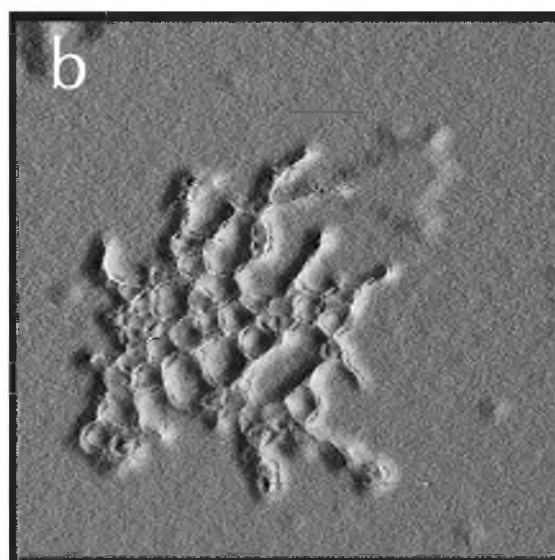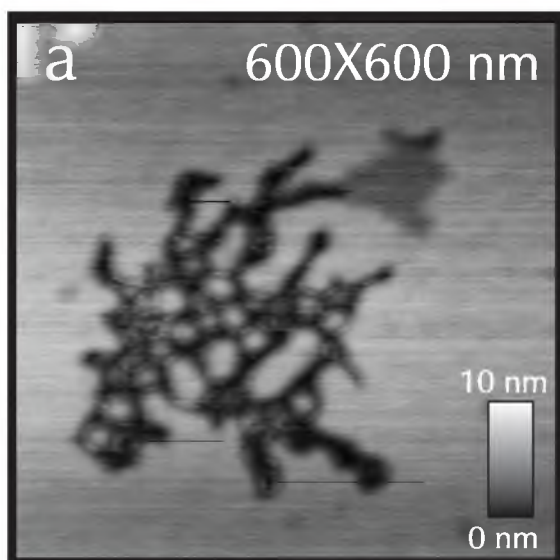
Figure 8.5 (a) Topographical and (b) corresponding amplitude image of an irregular etch hole on a freshly cleaved $K_2Cr_2O_7$ {001} face. On the flat surfaces of these fresh surfaces no layer/hole patterns can be distinguished. On the other hand, inside the holes layered structures can be seen in the deep parts, while the protruding parts are uncovered. Damping setpoint is 30%.

8.3.4 Tip shape

Most images of layers with holes on top of cleavage faces were recorded with tips that were used for longer periods. With 'fresh' tips used for the first time the characteristic patterns rarely could be detected. However, if in the case of a new tip the damping is set close to 100% for one second, which probably damages the tip, and then restored to normal values (about 30%), hole patterns could often be observed immediately. This suggests that the tip-sample contact area, which is larger for the worn or damaged tips, plays a role. To examine the tip influence, force-distance curves were recorded with several tips. This was done after the normal imaging, to prevent the influence of damaging during the recording of the force-distance curves, which is known to be potentially harmful with respect to the tip and sample in case of TM-AFM [19]. Indeed, differences between new and longer used tips were found, as is shown in fig. 8.6. The most striking, and very reproducible difference is the sudden increase of slope in the curve of the retracting tip, which is only found for old tips. Besides that, the hysteresis, *i.e.* the distance between the extending and retracting curve tends to be larger for these tips. Force-distance curves using contact-mode AFM (CM-AFM) showed the 'normal' features of the tip snapping into contact upon approach and of sticking to the surface upon retraction.
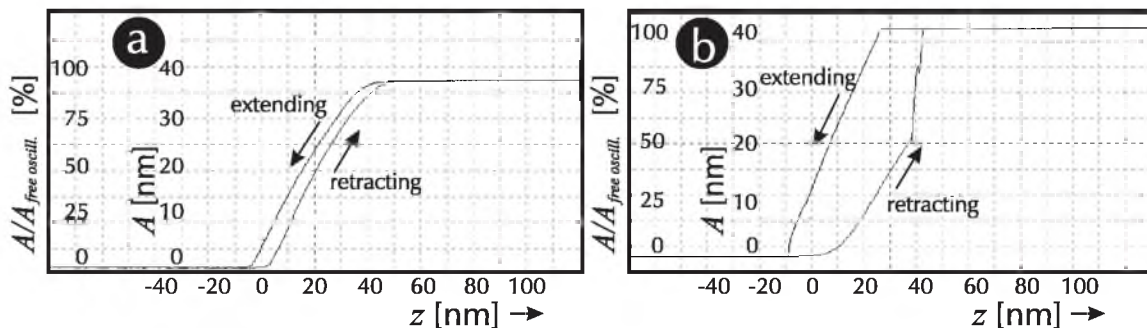
Figure 8.6 TM-AFM force calibration curves of {001} $K_2Cr_2O_7$ for (a) a new tip, and (b) a worn tip. The retracting curve has a sudden change of slope at 50% damping for the case of a worn tip, and the hysteresis, *i.e.* the separation between the extending and retracting curve is larger for that case. Both features point to higher capillary interaction between the crystal and the blunt tip as compared to the sharp tip.

8.3.5 Other crystals

In order to be able to compare the hole patterns on $K_2Cr_2O_7$ with other crystals, faces of three more crystals with high solubility in water were investigated: as-grown $Ba(NO_3)_2$ {111} faces, cleaved NaCl {001} faces and vapour-grown CsBr {111} faces. For both $Ba(NO_3)_2$ {111} and NaCl {001} the hole patterns could not be reproduced, irrespective of the air exposure time of the investigated faces. In both cases, the terraces between monomolecular steps were much more flat than cleaved $K_2Cr_2O_7$

{001} faces of a few days old. Strong reorganization of the NaCl {001} surface pattern due to adsorbed water present on the sample could readily be seen, as is showed in fig. 8.7a. If the scale of the TM-AFM images of NaCl is diminished to μm-level, they become unstable, probably to step movement. Vapour-grown CsBr {111} is shown here because of its lumpy appearance, which is somewhat analogous to the grainy surface of an aged $K_2Cr_2O_7$ {001} cleavage face. On the CsBr {111} faces, similar patterns as on older $K_2Cr_2O_7$ {001} faces were found (fig. 8.7b): the valleys between the grains seem filled with a layer, while the grains themselves seem to lie bare.

When force calibration curves were accomplished with one and the same tip on different types of crystals, no differences in the curves were found. This holds for both new and old tips.
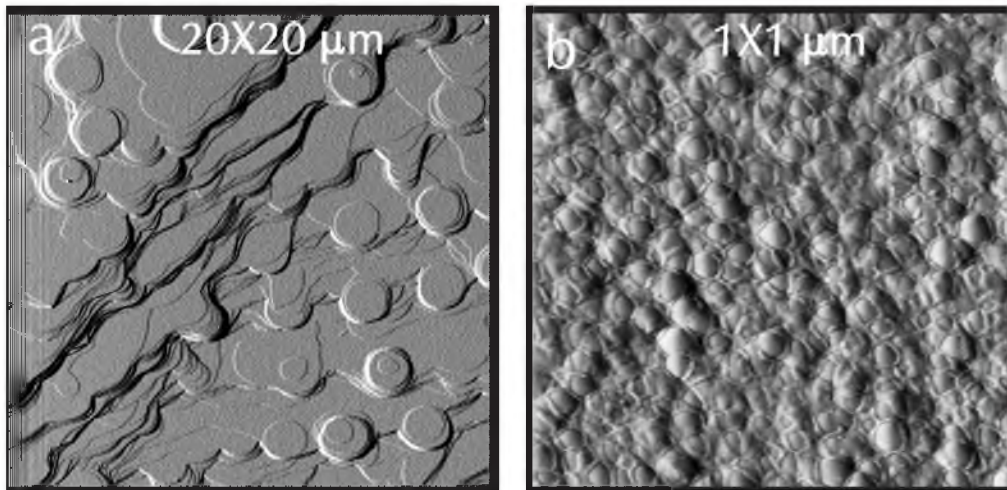
Figure 8.7 TM-AFM amplitude images of (a) {100} NaCl and (b) {111} CsBr. (a) The NaCl {100} cleavage face shows recombination after two days of storage in ambient air at RH = 40%. The terraces stay atomically flat and do not show any layer-hole patterns. (b) Vapour grown {111} CsBr has a lumpy structure, which shows layers in the valleys and bare crystal on the top of the grains.

8.4 Discussion

8.4.1 Bimodal switching

Our observations resemble to a great extent the results of earlier experiments showing non-topographical setpoint-dependent height differences in TM-AFM [16, 17]. These were attributed to the phenomenon of switching from a pure attractive tip-sample interaction to a mixed attractive-repulsive regime [16]. For low damping setpoints imaging occurs in the attractive mode, for high damping setpoints the partly repulsive mode is favoured, and for intermediate setpoints both modes are possible because of the discontinuous transition between the two [13, 15, 16]. Such a setpoint-

dependent imaging behaviour is exactly what is found in fig. 8.1.

When the oscillating tip is lowered from a non-contact position, initially the amplitude is damped by attractive forces only. Because of this damped amplitude the point of actual tip-sample contact is postponed. Only when the tip is so much lowered that the reduced average tip-sample distance compensates the reduced amplitude, the tip starts to tap on the surface [15]. Only at damping setpoints beyond this transition setpoint, corresponding to lower tip-sample distances, 'real' tapping, where the tip touches the sample, takes place. In the attractive mode the tip vibration is damped by attractive (adhesive, capillary) forces only, without touching the sample surface in a repulsive way. It has been shown experimentally that the position of the transition setpoint dramatically changes for increasing attractive force [15].

In the case of $K_2Cr_2O_7$, we will discuss that the layer-with holes pattern is a form of bimodal switching. The layer corresponds to the pure attractive mode, in the holes imaging occurs in the partly repulsive mode. The ultrathin water layer on the crystal faces, whose presence was shown in an earlier study [20], causes high capillary forces between tip and sample and therefore plays a crucial role in the bimodal switching.

8.4.2 Bimodal imaging conditions

The conditions at which the bimodal layer-with-holes pattern shows up in the case of imaging $K_2Cr_2O_7\{001\}$ are: *i)* scanning of an old, somewhat roughened crystal surface; *ii)* use of an old, probably blunt tip; *iii)* a somewhat increased damping setpoint.

The measurements on NaCl and $Ba(NO_3)_2$ crystals as well as on freshly cleaved $K_2Cr_2O_7$ crystals (fig. 8.5) indicate that the layer-with-holes pattern is not observed on atomically flat surfaces, while the hole observations on the rough vapour-grown CsBr surfaces (fig. 8.7) show that a rough crystal surface is needed for the layer pattern. The use of a dull tip is an important factor as follows from the fact that only after deliberately damaging a new tip or by using an old, worn tip the layer-with-holes pattern can be observed. Force calibration curves show a clear difference between new and blunt tips (fig. 8.6). A direct relation between the tip shape and the domination of either repulsive or attractive interaction was found in an experimental study on the surfaces of Si and polystyrene [22]. All of the above mentioned conditions for the occurrence of bimodal switching can be explained by the mechanism described in section 8.4.1. As mentioned above, the setpoints at witch bimodal switching occurs, is strongly dependent upon the attractive forces present. In case of rigid ionic crystals, such as $K_2Cr_2O_7$ and NaCl, the deformation of the crystal surface by the tip is supposed to be negligible. Therefore, the contact area between tip and crystal surface remains small, even for blunt tips, and the resulting direct adhesive force between tip and crystal will be limited.

However, the thin surface water layer that develops in ambient air causes a huge attractive capillary

force. The capillary force, and thereby the pull-off force needed to overcome it, will increase with increasing water layer thickness. Moreover, the capillary force will increase largely by the use of an old, blunt tip or a crashed tip because the water bridge between a dull tip and the sample will be larger. This explains the observed tip-dependence of the switching pattern. The relation between a crashed tip and higher attractive force was also found in another study [23], in which it was found that crashed tips led to higher corrugation in TM-AFM atomic resolution images because the tip comes closer to the sample surface.

The setpoint dependence of the switching can be explained by the limited range in which the switching occurs [13, 15, 16]. Apparently, for the imaging of $K_2Cr_2O_7$ with blunt tips the capillary force is so high that the transition damping setpoint between the attractive and the tapping regime is shifted towards higher damping setpoints. 'Normal' tapping-mode imaging with damping setpoints of $D_{setpoint}$ of 10 - 20% of $A_{free\ oscill.}$ takes place completely in the attractive regime (fig. 8.1a, b), mode switching occurs at $D_{setpoint}$ values roughly between of 30 - 70% (fig. 8.1c), while 'true' tapping takes place only at $D_{setpoint}$ values of 70- 90 % (fig. 8.1d; upper part). At damping values higher then 90% tip crashes occur. If a pure topographic image is desired using a dull tip, best imaging is in the pure attractive regime.

8.4.3 Site-dependent bimodal switching

As is clear from figs. 8.1 - 4, if mode switching occurs, it is often site-dependent. When going from low to higher damping setpoints, switching from the attractive to the partly repulsive regime occurs first at higher, protruding particles. At higher damping also the lower surface areas switch. The large range of $D_{setpoint}$ = 30 - 70% (fig. 8.1) to even 10 - 70 % (fig. 8.2) at which switching takes place, as well as for the reproducible site-dependent switching indicates large local differences in capillary forces. Enhanced switching at protruding particles was also found for CsBr (fig. 8.7b), as well as protruding proteins on mica [16]. In the case of the proteins the site-dependent contrast was explained by the different elastic properties of the proteins and the mica [16]. However, in the case of crystalline material, the surface normally consists of only one type of material, and, moreover, the dominant attractive force is thought to be the capillary force, which makes this explanation less probable. Therefore, in case of ionic crystals, we think that the local differences should be associated with differences in the adhering water layer thickness. It is expected that air-water interface is much more flat than the lumpy crystal-water interface, because of minimalization of the surface energy. Therefore, at protruding particles the water layer will be thinner, at crystal surface depressions it will be somewhat thicker. The water layer thickness variation will cause variation in capillary forces during TM-AFM as well. This is probably the main cause for the observed bimodal layer-with-holes topography.

For sharp tips the bimodal switching does not occur because of the relatively low capillary force in that case. For freshly cleaved surfaces and for crystal surfaces that do not roughen (NaCl, $Ba(NO_3)_2$) site-dependent switching does not occur, neither for sharp nor for dull tips. This is attributed to the simple fact that no height differences are present on the topography that induce local variations in capillary force. At intermediate setpoints the total surface is scanned in the repulsive mode or the attractive mode for sharp and dull tips respectively. The influence of tip shape and surface roughness is depicted schematically in fig. 8.8.

Figure 8.8 Schematic overview of the effect of tip shape and surface roughness on imaging mode. The tip is imaged in its lowest position in the oscillation cycle. (a) sharp tip, flat surface: low capillary force, repulsive mode everywhere; (b) sharp tip, rough surface: low capillary force, repulsive mode at most positions; (c) dull tip, flat surface: high capillary force, attractive mode everywhere; (d) dull tip, rough surface: high capillary force, repulsive mode at protruding sites, attractive mode elsewhere.
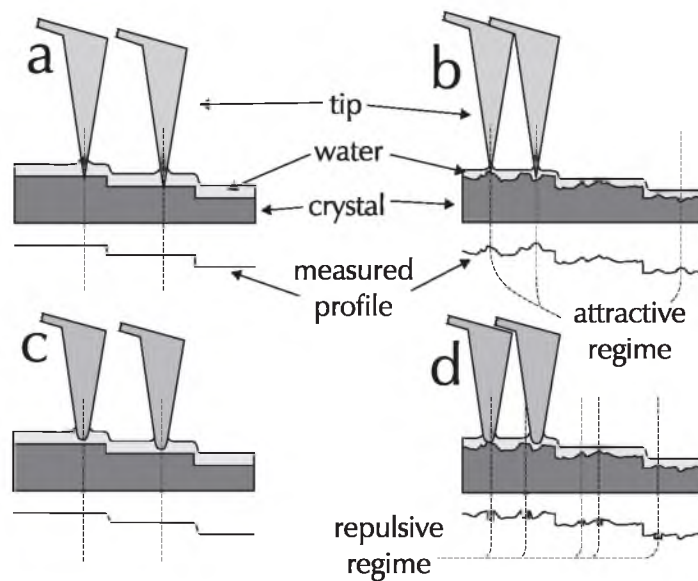
The only sites on freshly cleaved $K_2Cr_2O_7$ crystals that do show bimodal switching are the solution holes that form within five minutes after cleavage [20]. In these holes, capillary forces causing bimodal switching indicate the presence of solution inside these holes (fig. 8.5).

As is the case for the other images, in the time series of fig. 8.3 the high levels correspond to the attractive mode and the low levels correspond to the partly repulsive mode. In the end situation (fig. 8.3f) the characteristic holes appear at protrusions of the crystal. Interestingly, the imaging gradually changes from the repulsive mode (fig. 8.3a) to almost complete attractive mode (fig. 8.3f), while the setpoint setting did not change. In the non-protruding parts of this area, the bimodal switching is not site-dependent as can be noted from the stripy pattern. This indicates that this area is quite homogeneous with respect to the capillary force. At the protruding crystal parts the repulsive mode is continued throughout the time series, indicating permanent low capillary force at these positions. Because the feedback settings are constant, the increasingly attractive imaging with time points to

an increasing capillary force by a growing amount of water present on the surface. Two other possibilities, which are an increased tip wear during the short time of imaging or drift leading to a setpoint change, are less probable. Site-dependent bimodal switching on μm-scale is encountered in fig. 8.4. Because there are no topographical differences between the areas in which imaging is in the attractive and repulsive mode respectively, the detected difference in the attractive force is attributed to the difference in the amount of water present: In the attractive part of the image the water layer is thicker.

The reproducible holes on top of the protruding parts of figs. 8.2a-c, indicate smaller capillary forces on them relative to the flat cleavage part of the area. In this particular case, besides a topography contribution, the different surface structure may be responsible for this as well. At very high setpoints (fig. 8.2d), the layer structure remains only around the protruding particles, which points to increased capillary force due to the concave topograhpy.

The 2- 4 nm bimodal contrast does not directly relate to the thickness of the water layer on ionic crystals. This water later thickness is estimated by means of the amount of dissolved material of the top layer of a {001} $K_2Cr_2O_7$ face to be approximately 1 nm [20]. Ellipsometry measurements of the surface of highly soluble potassium dihydrogen phosphate (KH_2PO_4) crystals under ambient conditions indicate the presence of a water layer with a thickness of 1 - 5 nm [24].

8.4.4 Force calibration curves

The observed force calibration curves for sharp and dull tips, as imaged in fig. 8.6, once more demonstrate the influence of the tip shape on the interaction force. In the case of blunt tips, the main deviation from a 'normal' curve is in the retracting curve, which initially has a lower slope and finally a much higher slope then the approaching part. The lower and the higher sloped part are separated by a sharp transition. Moreover, there is a horizontal shift of about 20 nm between the approaching and retracting curve. We think that these large differences can be explained by the formation of a liquid bridge between tip and crystal during retraction, which has a damping effect on the amplitude. Starting the retraction curve from zero amplitude, initially a liquid bridge is present for the whole - blunt - tip cycle, which causes severe damping. At a tip-sample separation of about 35 nm, corresponding to an amplitude of about 20nm, this liquid bridge breaks and the amplitude increases very rapidly to its excitation value. This transition point marks the conversion from a mode in which the tip keeps connected to the fluid layer into a mode in which the tip is released and merely taps on the water layer. From the continuity of the approach curve it is deduced that during the approach the tip is never trapped completely in the fluid layer until zero amplitude. The discontinuity in the approach curve found in other studies [14-16], which is associated with the bimodal switching, was not found for both sharp and dull tips. In case of dull tips, this has possibly

to do with the long period in which the tip stays at zero amplitude during the recording of the calibration curves. This makes the tip even more dull and then it is constantly in the attractive regime except for zero amplitude itself. Therefore, the switching point cannot be detected. Though interesting in itself, the supposed mechanism for the TM-AFM calibration curves cannot be applied directly to describe normal imaging, precisely because of these zero amplitude effects, which do not occur during scanning. During imaging the formation and the breakage of liquid bridges will also occur. Simulations involving explicitly a fluid layer of ½ nm thickness forming a 2 nm bridge at tip retraction show that the tip penetrates the fluid layer only when its excitation amplitude is large enough [14]. The complete trapping in the water layer during imaging neither follows from the simulations, nor is observed in our observations at intermediate setpoints, and is therefore thought to occur only for very low setpoints, such as used in force calibration curves.

8.5 Conclusions

If TM-AFM is applied to the {001}cleavage planes of $K_2Cr_2O_7$, bimodal switching occurs for a large setpoint range. This leads to an image that resembles a 2 - 4 nm thick layer with holes in it superimposed on the crystal surface morphology. The occurrence of the switching is shown to be caused by the large capillary force that exists between tip and sample. This attractive force is induced by the presence of a thin water layer on the crystal surfaces. The switching is highly site-dependent. At protrusions of the surface the imaging is in the repulsive mode, because of the thinner water layer at those postions, at flat parts or depressions imaging is mostly in the attractive mode. Time series that show the increase of capillary forces indicate an increase of the water present on te sample. Imaging using dull tips is shown to be best in the pure attractive regime.

Acknowledgments

References

[1]   H. Shindo, M. Ohashi, K. Baba and A. Seo, Surf. Science **357-358** (1996), 111.

[2]   R.M. Overney, H. Haefke, E. Meyer and H.J. Güntherodt, Surf. Science **277** (1992), L29.

[3]   M. Plomp, K. Maiwa and W.J.P. van Enckevort, J. Cryst. Growth. **198/199** (1999), 246.

[4]   A.L. Weisenhorn, P.K. Hansma, T.R. Albrecht and C.F. Quate, Appl. Phys. Lett. **54** (1989), 2651.

[5]   J. Hu, X-D. Xiao and M. Salmeron, Appl. Phys. Lett **67** (1995), 476.

[6]   J. Hu, R.W. Carpick M. Salmeron and X-d. Xiao, J. Vac. Sci. Techn. B **14** (1996), 1341.

[7]   L. Xu, A. Lio, J. Ju, D.F. Ogletree and M. Salmeron, J. Phys. Chem. B **102** (1998), 540.

[8]   M.S. Salmeron, L. Xu, J. Hu and Q. Dai, MRS Bulletin, August 1997, 36.

[9]   H. Masuda, J. Japan Inst. Metals **62** (1998), 173.

[10]   H. Masuda, J. Japan Inst. Metals **62** (1998), 617.

[11]   Q. Dai, J. Hu and M. Salmeron, J. Phys. Chem B **101** (1997), 1994.

[12]   Q. Zong, D. Imniss, K. Kjoller, V.B. Elings, Surf. Sci. Lett. **290** (1993), L688.

[13]   N. Sasaki, M. Tsukada, R. Tamura, K. Abe and N. Sato, Appl. Phys. A **66** (1998), S287.

[14]   O.P. Behrend, F. Oulevey, D. Gourdon, E. Dupas, A.J. Kulik, G. Gremaud and N.A. Burnham, Appl. Phys. A **66** (1998), S219.

[15]   B. Anczykowski, J.P. Cleveland, D. Krüger, V. Elings and H. Fuchs, Appl. Phys. A **66** (1998), S885.

[16]   A. Kühle, A.H. Sørensen, J.B. Zandbergen and J. Bohr, Appl. Phys. A **66** (1998), S329.

[17]   G.W. Bao, M. Troemel and S.F.Y. Li, Appl. Phys. A **66** (1998), S1283.

[18]   M. Plomp, P.J.C.M. van Hoof and W.J.P. van Enckevort, submitted for publication.

[19]   Dimension 3100 Instruction manual v4.31re (1997), 8.17.

[20]   M. Plomp, W.J.P. van Enckevort and E. Vlieg, to be published.

[21]   M. Plomp, W.J.P. van Enckevort and E. Vlieg, to be published.

[22]   G. Bar, R. Brandsch and M.-H. Whangbo, Surf. Science **422** (1999), L192.

[23]   M. Bammerlin, R. Lüthi, E. Meyer, A. Baratoff, J. Lü, M. Guggisberg, C. Loppacher, C. Gerber and H.-J. Güntherodt, Appl. Phys. A **66** (1998), S293.

[24]   M. Reedijk, M. Devillers, E. Vlieg, unpublished.

Chapter 9:

Dislocation movement in

n-$C_{40}H_{82}$ paraffin crystals observed

by atomic force microscopy

Chapter 9:

Dislocation movement in

n-$C_{40}H_{82}$ paraffin crystals observed

by atomic force microscopy

M. Plomp, P.J.C.M. van Hoof, C.J. van de Streek and W.J.P. van Enckevort

RIM Laboratory of Solid State Chemistry, Faculty of Science, University of Nijmegen, Toernooiveld 1, 6525 ED Nijmegen, the Netherlands

Abstract

Ex situ atomic force microscopy was applied to the {001} surface of n-$C_{40}H_{82}$ paraffin crystals grown from n-hexane solution. Monomolecular platelets, small ultra thin crystals originating from one or two growth spiral(s), as well as aggregates of thicker crystals were found. Owing to post-growth stresses acting on the thin crystals slip movement by screw dislocations occurred, which is visible as crossing of as-grown and post-growth steps on the crystal surface. Furthermore, folding of the ultra thin crystals was observed, which is induced by thermal expansion.

Keywords: paraffins, slip, screw dislocation, crossing steps, atomic force microscopy.

9.1 Introduction

n-Paraffins are of great interest to the petrochemical industry, because they form a significant proportion of crude oil and its products. Because of the relatively high melting points of the higher n-paraffins, often crystallization of these paraffins in oil and its products will take place, resulting in waxing of fuel filters and formation of slack wax in lubricating oil production. Besides this industrial interest, n-paraffins are also interesting from a scientific point of view because of their crystallization behaviour. Crystallization behaviour and crystal structure depend on the number of C atoms in the chain and alternate as a function of the evenness/oddness of that number. Impurities can also influence the crystal structure.

Table 9.1. Unit cell parameters of the three crystal structures of n-$C_{40}H_{82}$

structure	a [nm]	b [nm]	c [nm]
$P2_1/a$ (β=91.67°)	0.558	0.742	4.68
$Pcab$	0.558	0.742	9.36
$Pca2_1$	0.742	0.496	10.52

In the past, dislocation studies and the investigation of plastic deformation were mostly carried out for metal and ionic crystals rather than molecular, organic crystals. It is therefore interesting to investigate the plastic deformation on a nanometer scale for this category of soft crystals.

Four different modifications are known for n-paraffin crystals: triclinic, monoclinic, orthorhombic and hexagonal [1]. The hexagonal or rotator phase modification, in which the molecules can freely rotate around their long axes, only occurs just below the melting point. For higher even alkanes with $m > 28$ (apart from the rotator phase) two basic crystal structures are

Monoclinic   **Polytypic**   **Orthorhombic**

$P2_1/a$, Z=2 $Pcab$, Z=4 $Pca2_1$, Z=4
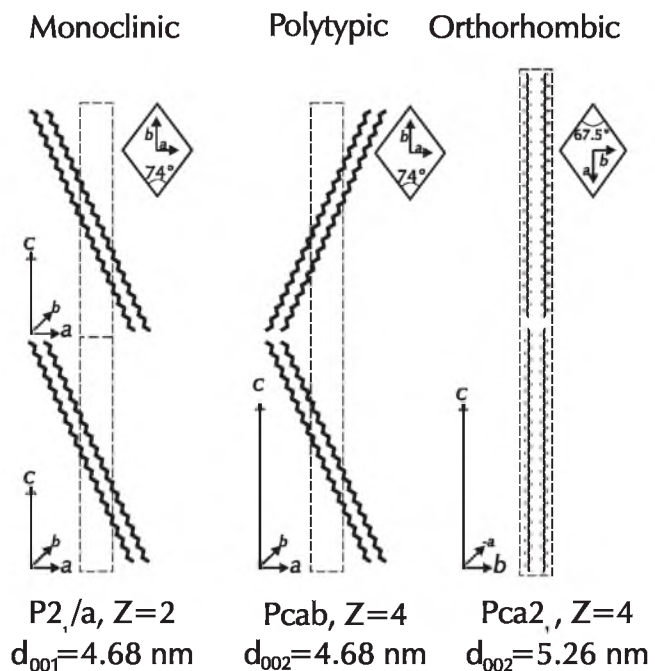d_{001}=4.68 nm d_{002}=4.68 nm d_{002}=5.26 nm

Figure 9.1 Schematic representation of the three known structures of n-$C_{40}H_{82}$ as seen along the longest axis of the lozenge-shaped crystals.

known: monoclinic and orthorhombic. One of the even n-paraffins of this length scale studied most is n-$C_{36}H_{74}$. For pure n-$C_{36}H_{74}$, the space group in which it crystallizes is monoclinic $P2_1/a$ (Z=2) [2] or the related polytypic $Pcab$ (Z=4) (which is orthorhombic, but is denoted here as polytypic, to prevent confusion with the orthorhombic $Pca2_1$ structure mentioned below) [3]. Because it is difficult to separate the higher n-paraffins from each other, n-$C_{36}H_{74}$ is often contaminated with impurities, being mostly other n-paraffins with a slightly different number of carbon atoms. With too many impurities, the crystals do not manage to crystallize in $P2_1/a$ anymore and instead the space group is orthorhombic $Pca2_1$ (Z=4) [4]. It has been shown [5, 6] that large even n-paraffins with almost the same length (e.g. n-$C_{36}H_{74}$ and n-$C_{38}H_{78}$) solidify in homologously isomorphous crystal structures. Hence, these space groups are expected to apply to n-$C_{40}H_{82}$ crystals as well. Table 9.1 gives the unit-cell parameters for the three structures, which are schematically drawn in fig. 9.1. For $Pca2_1$, the molecules are stacked perpendicularly to the molecular layers and $d_{002} = c/2 = 0.127m + 0.185$ nm $= 5.26$ nm [7], with $m = 40$ the number of C atoms. For $P2_1/a$, the n-$C_{40}H_{82}$ molecules are stacked tilted with an angle of about 65° to the molecular layers; as a result $d_{001} = 0.113m + 0.175$ nm $= 4.68$ nm [7] is lower. For the polytypic $Pcab$, the tilting angle of the molecules is the same, but the direction is reversed for alternating layers. The monomolecular layer thickness d_{002} is 4.68 nm as well. The melting point of n-$C_{40}H_{82}$ is 81.4 °C.

The surface morphology of the {001} faces of n-paraffin has been studied intensively. Already before the invention of atomic force microscopy (AFM), monomolecular steps could be observed by optical microscopy [8, 1] and electron microscopy [9, 1] with relative ease, because of the large step height. Attention was paid to space-group dependent symmetry of spirals [1], interlacing and polytypic step patterns [8, 1]. The first observations of dislocation movement in n-paraffin crystals were done by Anderson and Dawson [9]. Using transmission electron microscopy, they observed screw dislocation movement by glide in n-$C_{39}H_{80}$ crystals. For this purpose, the crystals were shadowed with palladium. The observed glide took place at those positions where a step occurs at the lower side of a platelet crystal. This step was transported 'through' the thin crystal via glide, and recombined with the top surface steps.

In the present study, the surfaces of n-$C_{40}H_{82}$ crystals grown from solution were examined using AFM. This technique, being able to measure steps down to 1 Å, experiences no difficulties at all in imaging the molecular height steps of about 5 nm on {001} n-$C_{40}H_{82}$, and therefore is well suited for imaging this crystal surface in a quantitative way without any further preparation. AFM revealed very flat surfaces covered with growth spirals originating from single screw dislocations. The most striking observation was the occurrence of mono-molecular steps crossing each other. Attention is also paid to the presence of folding patterns in the thin crystals.

9.2 Experimental

The crystals were grown from drops of a solution of n-hexane containing n-$C_{40}H_{82}$ at 22 C. These drops were placed on a glass plate, after which the n-hexane was allowed to evaporate slowly. This resulted in a glass plate partly covered with large crystals, partly covered with monomolecular crystal layers and some small, lozenge-shaped crystallites, and partly uncovered. The n-$C_{40}H_{82}$ with purity > 98% was purchased from Fluka, the ultra-pure n-hexane was purchased from Merck.

The AFM used was operating in tapping mode (TM-AFM) [10] instead of contact mode (CM-AFM), because in CM-AFM the forces on the sample imposed by the scanning tip can become so high that the surface of soft materials gets damaged or even destroyed. The probability of damaging the specimen surface is lowered in TM-AFM compared to CM-AFM because the tip exerts a perpendicular rather than a lateral force to the sample, and its surface is therefore not 'scratched' as in the case of CM-AFM. The AFM employed was a Topometrix 2010. The maximum scan size of the tripod scanner used was 75 μm. The tapping mode silicon cantilevers used had force constants of 25 - 85 N/m and resonance frequencies of 160 - 220 kHz.

9.3 Results

Basically, the crystals obtained by the solvent evaporation technique can be divided into three categories, namely 1) large monomolecular platelets of various sizes, 2) thin, 5-10 μm sized lozenge shaped crystals consisting of one or a few growth spirals, and 3) aggregates of thick crystals with sizes > 50 μm and thicknesses up to 1 μm, exhibiting many growth centres.

In all of the cases mentioned above, the typical growth morphology of n-paraffins, which is lozenge-shaped with the {001} faces covered by spirals, is clearly observed. The intersection lines of the crystal side faces with the {001} top and bottom faces as well as most of the step directions on the {001} face are /110/ (here, /110/ is defined as the set consisting of the [110] direction and its symmetrical equivalents in the (001) plane [11]). The majority of the observed steps is monomolecular. Their height was measured to be 5.3 ± 0.2 nm. Crossing steps could be discerned on all of the crystal types observed.

9.3.1 Monomolecular platelets

Fig. 9.2 gives an example of monomolecular platelets. Together with numerous needle-like crystals and some paraffin 'dots' these faceted crystals form the sample surface. The crystals and needles are

oriented randomly with respect to each other; probably they were grown in the solution and then landed on the glass plate. Fig. 9.2 depicts a common type of crossing steps. At places where the platelets or needles cover each other, the upper crystal is sometimes bent over the lower crystal. However, in most cases the crystals recombine: the covering part of the upper crystal layer becomes a separate layer on top of the lower layer and the non-covering part fuses with the lower crystal layer. The underlying step becomes a top surface step. This process is indicated by the black circles in fig. 9.2.
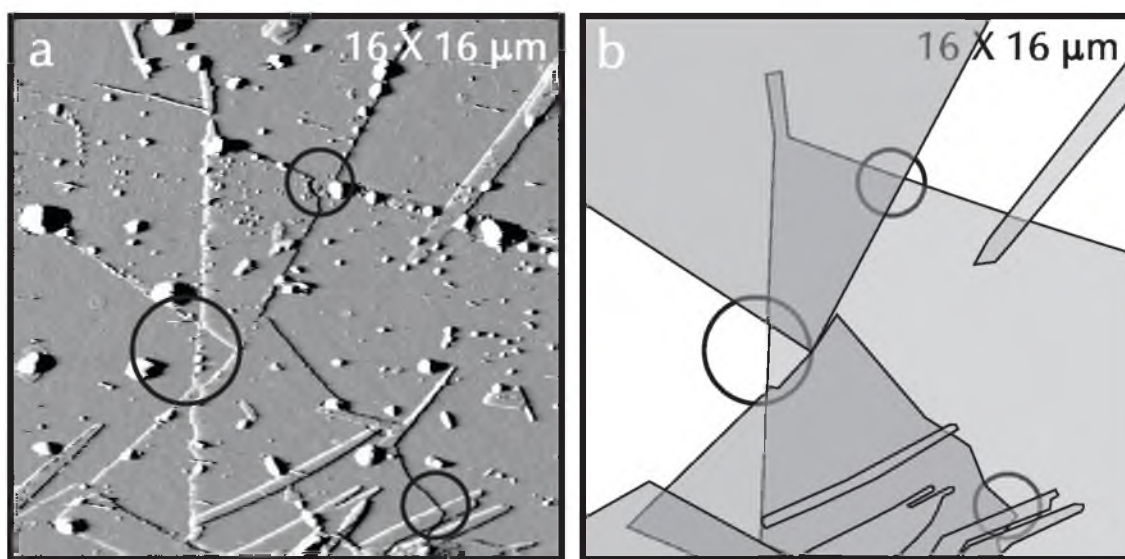
Figure 9.2 (a) TM-AFM error signal image of n-C$_{40}$H$_{82}$ {001} platelets of monomolecular height. Circles indicate recombination of platelets lying on top of each other, leading to crossing steps. (b) For clarity, the same area is depicted schematically, with the platelets coloured grey.

9.3.2 Spiral crystals

On the flat molecular layers, some very thin crystallites consisting of one or a few growth spirals, originating from screw dislocations are observed. Often these crystals are grown via two separate dislocations of opposite sign. Spiral steps are always of monomolecular height, i.e. d_{002}, indicating that the screw component of the burgers vectors is equal to ½ c. Sometimes, the spiral centres observed are obscured by three-dimensional particles. These particles may have induced the formation of the dislocations involved at the beginning of growth.

Crossing steps are observed on the spiral crystals as well. Figs. 9.3a,b show a crystal grown from two screw dislocations of opposite sign, of which the steps combine after a few spiral turns. The crystal, about 10 molecular layers thick, is seen to cover some particles (indicated by white circles).
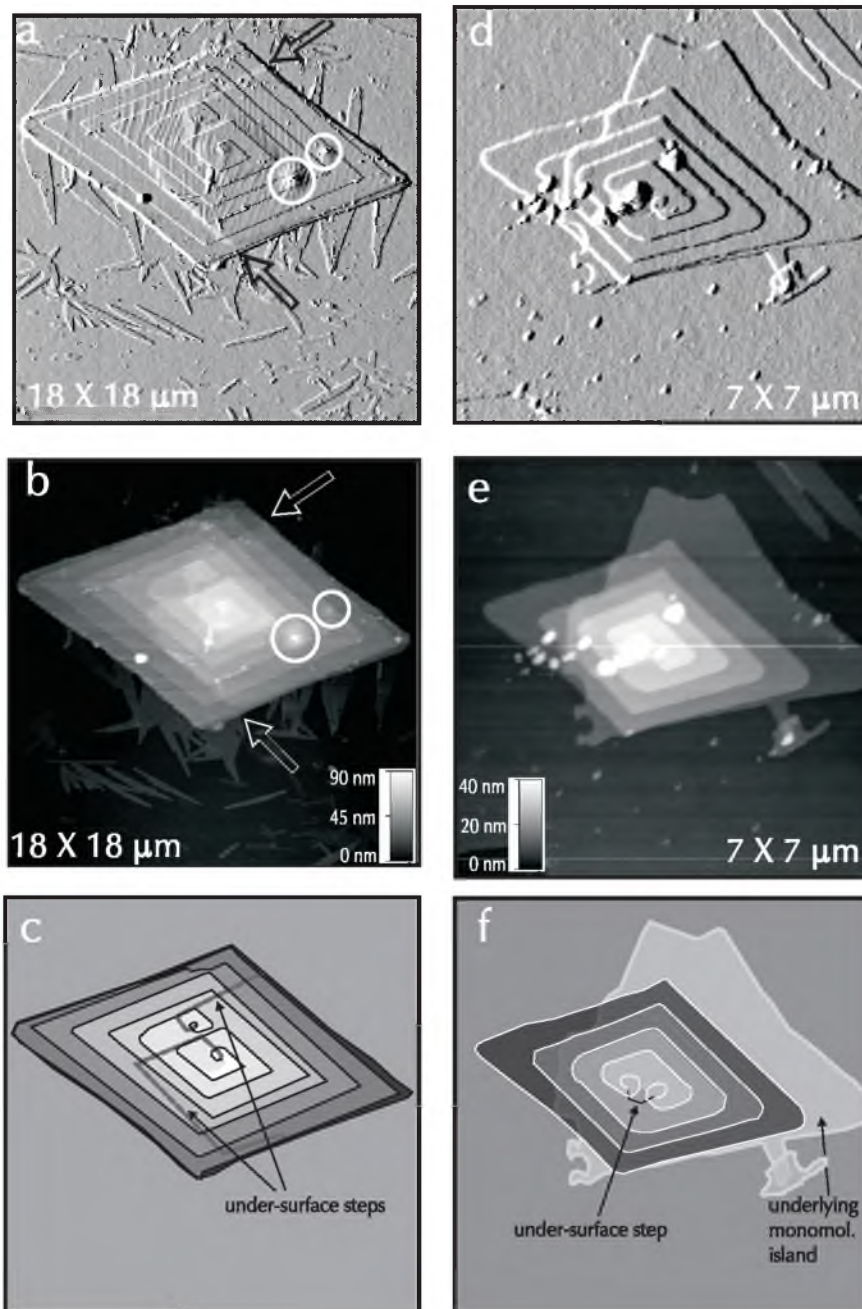
Figure 9.3 (a-c) TM-AFM images of a n-$C_{40}H_{82}$ two-spiral crystal in which steps below the surface are visible as diffuse lines (indicated by arrows). These steps run from the spiral centres towards the crystal edge. Small particles covered by the crystal are indicated by circles. (d-f) A n-$C_{40}H_{82}$ two-spiral crystal which has recombined with the underlying monomolecular platelet. The former edge of the platelet is now apparent as a step on top of the spiral crystal. The spiral centres are connected via a non-surface step. (a, d) are error images; (b, e) are height images; (c, f) are sketches for clarification.

Moreover, some 'under-surface' steps are distinguished, starting from the screw dislocations and going to the crystal edge as indicated by arrows in figs. 9.3a,b and by dashed lines in fig. 9.3c. These steps simply 'must' exist, because a dislocation cannot end within a crystal, i.e. if there is a screw dislocation outcrop at the top face of the crystal, there must also be one at the bottom face. Because these crystals are extremely thin and flexible, the steps on the lower crystal face can be 'seen' through the crystal; the upper surface covers the bottom side steps in a 'blanket-like' way and a diffuse step image is obtained. This is an example of a spiral crystal for which the upper layers do not recombine with the lower ones to form new steps at the crystal top surface.

An example where this recombination does appear is given in figs. 9.3d,e. Here, again a crystallite consisting of two screw dislocations of opposite sign is shown. The spiral pattern is interwoven with an underlying island of mono-molecular height with a capricious step edge. Here the spiral steps of the upper spiral crystal have recombined with the lower island steps, resulting in different heights along the spiral steps where they cross island steps. Fig. 9.3f gives a schematic drawing of the situation mentioned above in order to clarify the origin of the recombined steps and to show the position of the under-surface step connecting both spirals, of which a part is visible in fig. 9.3d.

9.3.3 Crystal aggregates

On the large aggregates of crystals, crossing steps were observed as well. An example of a 600 nm thick aggregate is given in fig. 9.4a. The crystals sometimes interpenetrate each other, as can be seen in the area above the white square. The white square is the area pictured in fig. 9.4b at a higher magnification. Here, it is clear that the overall crystal symmetry of the (001) plane is reflected in the spiral steps, which are parallel to /110/. Almost all spirals on this crystal part are seen to be left-handed, which is an indication that they have a common origin. Apart from the straight spiral steps, there are also some steps that have a more irregular shape and that often cross the straight spiral steps. An example of this crossing is shown in fig. 9.4c, which shows a zoomed-in part of fig. 9.4b. In these images, the depicted irregular step is first crossing a straight spiral step, then it is crossing itself (!) before turning into a straight step. Another region on a large aggregate with many crossing steps is shown in fig. 9.4d. The crossing steps in this area are always a pair consisting of one straight, crystallographically oriented step and an irregular step on the other side. Again, self-crossing steps are encountered.

9.3.4 Folding of the crystals

Besides crossing steps, other interesting features can be seen on the n-C$_{40}$H$_{82}$ crystals. One of them is the occurrence of wavy patterns on the {001} surfaces, as can be seen in fig. 9.3a. These features are often encountered on the small spiral crystals and sometimes on the large aggregates as well.
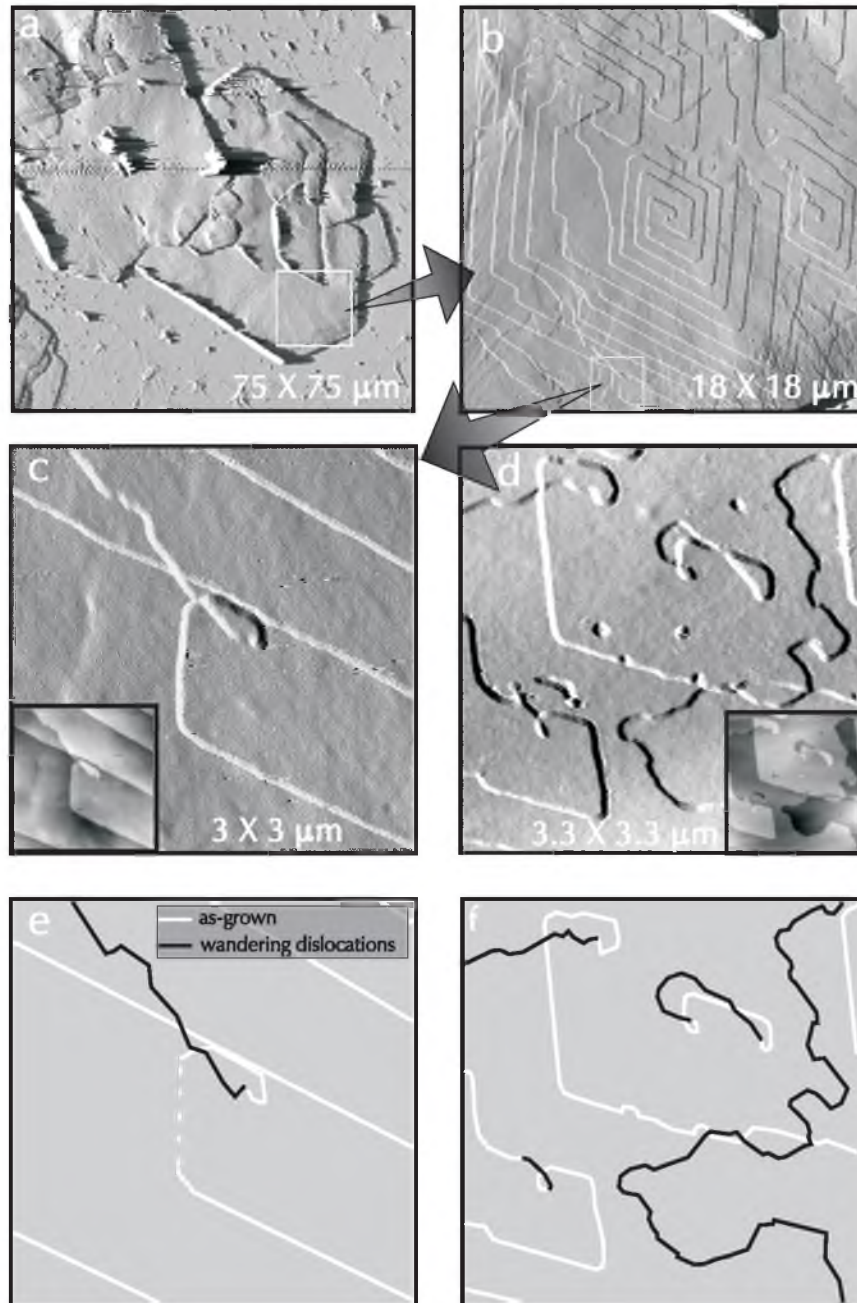
Figure 9.4 (a) Large aggregate of intergrown n-C$_{40}$H$_{82}$ crystals. (b) Zoomed-in part of (a) showing faceted as-grown single and double spirals. (c) Zoomed-in part of (b) showing an irregular step crossing a straight as-grown step and itself before turning into a straight step. (d) An area on another aggregate with many crossing and self-crossing steps and no dislocations left. Insets in (c, d): height images. (e, f): Sketches of the areas shown in (c, d) with as-grown steps drawn in white and steps caused by wandering dislocations drawn in black.

Analysis of the wavy patterns, oriented more or less towards /010/ (the long axis of the crystals), showed that these actually are folds of the crystal. Another example of a spiral crystal exhibiting this folding is given in fig. 9.5. Here, the folds change their orientation depending on the growth sector on which they occur. The height differences introduced by these folds are comparable to the height of the monomolecular steps, but the lateral distance over which these height differences are spread is much larger than in the case of steps. The wave pattern depicted in fig. 9.5 has an amplitude of about 4 nm and a period of about 300 nm, corresponding to about 500 molecules. The extra crystal surface introduced by the waves can be expressed by a relative increase in length in a direction perpendicular to the waves, $\Delta l/l$. Assuming a sinusoidal waveform and using the observed amplitude and period of 8 nm and 300 nm respectively, a value of $\Delta l/l = 1.8 \; 10^{-3}$ in the /100/ direction is calculated for the crystal depicted in fig. 9.5. For the calculation of Δl it is assumed that the crystal is bound to the glass substrate in such a way that it cannot expand freely, so that the expansion is completely expressed in the folding.
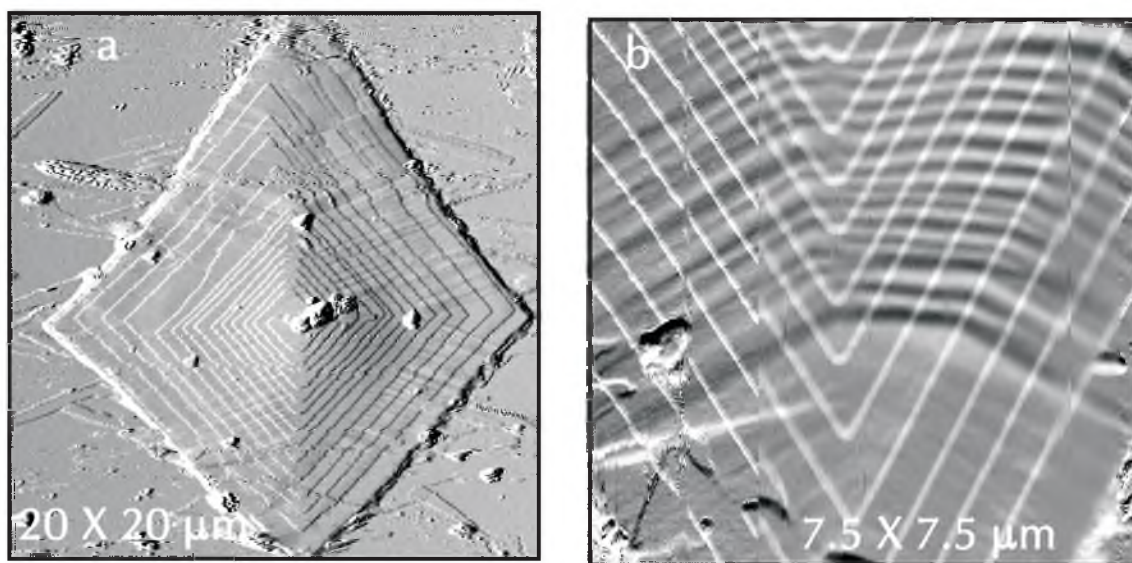
Figure 9.5 (a) 250 nm thick high triple spiral n-$C_{40}H_{82}$ crystal, which is folded. (b) Zoom-in of the 'southern' part of the crystal, where the folds change their orientation depending on the growth sector of the crystal. The period of folding is 300 nm, the amplitude is 4 nm.

9.4 Discussion

9.4.1 Space-group symmetry

As stated above, n-$C_{40}H_{82}$ crystals can crystallize in three different space groups, depending on temperature and the number of impurities. The monoclinic, polytypic and orthorhombic unit cells are drawn in fig. 9.1, as seen along the long crystal axis. Due to the tilted chains in the monoclinic/polytypic structure the a-axis is longer than the corresponding b-axis for the orthorhombic structure, while the other axis in the plane of the molecular layers, i.e. b for monoclinic/polytypic and a for the orthorhombic structure has an equal length. This results in different angles between the /110/ side faces of the crystal, as indicated in fig. 9.1. The acute angle of many crystals was measured to be 67 ± 1 , which proves the crystals under investigation to have the expected $Pca2_1$ symmetry.

This is confirmed by the AFM measurements. The average step height was measured to be 5.3 ± 0.2 nm, which is an indication that the actual structure is $Pca2_1$ ($d_{002}=5.26$ nm [7]) instead of $P2_1/a$ ($d_{001}=4.68$ nm). An even better confirmation comes from the step patterns observed. All observations by AFM indicate that the two-dimensional point-group symmetry of the spirals is $2mm$. If the space group is $P2_1/a$, steps on the left part and the right part of a spiral would behave differently, because one step edge would be concave and the opposite one convex (see fig. 1), resulting in different step speeds and necessarily different step separations [1]. In this case the two-dimensional point group of the spiral patterns on {001} would be m. For the polytypic (orthorhombic) $Pbca$ $2mm$ spirals would also be expected, but the slow steps and fast steps would alternate, resulting in step doubling and interlacing at the spiral corners [8]. Only for orthorhombic $Pca2_1$ all steps would be approximately of the same nature, yielding growth spirals of pseudo $2mm$ symmetry and of single step height. From the symmetric step separation of the spirals observed, like the one imaged in fig. 9.4b it is strongly suggested that the space group of the crystals is $Pca2_1$.

The only feature not understood is the occurrence of growth spirals with one monomolecular step originating from the centre. This corresponds to a burgers-vector screw component of length $d_{002} = \frac{1}{2}c$, whereas dislocations in primitive lattices must have burgers-vector lengths equal to an integer multiple of unit cell axis length. In other words, the sum of the height of the steps originating from the centre of a growth spiral on the {001} face in space group $Pca2_1$ must be an integer times $d_{001} = c$. This implies that the dislocations at the observed spiral centres must be partial, despite the fact that no evidence is found for the occurrence of stacking faults, which must be associated with this type of dislocations.

To enable a partial burgers vector screw component of $\frac{1}{2}c$ to occur, the structure of the second layer should be transformed into the structure of the first layer by translation only, by a vector $V_{trans} = (f_x$

$a, f_y b, \frac{1}{2} c$) in which f_x and f_y are fractional co-ordinates in the x- and y-direction, respectively, which define the accompanying edge dislocation. However, for the orthorhombic unit cell such a translation can not be made. The only translation vector V_{trans} that can approximate this in an energetically favourable manner is

$$V_{trans} \quad (0.786 , b/2, c/2 \quad 0.127) . \qquad (9.1)$$

When this V_{trans} is applied, the 'bulk' part of the second layer molecules transforms perfectly into that of the first layer molecules. The 'only' deviation from a perfect lattice is a shift of o carbon atoms in the z-direction, which results in a sub-step of 1, 3, 5, ... carbon atoms in height on the {001} surface. The consequence of this is a stacking fault coinciding with an unending sub-step originating from the dislocation. In spite of the fact that the existence of sub-steps of a few atoms in height cannot be excluded, during our measurements the occurrence of this type of stacking fault could not be demonstrated.

Consequently, on the basis of our observations, we cannot decide between the two basic solutions for the problem:

i)   There is some kind of partial dislocation with a stacking fault invisible to the AFM.

ii)   Despite all the evidence for $Pca2_1$, the crystals have another, yet unknown, structure resembling $Pca2_1$, but with a halved c-axis.

9.4.2 Step crossing by recombination of various ultrathin crystals

The crossing steps observed on the monomolecular platelets are formed in the process of several platelets covering each other. It is not clear whether this covering took place during growth in the solution, or whether the platelets were formed in the solution and then 'landed' on the glass surface on top of each other. In both cases the crystals were 'supported' by the solution, which has about the same density as the crystals. In the process of evaporation of the solution, the crystals are left in air lying on the glass and recombination can take place by collapse of the crystals under influence of adhesion. At the line where an upper crystal covers the edge of a lower one, force is exerted on the upper crystal and it may 'break' at this position, after which the lower part of this broken crystal recombines with the lower crystal, as illustrated in fig. 9.2. From the *a posteriori* observations, it can not be concluded whether this process proceeds parallel for the whole step at the same time, or serial via a screw dislocation moving along the step. From an activation energy point of view the second possibility is much more likely.

In most cases, separate crystal platelets covering each other do not have the same orientation of their a- and b-axes. Recombination of these plates, as shown in fig. 9.2, will therefore lead to a one-dimensional high angle grain boundary along the recombination line.

9.4.3 Step crossing by internal recombination of crystal layers within one crystal

A slightly different process occurs for the thin spiral crystals. The height difference due to the steps on the lower side of a crystal may be transformed into a height difference on the top side, because the flexible crystals bend over these 'under-surface steps' as a blanket, as is illustrated in figs. 9.3a-c. In many cases however, the adhesion induced shear force perpendicular to the crystal surface exerted at these positions can become so high that the whole crystal recombines and the step at the lower side becomes a top side step (see figs. 9.3d-e). A simultaneous displacement of the whole crystal volume one layer upwards is highly improbable, because of the high activation energy involved. Therefore, displacement of the material must have occurred via glide of a screw dislocation. This type of recombination by slip is the one that was observed by Anderson and Dawson [9] as well. On the basis of step recombination on single spiral crystals they concluded that dislocations had moved under influence of an external force. Earlier, Mott suggested that two dislocations attracted and cancelled each other on the basis of the observation of crystals with two recombined dislocations. [12].

The bonds between the alkane chains in a {002} slice have the highest energy of those present in the crystal. The force exerted on the crystals needed to split up and recombine in this slice must therefore be large compared to the forces needed to separate two {002} slices. However, due to the flexibility of the long chains and the almost vanishing thickness of the crystals, bending of the crystal slices is relatively easy (e.g. compared to ionic crystals) and shear forces exerted on the crystals (in this case: adhesion) are therefore concentrated at the positions of this bending.

9.4.4 Step crossing by dislocation movement

Besides recombination of several crystal platelets and transformation of downside steps to topside steps by slip, a third type of slip may occur. Namely, for the large aggregate crystals shown in fig. 9.4, a screw dislocation present in the crystal can be displaced by an external force, resulting in a slip step at the path of the moved dislocation. The principle of the process and direction of displaced crystal layers is the same as for the other types of slip. The difference is that for the thin spiral crystals simple adhesion forces between two crystal plates or a crystal plate and the glass surface caused the slip, whereas for the large aggregates the shear force needed for slip is probably generated when the solvent is evaporated from the more complex system of intergrown crystals. The latter results in crystal-crystal and crystal-glass adhesion forces which are not related to the presence of under-surface steps. Moreover, the crystals are too thick, and therefore too rigid, to make the other two mechanisms of slip operative. For clarity, the difference between transformation of downside to upside steps and pure dislocation movement is given in fig. 9.6.
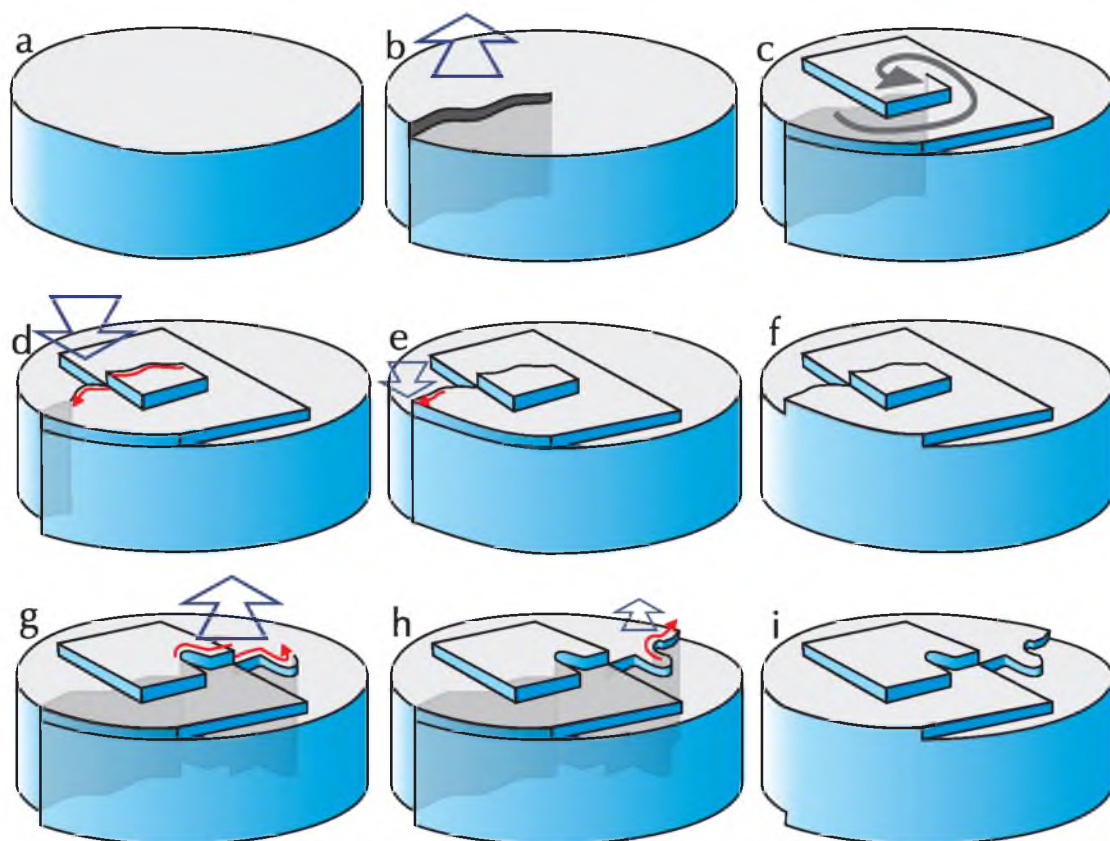
Figure 9.6 Two different ways of slip movement: (a) perfect crystal (b) a screw dislocation is introduced (c) spiral growth of the top side of the crystal, then (d, e, f) recombination of the steps along the originally created step by glide, or (g, h, i) further movement of the dislocation leading to extra steps on top and bottom of the crystal.

9.4.5 Why does slip occur?

Having discussed the three different types of slip movement, one question remains: why do these n-paraffin crystals exhibit slip movement? As stated above, this slip took place after evaporation of the supporting solution. This conclusion is mainly based on the observation of the crossing of faceted as-grown spiral steps and capricious steps, which are attributed to slip movement after cessation of growth. The shear forces needed for slip movement are probably caused by i) adhesion between thin crystal sheets covering each other or between a crystal sheet and the glass substrate, ii) adhesion between thicker crystallites in the agglomerates, and iii) a difference in thermal expansion of the glass substrate and the thicker crystals in the aggregates. On a molecular level the slip movement takes place along planes in which the alkane chains are bonded by van der Waals forces between the body-body contact of neighbouring molecules. All these bonds together are much stronger than e.g. the bonding between the methyl end groups of two crystal layers. But, for slip movement, which is

expected to proceed by a repeated displacement of the methylene groups in adjacent chains with respect to each other, the van der Waals forces per CH_2 group remain weak compared to the bonds in metallic and ionic crystals. Moreover, the alkane chains are almost perfectly 'smooth' without any protruding part, facilitating glide once more. This makes gliding perpendicular to {001} to occur at low forces compared to other types of crystals.

A first, rough, theoretical estimation of the shear force needed to slip one atom row one period over another atom row is

$$\tau_{th} \approx \frac{b}{a} \frac{G}{2\pi} , \qquad (9.2)$$

[13] in which a is the distance between the atom rows, b is the atomic distance in the direction of the applied shear stress τ_{th}, and G is the shear modulus. It turned out, however, that experimental values for these forces are about 10^{-3} to 10^{-5} times lower than theoretical values. This huge difference was accounted for by the presence of moving dislocations facilitating the slip process enormously [e.g. 13]. Around a dislocation, molecules are not at their equilibrium positions due to the dislocation stress, which lowers the force necessary for slip displacement.

In the case of n-$C_{40}H_{82}$, the third of the three types of slip observed (fig. 9.4) certainly involves moving dislocations. The second type, in which a downside step slips to the top face of a spiral crystal (fig. 9.3), probably proceeds via movement of dislocations as well, because such a defect was already available at the end point of the step at the lower side of these crystals prior to slip. It is likely that the slip starts from this end point and propagates along the downside step, which is a region of increased shear stress. For the first type of observed slip, a monomolecular platelet breaks up along the line where it covers another platelet. In this case, a dislocation is not observed. Probably, first a dislocation is formed at a position where the shear force locally equals the 'crystal strength', and then the slip proceeds by glide of this dislocation along the step edge of the underlying crystal.

9.4.6 Crystal folding

The occurrence of wavy patterns once more emphasizes the flexible nature of n-paraffin crystals. The folding, which is often encountered for spiral crystals (figs. 9.3a and 9.5) may find its cause in a thermal effect. Using optical and electron microscopy, striations and ridges have been observed earlier for n-paraffin crystals of triclinic n-$C_{28}H_{58}$ and orthorhombic n-$C_{36}H_{74}$ upon heating to a few degrees below their melting point T_m [1]. For n-$C_{36}H_{74}$, the striations were parallel to <100> (the 'long' direction of the lozenge shaped crystal) at $T=T_m$-7 C, and parallel to <010> (the 'short' direction) at $T=T_m$-5 C. For n-$C_{28}H_{58}$, sharp ridges parallel to <210> were shown to be accompanied by reorientation of the molecules in the strips between them, which was explained

as a result of slip along these ridges. For n-$C_{36}H_{74}$, this reorientation was not seen, but the striations observed were found to be ridges formed by a sequence of strips of tilted basal planes, where the molecules themselves kept their orientation with respect to the crystal surface. Upon lowering the temperature, the presence of the ridges is reversible, the change in the surface morphology is not. The differences between the present study and the earlier observations are the temperature and the nature of the folding. The current measurements were done at 35　C, which is much lower than the melting point of 81.4 °C of n-$C_{40}H_{82}$. The striations reported in literature were found to occur just below T_m. In the present experiments, the striations appeared to be smooth, sinusoidal oscillations of the crystal surface, while in the case of n-$C_{28}H_{58}$ the striations were sharp borders of regions with varying molecule orientations. Based on these two differences, we think that the folding of n-$C_{40}H_{82}$ has a simpler explanation: it is caused by thermal expansion of the crystals in contact with the glass substrate, without any reorientation of molecules. The crystals were grown at a temperature of 22　C, and observed by AFM at a temperature of about 35　C. This was verified by scanning a small thermocouple with the AFM tip [14]. The higher temperature during scanning is caused by the heat produced by the light bulb necessary for optical imaging of the crystals and the laser used for the feedback of the AFM. This temperature increase introduces a lateral expansion of the glass substrate and the n-paraffin crystals according to

$$\frac{\Delta l}{l}　\alpha_{uvw}　\Delta T ,$$

(9.3)

where α_{uvw} is the linear expansion coefficient of n-paraffin in the direction $<uvw>$; for glass α is isotropic. Because α_{glass} is negligible (α_{glass} is of the order of 1. $10^{-5}/$C [15]) compared to $\alpha_{paraffin}$ only the expansion of the n-paraffin has to be taken into account, which has been reported to be strongly anisotropic. Experimental values for the thermal expansion coefficients of n-paraffins measured for n-$C_{24}H_{50}$ [16] and n-$C_{36}H_{74}$ [17] are given in table 9.2 for the long $<100>$ and short $<010>$ directions of the crystal. This anisotropy follows from calculations of orientation dependent interaction energies as well [1].

Table 9.2. Linear thermal expansion coefficients of two n-paraffins [16, 17]

n-paraffin	α_{100} [$10^{-4}/$C]	α_{010} [$10^{-4}/$C]
n-$C_{24}H_{50}$	4.2	1.8
n-$C_{36}H_{74}$	4.8	0.4

In the present study, an expansion of $\Delta l/l = 1.8 \, 10^{-3}$, mainly in the $<100>$ direction is observed for the crystal of fig. 5 for a temperature increase of $\Delta T = T_{AFM} - T_{growth}$　13　C. From this we find $\alpha_{100} = 1.4 \, 10^{-4}$, and α_{010} negligibly small. The rough agreement in α_{100} with the literature values and the

observation that the expansion is mainly in the <100> direction suggests that the observed folding is indeed a thermal expansion effect.

9.5 Conclusions

Examination of the {001} faces of n-C$_{40}$H$_{82}$ crystals grown by evaporation of a n-hexane solution on top of a glass substrate using AFM revealed numerous monomolecular steps that were generated by slip after cessation of growth. This slip was induced by shear forces resulting from adhesion forces acting on the crystals after evaporation of the solvent. Three cases of slip movement, which are all due to the movement of screw dislocations with a burgers-vector component parallel to <001> were encountered, namely when ultra thin crystal plates lie on top of each other, when steps occur at the bottom of the grown spiral crystals, and when stress forces induce the propagation of existing screw dislocations in larger intergrown crystals. In all cases new steps arise on the crystal top faces, crossing existing as-grown steps.

Apart from slip, also folding of thin crystal plates has been observed. This phenomenon is attributed to thermal expansion of the crystals adhering to the glass substrate, due to heating by the AFM.

Acknowledgments

References

[1]   R. Boistelle, in: E. Kaldis (ed.), Current Topics in Materials Science, Volume 4, chapter 8, North-Holland, 1980.

[2]   H.M.M. Shearer and V. Vand, Acta Cryst. **9** (1956), 379.

[3]   R. Boistelle, B. Simon and G. Pèpe, Acta Cryst. **B32**, (1976), 1240.

[4]   P.W. Teare, Acta Cryst. **12** (1959), 294.

[5]   M. G. Broadhurst, J. Res. Nat. Bur. Standards A, **66** (1962), 241.

[6]   W.R. Turner, Ind. Eng. Prod. Res. Develop. **10** (1971), 238.

[7]   S.C. Nyburg and J.A. Potworowski, Acta Cryst. **B29** (1973), 347.

[8]   S. Amelinckx, Acta Cryst. **9** (1956), 217.

[9]   N.G. Anderson and I.M. Dawson, Proc. Roy. Soc. A **218** (1953), 255.

[10]   W.A. Ducker, R.F. Cook and D.r. Clarke, J. Appl. Phys. **67** (1990), 4045.

[11]   W.J.P. van Enckevort, J. Cryst. Growth **119** (1992), 177.

[12]   N.F. Mott, Nature **171** (1953), 234.

[13]   D. Hull, in *Introduction to Dislocations*, Pergamon Press, chapter 1.3 and 3.2, 1965.

[14]   M. Plomp, P.J.C.M. van Hoof and W.J.P. van Enckevort, submitted for publication.

[15]   H. Landolt and R. Börnstein, *Zahlenwerten und Funktionen (sixth edition)*, band II, part 1, 800, Springer Verlag, 1971.

[16]   A. Müller, Proc. Roy. Soc. London A **127** (1930), 417.

[17]   D.R. Holmes and E.A. Cole, J. Polym. Sci. **147** (1960), 245.

Chapter 10:

AFM-induced melt growth

on *n*-paraffin crystals

Chapter 10:

AFM-induced melt growth on

n-paraffin crystals

M. Plomp, P.J.C.M. van Hoof and W.J.P. van Enckevort

RIM Laboratory of Solid State Chemistry, Faculty of Science, University of Nijmegen, Toernooiveld 1, 6525 ED Nijmegen, the Netherlands

Abstract

The {001} surfaces of n-$C_{23}H_{48}$ paraffin crystals have been investigated by *ex situ* Alternative Contact mode Atomic Force Microscopy (AC-AFM). Although the crystals were scanned in air, without any solution present and below the melting temperature of n-$C_{23}H_{48}$, crystal growth or etching were revealed in any experiment, indepedently of the AC-AFM settings. Formation of 2D islands, growing spirals and pinning of advancing steps have been observed. It is shown that these crystal growth phenomena, which involve the nucleation and the propagation of monomolecular steps, are induced by the presence of the AFM tip. If the specimen crystal is cooled down, for about 15 C, the growth/etching effects are still present, but on a much smaller scale. Similar measurements on n-$C_{40}H_{82}$, which has a much higher melting point, revealed no crystal growth or dissolution at all, while n-$C_{19}H_{40}$ crystals, having a lower melting point, melted under influence of the AFM. It is concluded that the observed crystal growth on n-$C_{23}H_{48}$ crystals is caused by a combination of local heating by the AFM laser beam and the action of capillary forces at the AFM tip, which generate a liquid paraffin bridge between tip and specimen surface. Control over the occurrence of growth versus etching was limited and is associated with the amount of paraffin stored in the liquid bridge.

This type of *ex situ* investigations gives a good opportunity to study melt growth on a molecular scale, which would have been impossible by AFM *in situ* experiments, because of the extremely high requirements for temperature control needed for that case. Despite the different mechanism as compared to 'real' melt growth experiments, the current system behaves remarkably similarly. Furthermore, the method may be suitable for surface patterning applications.

Keywords: atomic force microscopy, crystallization, etching, growth, surface melting, alkanes, single crystal surfaces, surface defects.

10.1 Introduction

One of the advantages of atomic force microscopy (AFM) above other techniques for surface examinations (e.g., electron microscopy) is its ability to work in many different environments: in vacuum, in air, in liquids. In the field of crystal growth this versatility translates into the application for investigating ex situ and in situ crystal growth, whereby ex situ usually means that after separation from their growth environment crystals are examined by AFM in air, and in situ generally refers to crystals slowly growing from solution, which are examined in an AFM liquid cell. The in situ technique experiences difficulties with melt growth and solution growth of highly soluble materials, because of the high growth velocities involved. Taking into mind the small surface area imaged in an AFM scan (typically 10 nm - 100 μm) and the time needed to complete the scan (typically 10 s - few minutes) the velocity of the imaged steps (and hence the growth velocity R) is limited to about 1 μm/s for 100 μm scans and to even lower values for smaller scan ranges. In situ AFM can neither be applied to systems where extreme temperatures or corroding solutions are involved.

At first sight, this division in in situ and ex situ seems a very strict one. However, crystal morphology is known to be able to change ex situ. This may be due to a rearrangement of the crystal surface caused by a transition of the growth form to an equilibrium form, and/or by the influence of light (e.g. for AgBr crystals [1]), by water present on the crystal surface (e.g. NaCl [2] or Ba(NO$_3$)$_2$ [3] crystals) or by formation of a surface layer (e.g. oxygen in case of Si). In the specific case of AFM, changes of the observed ex situ morphology usually comes down to etching or 'scratching' of the surface by the scanning tip as a result of a too high force applied by the tip. Sometimes, this etching takes place in a more or less controlled way, such as in the case of AFM-induced layer-by-layer evaporation of soft HgI$_2$ crystals [4] or the layer-by-layer removal of Langmuir Blodgett films [5]. The scratching has also been used as a lithography tool to construct small-scale patterns. In the field of nanolithography AFM is applied to scratch <50 nm wide lines in thin films of polymer resist, like PGMA [6] or PMMA [7]) or spin-on-glass [8]. However, these lithography experiments have little in common with crystal growth. Only recently, AFM-induced ex situ growth of monolayers of alkanethiols on a gold substrate was reported [9]. For this, the AFM tip was coated with alkanethiols first. When the tip scanned the gold substrate, molecules were transported from the tip to the sample via the water meniscus present between tip and sample. This can be regarded as a form of ex situ tip-induced solution growth. In the present paper, ex situ experiments on n-C$_{23}$H$_{48}$ paraffin crystals are presented which show real crystal growth and etching during AFM scanning, despite the fact that there is no intended mother phase (solution, melt or vapour) present. This can be regarded as ex situ tip-induced melt growth.

The n-paraffin n-C$_{23}$H$_{48}$ used in this study has a relatively low melting point of 47.5 C, and is an

organic compound which is characterized by relatively weak van der Waals interactions that form the crystal structure. These properties make the compound suitable for investigating the influence of a scanning AFM tip on the surface dynamics. Because of their crystallization behaviour, n-paraffins are interesting from a scientific point of view as well. This crystallization behaviour changes as a function of the number of C atoms in the chain and alternates as a function of the evenness/oddness of that number. Impurities, often present because of the difficulties of separating paraffins $C_m H_{2m+2}$ and their neighbouring homologs $C_{m\pm x} H_{2(m\pm x)+2}$ (x is a small, even number), also influence the growth.

Paraffin crystals have been the object for study for a long time; a substantial amount of research has been summarized in a review paper of Turner [10]. For the current study, research concerning the crystal structure is important. There are four different modifications known for n-paraffin crystals: triclinic, monoclinic, orthorhombic and hexagonal [11]. The hexagonal or rotator phase modification, in which the molecules can freely rotate around their longitudinal axes, only occurs a few degrees below the melting point. Pure, even n-alkanes crystallize in the triclinic $\bar{A}$, $Z=1$ (m 28) or in the monoclinic $P2_1/a$, $Z=2$ (m 26) structure, while odd alkanes such as n-$C_{23}H_{48}$ crystallize in the orthorhombic $Pbcm$, $Z=4$ for m>11. Even alkanes containing impurities crystallize as well in an orthorhombic form ($Pca2_1$, $Z=4$).

In this paper, the {001} surfaces of n-$C_{23}H_{48}$ crystals grown from solution and vapour are examined using AFM. During imaging, crystal growth or etching took place. This technique, being able to measure steps of a few Å, experiences no difficulties at all in imaging the molecular steps of 3.1 nm on the {001} surfaces of n-$C_{23}H_{48}$ crystals, and is therefore a well suited technique to image the crystal surface in a quantitative way without any further preparation. For comparison, n-$C_{19}H_{40}$ and n-$C_{40}H_{82}$ crystals have been investigated as well.

10.2 Experimental

Most crystals were grown from drops of solution of n-hexane or n-butanol containing n-$C_{19}H_{40}$, n-$C_{23}H_{48}$ and n-$C_{40}H_{82}$. These drops were placed on a glass plate, after which the solvent was allowed to evaporate slowly. This resulted in a glass surface partly covered with large aggregates, and partly covered with a few monomolecular layers. For n-$C_{23}H_{48}$, also vapour growth has been carried out. These crystals were grown for a week on a cold finger in a vapour growth cell [12] at room temperature under a pressure of about 10^{-9} bar; the temperature difference applied between the source material and the growing crystals was a few degrees. All n-paraffins, with purity > 98%, were purchased from Fluka; the ultra pure n-hexane was purchased from Merck.

In AFM, a very sharp tip attached to a spring cantilever is scanned over the surface. In recording the AFM images, two different signals are monitored. In contact-mode AFM (CM-AFM) the deflection of the cantilever, which is a measure for the shearing force between the tip and sample, is gauged by a laser and the resulting signal is offered to a feedback loop that maintains a constant force by adjusting the tip-sample distance. The height adjustment needed, as well as the deflection signal can be depicted to give a height image and error image [13] (also called force image, deflection image or derivative image)of the surface scanned, respectively. Since the force is kept constant, the error image will be smooth except for locations with sudden height changes (i.e. at steps), where a short pulse in the error signal arises due to the fact that the feedback loop cannot compensate for the height difference immediately.

In CM-AFM, the forces on the sample imposed by the scanning tip can become so high that the surfaces of soft samples get damaged or even destroyed. To avoid this, alternative contact mode AFM (AC-AFM) can be employed [14]. In AC-AFM, the cantilever is forced to oscillate at its resonance frequency in free air. When the tip is lowered towards the sample, the measured amplitude of the oscillation decreases due to a attractive forces between tip and sample and, if the tip is lowered more, due to repulsive interaction when the tip actually touches the surface during the lowest part of its oscillation cycle. In AC-AFM, this amplitude damping is used as the feedback signal instead of direct cantilever deflection. As in CM-AFM, both a height image and an error image (now called amplitude image, and now representing the deviation of the actual amplitude from the amplitude setpoint) can be acquired. The probability of damage to the sample is lowered in AC-AFM with respect to CM-AFM because the tip imposes a normal force rather than a lateral force on the sample, and the sample is therefore not 'scratched' as it is in the case of CM-AFM.

Because of the softness of the paraffins, during the present experiments the AFM was operated in AC mode. The AFMs employed were a Digital Dimension 3100 (fig. 2) and a Topometrix 2010 Discoverer (all other figs.). The AC mode silicon cantilevers used had force constants and resonance frequencies of 25 - 85 N/m and 160 - 170 kHz (Discoverer), respectively 42 N/m and 260 kHz (Dimension). All images were recorded with AC mode amplitude setpoints of about 80% of the amplitude in free air. Small deviations from this setpoint did not result in other growth/etching behaviour. When the amplitude setpoint was set too low (approx. < 70%, this resulted in tip crashes; setpoints too high (approx. > 90%) caused lift-off of the tip. Unfortunately, calibration curves could not be made, because oscillating the tip with varying (average) height at one particular position at the surface resulted in destruction of the surface structure, creation of large holes, and very irreproducible results. Therefore, the forces between tip and sample could not be estimated.

In order to verify the crystal growth/etching behaviour at lower temperatures, an ex situ cooling cell was developed for the Discoverer AFM. This cell is an 8 mm high copper cylinder of 10 mm in

diameter, which can be attached onto the tripod scanner. The glass plates with solution-grown crystals were mounted on top of the cooling cell using carbon tape. Via a flexible inlet and an outlet this cooling cell was flushed with water from a cooling bath with a temperature control of 0.1 C. During water flow through the cell the AFM images recorded were unstable due to oscillations introduced by the pump of the waterbath. During imaging the water circulation was therefore temporarily stopped.
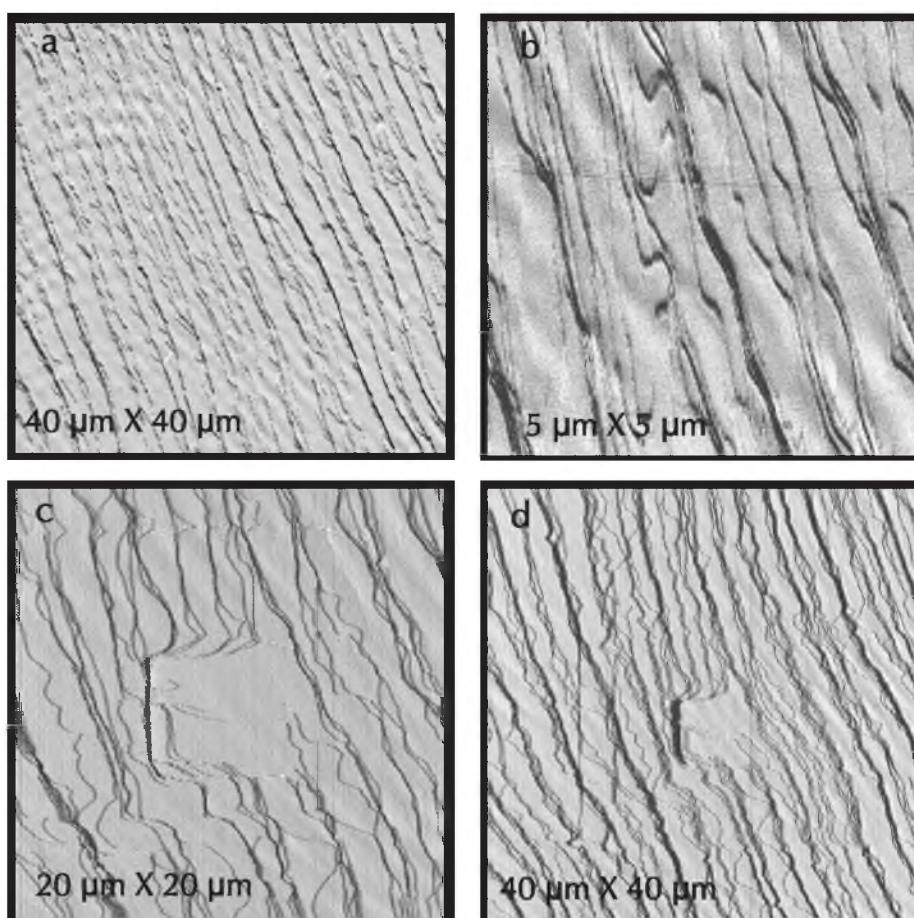
Figure 10.1 Series of contact-mode scans on the same area of a n-$C_{23}H_{48}$ crystal grown from vapour. (a) first measurement: bunched steps of about 10 monosteps in height. (b) Zoom-in of 5x5 μm^2 showing an irregular step pattern due to wear. (c) 20x20 μm^2 zoom-out showing the original 5μm-scan as a square hole. (d) original scan size showing both the 5 μm and the 20 μm scans as depressions. In both (c) and (d) step wear is encountered, leading to decomposition of the original bunches. All images are deflection images instead of topographic images in order to be able to distinguish the step edges. Time of imaging varies from 5 minutes for the 40 μm scans to 1 minute for the 5 μm scan. The imaging force is not measured. Instead, the force is minimized by minimizing the deflection setpoint in such a way that there is still a stable feedback.

10.3 Results

10.3.1 Contact mode AFM

Both CM-AFM and AC-AFM were applied for investigating the n-$C_{23}H_{48}$ crystals. The surface damage introduced by CM-AFM scans, even at the lowest possible forces that still enable stable feedback, can be best described as 'step wear'. If the tip encounters a step, it is displaced slightly. If small scan sizes of a few μm are applied, this effect becomes dramatic and many layers are removed, leading to square depressions with the dimensions of the AFM scan. Both step wear and the formation of scan-induced square holes can be recognized in fig. 10.1. This step wear and formation of depressions can be regarded as a 'normal' form of tip-induced wear, which is essentially different from crystal growth/etching. However, in all images the surface remains flat on a molecular scale, even at the bottom of the holes created. This indicates that the material removal occurs still in a more or less ordered layer-by-layer way.

10.3.2 Crystal growth and etching induced by AC-AFM

A less destructive force on the crystal surface is applied by the use of ex situ AC-AFM. There is still an interaction between tip and sample, but this is not a strong lateral force oriented in the scan direction, as is the case for CM-AFM, but a force acting perpendicularly to the specimen surface. This non-lateral AC-AFM interaction gives a different type of etching of the surface, and can even result in crystal growth of the n-$C_{23}H_{48}$ surface. In all the AC-AFM experiments, either etching or growth took place. Which of both processes occurred was not dependent on any AFM parameter such as scan rate, amplitude setpoint, drive amplitude and feedback parameters, and thus could not be controlled via this way. The only way in which the etching/growth type of scanning could be influenced was via the AFM tips: use of new tips often resulted in etching, while tips used before, as well as tips that had experienced a tip crash (e.g. deliberately by lowering the amplitude setpoint to 30% of the cantilever's oscillation amplitude in free air), often resulted in crystal growth.

An example of AC-AFM induced etching showing many distinct phenomena is displayed in fig. 10.2. The circular shape of the monomolecular deep etch holes shows clearly that the etching is independent of the scan direction. The average propagation velocity of the steps is -0.3 nm/s (where the - sign stands for etching) and crystal layers are removed with a rate of -0.3 ML/hr. After the scanning-induced etching the AFM tip is retracted, and a few scans are made only after 20 h respectively 70 h since the start of the experiment in order to check the behaviour of the crystal surface in absence of the tip. On this large timescale an AFM-independent recombination of the holes is found.
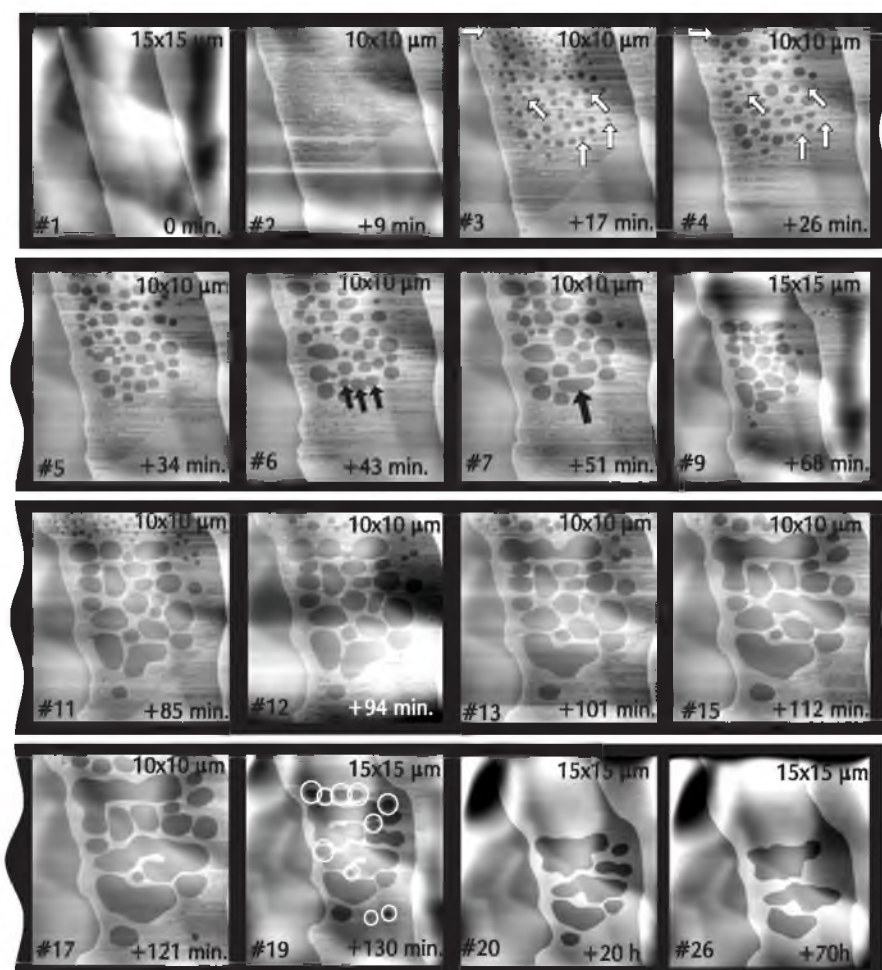
Figure 10.2 Series of topographic images of AC-mode scans on a solution-grown n-$C_{23}H_{48}$ crystal, showing 2D nucleation etching. Only 16 of the 25 scans of this series are shown. Upon repeated scanning, the central plateau of #1, which is bordered by monomolecular steps of 3.2 nm height, is seen to deteriorate (#2) before circles of monomolecular depth are etched away (#3). Some small holes disappear again (*e.g.* those indicated by white arrows in #3, which have vanished in #4), the larger holes expand with every scan (#4-11). When the holes become thus large that they grow together, the etching is temporarily accelerated to produce a rounded shape of a new, combined hole (see *e.g.* the three holes indicated by the black arrows in #6-7). After 130 minutes (#19) of continuous scanning the tip was withdrawn for 20 hours. During this period, the etched pattern turned out to be relatively unaltered (#20). The smaller holes (indicated by white circles in #19) have grown out, while the large ones have become somewhat larger. During this 20 h, there is no detectable nett change in the amount of paraffin present in the imaged area. After this period, no etching is observed anymore after repeated scanning (#21-25, not shown). During another scanning break of 50 h, the minimization of the step energy has continued (#26): only the three largest holes survived. Now, there has been a small nett flow of paraffin towards the imaged area. Scan sizes are as indicated; recording time of scans: 4-8 minutes; there is no pause between the scans (except for #19-20 and #25-26). The amplitude setpoint is 82% of the cantilever amplitude in free air for all images #1-19, 79% for #20 and 76% for #26. The vague white and black spots on all images represent height differences of an underlying crystal over which the top crystal sheet is lying like a blanket.
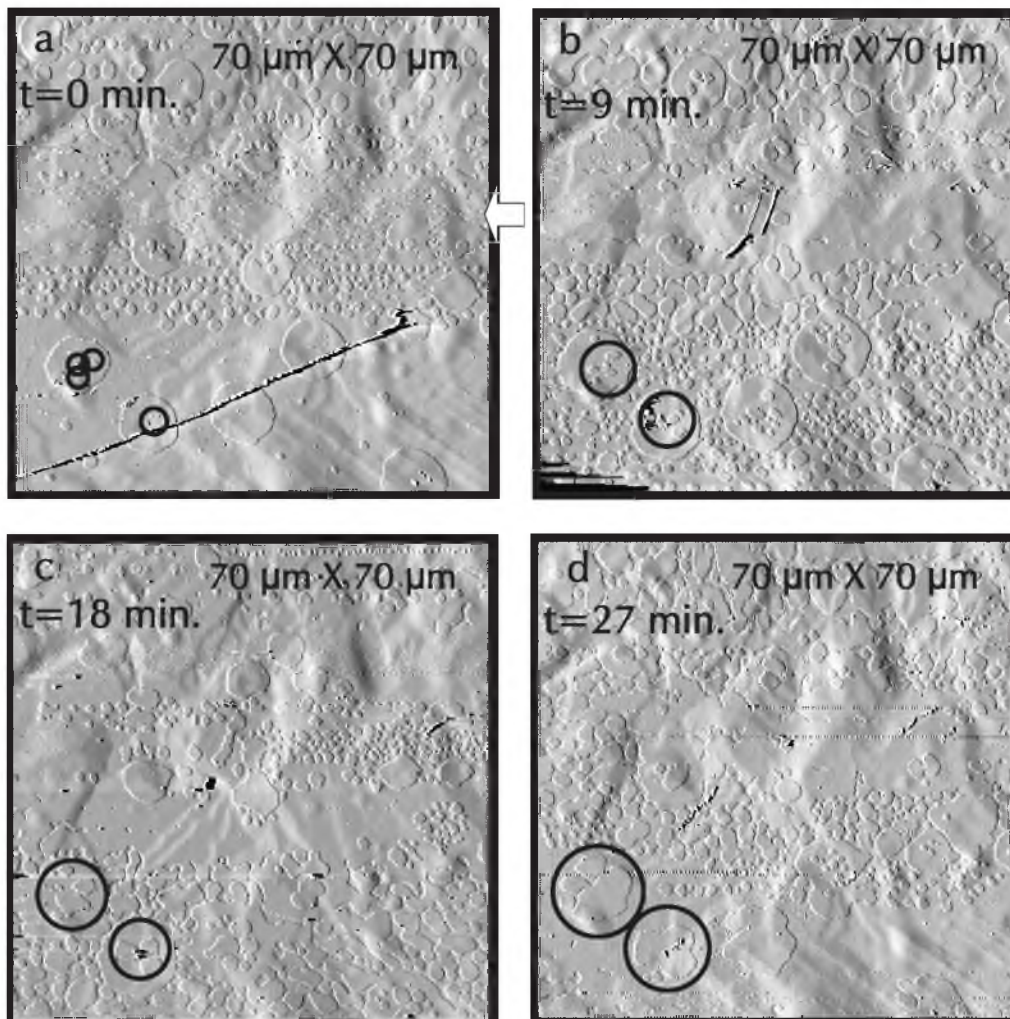
Figure 10.3 Series of amplitude images of AC-AFM scans of a solution-grown $n\text{-}C_{23}H_{48}$ crystal showing continuing 2D nucleation growth. (a) second scan showing the result of an initial uncompleted scan, which was stopped at the position indicated by the arrow. (b-d) uninterrupted successive scans showing further growth and coalescence of the nuclei in (a) as well as the nucleation of new islands. In (d) the nuclei of (a) have grown together to form a new growth layer, while the 'nuclei-on-nuclei', indicated in (a) by black circles, have grown out to form the next growth layer. Like in fig. 1, shallow foldings can be observed, which here indicate that lower crystals are covered by the upper crystal in a 'blanket-like' way. Recording time of the scans: 8 minutes. Amplitude setpoint: 86% of the oscillation amplitude in free air.

An example where AC-AFM scanning of $n\text{-}C_{23}H_{48}$ crystals resulted in growth instead of etching is given in fig. 10.3, where growth takes place via 2D nucleation. In the successive scans the resulting growth is only one monolayer, indicating a low 'effective supersaturation' σ_{eff}. The average step velocity is 1.6 nm/s; the 2D layer growth rate is 2 ML/hr.

For these experiments, besides solution-grown, also vapour-grown crystals have been used. No differences in etch/growth behaviour were found. This excludes any influence of remainders of solvent, for example by forming a thin solution layer on top of the surface, on the etch/growth behaviour.

To investigate the universality of the observed growth and etching phenomena, different AFMs (a Digital Dimension and a Topometrix Discoverer) were used to image the n-$C_{23}H_{48}$ crystals. No major differences were found. The same characteristic etch and growth phenomena were encountered using both AFM types. For both instruments, the occurrence of either growth or etching was merely dependent on the tip (new/used/crashed) rather than on the AFM settings.
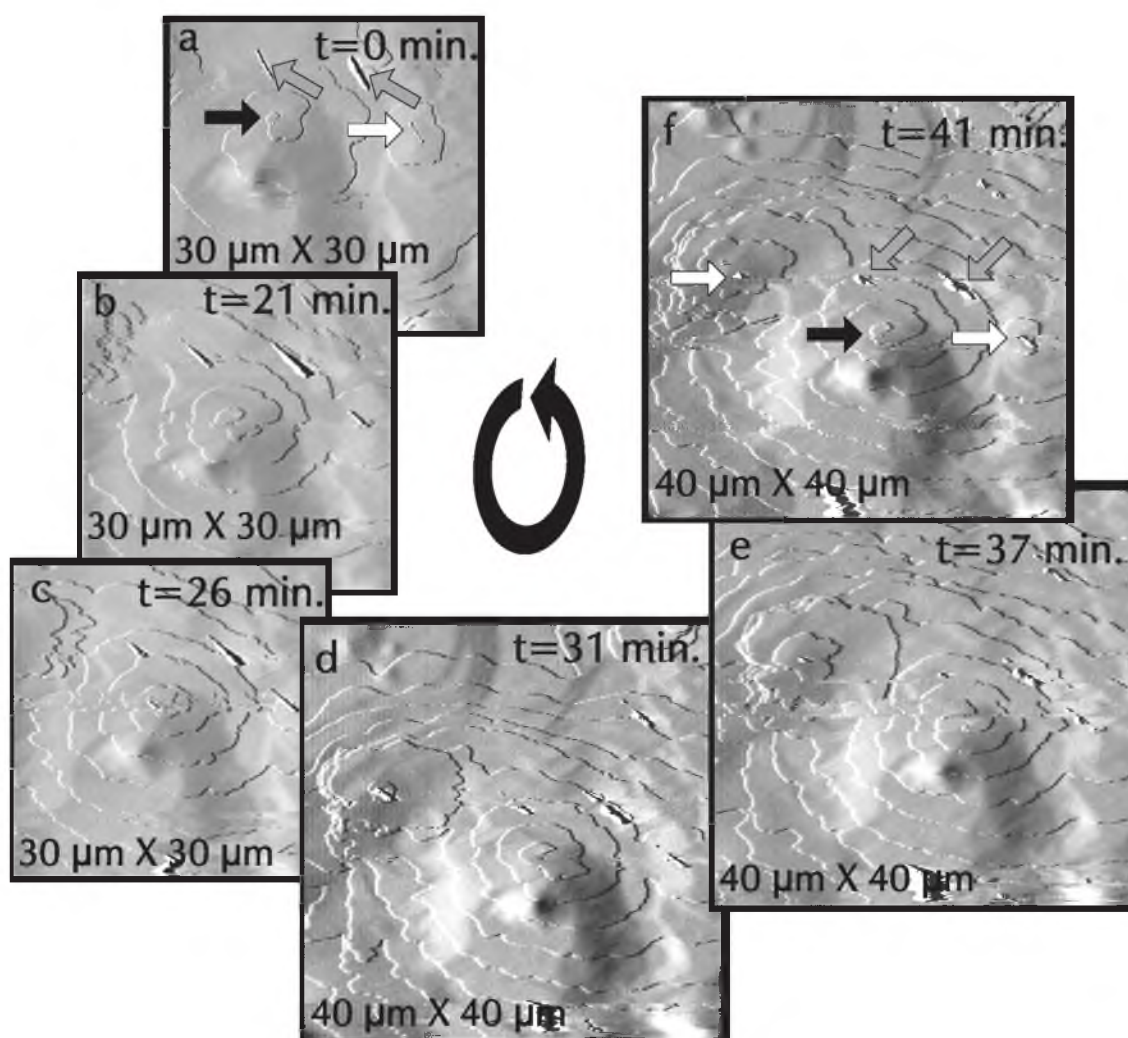
Figure 10.4 Series of amplitude AC-AFM images showing a growing spiral (indicated by black arrow) and two heterogeneous nucleation points of steps (white arrows). The particles indicated by grey arrows do not cause heterogeneous nucleation. Three additional images have been made between figs. (a) and (b); (b-f) are successive images. Time of imaging: about 5 minutes; amplitude setpoint: 75%-78%.

10.3.3 Crystal growth phenomena

Besides the above described 2D nucleation growth and etching, also other crystal growth phenomena were encountered. Fig. 10.4 shows an example of an area with a growing spiral, together with two heterogenous nucleation growth sources. The steps emitted from all growth sources advance regularly, and merge as they meet. The average step speed decreases from 10 nm/s to 2 nm/s from the beginning to the end of the experiment, and the layer growth is estimated to decline from 2 ML/hr to 0.5 ML/hr. Fig. 10.5 gives a growth series depicting a moving step-train. This
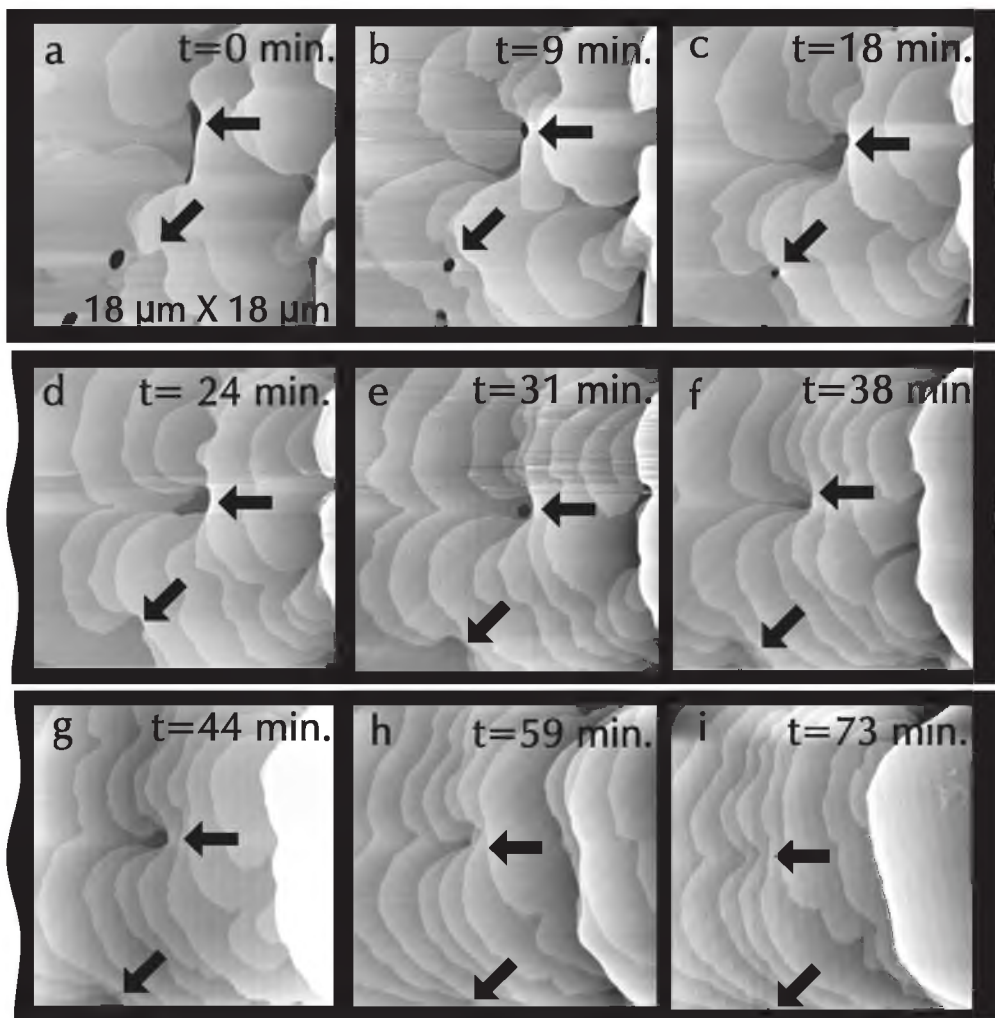
Figure 10.5 Series of topographic AC-AFM images showing a step train advancing from the right to the left. At the points indicated by arrows the monomolecular steps are pinned and get bunched. Steps are forced to flow around these points, creating holes behind the pinning positions. In course of time the bunching, and hence the pinning, becomes less and steps pass the pinning points in a normal way, as can be seen in the last picture. Recording time of each scan: 7 minutes. Additional images were made between figs. (g) and (h), and (h) and (i). Amplitude setpoint: 80%.

step-train is pinned at the indicated positions. However, in course of time the pinning becomes less and less, and in the last picture it has nearly vanished. This is a clear indication that the pinning is caused by some impurity which is buried by successive layers, whereby its pinning influence decreases. The average step speed is calculated to be 3.3 nm/s, the layer growth is 0.7 ML/hr. The objects causing the pinning cannot be discerned, limiting their possible size to 20 nm.

### 10.3.4 Linescans

In an attempt to understand the mechanism of growth/etching of n-$C_{23}H_{48}$ induced by ex situ AFM, additional experiments were carried out. In these, we applied line scans, where the AFM tip scans the same line over and over again, instead of following a 2D grid. The first example, where etching is observed, is given in figs. 10.6a-c. The surface is imaged before, during and after the line scan. During scanning the layer-by-layer removal of paraffin can be observed. The average edge speed of 120 ML/hr can be directly deduced from this linescan. After the line scan, a bone-like gap has developed. Both ends of the bone are wider because at the turning points of its scans the velocity of the tip is temporarily lower. As a consequence it spends more time in these two regions, where it can induce more etching of the crystal. The result of a similar line scan experiment where growth instead of etching is observed is depicted in fig. 10.6d. Here a growth point (at a position where the tip is kept fixed for a certain time) as well as a growth line (at a position of a line scan) have been formed. More growth has occurred at the turning points of the AFM tip, similar to the enhanced etching as imaged in fig. 10.6c. The observations shown in fig. 10.6 prove that both growth and etching are directly caused by the presence of the AFM tip. The line scan experiments indicate that this tip influence extends over an area of about A_{ti} 1 - 10 μm^2. From this, it can be concluded that the step propagation velocities as derived from figs. 10.2 - 5 are calculated too low. They should be corrected for A_{ti}, because growth only takes place when the tip is nearby a certain surface position. To obtain the actual step velocity or growth rate, the observed values should therefore be multiplied with the correction factor

$$C_{ti} \quad \frac{A_{ss}}{A_{ti}} \quad , \tag{10.1}$$

where A_{ss} is the scan size of the figure. Taking $A_{ti} = 1 \mu m^2$, C_{ti} varies from 4900 for fig. 10.3 to 324 for fig. 10.2. Even for $A_{ti} = 10 \mu m^2$ this factor is still large.

A welcome side-effect of this growth limited by the presence of the tip is the fact that the morphology of the images can be directly interpreted without the need for a correction of the scan speed in the slow scan direction, which should be applied for in situ AFM experiments (e.g. [15]).
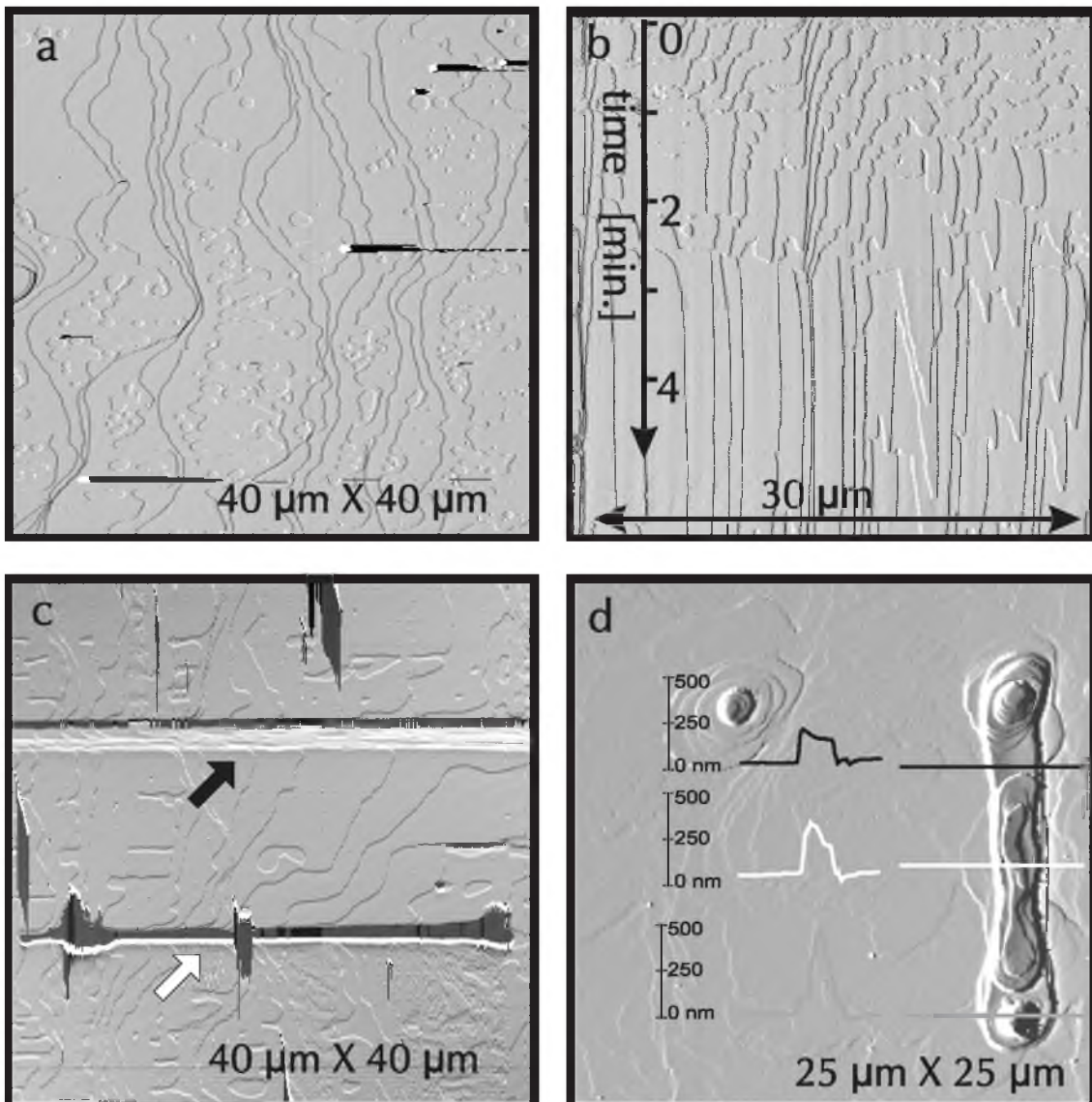
Figure 10.6 Series of amplitude AC-AFM images showing the result of a line scan repeated 50 times. (a) Surface area before the line scan. The 'normal' 2D nucleation etching amidst some steps is encountered. (b) Etching observed during the repeated line scans. For this picture, the x-axis depicts the distance as travelled by the tip, while the y-axis depicts time. (c) As a result of the repeated scanning a bone-like gap (white arrow) with a depth of about 10 molecular layers is formed. Part of a gap produced by another line scan is shown as well (black arrow). (d) The result of a similar line scan experiment in which growth of 50 to 100 molecular layers is observed. Besides line growth, point growth has been realized as well (upper left part of picture) at a position where the tip was kept fixed for a while. Time of imaging: 5 minutes (b and c); 7 minutes (a and c). Amplitude setpoint: 83% (a); 78% (b); 75% (c) and 80% (d) of the cantilever oscillation amplitude in free air.

10.3.5 Comparison with other *n*-paraffins

It is clear that the presence of the tip induces growth or etching. To investigate the role of the substance itself in the growth process, three different *n*-paraffins were measured: n-$C_{19}H_{40}$ (melting point $T_m=32$ C [16]), n-$C_{23}H_{48}$ ($T_m=47$ C) and n-$C_{40}H_{82}$ ($T_m=82$ C). The melting point of the *n*-paraffins is expected to be important for their behaviour with regard to the AFM induced growth/etching. In order to determine the local temperature at the place of scanning, AFM scans were also performed on the surface of a thermocouple. This resulted in a 'scanning temperature' of $T_s=34$ C. This temperature is higher than room temperature (24 C) due to heating from *i)* the light bulb present in the AFM, which is used as a light source for the built-in optical microscope, *ii)* the AFM laser itself, and *iii)* the AFM tip, which is indirectly heated by the laser beam. *i)* and *ii)* are relatively global effects that can be accurately measured by the thermocouple. However, *iii)* is a very local effect, which causes an additional temperature increase at the tip-surface region, which could not be measured.

Measurements on n-$C_{19}H_{40}$ could not be performed as this *n*-paraffin melted upon scanning. This is in agreement with the thermocouple measurements, comparing the melting point of n-$C_{19}H_{40}$ $T_m=32$ C with the measured scanning temperature $T_s=34$ C. Conversely, measurements on n-$C_{40}H_{82}$ could be made without any problem, and moreover, no crystal growth or etching was observed [17]. These additional measurements demonstrate that the melting temperature of the *n*-paraffins plays a key role in the occurrence of AFM-induced *ex situ* crystal growth.

To prove this point once more, measurements on n-$C_{23}H_{48}$ were performed at a different temperature (next section).

10.3.6 Effect of cooling the specimens on crystal growth/etching

In order to verify the temperature dependence of the growth/etching behaviour, the experiments were repeated for a cooled sample containing n-$C_{23}H_{48}$ crystals. For that purpose, the cooling cell described in the *experimental* section was used. In order to be able to get undisturbed images, the water flow through the cell had to be stopped during scanning. Nevertheless, due to the buffering action of the copper cell itself and the water in it, the sample could be cooled down to about $T_{sc}=$ 20 C permanently during imaging, compared to the $T_s=34$ C without cooling.

This cooling resulted in images in which growth and etching still were observed. However, the growth and etch rates decreased one order of magnitude. An example showing a pair of islands growing very slowly is given in fig. 10.7. During two hours of observation, the maximum step growth rate observed was 0.4 nm/s, while many parts of the island edges did not grow at all. The average layer growth speed of the islands is 0.1 ML/hr, which is much lower than the typical 2 ML/hr (fig. 10.3) or the 1 ML/hr (fig. 10.4) for growth at not cooled crystals.
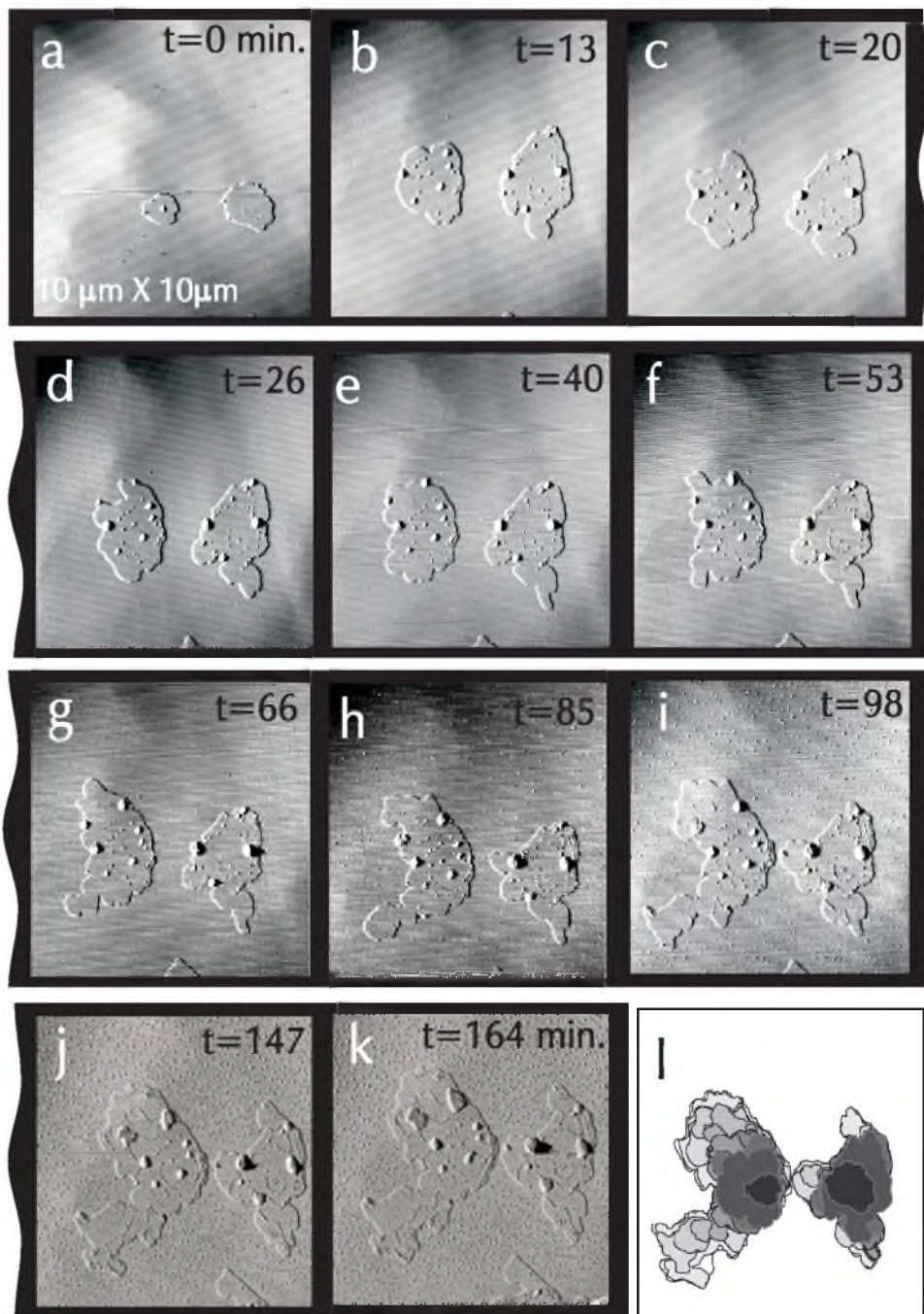
Figure 10.7 (a-k) A few pictures from a 3 hours series of AC-AFM images recorded at approx 20 C, showing the slow growth of two islands of monomolecular height. In the pictures the time of imaging relative to fig. 7a is indicated in minutes. Besides the slowly expanding islands, small nuclei are developing everywhere and bigger three-dimensional nuclei are formed on the islands. (l) Map indicating the growth of the islands in time: The dark parts are the oldest parts, the white part is the newest part. Some crystal areas are seen to be severely hindered in growth, while other parts expand freely. Step speeds vary from 0 nm/s for pinned steps to 0.4 nm/s for the fastest growing steps. The recording time of each scan is 6.5 minutes. All images are sized 10 μm x 10 μm. Amplitude setpoint is 84% of cantilever oscillation amplitude in free air.

Besides the largely decreased crystal growth/etching at lower temperatures, other interesting features can be discerned from these experiments. This is illustrated in fig. 10.8, which is an enlarged view of image k) from the series given in fig. 10.7. All over the islands, thin, stable ridges can be seen which actually mark their former edges. Furthermore, small nuclei with a height of about one molecular layer are found everywhere, as well as a few large, three-dimensional nuclei on the islands. The small nuclei are stable and their number increases with time (fig. 10.7). Some of the large nuclei get flattened, which is visible in fig. 10.8.
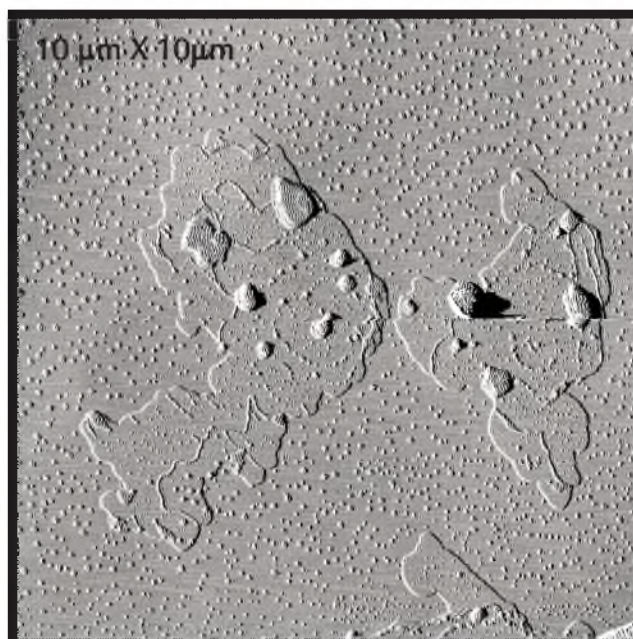
Figure 10.8 Image (k) of the low temperature series shown in fig. 7, displayed on a larger scale. Ridges of about 5 nm in height on former island border positions are clearly resolved. Furthermore, some of the larger three-dimensional nuclei present on the islands are seen to 'flatten out' and get a molecularly flat surface.

10.4 Discussion

10.4.1 Growth and etching mechanism

The 'etching' as observed in the CM-AFM images is caused by the shear forces exerted by the tip on the paraffin crystal surface. This wear is not unusual for soft crystals. It has been observed for mercuric iodide [4] and LB films [5] as well. The fact that in all images the surface remains molecularly flat, even at the bottom of the square hole created in fig. 10.1 indicates that either the etching occurs in a layer-by-layer way, or that the ploughed surface rearranges quickly in an ordered, crystalline way.

In the case of AC-AFM, a shear force is no longer present, which is confirmed by the rounded shape of the 2D holes and islands in figs. 10.2 and 10.3. Instead, a normal force is exerted by the oscillating tip on the surface, which, in the case of etching, results in removal of molecules from the crystal, preferably from the step edges (fig. 10.2), followed by a nett flow of these molecules from the surface to the tip. Growth of the crystal is observed as well and is associated with a nett flow of molecules from the tip to the crystal. The central role of the AFM tip in the growth/etching is proven by the

linescans (fig. 10.6), which indicate that the growth/etching occurs only in a region of 1 - 10 μm^2 around the tip. Moreover, zoom-out pictures after repeated etching, resp. growth, scans in general do not show growth, resp. etching, around the original scan area. This indicates that molecules do not migrate over the crystal surface from or to the scanned region, excluding any long-range surface diffusion at this timescale. The similar behaviour of solution-grown and vapour-grown crystals excludes any effect of a solution layer possibly present on the solution-grown crystals. The only conclusion left is that molecules are transported to and from the tip. Because growth or etching is found for every n-$C_{23}H_{48}$ experiment, irrespective of the AFM settings and the type of AFM, we conclude that this transport, irrespective of its direction, always occurs during imaging. The only factor that is found to influence the direction of this mass flow is the tip. For new, clean tips there is often a flow towards the tip, resulting in etching of the surface; for tips used before or that have experienced tip crashes crystal growth is dominating, which must be caused by a paraffin flow fro the tip towards the crystal.

The effect of the melting temperature of the paraffin is clearly shown by the comparison of measurements on n-$C_{19}H_{40}$ (melting point $T_m=32$ C), n-$C_{23}H_{48}$ ($T_m=47$ C) and n-$C_{40}H_{82}$ ($T_m=82$ C) and the 'global' scanning temperature $T_s = 34$ C. Moreover, for the only n-paraffin found in literature on which AFM is applied, n-$C_{33}H_{68}$, with a high melting point of $T_m =71$ C [18], no growth or etching is reported [19], just as for the case of n-$C_{40}H_{82}$ [17]. If a n-paraffin crystal is scanned at or just below its melting temperature, imaging becomes impossible; if a sample is scanned well below its melting point no growth/etching is observed; only if a n-paraffin crystal is scanned about 10 - 20 C below its melting point the characteristic growth/etching takes place. This temperature dependence is once more illustrated by the cooling experiment, where scans on a n-$C_{23}H_{48}$ crystal cooled down to 20 C result in a largely decreased growth/etching behaviour as compared to the experiments without cooling.

The facts that growth and etching occur in such a controlled way that imaging is possible, and that growth takes place layer-by-layer, strongly suggest that n-paraffin is present in a fluid state mother phase. Since the presence of a remainder of solution is excluded, and dissolution in a water layer present on the crystal surface can be disregarded as well because of the low solubility of paraffins in water, this fluid in the AFM tip region must be a melt. The 'global' scanning temperature of $T_s = 34$ C, which is caused by the heat produced by the light bulb and the laser, is not enough to melt the crystal (in that case scanning would have become impossible, as in the n-$C_{19}H_{40}$ case). The very local temperature increase needed for melting in the tip region is probably introduced by the laser beam focussed on the cantilever end.

All of the observations given above lead us to propose the following mechanism of tip-induced etching and growth. In both cases there exists a bridge of liquid n-paraffin between tip and sample

and around the tip. This is created by the combined action of *i)* local melting caused by heat from the laser beam focussed on the cantilever end, which is transferred to the tip and the crystal, and *ii)* capillary forces causing the liquid bridge to follow the tip. In a steady state, a certain equilibrium amount of liquid n-paraffin sticks to the tip. This amount depends on the scanning temperature, the melting temperature of the n-paraffin and not or very little on the scan parameters, such as amplitude setpoint/tip-sample distance and scan speed. If the tip is still clean, there is a nett flow of molten paraffin to the tip in order to reach an equilibrium state, and etching occurs (fig. 10.9, left side). Because at step edges molecules are relatively weakly bound, layer-by-layer removal will be favoured over 2D nucleation etching, and certainly over 3D etching, as can be seen in fig. 10.2. When a tip is retracted after a scan, adhesive forces can lead to large holes in the surface resulting in large amounts of paraffin sticking to the tip. The same can happen at a tip approach. Large holes and debris around it have indeed been observed. If the amount of n-paraffin sticking to the tip is larger than the equilibrium amount, there will be a nett flow from tip to surface and growth will occur (fig. 10.9, right side). From the growth and etch rates of the figures, the flow rate to or from the tip is calculated to vary from $2 \cdot 10^4$ nm^3/s ($4 \cdot 10^5$ molecules/s) for fig. 10.2 and $+2 \cdot 10^5$ nm^3/s ($4 \cdot 10^6$ molecules/s) for fig. 10.5 to $+1 \cdot 10^7$ nm^3/s ($2 \cdot 10^8$ molecules/s) for fig. 10.3.

In case of growth, n-paraffin flowing from the tip to the crystal crystallizes in different ways. In most cases a remarkably regular layer-by-layer crystal growth in the form of filling holes (fig. 10.2), 2D nucleation (fig. 10.3), spiral growth (fig. 10.4) or step growth (figs. 10.5, 7) occurs. Sometimes portions of paraffin that are released from the tip lead to 10 nm - 100 nm sized particles, as are present in figs. 10.2 and 10.8. In cooling experiments large 3D nuclei are formed as well (figs. 10.7, 8), which can slowly flatten in time (fig. 10.8). These 3D nuclei may represent 'drops' of paraffin flowing from the tip which have crystallized before they could spread out in a 2D way, because of the lower temperature in the cooling experiments.

The origin of the ridges at the positions of former island borders observed in cooling experiments (e.g. fig. 10.8) is not yet understood. A possible explanation is that the molecules at the edges are not correctly oriented. When the tip comes by for a new image, it delivers new n-paraffin which crystallizes at the edges of the existing island. In contrast to the experiments without cooling, now the temperature is too low to overcome the activation barrier necessary to correct the wrongly oriented molecules at the edge. This leads to the chaotic border patterns that get 'frozen in' into the island. Whatever their cause may be, the ridges again prove that the crystal growth is not a continuous process, but only occurs when the tip passes the surface region in question.

An estimate of the minimum amount of liquid n-paraffin stored in the tip-sample bridge can be derived from the amount of material deposited or etched away during a series of scans. For growth these volumes range from 0.3 μm^3 (fig. 10.7) to 16 μm^3 (fig. 10.6d). In case of etching these are -0.2
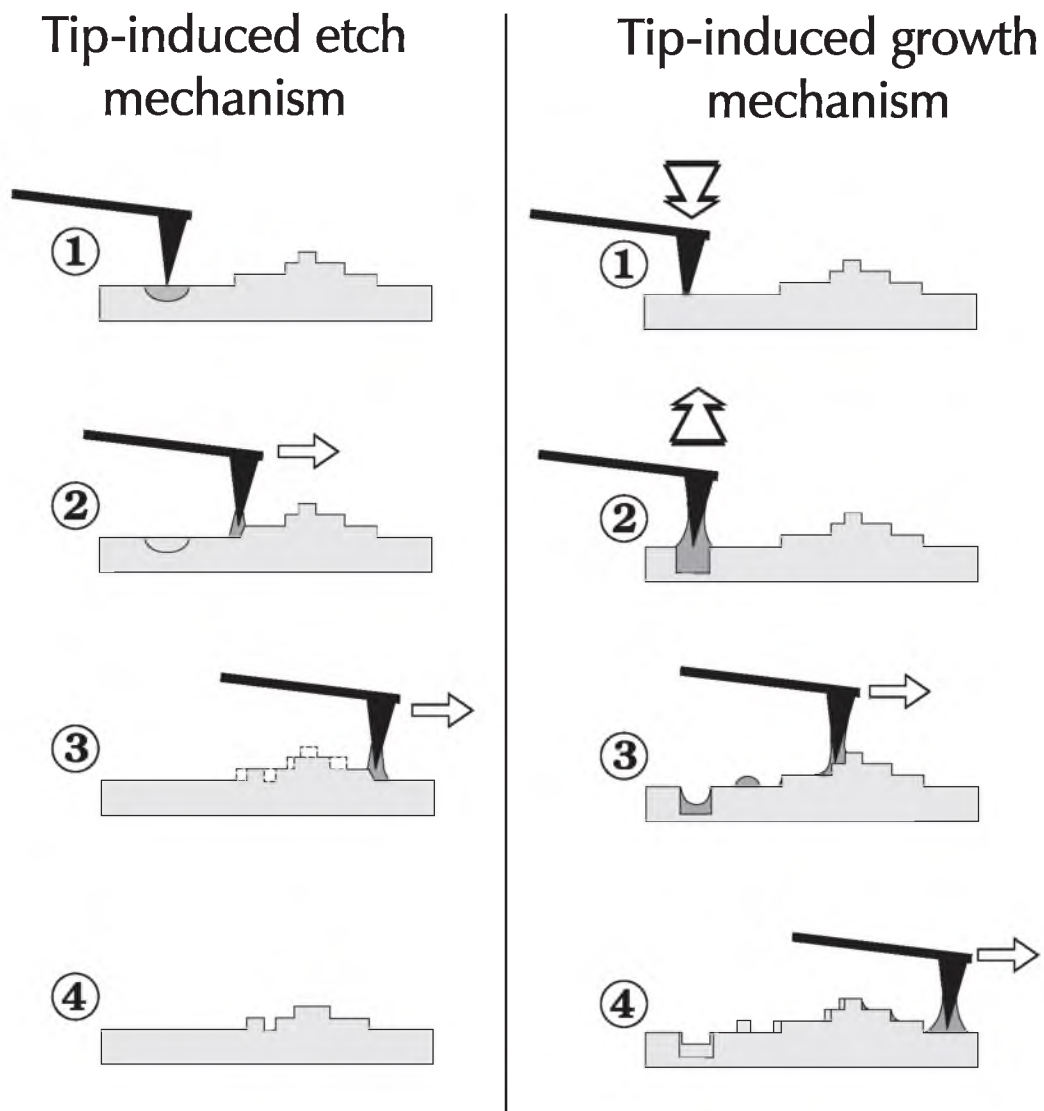
Figure 10.9 Model for tip-induced crystal etching (left) and growth (right). In case of etching the clean tip locally melts the surface (1). If the tip moves further, the surface solidifies again, but due to adhesive forces some molten paraffin is taken away by the tip (2). This effect will be greatest at step edges, because here the solid molecules melt most easily away, because no activation barrier for 2D nucleation has to be overcome (3). The nett effect of the tip-sample interaction will be etching (4).

In case of growth, the scanning starts with a tip covered by paraffin captured during a former scan or due to a rough tip approach making a large hole in the sample (1, 2). In the latter case, most of the paraffin will stay in the hole and recrystallize, but some of it will be transported elsewhere by the tip (3). This surplus of molten paraffin is delivered in a relatively regular way at the surface, preferably at step edges (3) where it crystallizes (4), leading to step growth and the formation of 2D nuclei.

μm^3 (fig. 10.2) and -2 μm^3 (fig. 10.6c). If an average section of 4 μm^2 for the liquid bridge is assumed from the linescan experiments (section 10.3.4), an amount of 15 μm^3 paraffin adhering to the tip now corresponds to a height of the liquid bridge of 4 μm. Since this 15 μm^3 is a minimum estimate, the bridge will probably be higher. The estimated bridge size seems reasonable comparing it with the tip size: The silicon tips are conically shaped with a base of 3-6 μm and a height of 10-20 μm (Topometrix [20]) respectively 10 μm (Digital [21]).

The amplitude of the cantilever in free air is about 40 nm; during imaging it is about 80% of that value. In 'normal' AC-AFM, the tip is in (repulsive) contact with the sample only during a part of its oscillation cycle. During the rest of the cycle there are some attractive forces (capillary forces, van der Waals forces) present. Depending on the relative contributions of repulsive and attractive forces, imaging can occur in a pure attractive mode or in a partly repulsive, partly attractive mode (e.g. [22, 23]). Because of our estimated minimum liquid bridge size, which exceeds the cantilever amplitude by far, we conclude that in the case of the AC-AFM imaging of n-$C_{23}H_{48}$, the tip is surrounded by liquid paraffin during the whole cycle. This probably causes the imaging being in an attractive mode all the time, because of the capillary forces present. From this it is suggested that the tip is never tapping on the solid part of the crystals or penetrating into them during stable imaging, and is more or less stabilized by the liquid bridge, which can explain the stable way of imaging observed.

10.4.2 Crystal growth features

The ex situ growth and etching processes elaborated in this work cannot be regarded simply as a case of 'normal' in situ crystal growth/etching in a melt. Nevertheless, the AFM-induced melting or growth acts in such a regulated way that its behaviour provides essential information on the mechanism of melt growth. In situ AFM observation of real melt growth experiments probably will never be carried out because of the necessary temperature control within 0.001 C.

The generally rounded shape of 2D holes, 2D islands, spirals and steps present on the n-$C_{23}H_{48}$ crystals reflects a complete lack of the influence of crystal symmetry on step propagation, contrasting the observations of solution-grown n-$C_{40}H_{82}$ crystals, which show a step pattern reproducing the macroscopic, lozenge shape crystals with {110} side faces [17]. This lack of symmetry is caused by a higher density of kink sites at the steps, introduced by i) the experimental temperature being close to the melting point of the crystals and ii) the high supersaturation during the fast crystallization of the liquid paraffin coming from the tip. Observation of crystals growing from the melt by optical microscopy showed completely roughened side faces for n-$C_{23}H_{48}$ crystals, even when growth occurred at only 0.01 C below the melting point T_m=47 C [24]. Assuming a similarity between the relatively high steps on the {001} face and the narrow side faces of the crystals, this is in agreement with the present observations.

An interesting parameter that can be calculated from the AFM measurements is the critical radius r_c for two-dimensional nucleation growth (e.g. [25]). This cannot simply be measured from the smallest nuclei present in fig. 10.3, because these nuclei are directly created by the tip-sample transfer. More reliable ways to calculate r_c for this case are [26] i) measurement of the radius of the curved step near a spiral centre; ii) measurement of the distance between spiral arms d_s far away from the centre, which according to the Cabrera-Levine theory [25] equals

$$d_s \quad 19r_c \quad . \tag{10.2}$$

When these measurements are carried out for the spiral of fig. 10.4, r_c=0.3 μm and r_c=0.2 μm are obtained by methods i) and ii) respectively. This r_c indicates a critical nucleus containing about 500,000 molecules.

The single spiral of fig. 10.4 consists of one step, indicating a screw component of the dislocation burgers vector equal to $\frac{1}{2}$ c, because the orthorhombic Pbcm, Z=4 unit cell consists of two layers each one molecule high. This implies that after each turn of the spiral the crystal structure does not fit anymore, and some kind of stacking fault has to be created, which is not observed. One possible explanation is that the crystals are in the rotator crystalline state, in which the molecules have large rotational freedom and the unit cell consists of only one layer of one molecule in height. However, the rotator phase only exist between 40.6 C and the melting point [18], so in the present case this phase is expected to be only a temporary state in the melting-recrystallization process during the tip passage: at the tip position the top layer of the crystal locally melts. After passage this melt recrystallizes via the rotator phase into the orthorhombic phase. Deeper layers do not melt and stay in the orthorhombic phase. Another reason to question the rotator phase explanation is the observation of dislocation burgers vectors of $\frac{1}{2}$ c on orthorhombic Pca2$_1$, Z=4 n-C$_{40}$H$_{82}$ crystals [17]. n-C$_{40}$H$_{82}$ has a melting point of T_m=82 C and will therefore never be in the rotator phase. Nevertheless, both in the n-C$_{40}$H$_{82}$ study and in the present study no evidence was found for the occurrence of stacking faults, which should be associated with the occurrence of partial dislocations. The paper on n-C$_{40}$H$_{82}$ [17] discusses this issue in more detail.

The pinning shown in figs. 10.4, 5 and 7 is another phenomenon encountered during the AFM-induced crystal growth. In all cases, no visible pinning points could be discerned, indicating that these are of molecular scale. The blocking centres could be formed by homologs (e.g. n-C$_{21}$H$_{44}$ or n-C$_{25}$H$_{52}$) which do not fit in the n-C$_{23}$H$_{48}$ crystal lattice, thereby hindering growth. In fig.10.5, the pinning action diminishes in course of time, implying burying of the pinning points. This indicates that growing n-paraffin crystals can overcome the presence of homologs by incorporating them into the lattice. As the 'driving force' is lower for the cooling experiments, the pinning points of fig. 10.7

are overcome with more difficulty.

Fig. 10.2 shows the occurrence of accelerated etching when two 2D holes meet, in order to minimize the step energy. A special kind of step energy minimization is also illustrated in this figure in the form of a 2D Oswaldt ripening effect. During scanning as well as during the 20 h and 50 h breaks the smaller holes disappear, while the larger holes increase in size.

The rearrangements during the breaks indicate that without any scanning the n-paraffin molecules still have some mobility. So, besides the scan-induced growth/etching, there is also some 'natural' surface diffusion taking place. However, this diffusion is such slow that it can be neglected in the description of the scan-induced phenomena observed.

10.5 Conclusions

The surfaces of solution-grown n-$C_{23}H_{48}$ (T_m=47 C) crystals showed both crystal growth and etching upon ex situ AC-AFM scanning. Based on line-scan experiments, cooling experiments and comparison with vapour-grown n-$C_{23}H_{48}$ crystals as well as n-$C_{19}H_{40}$ (T_m=32 C) and n-$C_{40}H_{82}$ (T_m=82 C) crystals, it was concluded that both growth and etching occur via material exchange with a liquid present around the AFM tip. This liquid bridge, which has a volume of at least 15 μm^3, is formed by local melting of the surface due to heat from the laser spot focussed on the cantilever end and the presence of capillary forces around the tip. If the tip bridge contains an amount of paraffin larger, resp. smaller, than a certain equilibrium value, a nett flow of paraffin to, resp. from, the sample occurs and crystal growth, resp. etching takes place. The nett flow between tip and sample is of the order of 10^7 to 10^8 molecules/s depending on the experimental conditions. The direction of the flow, corresponding to crystal growth or etching, could only be influenced by the use of clean tips or already used and crashed tips, which induce a nett flow towards and from the tip, respectively.

This phenomenon presents an excellent opportunity to study melt growth on a molecular scale, which would not have been possible in 'real' AFM in situ experiments. Despite the difference from 'real' melt growth, the current system behaves remarkably similarly. Formation of 2D islands, 2Dholes, growing step trains and spirals were observed. The rounded shape of the step patterns corresponds to the rounded, roughened crystal side faces observed previously during melt growth experiments using optical microscopy. In addition, a two-dimensional Oswaldt ripening effect and an AFM-independent surface diffusion were noticed. Furthermore, the incorporation of impurities could be followed, a process that is accompanied by the occurrence of step pinning diminishing in time. Finally, the size of the critical nucleus r_c was calculated from a growing spiral.

Acknowledgments

References

[1]   M. Plomp, J.G. Buijnsters, G. Bögels, W.J.P. van Enckevort, submitted for publication, 1999.

[2]   H. Shindo, M. Ohashi, K. Baba and A. Seo, Surface Science **111-114** (1996), 357.

[3]   M. Plomp, K. Maiwa and W.J.P van Enckevort, J. Crystal Growth **198/199** (1999), 246.

[4]   H.P. Lang, A. Rossberg, M. Piechotka and E. Kaldis, J. Crystal Growth **144** (1994), 371.

[5]   M. Fujihira and J. Takano, J. Vac. Sci. Technol. B **12** (1994), 1860.

[6]   S. Yamamoto, H. Yamada and H. Tokumoto, Jpn. J. Appl. Phys. **34** (1995), 3396.

[7]   L.L. Sohn and R.L. Willett, Appl. Phys. Lett. **67** (1995), 1552.

[8]   S.W. Park, H.T. Soh, C.F. Quate and S.-I. Park, Appl. Phys. Lett. **67** (1995), 2415.

[9]   R.D. Piner, J. Zhu, F. Xu, S. Hong and C.A. Mirkin, Science **283** (1999), 661.

[10]   W.R. Turner, Ind. Eng. Prod. Res. Develop. **10** (1971), 238.

[11]   R. Boistelle, in: E. Kaldis (ed.), *Current Topics in Materials Science, Volume 4, chapter 8*, North-Holland, 1980.

[12]   L.J.P. Vogels, P.J.C.M. van Hoof, R.F.P. Grimbergen, J. Cryst. Growth **191** (1998), 563.

[13]   C.A.J. Putman, K.O. van der Werf, B.G. de Grooth, N.F. van Hulst, J. Greve, P.K. Hansma, SPIE **1639** Scanning Probe Microscopies (1992) 547.

[14]   W.A. Ducker, R.F. Cook and D.R. Clarke, J. Appl. Phys **67** (1990), 4045.

[15]   T.A. Land, J.J. De Yoreo, J.D. Lee, Surface Science **384** (1997), 136.

[16]   M.G. Broadhurst, J. of Research **66A** (1962), 241.

[17]   M. Plomp, P.J.C.M. van Hoof, W.J.P. van Enckevort, submitted for publication.

[18]   G.S. Parks, H.M. Huffman and S.B. Thomas, J. Am. Chem. Soc. **52** (1930), 1032.

[19]   K. Matsushige, T. Hamano and T. Horiuchi, J. Crystal Growth **146** (1995), 641.

[20]   Topometrix, numbers for the high-resonance cantilever E (model # 1650-00).

[21]   Digital, numbers for tapping-mode OTESPA cantilever.

[22]   B. Anczykowski, J.P. Cleveland, D. Krüger, V. Elings and H. Fuchs, Appl. Phys. A **66** (1998), S885.

[23]   A. Kühle, A.H. Sørensen, J.B. Zandbergen and J. Bohr, Appl. Phys. A **66** (1998), S329.

[24]   P.J.C.M. van Hoof, R.F.P. Grimbergen, H. Meekes, W.J.P. van Enckevort and P. Bennema, J. Cryst. Growth **191** (1998), 861.

[25]   N. Cabrera and M. Levine, Phil. Mag **1** (1956), 450.

[26]   P. Bennema, J. Crystal Growth **69** (1984), 182.

Chapter 11:

A 2D Hartman-Perdok analysis of polymorphic fat surfaces observed with atomic force microscopy

Chapter 11:

A 2D Hartman-Perdok analysis of polymorphic fat surfaces observed with atomic force microscopy

F.F.A. Hollander, M. Plomp, C.J. van de Streek and W.J.P. van Enckevort

RIM Laboratory of Solid State Chemistry, Faculty of Science,
University of Nijmegen, Toernooiveld 1, 6525 ED Nijmegen, The Netherlands

Abstract

The surfaces of pure triacylglycerol crystals of polymorphic type β (16.16.16) and β' (16.18.16) are studied *ex situ* using atomic force microscopy. Molecular resolution images show no reconstructed surfaces. On both types of triacylglycerol crystals, the overall 3D morphology is reflected in the shape of the monomolecular step patterns on the large {001} faces. The shape of the observed 2D nuclei and growth spirals on these faces can be explained by a combination of a two-dimensional Hartman-Perdok analysis based on the topology of the crystallographic surface structure, and the theory of Burton, Cabrera and Frank. For the β polymorph, extended sub-steps with half the molecular height were found, which are related to planar faults in the crystal and do not act as growth source. Melt grown β' crystals sometimes show vicinal {10*l*}-faces, which indicates a strong interaction between closely separated steps.

Keywords: Hartman-Perdok, 2D morphology, fat, polymorph, AFM.

11.1 Introduction

One of the most important components used in food industry is fat. The physical properties that determine taste, mouth feel and spreadability of the consumer product are mainly determined by the chemical composition of the fat mixture, the polymorph and the morphology of the fat crystals. Fat crystals occur in three different crystal structures, which are called, according to increasing stability, the α, β' and β polymorph [1]. The third polymorph is, for example, important in chocolate, while the β' polymorph is mainly used in margarine.

All fat molecules or triacylglycerols (TAGs), are esterifications of three different fatty acids (R_1, R_2 and R_3) with glycerol. Therefore, we can abbreviate the nomenclature of the TAGs by indicating merely the fatty acids used [2], i.e., $R_1.R_2.R_3$. For example, this leads to 16.16.16 for tripalmitate, which is an esterification of palmitic acid ($C_{15}H_{31}COOH$) and glycerol. In food industry always a mixture of various TAGs is used. In this study however, we shall restrict ourselves only to the crystal morphology of pure 16.16.16 and 16.18.16 TAGs, which crystallise in the β and β' polymorph respectively.

The β polymorph is a member of the homologous series of $n.n.n$ TAGs, where n is even and $10 < n < 24$, of which the crystallographic structure has been elucidated recently [3]. The crystal setting used is this paper is the same as the one used earlier [4].

The crystallographic structure of 16.18.16, which belongs to another homologous series of $n.n+2.n$ TAGs is, despite a lot of effort to solve it, still unknown. The problem in elucidating this structure is the presence of micro-twinning in the grown crystals [5]. The space-group of this series of TAGs is pseudo-orthorombic, (p-Ib2a), because   is close to 90 . Based on the suggestions Birker made in his paper and using elements from other alkane chain containing structures, van de Streek [6] constructed a molecular structure of this series by application of molecular mechanics. This trial structure lead to calculated powder spectra comparable with the experimental ones. In an identical way, van Langevelde et al. [7] derived an alternative packing concept for this β'-polymorphic series. The main difference between both models is that van de Streek suggested a folded molecule, while van Langevelde et al. proposed a straight molecule. The unit cell parameters of both TAGs used are given in table 11.1.

In this study, firstly the two-dimensional equivalent of the Hartman-Perdok (2D-HP) theory [8] is derived. Next, the surface morphology, of the {001} surfaces of both 16.16.16 and 16.18.16 is calculated using this theory. To make this HP analysis useful, the surface structure is verified to be identical to the bulk crystallographic structure by molecular resolution imaging of the {001} face by Atomic Force Microscopy (AFM). Hereafter, the morphology of the step patterns, such as growth

spirals and 2D nuclei and some other remarkable observed features also observed by AFM on both TAGs are described. In the last section, the actual comparison between the calculated and observed growth spirals is presented.

Table 11.1. Bulk and surface unit cell parameters of both the β (16.16.16) and β' (16.18.16) TAGs used.

| TAG	cell type	a [Å]	b [Å]	c [Å]	α [ ]	β [ ]	γ [ ]	Symm.	Z
16.16.16	bulk	13.91	5.46	46.95	106.9	121.1	57.7	P-1	2
	surface	13.91	5.46				57.7		2
16.18.16	bulk	22.8	5.43	86.58	90	89	90	p-Ib2a	8
	surface	12.6	5.43				65.5		2

11.2 Surface Hartman-Perdok theory

The HP-theory offers the most appropriate way to predict the morphology of a crystal from its crystallographic structure [8]. This theory is based on the concepts of Periodic Bond Chains (PBCs) and connected nets. Since more than a decade, this theory is extended with the thermodynamic and statistical mechanical concepts of roughening temperature [9, 10]. A PBC can be considered as a continuous, periodic chain of *inter*-molecular interactions, or bonds, with an overall direction [*uvw*]. A "connected net" is now defined as a two-dimensional network of interconnected PBCs within a slice d_{hkl}. Below a critical temperature, the so-called roughening temperature, faces parallel to the connected net grow layer-wise involving steps. Such faces are denoted as F-faces. The bonds making up the PBCs and connected nets are normally calculated using computational chemistry choosing a suitable force field. The energy-sum of all bonds per mol within the connected net is the slice energy (E_{slice}). All bonds that are interconnecting the individual connected nets make up the attachment energy (E_{att}). The total crystal energy (E_{cryst}) is the sum of E_{slice} and E_{att}. In the HP-theory, it is then assumed that the F-faces {hkl} that have the lowest E_{att} are the ones that appear on the growth morphology. Recently a series of papers [11-13] was published that shows the key role of the actual connected net topology on the morphology of the crystal. In this series of papers, it is shown that for each face {hkl} to appear on the morphology, besides being parallel to a connected net and having a low attachment energy, the topology of connected net must lead to considerably high step energies. Such high step energies make the formation of new growth layers the rate limiting step in the growth process. This very important concept was shown to be essential for the morphology prediction of $n.n.n$ TAG crystals [4]. In the following section a two-dimensional variant of the HP

theory (2D-HP) will be derived and applied to the step patterns on the surfaces of β and β' TAG crystals.

11.2.1. Analogy of 2D-HP and 3D-HP theory

Like for the three-dimensional morphology, the same concepts of the HP theory can be used to predict the two-dimensional morphology of islands and growth spirals present on crystal surfaces [14,15]. In doing this it is assumed that growth is not limited by surface or volume diffusion, but by processes occurring at the growth steps. Carrying out a 2D-HP analysis of a given crystal surface starts with the selection of the most stable connected net parallel to this face, which is obtained from a 3D-HP analysis. Like in the 3D-HP analysis, the crystallographic structure is reduced to a 2D surface graph in which "connected chains" (in fact PBC's!) making up the connected net are identified. The bulk crystallographic structure can only be used if the surface of interest is not reconstructed. The connected chains with Miller indices (hk) and direction $[uv]$ must be located within a line width δ_{hk}, which is the 2D equivalent of the slice thickness d_{hkl}. Here (hk) must be corrected for the selection rules of the 2D space group of the connected net. It must be noted that the direction of the chain, $[uv]$, is perpendicular to (hk), i.e. $[uv].(hk) = 0$. In this paper we will only use the $[uv]$ indices to indicate the steps. The slowest propagating steps on a crystal are parallel to these connected chains and will be denoted as f-steps in the following. For example, as shown in fig. 11.1, the (001) F-face of a Kossel crystal contains 2 PBC's, being parallel to [100] and [010] (which are [10] and [01] in a 2D setting). Therefore, the steps on this face are expected to be parallel to these directions, leading to square shaped step patterns. The line thicknesses δ_{10} and δ_{01} are equal to the unit axis length.
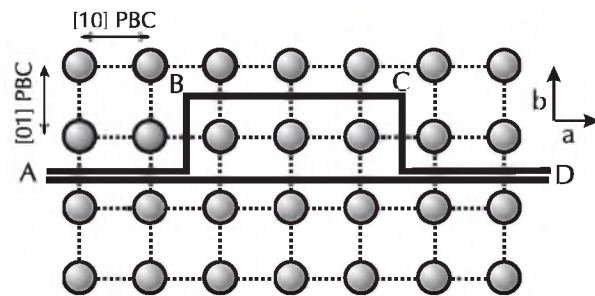
Figure 11.1 Top view of the {001} surface of a Kossel crystal showing two steps, ABCD and AD, of which the first step contains one kink up and one down. The kink energy E_{kink} is half the difference of the broken bond energies of both step lines.

Using the analogy of the connected chain and the connected net in 2D-HP and 3D-HP theory respectively, one can introduce an equivalent for $E_{cryst} = E_{att} + E_{slice}$. Namely,

$$E_{slice}^{h\,k\,l} \qquad E_{step}^{hk} \qquad E_{chain}^{hk} \qquad\qquad (11.1)$$

Here, E_{chain}^{hk} is the sum of the bonds per stoichiometric unit within the line width δ_{hk} in the slice $d_{h'k'l'}$ (2D analogue of E_{slice}). E_{step}^{hk} is the sum of the bonds within the slice $d_{h'k'l'}$ that interconnect adjacent chains in the slice (2D analogue of E_{att}). The kink energy, E_{kink}^{hk}, is defined as the energy of the "cheapest cut" through the connected chain (hk) and gives the energy of the most favourable kink site in the step for a vacuum-solid system. Note that certain connected net topologies sometimes require the use of the difference of two bonds instead of a single bond energy to calculate E_{kink}^{hk} [11, 4]. Therefore, E_{kink}^{hk} is not always directly related to the calculated bond strengths that make up the kinks. Secondly, using the proportionality condition formulated by Bennema [10], one can estimate the effective kink energy in a solid-fluid system in stead of a vacuum-solid system, according to

$$\Phi_{kink} \kappa \frac{E_{kink}}{E_{cryst}} \Delta H \quad , \tag{11.2}$$

where ΔH is the heat of melting or dissolution and κ is a measure for wetting of the fluid phase to the crystal surface. In fact, κ is similar to the constant introduced by Liu et al. [16] for calculating effective bonding energies at the surfaces of paraffin crystals. If the interaction of solvent molecules with the crystal surface is identical to that with solute molecules in the liquid, then $\kappa = 1$, which is indicated as "equivalent wetting" [10].

Using the concepts of E_{step}, E_{kink}, Φ_{kink} and δ_{hk} one can define criteria for the morphological importance (MI) of steps on a crystal surface. Like in the 3D-HP theory, the dominant step directions must be parallel to a connected chain, i.e. a PBC. To establish criteria for the MI of the various f-steps on a crystal surface one can take resort to a 2D equivalent criterion of Bravais Friedel Donnay Harker (BFDH) criterion as well as to the classical growth criterion used in the HP theory [16]. These are respectively:

$$(i) \qquad v_{step}^{hk} \quad \frac{1}{\delta_{hk}} \qquad (BFDH) \tag{11.3}$$

$$(ii) \qquad v_{step}^{hk} \quad E_{step}^{hk} \qquad (HP) \tag{11.4}$$

The second criterion is known as the *growth* form of the crystal. Sometimes this criterion is multiplied by $_{hk}$, which results in the *equilibrium* form, because it represents the shape with the lowest line energy [8]. However, this criterion normally leads to more isotropic shapes compared to the growth form this criterion is not used in our analysis. Since growth steps are always rough at $T > 0K$, criteria based on the roughening temperature cannot be used. However, in comparision to the overall

growth of a crystal surface, the propagation of a single step is less complicated and a third criterion based on step kinetics can be derived. If we now assume that the rate-limiting step for crystal growth is the direct integration of growth units in a step, then the step velocity v_{step}^{hk} is proportional to the kink density, n_{kink}^{hk} [17,18], or:
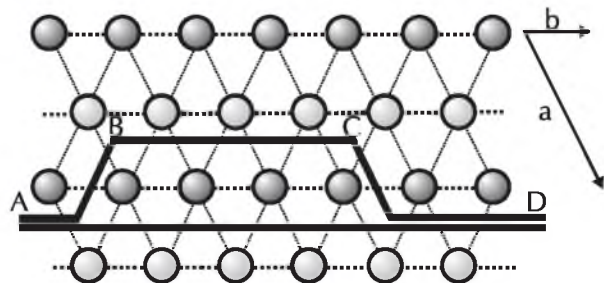
$$v_{step}^{hk} \quad \frac{kT}{h}\chi.\exp(-\frac{\Delta G_{hk}}{kT}).n_{kink}^{hk}.\frac{\Delta\mu}{kT}.\delta_{hk} \quad , \tag{11.5}$$

where T is temperature, and h and k are the Planck and Boltzmann constants respectively. ΔG_{hk} represents the activation barrier for the addition of a growth unit at a kink position and χ is the mole fraction of growth units in the liquid. Here it is assumed that for a given f-step only one type of kink is dominant and determines the step propagation.

Using the connected chain topology found by the 2D HP theory, n_{kink}^{hk} can be estimated using a similar expression as derived for Kossel-like crystals by Burton, Cabrera and Frank [19]. Assuming polygonized step patterns, which means that Φ_k is larger than two times kT, for an f-step n_{kink}^{hk} can be approximated by

$$n_{kink}^{hk} \quad 2\exp(-\frac{\Phi_{kink}^{hk}}{kT}) \tag{11.6}$$

A broken bond model based on the 2D crystal graph can be used to calculate Φ_{kink}^{hk}. For the {100} surface of a Kossel crystal as shown in fig. 11.1, the difference in broken bond energy of the lines ABCD and AD equals twice the bonding energy, φ, between adjacent growth units. Since the kinked step ABCD contains one kink up and one kink down, this implies that $\Phi_{kink}^{01} \quad \varphi$. In the case of fat crystals, a similar figure as 11.1 is given in fig. 11.2. Here, it can be seen that only the bonds along the b-axis add to the kink energy, because the other bonds are cut in an equal amount for both steps AD and ABCD.

The f-steps correspond to the step directions with a minimum in kink density and thus coincide with the minima in the 2D (kinetic) Gibbs-Wulff plot, which relates step energy/velocity to step orientation. Therefore, f-steps determine the shape of growth spirals and 2D nuclei. The relative velocities of f-steps on a given crystal surface can be calculated using relation (11.6). Compared to

Figure 11.2 Schematic projection of the {001} surface structure of both TAGs, from which E_{kink} can be calculating the broken bond energies of the lines ABCD and AD. Line ABCD represents a straight step with a kink-up and a kink-down.

a reference f-step, REF, an f-step with direction (hk) and thickness $\square_{hk}$ advances at a rate of

$$
(iii) \qquad v_{step,rel}^{hk} \quad \frac{n_{kink}^{hk}\delta_{hk}\exp(\ \Delta G_{hk}/kT)}{n_{kink}^{REF}\delta_{REF}\exp(\ \Delta G_{REF}/kT)} \qquad (\text{HP-BCF}) \qquad (11.7)
$$

$$
\exp(\frac{\Phi_{kink}^{REF}}{kT}\ \frac{\Phi_{kink}^{hk}}{kT}).\exp(\frac{\Delta G_{REF}}{kT}\ \frac{\Delta G_{hk}}{kT}).\frac{\delta_{hk}}{\delta_{REF}} \quad ,
$$

This third criterion for the MI of steps is based on the PBC topology found by the 2D-HP theory and the BCF theory, and is therefore called HP-BCF.

Using the relative velocities of the various f-steps for a given two-dimensional connected net and assuming, $\Delta G_{hk} \quad \Delta G_{REF}$, the final shape of the islands and spirals can now be calculated using the Gibbs-Wulff construction [20], as can be done for the other two criteria.

11.2.2 The 2D-HP analysis of the {001} face of 16.16.16 and 16.18.16

To calculate the 2D-HP morphology, first the set of bonds which makes up the surface graph has to be selected. Analogous to the 3D crystal graph the molecules are reduced to their centres of mass and the bonds between these centres represent their mutual $inter$-molecular interactions. It should be noted that due to the selection rules of the space groups P1and pseudo-Ib2a the slice thickness is d_{001} for 16.16.16 and d_{002} for 16.18.16. This implies steps of monomolecular height for both TAGs, which agrees with the AFM observations elaborated in section 11.4. From the assumption that the surface morphology for 16.18.16 is determined by one layer, the {001} surface graphs of both TAGs appear to be isomorphic, if a cut-off energy of 9.0 kJ/mol is used for the bond strength calculations. This cut-off energy was used in an earlier 3D-HP prediction for $n.n.n$ TAGs [4], which led to a good agreement with the experimental observed morphology. To obtain a similar crystallographic setting for the surface graph of 16.18.16, compared to 16.16.16, the following transformation for 16.18.16 is performed (see table 11.1):

$$
\begin{array}{ll} a & \tfrac{1}{2}a\ \ b \\ b & b \end{array} \qquad (11.8)
$$

The calculated bond strengths are calculated using the Cerius^2 software package [21] and a CVFF force field [22] in the same way as was done for the 3D-HP analysis of $n.n.n$ TAGs [4]; the results are given in table 11.2. The resulting surface graph is given in fig. 11.3, including the directions of the bonds.

Table 11.2. Different bond strengths between the central molecule M_1 and the surrounding molecules M_2 of the surface graph depicted in fig. 3, calculated using the Consisted Valence Forcefield CVFF [22] with the software package Cerius2 [21]. The bonds of 16.16.16 are taken from Hollander *et al.* [4].

Label	$M_1.M_2$ [*uvw*]	16.16.16 [kJ/mol])	16.18.16 [kJ/mol]
p	1.1 [0 1 0] & 1.1 [0 $\bar{1}$ 0]	-136	-168
q_2	1.2 [0 $\bar{1}$ 0]	-122	-120
r_2	1.2 [$\bar{1}$0 0]	-120	-107
q_1	1.2 [0 0 0]	-102	-120
r_1	1.2 [$\bar{1}$1 0]	-100	-107

To predict the morphology of the step patterns, firstly the various connected chains have to be determined from the surface graph. From this analysis, eight different connected chains are found for four different directions, which are [010] (4), [100] (1), [1 $\bar{1}$0] (2) and [1$\bar{2}$0] (1), of which the important ones are given in table 11.3. The calculated morphology for these directions are given in the form of step velocities that are normalized on v_{step}([010]). For the 2D-BFDH approach, in principle every direction [*uv*] is possible, but carrying out this analysis showed

a) surface graph: b) PBC directions:

Figure 11.3 a) Surface graph of the {001} face of the and ' polymorphic types after a coordinate transformation of the latter. Translational symmetric molecules are depicted in the same colour; type 1 is coloured dark; type 2 is coloured light. All bonds are the interactions between the central molecule and the other molecules given. Each bond is denoted by its type (*p*, $q_{1,2}$ or $r_{1,2}$) and by the label *xy*[*uvw*] at the end molecule, which denotes the type of both molecules involved (*x,y* = 1,2; *x* is the central molecule) and the lattice translation [*uvw*] that is made to connect both molecules. The unit cell is indicated in grey. b) The directions of the PBCs found from the PBC analysis, as given in table 11.3.

that only the four directions given above are important for the morphology. Using the three given criteria for v_{step}, the MI for each direction can now be predicted. However, criterion *(iii)*, as formulated in eq. (11.7), needs knowledge of Φ_k, which again needs ΔH_{diss}. Unfortunately, ΔH_{diss} is not determined experimentally and is therefore estimated from the molar enthalpy of fusion ΔH_{fus}. Assuming ideal mixing, which is reasonable for TAGs in alkane solutions, the following formula can be used [23]:
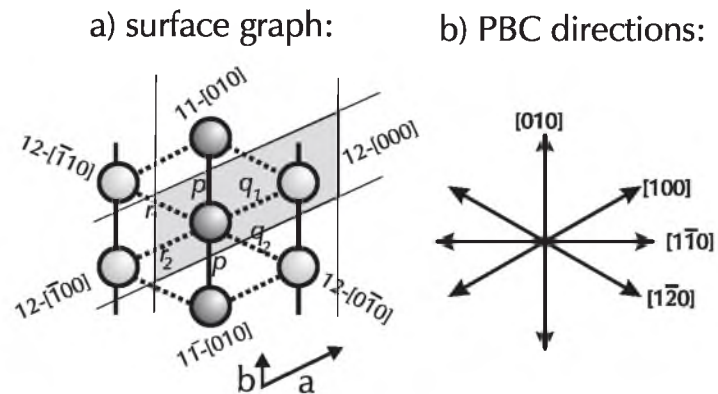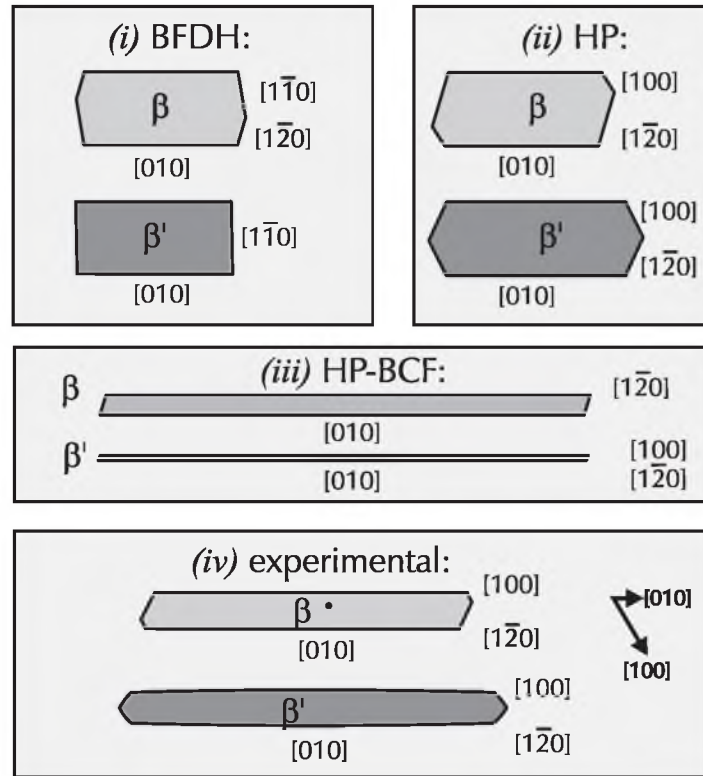
$$\frac{\Delta H_{diss}(T)}{RT} \quad \frac{\Delta H_{fus}(T_m)}{RT_m} \quad \ln x(T) \quad \frac{1}{R}\int_T^{T_m}\frac{\Delta C_p}{T}dT \quad , \tag{11.9}$$

where ΔC_p 0.2 kJ/mol is the difference in molar heat capacity of the solid and undercooled liquid phase. For 16.16.16 and 16.18.16, ΔH_{fus} is 171.3 and 165.5 kJ/mol respectively [24]; $x(T)$ is the equilibrium concentration of the solute expressed as a molar fraction at the growth temperature T. For 16.16.16, $T_m=339.1$ K, $T=301$ K and $x=1.43\times10^{-3}$. For 16.18.16, $T_m=341$ K, $T=304.4$ K and $x=1.26\times10^{-3}$. Using eq. (11.9) this gives $H_{diss}(16.16.16) = 175.6$ kJ/mol and $H_{diss}(16.18.16) = 171.5$ kJ/mol. Assuming equivalent wetting ($\kappa=1$) and taking the calculated crystal energies, $E_{cryst}(16.16.16) = 732$ kJ and $E_{cryst}(16.18.16) = 788$ kJ/mol gives $\varphi_{kink}(16.16.16)= 0.24E_{kink}$ and

Figure 11.4 a) Calculated morphology of the - and '-polymorphs using the three methods presented: *(i)* v_{atep} 1/ $_{hk}$ (BFDH), *(ii)* v_{step} E_{kink} (HP), *(iii)* v_{step} exp( )($_{h'k}/_{hk}$) (HP-BCF). At all morphologies the resulting steps [$uv0$] are indicated. *(iv)* The observed morphology, which will be treated in section 11.4. The centre of the growth spirals, which is slightly off centre in the case of , is indicated for both polymorphs.

$\varphi_{kink}(16.18.16)= 0.22E_{kink}$. Using these assumptions, the relative step velocity is calculated using equation (11.7). For both the β and β' polymorph the strong [010] direction is used as a reference. All calculated values of the step velocities for the various step directions parallel ot the connected chains are given in table 11.3 and the resulting idealized shapes, constructed by the Gibbs-Wulff method, are depicted in fig. 11.4 together with the results of the BFDH and the HP methods. In table 11.3, also the anisotropy is given, which is defined as the ratio of the average length of the step pattern along [010] and the width of the pattern perpendicular to [010]. The results will be compared with the experimental shapes, which are also depicted in fig. 11.4 and described in section 11.4, in section 11.5.

Table 11.3. Step velocities and anisotropy of the 4 different PBC directions found for both β and β'-polymorph.

PBC		(i) BFDH		(ii) HP		(iii) HP-BCF		(iv) experiment	
direction	bonds	β	β'	β	β'	β	β'	β	β'
[010]	p	1	1	1	1	1	1	1	1
[100]	r_2-q_1	2.60	2.31	2.24	2.63	24	87	9	12
[1 0]	r_1-q_1/	2.23	2.12	3.23	-		-	-	-
	r_2-q_2					$6\,10^5$			
[1 0]	r_1-q_2	2.28	2.35	2.24	2.63	23	87	8	12
anisotropy		2.1	1.9	1.6	1.6	30	75	9	11

11.3 Experimental

11.3.1 Crystal growth

As a source material for crystal growth TAGs with a purity of 99% (Sigma) were used. All 16.16.16 and some 16.18.16 crystals were grown from solution using the same set-up as described by Vogels et al. [25]. For the 16.16.16 crystals, dodecane was used as the solvent, while for 16.18.16 acetonitril was used. The crystals were grown with a mass fraction of 0.022 at 43.4 °C (16.16.16) and 0.021 at 29.2 °C (16.18.16). Using acetonitril as a solvent for the growth of 16.18.16 resulted in spherulitic two-phase like growth that is characteristic for protein crystallisation from solution [26]. All single crystals show a needle-like morphology with a large {001} face. To be able to observe the side faces of 16.18.16, some crystals of this compound were also grown from the melt. These 16.18.16 crystals were grown between a sapphire substrate and a thin cover glass. This two-dimensional growth cell was placed in a copper holder, which was kept at constant temperature of 62 °C, which is 2 °C below the melting point. The temperature during growth was kept constant within 0.01 °C using water flow from a thermostatic water bath. Solidification occurred in the form of spherulites with radii up to 5 mm. After growth the cover glass was removed and the radially oriented single crystals, with {001} basal or {100} side faces oriented upwards were examined with the AFM.

11.3.2 Atomic force microscopy

In order to prevent damaging of the soft crystal surface, AFM imaging has to be carried out with great care. Especially at scan sizes of about 1 μm and less, step edges are easily deteriorated by the AFM tip. Therefore, most images were made by tapping mode AFM (TM-AFM), which lowers the lateral forces on the surfaces as compared to contact mode AFM (CM-AFM) [27]. When CM-AFM was utilised, minimised forces which still allowed for a stable feedback were used. For some experiments, especially when imaging the surfaces of the ' crystals, the crystals were immersed in water to enable lower forces [28]. The AFM employed for 16.16.16 was a Topometrix 2010 Discoverer. To image the spiral patterns a 75 μm tripod scanner was used. The molecular resolution images were obtained with a 1 μm scanner using CM-AFM. For 16.18.16 surfaces, a Digital Dimension 3100 with a 120 μm scanner was utilised. Both TM-AFM in air and CM-AFM in water were applied for imaging of these crystals.

11.4. AFM results and discussion

### 11.4.1 Growth spirals on 16.16.16

In fig. 11.5a-b an overall view and a zoom-in of a typical growth spiral observed on 16.16.16 are depicted. In addition, several 2D nuclei are observed as shown in fig. 11.5c. Virtually all observed growth steps are of monomolecular height, i.e. d_{001}. This indicates that for the growth spirals the screw component of the central dislocation is equal to length of the c-axis. The spirals and 2D nuclei are highly anisotropic and are bounded by steps parallel to [010], [100] and [1$\overline{2}$0]. The steps parallel to the [010] direction are polygonized from the beginning, while the other steps get more polygonized further away from the spiral centre. The relative velocities of the various steps determine the shape of a growth spiral far from its centre. The actual values are given in table 11.3. A similar dependence was found for the 2D nuclei. In many cases it was observed that for step directions deviating from [010] the step patterns show morphological instabilities, which led to finger-like features as shown in fig. 11.5d. These patterns indicate mass transport limited growth. Since surface diffusion for such large molecules is unlikely to occur for the μm distances corresponding to the scale of the instability patterns, it follows that here volume diffusion towards the step is rate limiting.
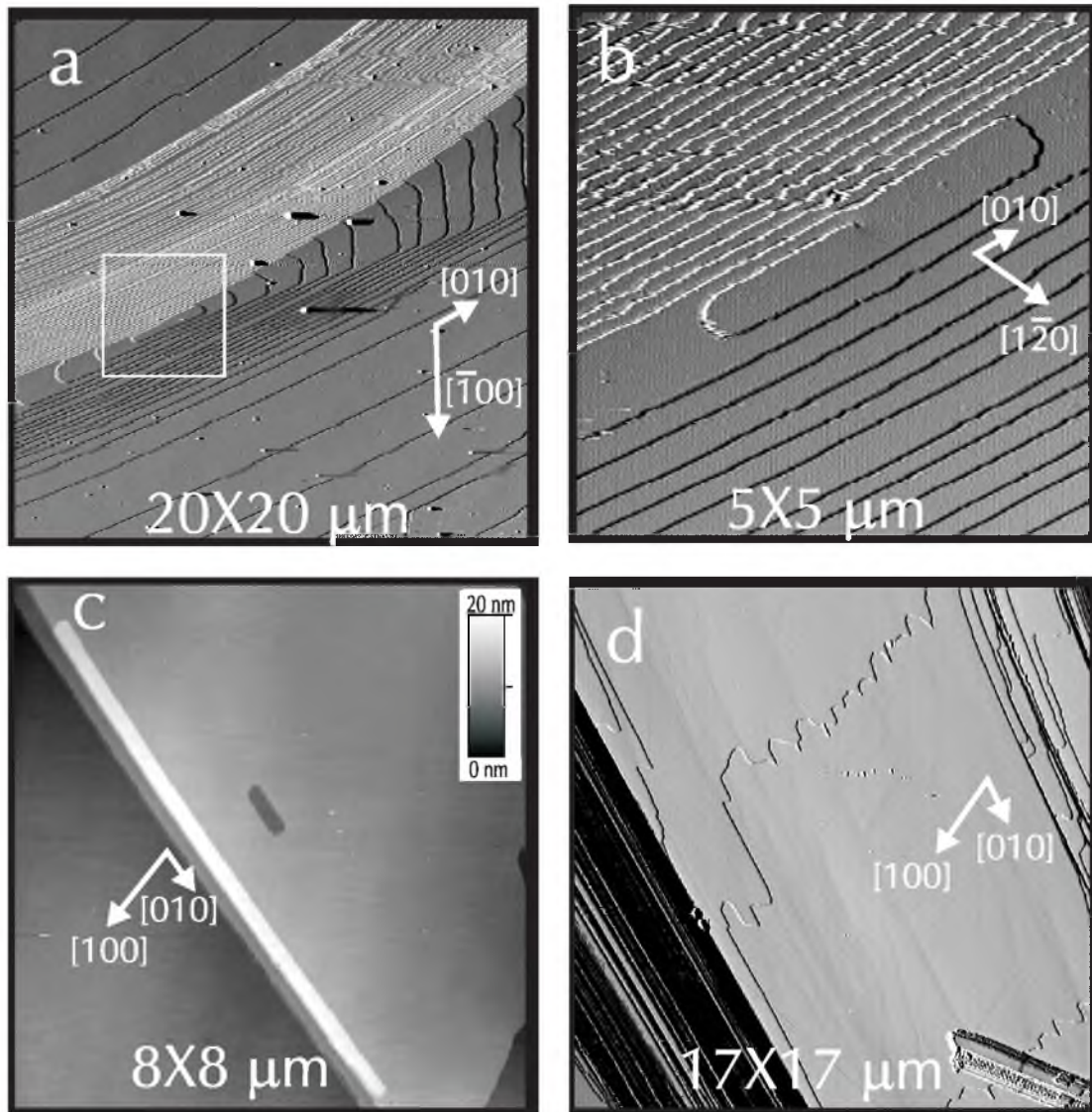
Figure 11.5 AFM images of the {001} face of 16.16.16. (a) Deflection image of a faceted growth spiral. (b) Zoom-in of the marked region in (a) showing the centre of the spiral. (c) Height image of faceted 2D nucleus. (d) A fingered pattern of a step with average alignment perpendicular to [010].

11.4.2 Growth spirals of 16.18.16

Compared to the {001} faces of 16.16.16, the {001} faces of solution grown 16.18.16 TAGs show similar spiral and 2D nuclei patterns, which now are more anisotropic in the needle direction. In fig.
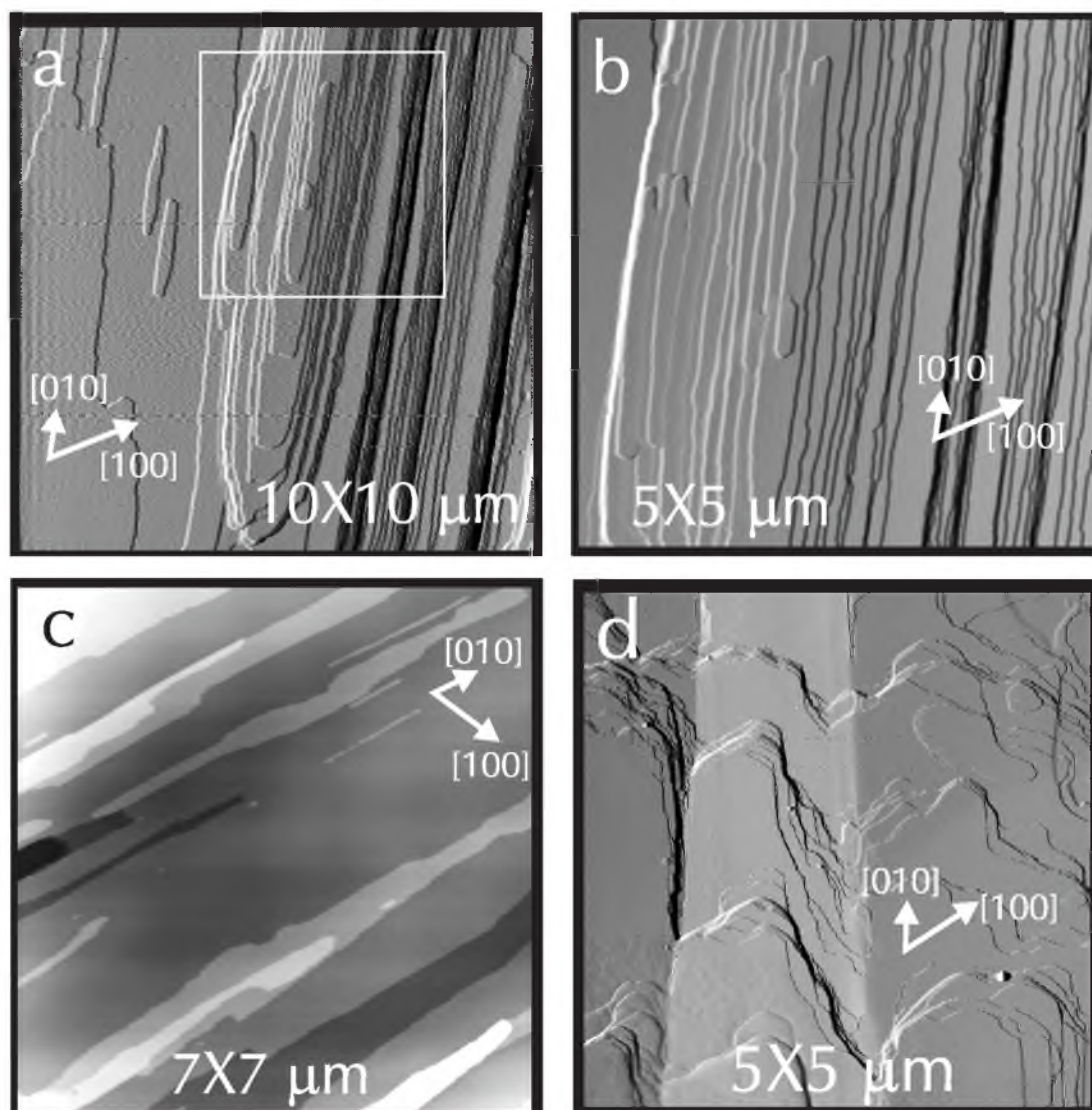
Figure 11.6 AFM images of the {001} face of 16.18.16. (a) Deflection image of two cooperating growth spirals and some 2D nuclei. (b) Zoom-in on the centers of both spirals. (c) Height image of highly anisotropic 2D nuclei. (d) A fingered patterns with average alignment perpendicular to [010].

6a-b both phenomena are shown, including a zoom-in of the two interacting growth spiral centres. Besides the strong [010] steps, the steps in the other directions that make up the islands and spirals are less polygonised and are more rounded as compared to 16.16.16. In general, these off [010] directions become only polygonised if the steps bunch together to small macrosteps, which are parallel to [100] and [120] as depicted in fig. 11.6d. The relative step velocities are given in table 11.3. The step height of these and other growth spirals are again of monomolecular height, which

in this case equals ½c. This points to a screw component of ½c, which is in conformity with the I-lattice in which 16.18.16 crystallises. The morphological instable finger patterns were also found for solution grown 16.18.16 as can be seen in fig. 11.6d. This implies that also in this case the step propagation in the off [010] directions is largely limited by volume diffusion.

For a number of growth spirals on both {001} 16.16.16 and {001} 16.18.16, the shape is measured from the AFM micrographs .The average results are summarized in table 11.3 and depicted in fig. 11.4, together with the predicted shapes for the three different methods. In table 11.3, also the anisotropy is given.

The frequent observation of spiral growth on 16.16.16 and to a lesser extent 16.18.16 indicate that this is, at least for our growth conditions, an important growth mechanism. From this, it can be concluded that twinning along {001} is not abundantly, if at all, present on our crystals, because this requires 2D nucleation growth. It is thus concluded that the grown crystals are probably single crystals.

11.4.3 Molecular resolution

Birker and Blonk already obtained molecular resolution of the {001} face for 12.14.12 [29], which belongs to the same homologous
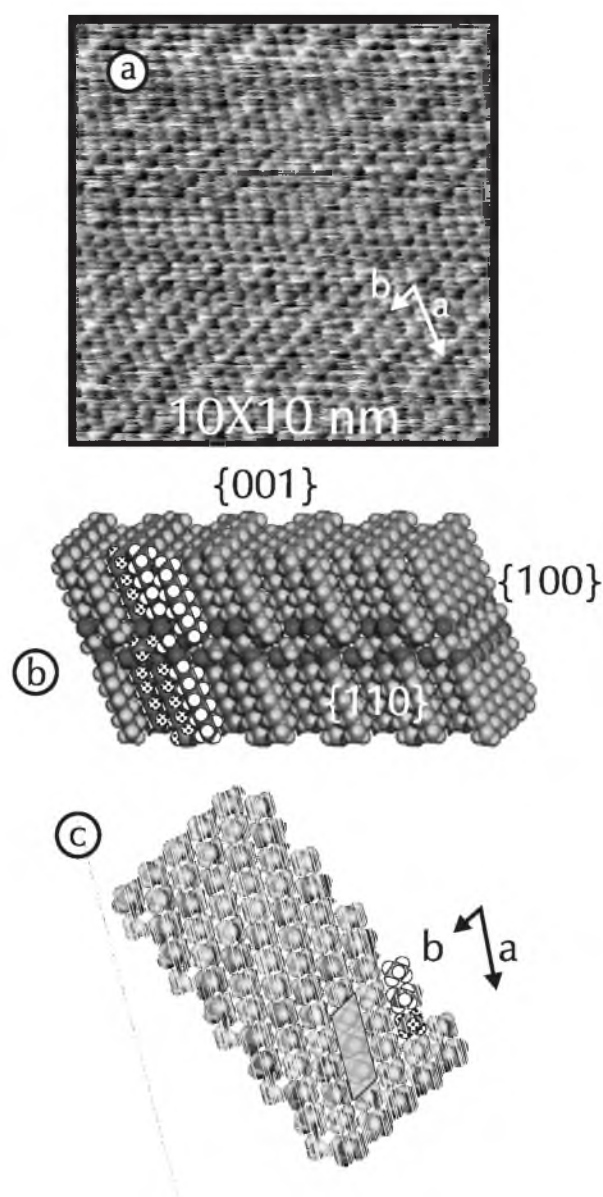
Figure 11.7 (a) Molecular resolution image on {001} 16.16.16. recorded by CM-AFM. Each sphere is a methyl end group. The rows visible in the image correspond to somewhat protruding methyl groups as can be seen by comparison with the image obtained from x-ray diffraction measurements (b, c). (b) side view of the 16.16.16 structure, clearly showing three rows of methyl groups corresponding to rows of 'chair-like' TAG molecules. (c) Top view of the stack of molecules depicted in (b). One unit cell is coloured grey. In (b) and (c) a 'standing up' chair molecule as well as a 'standing down' chair molecule are accentuated by dotted and white H atoms respectively.

series as β' stable 16.18.16. The molecular image shows a nice hexagonal pattern, which corresponds to the molecular structure predicted by van de Streek [6]. Moreover, this correspondence makes the result of the 2D-HP analysis, based on the bulk-crystallographic structure reliable.

In our experiments, in contrast to 16.18.16, clear molecular resolution images were obtained for the {001} surface of the β polymorph 16.16.16. As can be seen from fig. 11.7a, this face looks different from the {001} surface of the β' polymorph as observed by Birker and Blonk [29]. Comparing the 2D unit-cell, constructed from this molecular image, with that derived from X-ray measurements [Lang99], a good agreement is obtained. In the molecular resolution image, clearly three rows parallel to the [010] direction with different heights can be distinguished. The pattern closely match a molecular model built from the crystallographic structure as depicted in fig. 11.7b-c. Moreover, the measured angle $\gamma = 57 \pm 5°$ and the lengths of the crystallographic axes, $a = 10 \pm 1$ Å and $b = 5 \pm 0.5$ Å obtained from the AFM image are close to the unit cell parameters $a = 14.2$Å, $b = 5.4$Å and $\gamma = 57.7°$ as determined by van Langevelde et al. [3].

It can now be concluded that molecular resolution images of β and β' polymorphs resemble the (proposed) molecular structure, and no evidence for the occurrence of surface reconstruction was found. Therefore, these (bulk)-structures can be used as the input for the 2D-HP analysis.

11.4.4 Half step on 16.16.16

Fig. 8a-c shows the outcrop of a remarkable type of stacking fault which is sometimes observed on the {001} surface of 16.16.16. This 120 μm long outcrop appears as a straight step parallel to [010] with a height of 1/2 d_{100}, i.e. half the height of a normal monomolecular step. The presence of this stacking fault implies that one plane of tuning-fork shaped TAG molecules is shifted over the length of one alkyl chain, i.e. half a tuning fork. The beginning and end of this stacking fault are forced by two partial screw dislocations of opposite sign. Sub-steps have been reported for other crystals and sometimes enhance the growth rate according to the Ming mechanism [30,31]. In the present case however, from the observed step patterns around the stacking fault it is concluded that the sub-steps created at the stacking fault do not act a growth source. Possibly, the long TAG molecules have difficulties in aligning along this sub-step and the activity of this step source is by far less than that of the growth spirals.
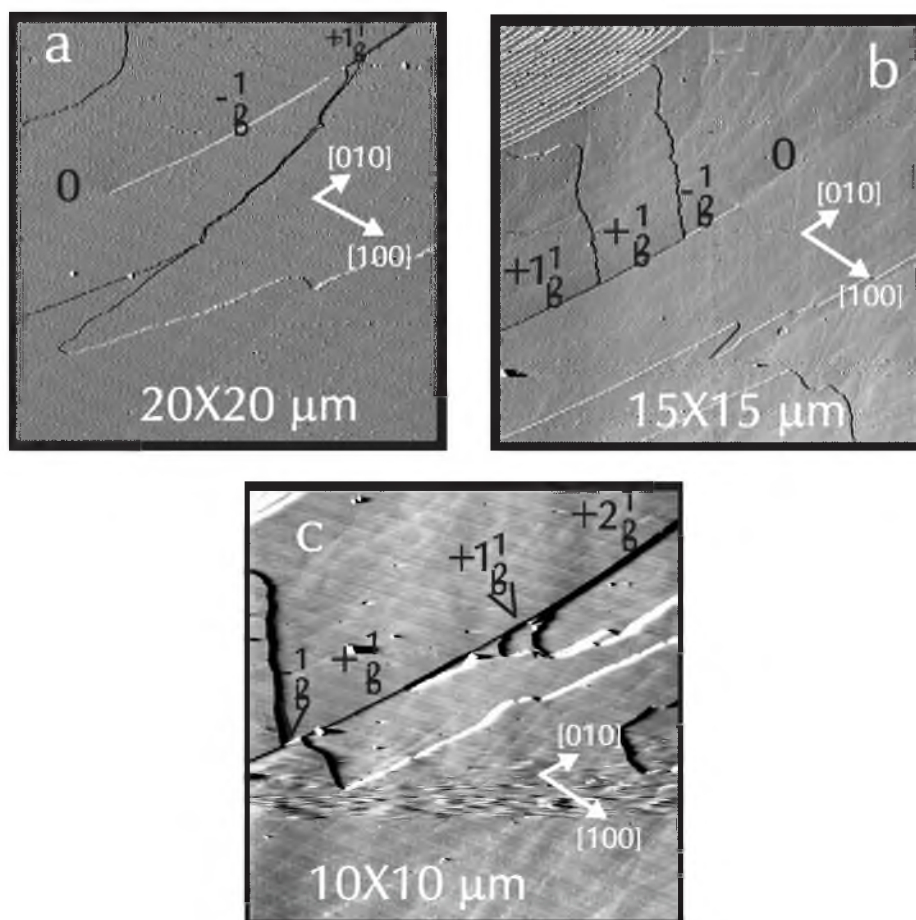
Figure 11.8 Stacking fault on the 16.16.16 {001} surface. Heights at the [ĪOO] side of the half-step are indicated in fractions of d_{001} relative to the [100] side. (a) Start of the stacking fault at a partial dislocation with screw component $1/2c$. (b) End of the fault at a similar dislocation of the opposite sign. (c) Central region of the stacking fault.

11.4.5 Vicinal side-faces and morphology on the side faces of 16.18.16

For the 16.18.16 crystals grown from the melt, in addition to {001} also vicinal faces {10l} were commonly imaged by AFM. In fig. 11.9 two different vicinal regions are depicted as A and B; the boundary between these regions is inclined with respect to the [010] direction. The average step height in region A is 1.8 ± 0.2 nm, which corresponds to the monomolecular height d_{100}. For region A, the terrace-width is approximately 39 nm, while for region B it is 22.5 nm, which corresponds to $4.5\ d_{001}$ (9 molecules) for region A and $2.5\ d_{001}$ (5 molecules) for region B. The strictly equidistant trains of closely separated steps in region A and B suggest a strong interaction between adjacent steps, which stabilises both kinds of vicinal surfaces. A similar stabilisation of vicinal faces, owing to

repelling steps, has been observed for metals [32]. The boundary between the two regions is rather strange. The angle between the step directions in the regions A and B is approximately 20°, which would imply that the border represents a high angle grain boundary between two single crystals. However, the steps transform smoothly from one to the other region, so the whole crystal is single and vicinal face B must be of type $\{1kl\}$ rather than $\{10l\}$.
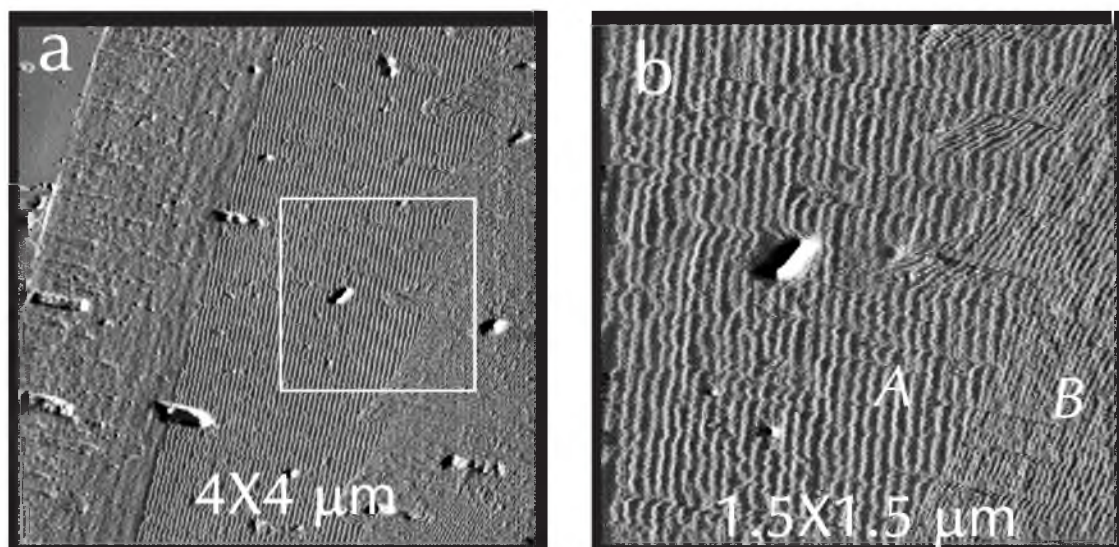
Figure 11.9 (a) AFM deflection image of vicinal faces on 16.18.16 crystals grown from the melt. **(b)** Zoom-in of the marked region in (a). Both regions A and B show steps of height 1.8 ± 0.2 nm, which corresponds to d_{100}. The step spacing is 39 nm for region A, and 22 nm for region B.

11.5. Comparison of calculated and observed step patterns

11.5.1 Comparing observed step patterns with overall 3D morphology

It is useful to compare the 2D surface morphology with the 3D crystal morphology, because interaction energies in $\{001\}$ layers are much larger than the bonds between these layers. In other words: $E_{slice} \gg E_{att}$. For such large bond anisotropy, the 2D morphology is expected to resemble the 3D morphology to a great extent [33].

The $\{001\}$ surfaces of both 16.16.16 and 16.18.16 show dominant [010] steps, which are parallel to the side faces $\{100\}$. Besides this [010] direction, [100] and [1$\overline{2}$0] step directions were observed which were less dominant. Together, these three directions, which are parallel to PBCs in the surface graph of the $\{001\}$ face, make up the polygonized spirals as depicted in fig. 11.5,6. The analogous

{100}, {01l}, and {21l} faces were also predicted and found on the 3D morphology of 16.16.16 crystals [34,4]. Analogous to the never observed {11l} faces on the 3D morphology, the [110] step direction has not been found on the surfaces of 16.16.16. This is due to a very low kink energy, caused by two interacting PBCs, within the linewidth δ_{17} as was explained previously by Grimbergen et al [11] for growth faces and by van Enckevort for steps [15]. Recent work has shown that because of similar reasons the {11l} faces of TAGs exhibit a very low step energy which explains their high growth rate [4].

11.5.2 Comparing observed step patterns with calculated patterns

The predicted step patterns with (*i*) BFDH, (*ii*) HP and (*iii*) HP-BCF for both β and β' are depicted together with the observed patterns in fig. 11.4 using the data of table 11.3.

All the observed steps are parallel to strong PBCs found from the various predictions. The strongest PBC in all predictions, which is [010], is indeed the dominant step on the observed morphology.

(i) The 2D-BFDH method predicts also dominant [1 0] steps, which are not observed. The reason is that the BFDH criterion does not take into account the two interacting PBCs in this direction, as mentioned above.

(ii) The HP method predicts the steps that are present on the 16.16.16 and 16.18.16 {001} faces. However, the predicted shape has less anisotropy than the observed morphology. Moreover, there is no difference predicted between the β and β' morphology.

(iii) For the HP-BCF model, the steps are predicted well. In case of 16.16.16, the observed difference between [100] and [1 0] is predicted, although the difference is predicted to be so large that the [1 0] steps disappear from the morphology. This model is the only one that predicts the observed large anisotropy in both β and β'. Moreover, the larger anisotropy for β' is calculated well. The only inaccuracy is that the predicted anisotropy is too large. This may be caused by the rather crude assumptions for κ and ΔG, as well as by the volume diffusion that is probably the growth limiting factor (sections 4.11.1,2). If the growth was not volume diffusion limited, the anisotropy would probably higher like predicted by the HP-BCF model.

11.6 Conclusions

Three different criteria were employed or developed to predict 2D crystal morphology. These were theBravais Friedel Donnay Harker (BFDH) criterion, the Hartman Perdok (HP) criterion and the Hartman Perdok - Burton Cabrera Frank (HP-BCF) criterion. These criteria were applied to predict the step patterns on the {001} faces of β 16.16.16 and the β' 16.18.16 fat crystals. The HP-BCF method explained the observed patterns the best. The observed types of steps, the anisotropy of them, as well as the differences between β and β' were predicted by this method.

The HP-BCF method can be a powerful method to predict and understand the morphology and the behaviour of steps of growing crystal surfaces.

Acknowledgements

References

[1]   J.W. Hagemann, in *Crystallization and Polymorphism of Fats and Fatty acids*, edited by N. Garti and K.Sato, Marcel Dekker, New York, 1988, 9-95.

[2]   S. de Jong and T.C. van Soest, Acta Cryst. B **34** (1978), 1570.

[3]   A. van Langevelde, K. van Malssen, F. Hollander, R. Peschar and H. Schenk. Acta Cryst. B. **55** (1999), 104.

[4]   F. Hollander, S. Boerrigter, J. van de Streek, R. Grimbergen, H. Meekes and P. Bennema, accepted for publication in J. Phys. Chem.

[5]   P. Birker, S. de Jong, E. Roijers and T. van Soest, J. Am. Oil. Chem. Soc. **68** (1991), 895.

[6]   J. van de Streek, accepted for publication in J. Am. Oil Chemist' Soc.

[7]   A. van Langevelde, K. van Malssen, E. Sonneveld, R. Peschar and Henk Schenk, J. Am. Oil Chem Soc. **76**, (1999), 603.

[8]   P. Hartman and W. Perdok. Acta Cryst. **8** (1955), 49; Acta Cryst. **8** (1955), 521; Acta Cryst. **8** (1955), 525.

[9]   P. Bennema and J.P. van der Eerden, in *Morphology of crystals*, Terra Scientific Publishing company (TERRAPUB), 1987, 1.

[10]   P. Bennema, in *Handbook of Crystal Growth*, edited by D.T.J. Hurle, North Holland, Amsterdam, 1993, ch. 7.

[11]   R.F.P. Grimbergen, H. Meekes, P. Bennema, C.S. Strom and L.J.P. Vogels, Acta Cryst. A **54** (1998), 491.

[12]   H. Meekes, P. Bennema, and R.F.P. Grimbergen, Acta Cryst. A **54** (1998), 501.

[13]   R.F.P. Grimbergen, P. Bennema and H. Meekes, Acta Cryst. A **55** (1999), 84.

[14]   W.J.P. van Enckevort in *Science and Technology of Crystal Growth*, edited by J. van de Eerden and O. Bruinsma, Kluwer Academic Publishers, Dordrecht, 1995, 355.

[15]   W.J.P. van Enckevort, in *Facets of 40 years of Crystal Growth*, edited by W.J.P. van Enckevort, H. Meekes and J. van Kessel, University of Nijmegen, 1997, 51.

[16]   X.Y. Liu and P. Bennema, J. Chem. Phys. **98** (1993), 5863.

[17]   J.P. van der Eerden, in *Handbook of Crystal Growth*, edited by D.T.J. Hurle, North Holland, Amsterdam, 1993, ch 6.

[18]   H, Müller-Krumbhaar, T. Burkhardt and D. Kroll, J. Crystal Growth **38** (1977) 13.

[19]   W.K. Burton, N. Cabrera and F.C. Frank, Phil. Trans. Roy. Soc. A **243** (1951), 299.

[20]   J. van Suchtelen, *Morphology of Crystals: Part C: the Geometry of Crystal Growth*, edited by I. Sunagawa, Terra Scientific, Tokyo (1995).

[21]   Cerius² User Guide, Version 3.7 PDC version, Molecular Simulations Inc, 9685 Scranton Road, San Diego, CA, SA, April 1998.

[22]   P. Dauber-Osguthorpe, V.A. Roberts, D.J. Osguthorpe, D. Wolff, M. Genest, A. Hagler and T. Hagler, Proteins: Structure, Function and Genetics **4** (1988), 31.

[23]   P. Bennema, in *Surface Mobilities on solid materials*, edited by Vu Thien Binh, Plenum Press, New York 1981, 288.

[24]   L.H. Wesdorp, thesis, Delft University, 1990.

[25]   L.J.P. Vogels, H. Marsman and M. J. Verheijen, J. Crystal Growth **100** (1990), 439.

[26]   F. Rosenberger, in *Theoretical and technological aspects of crystal growth*, edited by R. Fornari and C. Paorici, Trans Tech Publications, Switzerland, 1998.

[27]   W.A. Ducker, R.F. Cook and D.R. Clarke, J. Appl. Phys. **67** (1990), 4045.

[28]   A.L. Weisenhorn, P.K. Hansma, T.R. Albrecht and C.F. Quate, Appl. Phys. Lett. **54** (1989), 2651.

[29]   P. Birker and J. Blonk, J. Am. Oil. Chem. Soc. **70** (1993), 319.

[30]   Ming Nai-Ben and I. Sunagawa, J. Crystal Growth **87** (1988), 13.

[31]   G. Bögels, T.M. Pot, H. Meekes, P. Bennema and D. Bollen, Acta Cryst. A **53** (1997), 84.

[32]   J.W.M. Frenken and P. Stoltze, Phys. Rev. Letters **82** (1999), 3500.

[33]   R. Boistelle, in *Current topics in materials science*, volume 4, edited by E. Kaldis, North-Holland, 1980, chapter 8.

[34]   W. Skoda and M. van den Tempel, J. Crystal Growth **1** (1967)**,** 207.

Chapter 12:

Atomic force microscopy studies of insulin crystal growth

Chapter 12:

Atomic force microscopy studies of insulin crystal growth

K. Waizumi[1], M. Plomp[2] and W.J.P. van Enckevort[2]

[1]*Department of Chemistry, Faculty of Education, Yamaguchi University, Yamaguchi 753-8513, Japan*
[2]*RIM Laboratory of Solid State Chemistry, University of Nijmegen, Toernooiveld 1, 6525 ED Nijmegen, the Netherlands*

Abstract

The morphology and the growth mechanism of the {100} surfaces of 2Zn-insulin crystals were investigated by *in situ* and *ex situ* atomic force microscopy. The dominant growth mechanism of the insulin crystals is the formation and lateral expansion of two-dimensional nuclei on the growing surfaces. Besides that, also spiral growth and growth starting from particles that landed on the surface were observed. The single step height was 3.2 nm, which corresponds to the height of a single layer composed of insulin hexamers. An anisotropy of step velocity was revealed from a series of sequential images of growing crystal surfaces. This anisotropy is caused by the different structure of differently oriented steps. Images showing formation of a two-dimensional nucleus indicate that the critical diameter for two-dimensional nucleation is roughly 30 - 60 nm. Several types of dislocation spirals, such as conventional single, double and triple spirals as well as spirals generated by a planar defect, were observed. High islands with steep edges, which represent one of the important growth mechanisms of protein crystals, were also recorded. The step velocity of the multilayer stacks was about 50 % of that of a single step, which implies that no significant overlap of the diffusion fields exists. On the other hand, the degeneration behaviour of the multilayer steps provided evidence for surface diffusion as the mechanism of solute transport towards the steps. Surface vacancies and step edge structures were also recorded with molecular resolution. Small particles present on the (100) surfaces suggest a form of pre-crystallization.

Keywords: atomic force microscopy, insulin, two-dimensional nucleation, spiral growth, aggregates, defects

12.1 Introduction

It is well known that most of the important biological activities of proteins are correlated with their three-dimensional structure. Single crystals of proteins having suitable size and quality for X-ray diffraction are essential to obtain this information by structural analysis. However, compared to low molecular weight substances, protein crystals are relatively difficult to grow, and therefore knowledge about their growth mechanism is important to obtain protein crystals suitable for X-ray measurements. One way to gather this information is by surface examination of the growing crystals using microscopic techniques. Over the past decade, atomic force microscopy (AFM) has been applied to examine the surface morphology of protein and virus crystals, such as lysozyme, canavalin, thaumatin, catalaze, and satellite tobacco mosaic virus [1-18]. From the observations, two-dimensional nucleation, spiral growth, adsorption of three-dimensional nuclei or aggregates, incorporation of microcrystals and normal growth have been revealed as possible growth mechanisms of these macromolecular crystals.

Insulin, which in crystalline form consists of ordered arrangements of hexamers, is one of the most important and thoroughly studied hormone proteins. It is essential for controlling the amount of sugar in the blood and it is utilized as a medicine for diabetes. Interestingly, insulin is stored in the secretory granules of pancreatic β-cells in crystalline form. An AFM study of insulin single crystals has been performed previously by Yip and Ward [7], who showed that insulin crystallization proceeds layer-by-layer and that aggregates landed on the surfaces incorporate into growing terraces. However, they could not reveal other possible growth sources such as two-dimensional nuclei, spiral dislocations and islands with a multilayer stack, which is probably due to the limited scan range of their AFM. Therefore, further AFM observation was needed to study the growth mechanism of insulin crystals in detail.

In this study, attention is focussed to the {100} face as indexed on rhombohedral setting of 2Zn-insulin crystals [19], because this face is dominant and therefore is expected to provide information on the growth mechanism of this protein crystal. The surfaces were examined by in situ and ex situ AFM. Growth by two-dimensional nucleation, screw dislocations and adsorption of three-dimensional nuclei generating multilayer stacks islands was successfully shown on growing crystals. Molecular resolution images of the surfaces and steps were also recorded. Some topics, such as the growth rate controlling factor, aggregation phenomena and the occurrence of point and planar defects, are also discussed on the basis of the observations.

12.2 Experimental

Bovine insulin used in this study was obtained from Wako Pure Chemistry; the other reagents were high purity grade without further purification. 25 mg insulin was dissolved in 100 ml aqueous solution of 0.02 M HCl, together with a small amount of NaN_3 to prevent deterioration of the protein. 2.5 mg $ZnCl_2$ was also added to the insulin solutions, because Zn^{2+} ions promote the formation of insulin hexamers, which are the growth units of the crystals. In this way 2Zn-insulin crystallization is easily achieved. Crystallization was induced by mixing 2 ml of 0.10M sodium citrate solution with 2 ml of the insulin solution at room temperature. Small rhombohedral shaped 2Zn-insulin crystals were formed within a week, and large crystals with a sizes of a few hundred μm were obtained after several weeks. After a period varying from two weeks to two months, crystals were transported to the AFM in situ cell for in situ imaging, or taken out of the solution for ex situ observation. We do not know the supersaturation during the experiments, but we estimate it to be very low ($<$ 1%), judging from the low step velocities observed during in situ AFM imaging.

For AFM imaging, crystals are needed with two large parallel faces. In that case, one face lies on the bottom of the AFM in situ cell, and the opposite face, is imaged. In this stable configuration crystals did not move during scanning. Suitable crystals were selected and placed in a petri-dish of 35 mm diameter, which is used as a AFM fluid cell. Crystals to be measured were selected according to their size, quality, and orientation by examination using the optical microscope integrated with the AFM. The in situ and ex situ AFM images were obtained by using a Digital Instruments Dimension 3100 and a Topometrix Discoverer, respectively. Images were collected in contact mode using Si_3N_4 cantilevers with nominal force constants of 0.06 N/m. The force exerted by the AFM tip was approximately 0.2 nN or less during imaging during the in situ imaging. When scanning, care was taken to continuously adjust the setpoint force to the lowest value for which tip-crystal contact was maintained in order to minimize the force applied to the crystalline surface, because too high a force results in mechanical etching of the sample by the tip.

In case of in situ imaging with the Dimension 3100, scanning of horizontal lines (along the 'fast' horizontal scan axis) proceeds downwards or upwards in the 'slow' scan direction in an alternating way for subsequent scans. In a number of figures the slow scan direction is indicated by an upwards or downwards directed arrow. Due to the non-zero time needed to record an image, recordings of growing steps will be distorted in a direction depending on the slow scan speed direction. However, because the growth velocity of the insulin steps proved much lower than the 'slow' scan speed, the image distortion is small in our case. Nevertheless, all measured step velocities are corrected for this effect.

12.3 Results and discussion

12.3.1 Lattice imaged with molecular resolution

The crystal structure of 2Zn-insulin is rhombohedral, space group $R3$, with unit cell dimensions $a =$ 4.9 nm and $\alpha_R = 114.8$ [19], consisting of a three-dimensional (3D) array of insulin hexamers as shown in fig. 12.1a. Each individual insulin hexamer forms a cylinder with an diameter of about 5.0 nm and a thickness of about 3.5 nm. In the rhombohedral structure, these cylinders are canted out of the {100} plane by an angle of 25°, and the thickness of a d_{100} layer is 3.2 nm.

A molecular resolution image of a {100} surface of an insulin crystal is shown in fig. 12.1b; this *in situ* AFM topograph is acquired in contact mode in solution. The rhombohedral lattice is clearly visible. The lattice spacing and angle estimated from the AFM images are $a = 4.7$ nm and $\alpha_R = (117\pm5)$, respectively, which correspond well with the values deduced from X-ray diffraction measurements.


(a)   **(b)**
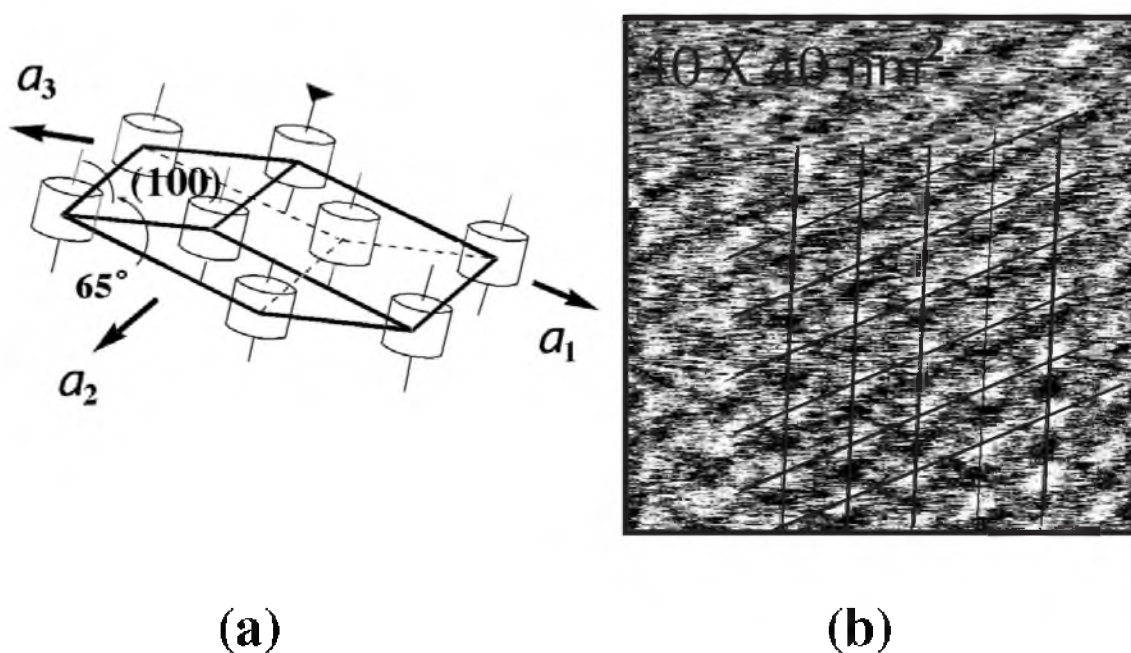
Figure12.1 (a) The $R3$ rhombohedral unit cell of 2Zn-insulin crystal showing the tilted orientation of the hexamers with respect to the (100) plane. (b) Molecular resolution image of the (100) face obtained by *in situ* AFM. Each white dot represents an insulin hexamer. Inter-hexamer distance and angle between the crystal axes are about $a = 4.7$ nm and $_R = 117\pm5$, respectively, which is in good agreement with $a = 4.9$ nm and $_R = 114.8$ determined by X-ray diffraction[19].

12.3.2 Two-dimensional nucleation

Growth by the two-dimensional nucleation mechanism was commonly observed for insulin {100}. The edges of the two-dimensional nuclei have a characteristic lozenge-shaped morphology that is

parallel to the crystal side faces as well as to rows of molecules. This was checked by optical microscopy and the molecular resolution AFM images described above, respectively. These directions correspond to the Periodic Bond Chain [20, 21] <100> directions in the insulin crystal structure.
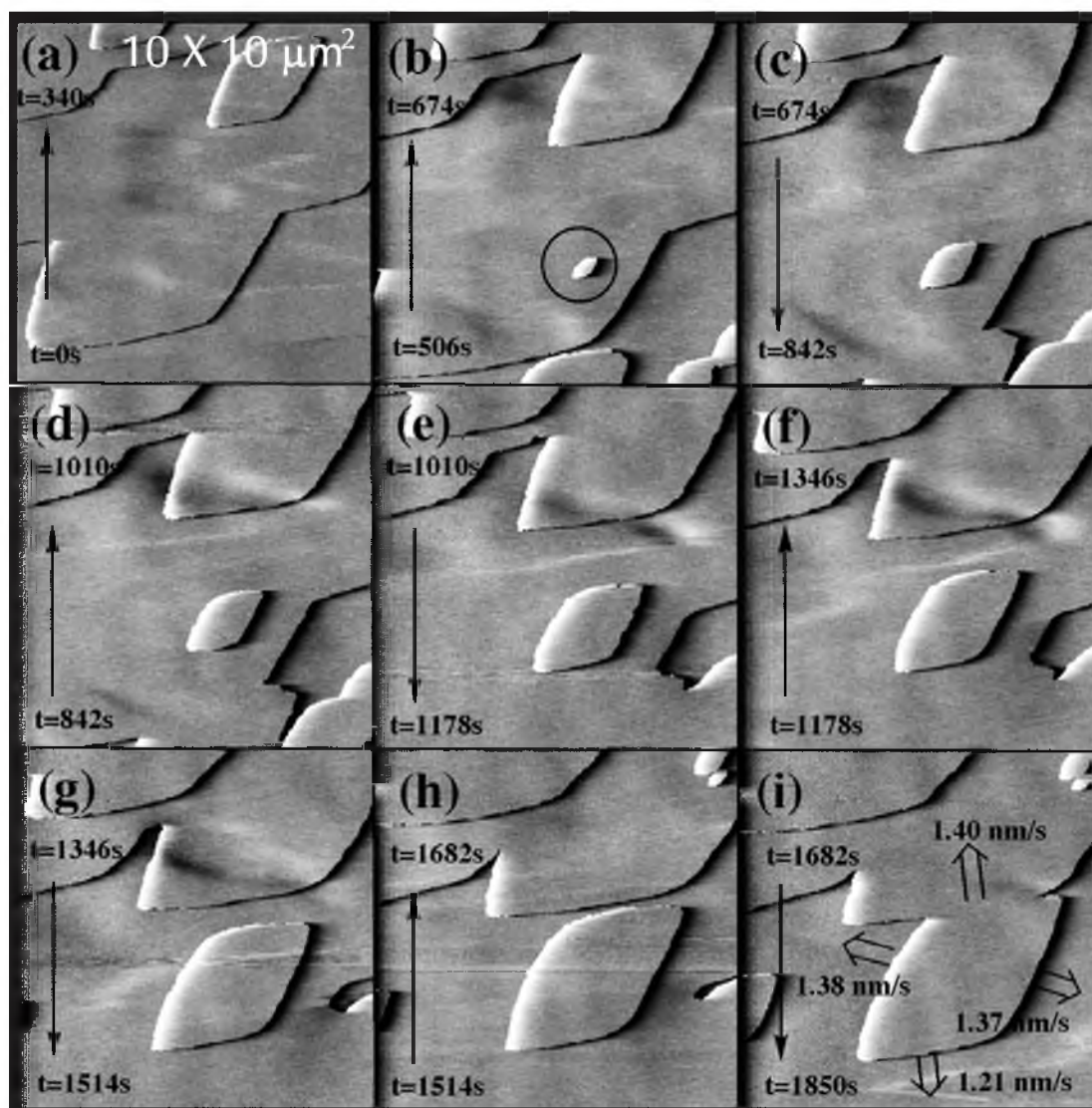
Figure 12.2 Time series of *in situ* AFM images on the (100) surface of a 2Zn-insulin crystal growing by two-dimensional nucleation. A new two-dimensional nucleus is born in (b) and spreads continuously. The velocity of the step advancing downwards from the nucleus was significantly less than that of the other three steps as shown in (i). The slow scan direction is indicated by arrows (see section 12.2).

A series of *in situ* AFM images of a (100) surface growing by 2D nucleation is shown in fig. 12.2. A new two-dimensional nucleus is born in fig. 12.2b and spreads continuously in subsequent images. The scanned region usually shows some drift, which makes direct measurement of step velocities inaccurate. However, the rates of steps could be precisely measured by the use of small, persisting holes frequently observed on the surface (see section 12.3.4.) as reference points. The tangential velocity of the step advancing downwards within the images was about 1.21 nm/s, which is about 15% lower than the rate of 1.37 - 1.40 nm/s of the other three steps as indicated in fig. 12.2i. This step anisotropy is in accordance with the difference in molecular structure of growth steps advancing in different crystallographic directions, *i.e.* the 2D pointgroup 1 of the {100} surface.
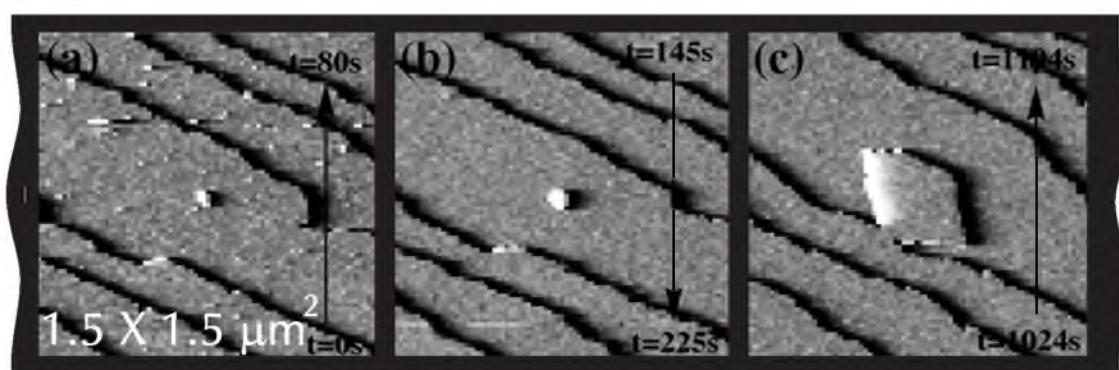

Figure 12.3 *In situ* AFM images indicating the critical size for two-dimensional nucleation. (a) Appearance of subcritical and supercritical nuclei. The diameter of the larger particle at the center of (a) is approximately 60 to 80 nm, and the size of the smaller particles present, imaged as tiny white dots, is about 10 to 30 nm. In (b) and (c), the larger island continues to grow forming a two-dimensional island with a crystallographic contour, while the smaller particles shown in (a) disappear.

On sub-μm-scale, *in situ* AFM images provided information on the critical size of a two-dimensional nucleus. The diameter and height of the larger particle near the center of fig. 12.3a were approximately 60-80 nm and 3 nm, respectively, and the smaller particles imaged as tiny white dots have diameters of approximately 10 to 30 nm and the same mono-hexamer step height. As shown in fig. 12.3, the larger particle continues to grow to a two-dimensional island with edges along the crystal lattice, while the smaller particles disappeared from the surface in the later images fig. 12.3b and c. This series of the images indicate that the critical diameter of two-dimensional nucleation within the experiment was roughly 30 - 60 nm.

Small particles adsorbed on the (100) face of insulin crystals were observed with molecular resolution as shown in fig. 12.4. The particles seem to consist of a few insulin hexamers as judged from comparing their sizes with the size of the individual hexamers of the underlying crystal surface,

although individual hexamers could not be recognized within the small particles. The subcritical particles found in fig. 12.4 may consist of a few insulin hexamers like the small particles in fig. 12.4. Small particles have been found on the surface of insulin crystals by Yip and Ward as well [7]. In their paper, they mentioned that these features reflect the attachment of pre-crystallization aggregates formed in solution [7, 22]. Recently, concentration changes of supersaturated solutions of 2Zn-insulin during crystallization have been measured and interpreted by using a self-assembly theory, which suggested that aggregates of insulin at the pre-crystallization stage are composed of four insulin hexamers [23]. The small particles observed during the current investigations are in accordance with these results.

(a)   300 X 220 nm²

(b)   100 X 50 nm²
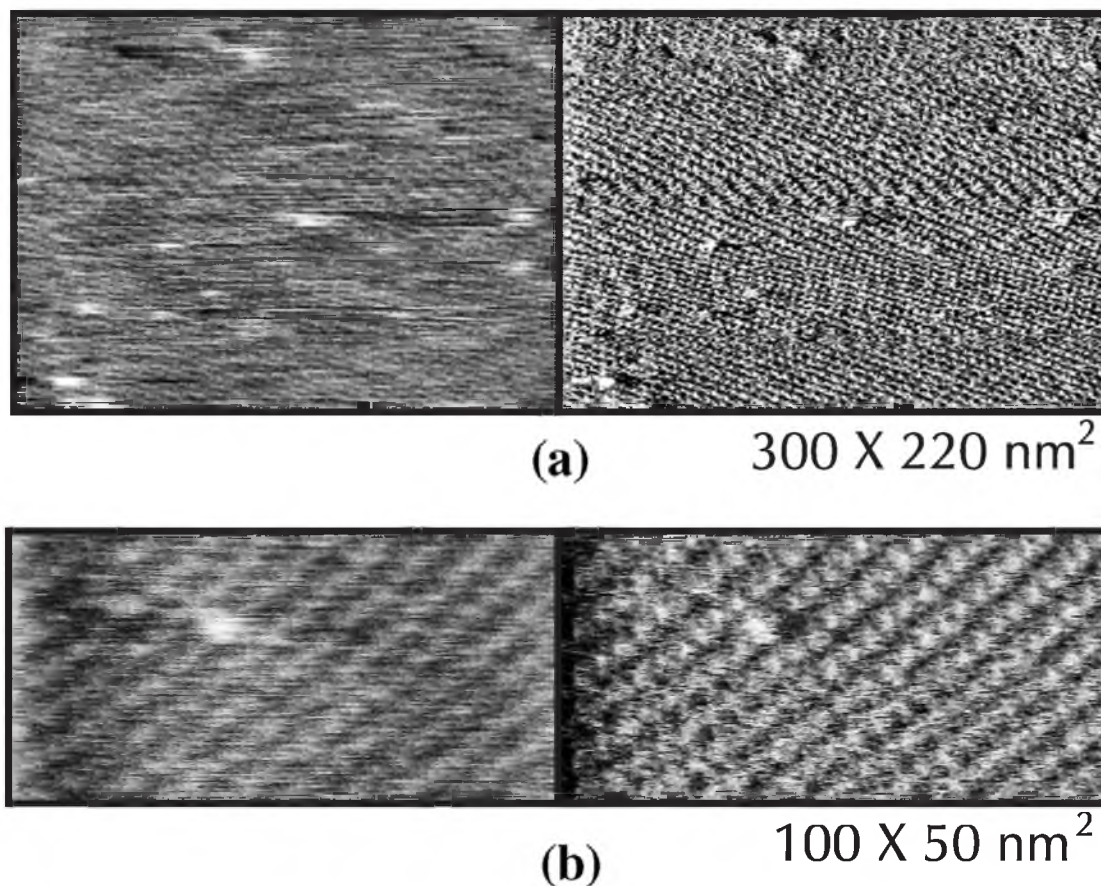
Figure 12.4 Small particles on the (100) face of insulin crystals imaged *in situ* with molecular resolution. The left and right part of each picture represent the height and the corresponding deflection image, respectively. The particles seem to consist of a few insulin hexamers, as was concluded by comparing them with the sizes of hexamers in the underying (100) lattice.

In the case of three-dimensional nucleation in solution of other protein crystals, several investigators have mentioned that the process of protein crystal growth starts with the formation of small aggregates. Sazaki et al. [24] have proposed that the crystallization proceeds in two steps: first primary particles are formed, and then crystal growth takes place by highly ordered aggregation of these primary particles. Ataka and Asai [25], and Bessho et al. [26] concluded that the nucleation of lysozyme is induced by the aggregation of a few lysozyme molecules. Recently, Michinomae et al. [27] have also reported that the crystal growth of lysozyme starts with formation of aggregates consisting of a few molecules, which grow together into larger, spherical, amorphous aggregates that change to crystalline structures. In our case, it may be possible that too small aggregates on the surface are detached not only by a conventional dissolution due to lower effective supersaturation, but also by the AFM tip movement. However, it is suggested that, at least at the pre-stage of two-dimensional growth, aggregates consisting of a small number of crystal-building units are essential for 2D nucleation in a similar manner as for conventional three-dimensional nucleation mechanism in a bulk solution. In other words, the formation of a 2D nucleus should start from an aggregate composed of a small number of growth units.

The density of 2D nuclei is the same for the central parts and the periphery of the {100} surfaces, which indicates that the 2D nucleation is limited by incorporation kinetics rather than volume diffusion. We investigated the influence of the AFM tip on the process by scanning a certain area a few times, followed by an expansion of the scan size. We found that there was no significant difference in growth rate inside or outside the originally scanned area, as was found by Yip and Ward [7]. This indicates that, with the low scan forces applied, the influence of the AFM was negligible, with respect to possible surface damage and stirring of the solution by the scanning tip and cantilever. The latter confirms that volume diffusion is not the growth limiting factor. In the case of canavalin, Land et al. [4] have reported that mixing of the stagnant solution by the AFM tip near the crystal surface increases the growth rate, which suggests that in their case crystallization is limited by mass transport. However, in the following paper by Land et al. [12], the kinetics of canavalin crystallization was also ascribed to be controlled by surface diffusion coupled with the up-step diffusion bias model (see section 12.3.4). The insulin hexamer is slightly smaller than the canavalin trimer growth unit, which has a similar cylindrical shape. In addition, Kadima et al. [27, 28] have found by dynamic light scattering methods that in solution the insulin hexamers form less easily 3D aggregates than the canavalin trimer in solutions. Thus, because of the smaller diffusing unit as compared with canavalin crystallization, effects of limited bulk diffusion should be less important for the growth kinetics of insulin crystals.

12.3.3 Dislocation spirals

Dislocation spirals were rarely observed on the insulin crystals. If they were present, they dominated the whole surface, and no 2D nuclei were found. This indicates that the supersaturation is in the low regime, where spiral growth dominates two-dimensional nucleation. Only on screw dislocation-free crystals, which are in the majority, growth by 2D nucleation dominates. The different type of spirals encountered, which are single, double, triple and closed loop spirals, are shown in fig. 12.5 The steps are parallel to the crystal edges, as was the case for 2D nucleation. These spirals are consistent with the classical model of crystal growth at dislocations.
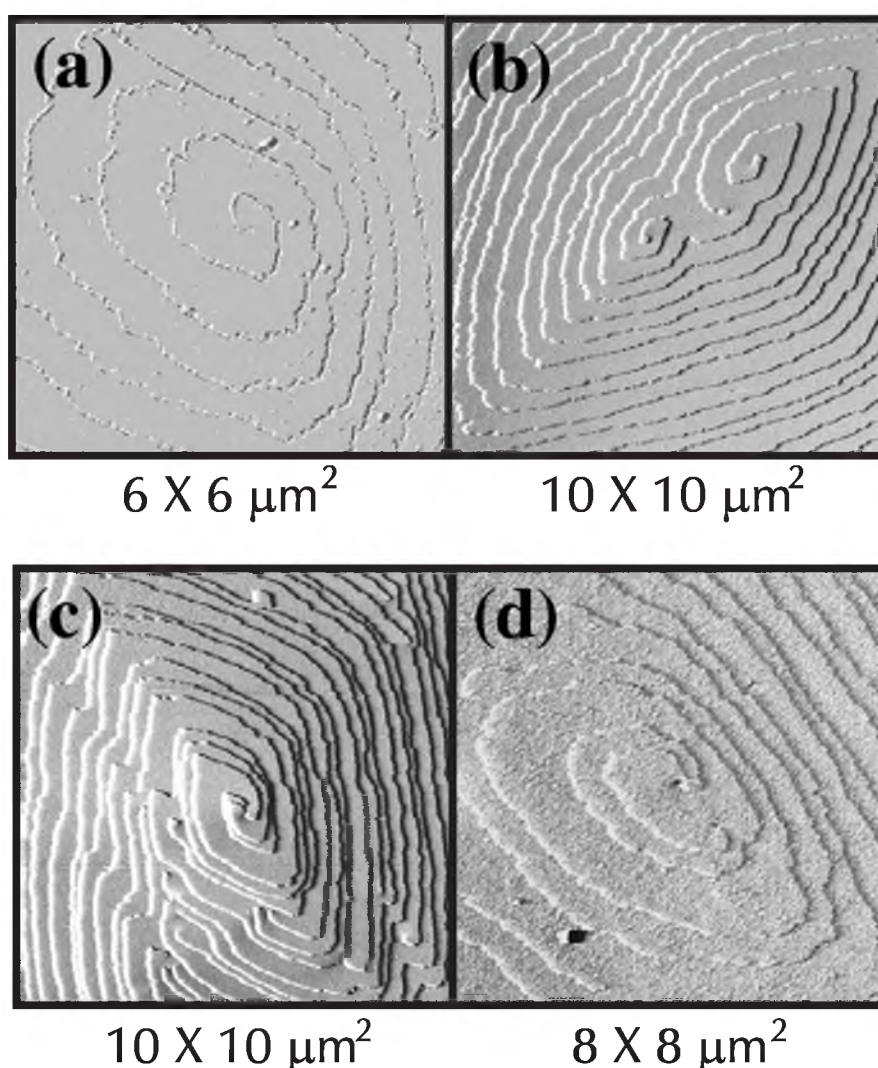

**Figure 12.5** Different types of growth spirals observed on the (100) surfaces of the 2Zn-insulin crystals: a single spiral (a), three single spirals (b), a triple spiral with several minor spirals (c), and a single right-handed and a double left-handed spiral forming a loop (d). The images of (a) and (d) were obtained from the *ex situ* experiments, whereas (b) and (c) were acquired by *in situ* experiments.

From the asymmetric shapes of spirals, especially as shown in the ex *situ* image of figs. 12.5a,d it follows that the step advancement shows a slight anisotropy in a similar way as observed for the growth of two-dimensional nuclei as mentioned in the former section. Anisotropy in the step propagation rate of spirals was dirctly measured by *in situ* AFM measurements of growth spirals. A series of *in situ* AFM images showing a growing spiral are depicted in fig. 12.6. Step rates were precisely measured with reference to the dislocation center. The velocity of the steps advancing to the left is 0.09 nm/s, and the rate of the steps going down is 0.12 nm/s. Both are slower than the remaining two step directions, which have a velocity of 0.14 nm/s. This behaviour is consistent with the behaviour of the growing two-dimensional nuclei as described in the previous section, although the anisotropy is much larger for the spiral a compared to the 2D nucleus of fig. 12.2. This is probably caused by the lower growth speed, by a factor of 10, in the spiral case. It is reasonable to expect that the anisotropy in step velocity is stronger emphasized at lower supersaturation, for which the number of kinks is more sensitive to step orientation.

As mentioned before, insulin crystallizes in spacegroup R3, which means that the crystals have no inversion centre. This implies that morphological differences on opposite faces can occur. However,
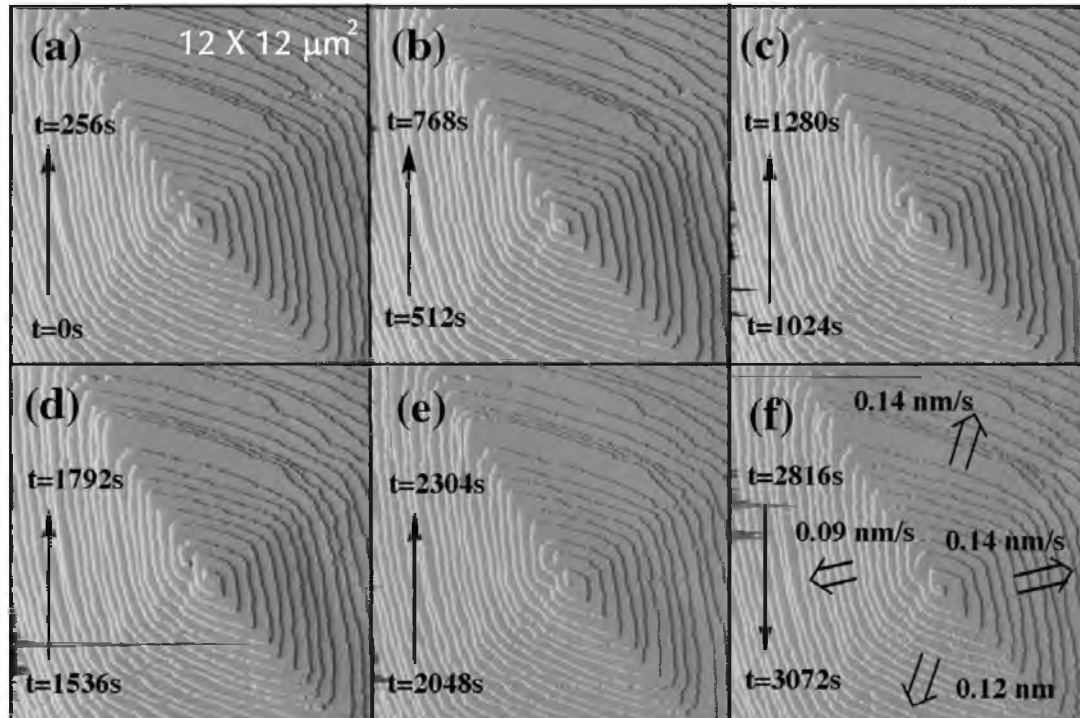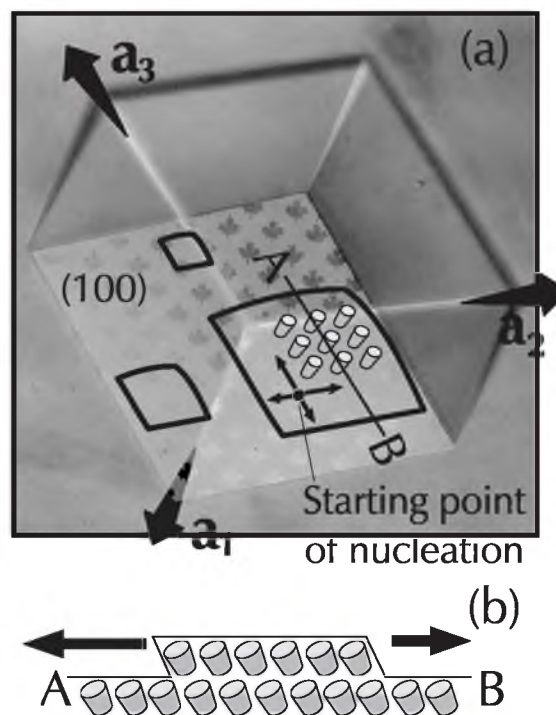

Figure 12.6 Series of *in situ* AFM images of the (100) surface of a 2Zn-insulin crystal, showing a slowly growing spiral. The velocity of the steps advancing towards the left is significantly lower than for the steps propagating in the other three main directions. The step velocities estimated from the sequence of the images are depicted in (f).

on all observed crystal faces a similar, anisotropic morphology is encountered for the spirals and 2D nuclei. Apparently, the differences between opposite faces are small. Although we do not know the absolute crystallographic orientation of the observed crystals in the absence of X-ray diffraction measurements, we can determine the tilt direction of the hexamers from the orientation of the crystal faces as checked with the AFM's internal optical microscope. As is depicted schematically in fig .12.7a, is The lateral anisotropy observed for both 2D nuclei and spirals, can be related to the tilted orientation of the insulin hexamers. This tilt introduces the existence of opposite acute and obtuse step edges, as depicted in fig. 12.7b. From the simultaneous AFM and optical microscopic observations we determined the tilt of the hexamers with respect to the anisotropic 2D nuclei and

Figure 12.7 (a) Schematic representation of the step velocity anisotropy at 2D nuclei onto an optical microscopy image of an insulin (100) face (which is indicated by a maple leaf pattern). The orientation of the cylindrical insulin hexamers is also indicated. (b) Cross-section along the line A-B indicated in (a), showing the accute (A) and obtuse (B) steps.

spirals steps, and we deduced that the obtuse steps are the slow ones and the acute steps the fast ones. This difference in step velocity can be explained by difference in opposite sides of the hexamers, which determine the structure of opposite steps <100> and <100>. Moreover, the tilted hexamer orientation can influence the growth kinetics at opposite step directions: The integration of new growth units is probably quicker at obtuse steps because of easier removal of water molecules. On the other hand, the probability of removal of an integrated unit at the obtuse step is larger because of the step shape. The observation that the acute steps are the fastest suggests that the latter effect is most important.

Two types of planar defects were occasionally observed on the insulin {100} surfaces. The planar defect near the center of the imaged area of fig. 12.8 generates two steps rotating around it, i.e. the defect is bound by two screw dislocations of opposite sign. Such stacking fault outcrops with spirals have also been found on the surfaces of satellite tobacco mosaic virus crystals (STMV) [9,11] and thaumatin crystals [15]. A second type of planar defect, shown as a black, perpendicular line located

at the left side of the imaged area, does not produce spiral growth. It propagates through the crystal and does not emerge during passage of steps; in addition it locally retards step propagation as can be seen in figs. 12.8a, c. The surface outcrops of both defects are parallel to a crystallographic axis. Similar planar defects have also been found on the surface of thaumatin crystals [11]. Since the detailed structure of both planar defects observed during the present study is not yet known, the difference in their behaviour can not be explained. However, it has been reported that the formation of complex defects, such as planar defects, can be induced by the incorporation of microcrystals or foreign particles [2,8,11].
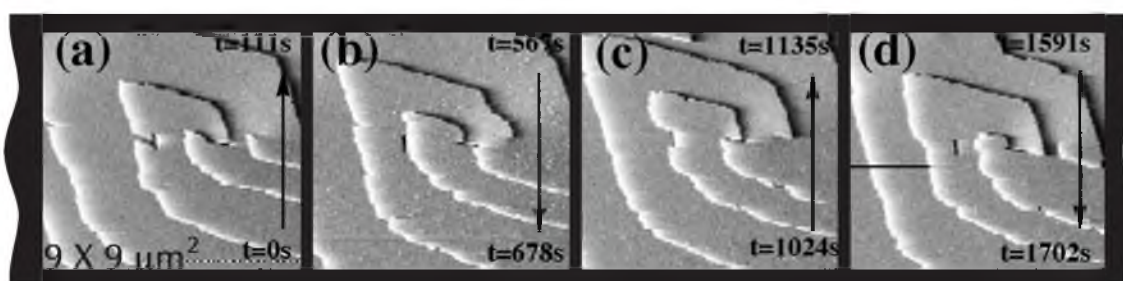
Figure 12.8 Sequence of *in situ* AFM images showing planar defects with and without spirals. On the right, a 'normal' dislocation without a planar fault emits spiral steps. Near the centre of the images, two steps rotate around a horizontally aligned planar defect. Another type of planar defect, that does not emit steps itself, which shows up as a black, vertical line at the left side of the imaged area, locally blocks passing steps (a, c) and persists after passage of these steps (b, d).
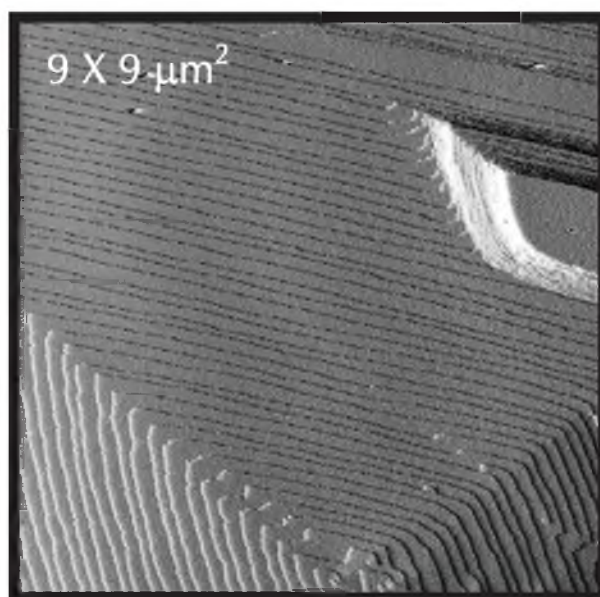
12.3.4 Islands with multilayer stacks

The development of multilayer stacks upon adsorption of three-dimensional clusters on surfaces is an important mechanism in the growth of protein and virus crystals such as lysozyme [1,2,9,18], thaumatin [9,10,18], STMV [5,6,8,9,11], canavalin [8,9,12] and catalase [13,18]. The formation and further growth of such 3D islands with multilayer stacks were observed during the present *in situ* studies of insulin surfaces growing by a spiral growth mechanism (fig. 12.9a) as well as by two-dimensional nucleation (fig. 12.9b). Upon recording the development of these multilayer stacks for a longer period, it was observed that they grow out only laterally, and that they gradually get covered by new spiral steps or 2D nucleation steps.

The morphology of these multilayer stacks on insulin {100}, with steep edges and a flat top, strongly suggests the same mechanism of adsorption and subsequent lateral growth of similar 3D islands as observed on the macromolecular crystals mentioned above. The islands with multilayer stacks generally exhibited characteristic orientations, which are consistent with the lattice of the crystal,

which proves that after adsorption the 3D particles merged in a contiguous manner with the underlying crystal surface. In previous reports, it was suggested that initially almost all of the protein aggregates adsorbed at the crystal surface are amorphous particles, and then transition of protein aggregates to crystals may occur by the contact with the underlying host crystal [15]. The occurrence of amorphous aggregates has been observed for insulin [30] as well as for thaumatin, concanabalin, A, a-amylase and t-RNA [31]. The observed islands with multilayer stacks may be also formed by a process of amorphous aggregates that migrate from the solution towards the crystal surface, which is reasonable considering the Ostwald rule of stages. Another possible cause may be the landing and subsequent of small crystallites on the host crystal surface.

A series of *in situ* AFM images of the growth of a three-dimensional island with multilayer stacks on the surface of an insulin crystal is shown in fig. 12.10. The island edge is composed of 23 monomolecular steps with an average terrace width of about 50 nm. This macrostep is growing outwards with an average rate of 0.64 to 0.75 nm/s, depending on its direction (fig. 12.10c). The island of fig. 12.10 was found on the surface growing by 2D nucleation as

Figure 12.9 *In situ* AFM image of a three-dimensional island with multilayer stacks on the surface of an insulin crystal. The island was found on area growing by dislocation spirals. The contours of the island are parallel with the crystallographic axes of the underlying crystal.

10x10 μm²   3.4x6.8 μm²
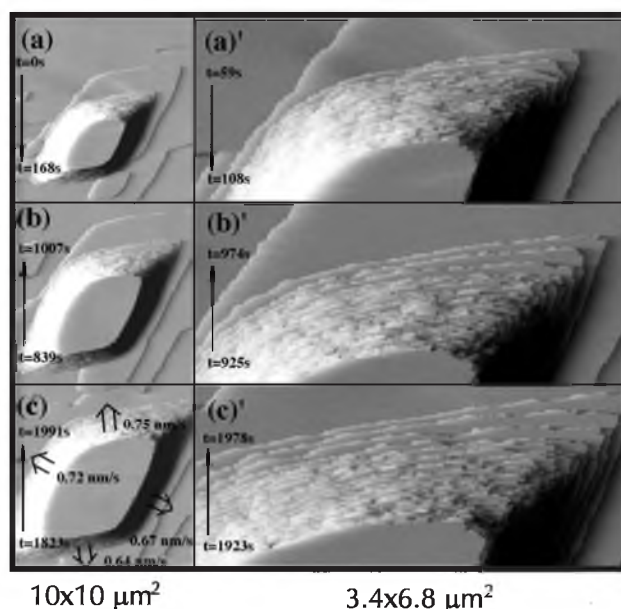
Figure 12.10 A series of *in situ* AFM images showing the growth of a multilayer stack on the (100) surface of an insulin crystal. Images primed, (a)' - (c)', are enlarged views showing the step spacing development of the upper macrostep. The width of the lowest terraces in the multilayer stack significantly increases with time.

shown in fig. 12.3. Because it is imaged at about the same time, we can compare the velocities of single and multilayer steps. The rates of the multilayer steps turned out to be roughly 50% of those of single steps. The downwards directed macrostep is again the slowest; the upwards directed macrostep is again the fastest, just as in the case of single steps. The retardation of the macrostep velocity may be explained by overlap of the surface diffusion field and volume diffusion. Because of the findings of section 12.3.2, we do not think that volume diffusion is responsible, which leaves surface diffusion as the most probable cause.

At the initial stages of the formation of multilayer stacks, the slopes of developing macrosteps are steep, but in the process of expansion, their slopes gradually decrease. Especially, the steps at the lower level advance faster than the upper steps, as is clear from fig. 12.10. The difference of the growth rates can be explained by the overlap of surface diffusion fields between adjacent steps coupled with the up-step diffusion bias model as is proposed by Ehrlich and Schwoebel [32, 33] and is illustrated in fig. 12.11a. Upon diffusing towards the step position, the molecule on the upper

terrace experiences a higher potential barrier at the step because of the decreased coordination at the transient state, whereas the molecule on the lower terrace quickly adhires to a step front or kink position as a result of the increased coordination. The probability of an adsorbed molecule on the lower terrace to move into the step is higher than that of a molecule from the upper terrace. Therefore, in the diffusion bias model, assuming that the diffusion length of an adsorbed molecule is

(a)   **(b)**
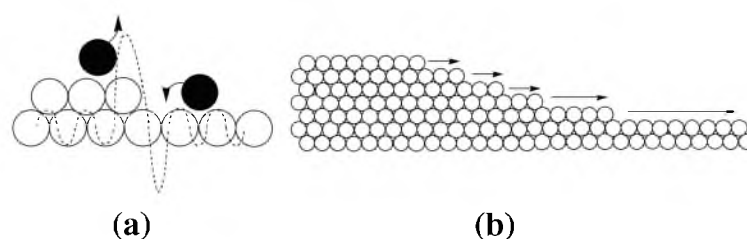
Figure 12.11 Up-step diffusion bias model [31]. (a) The hypothetical potential (dashed line) for molecules diffusing on the upper and lower terraces adjacent to the step. Due to the decreased coordination, the molecule on the upper terrace experiences a higher potential barrier for entering the step, whereas the molecule on the lower terrace stabilizes directly at the step as a result of its increased coordination. (b) Cross section of a multiple stacked layer of monomolecular steps, which schematically shows that the steps with a wider terrace at the lower side advance faster than the ones with a narrow terrace ahead.

larger than the step spacing, a step with a wide terrace at the lower side advances faster than a step with a narrow terrace ahead (fig. 12.11b). In order to explain the process of the terrace width homogenization by the step movements observed on canavalin crystals, Land et al. [12] have also used the up-step diffusion bias model and concluded that the kinetics of canavalin crystallization was controlled by the surface diffusion coupled with the up-step diffusion bias model. The fact that during the present study bunching of the step trains originating from growth spirals was never observed, confirms the up-step diffusion model once more. From the above it follows that the

surface diffusion process exists on the insulin crystals, although it may not be the decisive factor in the growth kinetics of a single step.
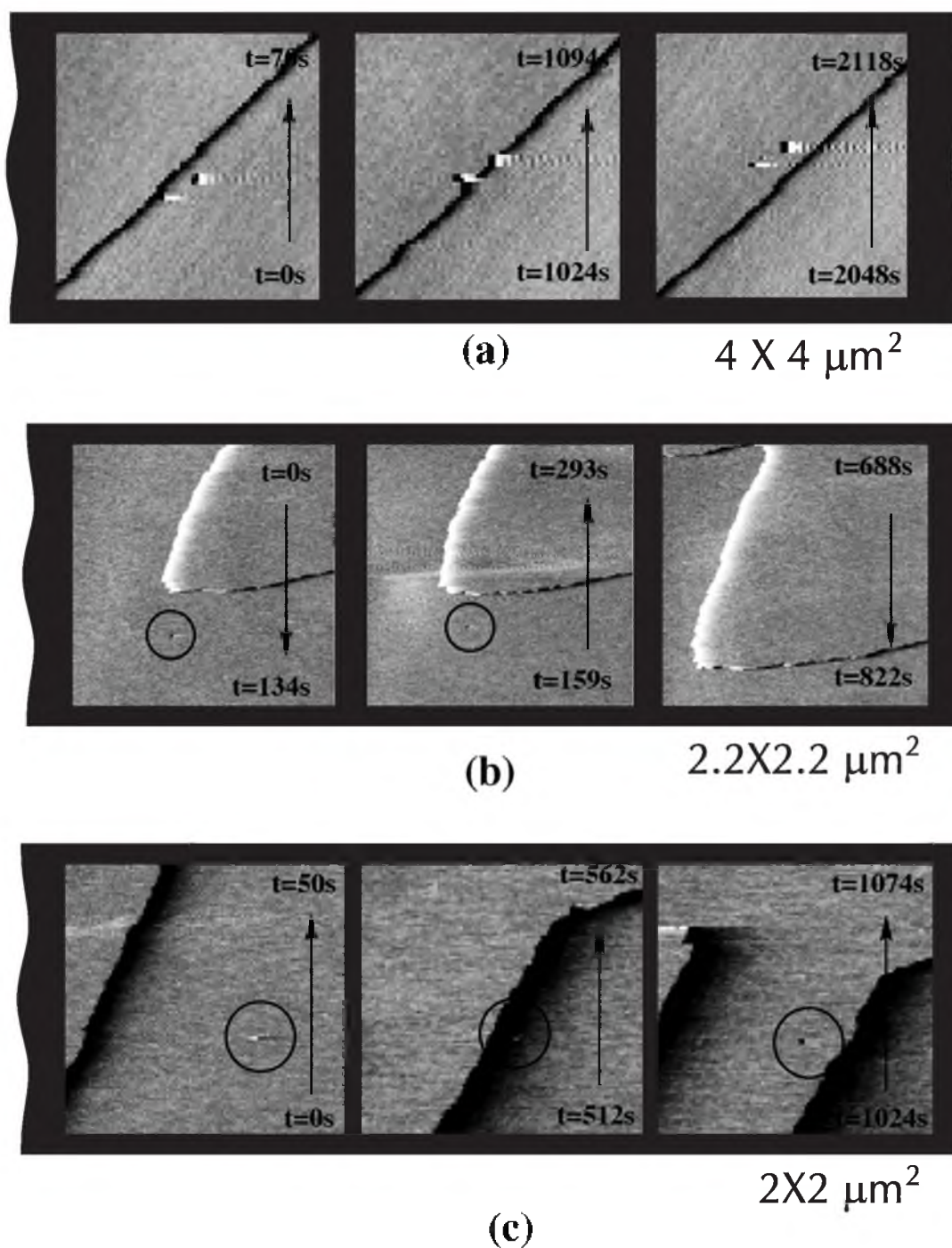

Figure 12.12 Interaction between holes and steps on the (100) insulin surface. (a) Two holes 'survive' the passage of a new step. (b) The hole indicated by a circle is buried under a passing step. (c) Formation of a hole upon passage of a step over an adsorbed, small particle.

12.3.5 Holes and vacancies on the crystal surface

We observed a large number of holes on the surface of insulin, which persisted after the over-growth by steps, such as shown in fig. 12.12a. These holes were found to be useful as reference points for measuring the rate of advancing steps on the surface. The holes were not connected to steps. In rare cases, some holes were buried under a new growth layer as is demonstrated in fig. 12.12b. Occasionally, we observed the formation of a hole as shown in fig. 12.12c. The new hole was created when a step advanced over a particle adsorbed on the surface. The step height in fig. 12.12c is about 3.5 nm, which is the single hexamer step height. Because the particle position turned into a hole in the surface, it is suggested that the size of the particle is less than that of an insulin hexamer. The particle may be an insulin monomer or another smaller oligomer, such as a dimer or tetramer. Recently, Nakada et al. [16] have reported that lysozyme dimers act as impurities on the (101) surface of tetragonal lysozyme crystals. It has also been reported that the site of incorporation of a foreign particle becomes a hollow channel [2,5,7,11]. Therefore, we believe that many of the holes found on the surface of insulin crystals are caused by the incorporation of foreign particles including insulin oligomers smaller than a hexamer.

Vacancies in the surface layer of the insulin crystals, arising from the absence of insulin hexamers from individual surface lattice points, were observed from the high-resolution images as shown in fig. 12.13. Detailed images of these point defects are shown in the insets. Possibly, part of the 'vacancies' are occupied by foreign particles such as small insulin oligomers that prevent hexamers filling up the complete crystal lattice. Because these particles are smaller than the hexamers, they appear as holes in the surface, in a way shown in fig.
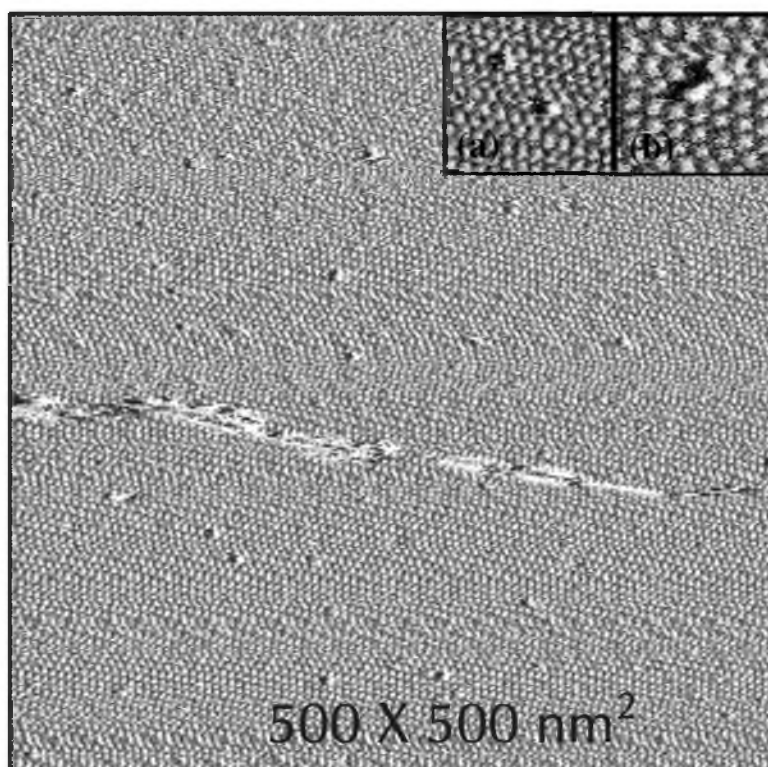

Figure 12.13 Vacancies on the (100) face of an insulin crystal on a molecular scale. The irregular white, broad line near the middle of the image is a step. The Insets show detailed images of these vacancies, indicating the absence of individual hexamers.

12.12c. The density of the vacancies in fig. 12.13 is about $2 - 3 \times 10^{-4}$, which is comparable to that of $4 - 6 \times 10^{-4}$ reported for thaumatin crystal [11]. However, this similarity may be accidental, because sometimes we observed surfaces with almost no vacancies.

Molecular resolution images of step edges on the insulin {100} crystal surfaces were obtained as is shown in fig. 12.14. Kink sites can be recognized at the steps. Neither a significant displacement nor a reconstruction of atoms at the edge position is identified from the images, despite the fact that the hexamers at the kink sites and the edge of a curved step have fewer neighbours and therefore are more likely to displace from the ideal lattice position than the atoms in the surface layer. Unfortunately, a time series of step motions could not be made, because at these small length scales the passing AFM tip had a deteriorating effect on the steps.
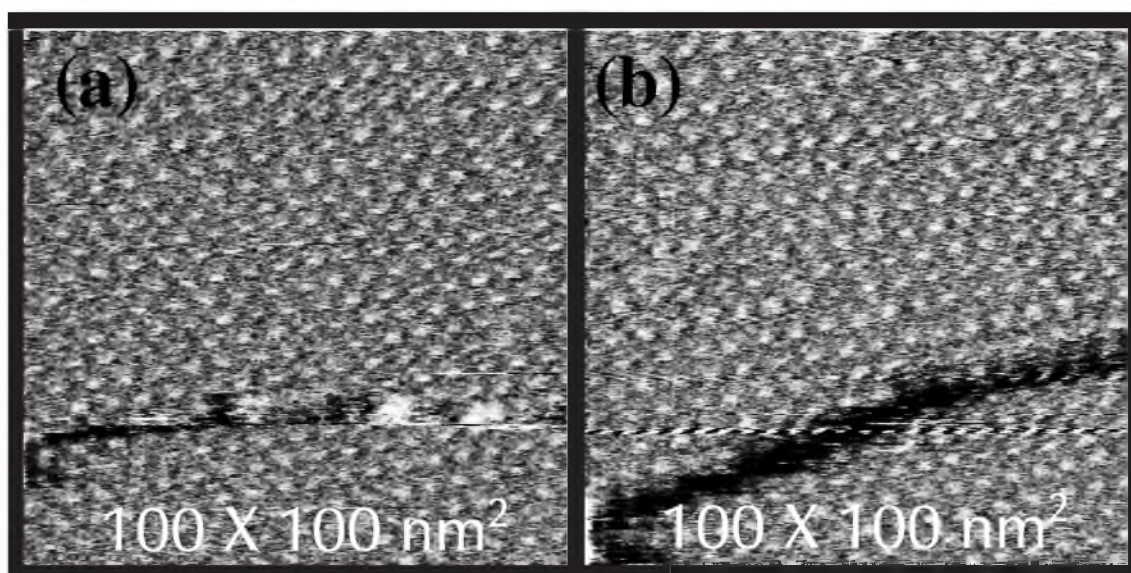
Figure 12.14 Molecular resolution *in situ* AFM images of steps with discernable kink positions on the (100) insulin surface.

Conclusions

At the low supersaturations applied, during the present investigation the {100} faces of 2Zn insulin crystals grow by three mechanisms, namely two-dimensional nucleation growth, spiral growth (if screw dislocations are present in the crystals) and lateral growth from particles that land on the surface. It was found that 2D nucleation growth is the mechanism that mostly occurs one. 2D nuclei, growth spirals and multilayer stacks all show anisotropy for the four major step directions, which

corresponds to differences in the structure of the growing steps. The critical diameter for 2D nucleation was estimated to be 30-60 nm.

The most probable growth-limiting factor is step integration, but surface diffusion can not be excluded. Adsorbed particles diffuse preferentially from the lower terrace towards a step, stabilizing step trains according to the Schwoebel effect. Mass transport is believed to be of no importance at the low growth rates applied.

Small holes in the surface, which survive the passages of several steps are possibly formed by the incorporation of foreign particles including insulin oligomers. Molecular resolution images show non-reconstructed crystal faces and steps, the presence of single vacancies in the lattice and the occurrence of very small particles on the surface.

Acknowledgments

References

[1]　　S.D. Durbin, W.E. Carlson, J. Crystal Growth 122 (1992), 71.

[2]　　S.D. Durbin, W.E. Carlson, M.T. Saros, J. Phys. D. 26 (1993), B128.

[3]　　J.H. Konnert, P. D'Antonio, K.B. Ward, Acta Crystallogr. D 50 (1994), 603.

[4]　　T.A. Land, A.J. Malkin, Yu.G. Kuznetsov, A. McPherson, J.J. De Yoreo, Phys. Rev. Lett. 75 (1995), 2774.

[5]　　A.J. Malkin, T.A. Land, Yu.G. Kuznetsov, A. McPherson, J.J. DeYoreo, Phys. Rev. Lett. 75 (1995), 2778.

[6]　　A.J. Malkin, Yu.G. Kuznetsov, T.A. Land, J.J. DeYoreo, A. McPherson, Nature Struct. Biol. 2 (1995), 956.

[7]　　C.M. Yip, M.D. Ward, Biophys. J. 71 (1996), 1071.

[8]　　A.J. Malkin, Yu.G. Kuznetsov, A. McPherson, Protein 24 (1996), 247.

[9]　　Yu.G. Kuznetsov, A.J. Malkin, W. Glantz, A. McPherson, J. Crystal Growth 168 (1996), 63.

[10]　　A.J. Malkin, Yu.G. Kuznetsov, W. Glantz, and A. McPherson, J. Phys. Chem. 100 (1996), 11736.

[11]　　A.J. Malkin, Yu.G. Kuznetsov, A. McPherson, J. Struct. Biology 117 (1996), 124.

[12]　　T.A. Land, J.J. De Yoreo, J.D. Lee, Surface Sci. 384 (1997), 136.

[13]　　A.J. Malkin, Yu.G. Kuznetsov, A. McPherson, Surf. Sci. 393 (1997), 95.

[14]　　Yu.G. Kuznetsov, A.J. Malkin, T.A. Land, J.J. DeYoreo, A.P. Barba, J. Konnert, A. McPherson, Biophys. J. 72 (1997), 2357.

[15]   Yu.G. Kuznetsov, A.J. Malkin, A. McPherson, J. Crystal Growth **196** (1999), 489.

[16]   T. Nakada, G. Sazaki, S. Miyashita, S.D. Durbin, H. Komatsu, J. Crystal Growth **196** (1999), 503.

[17]   A. McPherson, A.J. Malkin, Y.G. Kuznetsov, S. Koszelak, M. Wells, G. Jenkins, J. Howard, G. Lawson, J. Crystal Growth **196** (1999), 572.

[18]   A.J. Malkin, Yu.G. Kuznetsov, A. McPherson, J. Crystal Growth **196** (1999), 471.

[19]   E.N. Baker, T.J. Blundell, J.F. Cutfield, S.M. Cutfield, E.J. Dodson, G.G. Dodson, D.C. Hodgkin, R.E. Hubbard, N.W. Isaacs, C.D. Reynolds, K. Sakabe, N. Sakabe, and N.M. Vijayan, Phil. Trans. R. Soc. Lond. **319** (1988), 369.

[20]   P. Hartman and W. Perdok, Acta Cryst. 8 (1955), 49; 521; 525.

[21]   P. Hartman and P. Bennema, J. Crystal Growth 49 (1980), 145.

[22]   P.D. Jeffrey, Biochem. **13** (1974), 4441.

[23]   K. Waizumi, T. Matsumoto, N. Fukushima, H. Masuda, Chem. Lett. (1998), 999.

[24]   G. Sazaki, H. Ooshima, J. Kato, Y. Harano, N. Hirokawa, J. Crystal growth **130** (1993), 357.

[25]   M. Ataka, M. Asai, Biophys. J. **58** (1990), 807.

[26]   Y. Bessho, M. Ataka, M. Asai, T. Katsura, Biophys. J. **66** (1994), 310.

[27]   M. Michinomae, M. Mochizuki, M. Ataka, J. Crystal Growth **197** (1999), 257.

[28]   W. Kadima, A. McPherson, M.F. Dunn, F. Jurnak, J. Crystal Growth **110** (1991), 188.

[29]   W. Kadima, A. McPherson, M.F. Dunn, F.A. Jurnak, Biophys. J. **57** (1990), 125.

[30]   J. Schlichtkrull, Acta Chem. Scand. **11** (1957), 439.

[31]   J.D. Ng, B. Lorber, J. Witz, A. Theobald-Dietrich, D. Kern, R. Giege, J. Crystal Growth **168** (1996), 50.

[32]   G. Ehrlich and F.G. Hudda, J. Chem. Phys. **44** (1966), 1030.

[33]   R.I. Schwoebel, E.J. Shipsey, J. Applied Phys. **37** (1966), 3682.

Summary

This thesis is a collection of eleven crystal growth studies, which have their subject and the observation technique used in common. All of them deal with crystal faces, which are studied mostly with the help of atomic force microscopy (AFM).

The basic question that the science of crystal growth tries to answer is: *How does a large amount of separate building blocks (atoms, ions, molecules) evolve into a macroscopic crystal with a number of specific crystal faces?* The research presented in this thesis is addressed to one aspect of this general question: *How does one particular crystal face grow?*

In many cases, crystal faces are not roughened en growth proceeds layer by layer, in which every new layer of growth units spreads over the surface via steps. *In situ* and *ex situ* AFM provides a relatively easy way to image these monomolecular step patterns. The high resolution of AFM even enables direct imaging of the molecular surface lattice.

Within the general resemblances mentioned above, there is a large diversity of the subjects in this thesis. Most eye-striking is the difference in investigated crystals: ionic crystals on one hand, and organic crystals (paraffins, fats and proteins) on the other hand. In addition, the topic of the various crystal surface studies also varies: crystal growth, crystal dissolution, cleavage, the influence of the AFM itself on the crystals.

The first two chapters treat the growth mechanisms of barium nitrate crystal faces. The presence of several types of screw dislocations, leading to different types of growth spirals on the {111} and {100} crystal faces, as well as the occurrence of 2D nucleation on these faces, is elaborated in chapter 1. Chapter 2 deals with the occurrence and the size of the hollow cores that can emerge at the spiral centres. The size depends on both the dislocation's burgers vector magnitude and the supersaturation during growth. This behaviour is predicted by theoretical calculations, which seem to hold remarkably well for the small burgers vectors involved.

The third chapter addresses the growth of silver bromide tabular crystals, which are important for the photographic industry. Several *ex situ* and *in situ* AFM observations indicate that these crystals grow with layers of one AgBr growth unit. Furthermore, observations of nucleated crystals confirm the occurrence of twinning, which is the key mechanism for the growth of tabular crystals.

The next four chapters are all about potassium bichromate (KBC). This crystal has many interesting properties, such as the opposite (001) and (00$\bar{1}$) crystal faces that grow completely different, despite the 1crystal symmetry as determined by X-ray diffraction. Further, the crystal structure is composed of alternating ionic layers A and B parallel to {001}. In the first KBC chapter the growth of the

deviating (001) face is studied. It appears that the steps of one or a few unit cells in height are relatively easily blocked, while macrosteps of hundreds or even tens of thousands unit cells in height can still grow, and will develop to micro-facets. This phenomenon often leads to the formation of 'caves' in the crystals, which is attributed to the combination of impurity blocking and volume diffusion effects. In the second KBC chapter the double layered structure perpendicular to <001> is treated in more detail. In case of cleavage of a crystal along {001}, the cleavage plane is between layers A and B or between B and A, depending on the cleavage direction, as a result of the crystal symmetry. From these experiments, together with the KBC dissolution experiments described in chapter 7, it is proven that the A layer is thermodynamically the most stable layer, and is almost always on top of both opposite {001} crystal faces. When freshly cleaved crystals are exposed to air, the upper B layer that is present on one crystal half dissolves and recrystallizes as A. This process is facilitated by the ultrathin water layer that forms on most crystals exposed to air. This water layer is also detected by the use of tapping mode AFM (TM-AFM) on KBC crystals exposed to air, as is demonstrated in chapter 8. The water layer introduces a large attractive capillary force between the TM-AFM tip and the crystal, and this again induces mode switching between an attractive and a partly attractive, partly repulsive mode. This results in an AFM image having holes of a few nm depth, which correspond to these mode switches rather than to real topographic height differences.

The first part of the thesis deals with ionic crystals, while in the second part some crystals of organic substances are studied. These molecules form much larger growth units than ions. The Van der Waals bonds keeping the crystals together are relatively small, which makes the crystals softer than in the ionic case.

The first 'organic' chapter deals with the spontaneous movement of screw dislocations in paraffin crystals after cessation of growth. If this happens, a screw dislocation leaves a capricious step as a trace, that can intersect the straight spiral steps formed during growth and even itself. The movements are induced by shear strains, which probably are caused by adhesion between thin crystal sheets. In chapter 10 paraffin crystals with a melting point that is relatively low, but still well above room temperature, are studied by means of TM-AFM. It appears that the AFM tip, which is heated by a focused laser beam in order to measure its deflection, locally melts the crystal surface. A liquid bridge between tip and sample evolves, and transport of liquid paraffin molecules towards or from the tip takes place, which corresponds to etching or growth of the crystal surface, respectively. In this way, melt growth of paraffin can be studied 'in situ' by AFM.

In chapter 11, the relation between crystal structure and surface morphology is examined in a detailed way. As an example, the morphology of growth spirals on fat crystals is compared with the surface morphology as deduced from the crystal structure by different methods. It follows that the combination of Hartman Perdok theory and step kinetics is the best method to predict two-

dimensional morphology.

The final chapter consists of an *in situ* AFM investigation of the growth of insulin protein crystals. Three types of growth were discerned: 2D nucleation, spiral growth and a form of 3D nucleation. If screw dislocations are present in the crystal, spiral growth dominates at the low supersaturations applied. If these are absent, the crystals are forced to grow by 2D nucleation. Occasionally, large aggregates or crystallites land on the mother crystal and grow out laterally. Only a weak overlap of the diffusion fields of the steps was recorded.

Samenvatting

In dit proefschrift zijn elf verschillende kristalgroeistudies opgenomen, die hun onderwerp en de gebruikte waarnemingstechniek gemeen hebben. Ze gaan alle over kristaloppervlakken, welke veelal zijn bestudeerd met atomaire-kracht-microscopie (*Atomic force microscopy, AFM*).

Zeer kort samengevat luidt de kernvraag in de kristalgroei wetenschap: Hoe ontstaat uit losse bouwstenen (atomen, ionen, moleculen) een macroscopisch kristal met een aantal kenmerkende kristalvlakken? Het onderzoek gepresenteerd in dit proefschrift richt zich op een specifiek onderdeel van deze vraagstelling: Hoe groeit één bepaald kristalvlak?

Vaak blijkt dit laag voor laag te gaan; elke nieuwe laag van groei-eenheden breidt zich via tredes uit over het kristaloppervlak. Door de bestudering van deze tredepatronen na of tijdens de groei kan een goed beeld worden verkregen van de precieze manier waarop een kristal groeit. Met de gebruikte AFM techniek is het relatief eenvoudig om deze extreem lage tredes (vaak slechts één miljoenste millimeter hoogteverschil!) af te beelden. Zelfs individuele moleculen en atomen kunnen met deze techniek worden onderscheiden.

Ondanks de hierboven beschreven overeenkomsten, zijn er ook duidelijke verschillen tussen de hoofdstukken van dit proefschrift. Het meest in het oog springende is de diversiteit in verschillende kristalsoorten die zijn onderzocht; ook varieert het precieze onderwerp van studie aan de kristaloppervlakken: kristalgroei, oplossen van kristallen, kloven van kristallen, de invloed van de AFM techniek op de kristaloppervlakken.

Het proefschrift begint met twee hoofdstukken over bariumnitraat. De nadruk ligt hier op het spiraalgroei-mechanisme, een veel voorkomende groeiwijze van kristallen. De spiraalvormige patronen van monomoleculaire treden worden veroorzaakt door schroefdislocaties (lijnfouten) in het kristal. Specifiek wordt er gekeken naar holle pijpen in het centrum van de spiralen, die ontstaan door de mechanische spanning die door de dislocaties worden geïntroduceerd.

Vervolgens is er een hoofdstuk over de groei van zilverbromide kristallen, die belangrijk zijn voor de fotografische industrie. Verscheidene waarnemingen duiden erop dat ook deze kristallen met laagjes van één AgBr groeieenheid dik groeien.

Dan volgen maar liefst vier hoofdstukken over kalium bichromaat (KBC). Dit kristal heeft tal van interessante eigenschappen, waaronder de tegenover elkaar liggende (001) en (001̄) kristalvlakken die geheel verschillend groeien en de dubbellaags *AB* kristalstructuur. In het eerste kalium bichromaat hoofstuk uit de serie van vier wordt gedetailleerd het apart groeiende (001) vlak beschreven. Het blijkt dat de tredes met een hoogte van één groeieenheid lastig groeien,

217

terwijl tredes van honderden tot tienduizenden groeieenheden hoog nog wel kunnen groeien. Dit verschijnsel, dat gepaard gaat met de vorming van grote 'grotten' in de kristallen wordt deels toegeschreven aan verontreinigingen tijdens de groei. In het tweede KBC hoofdstuk wordt dieper ingegaan op de dubbellaags structuur. Als een kristal vanaf één bepaalde kant gekloofd wordt, blijkt dat de *AB*-structuur altijd op één van de twee mogelijke manieren wordt gespleten. Wordt een kristal nu van de andere kant gekloofd, dan 'kiest' het kristal het andere mogelijke splijtvlak. Bovendien blijkt na het kloven dat één van de twee lagen (*A*) energetisch stabieler is dan de andere (*B*). De identificatie van deze lagen *A* en *B* is deels mogelijk dankzij de experimenten met in alcohol oplossende KBC kristallen beschreven in het volgende hoofdstuk. Dit oplossen wordt *in situ* gevolgd met de AFM. Uit deze experimenten blijkt dat gekloofde kristalvlakken die in aanraking met lucht zijn geweest, resistent worden tegen oplossen, doordat zich een beschermend laagje vormt. Pas als dit laagje doorbroken wordt, kan het eigenlijke kristal oplossen. In het laatste KBC hoofdstuk worden eigenaardige patronen in AFM plaatjes gerelateerd aan de aanwezigheid van een ultradun waterlaagje op de kristallen dat ontstaat als ze aan lucht worden blootgesteld.

Na het eerste boekdeel over ionogene kristallen, volgt een tweede deel waarin kristallen van organische moleculen worden bestudeerd. Deze moleculen vormen veel grotere groei-eenheden dan ionen; de krachten die de moleculen in kristallen bindt zijn relatief kleiner dan in ionogene kristallen, wat de kristallen veel zachter maakt.

Het eerste organische hoofdstuk behandelt het spontaan verplaatsen van dislocaties in paraffine-kristallen nadat ze gegroeid zijn. Dit verplaatsen gaat vrij makkelijk door de zachtheid van de kristallen. Als een dislocatie zich verplaatst, laat deze een grillige trede achter als spoor. Deze treden kunnen de oorspronkelijke, rechte groeitreden, alsook zichzelf kruisen. In hoofdstuk 10 wordt gekeken naar de invloed van de AFM tip, die enigzins opgewarmd is door de gefocusseerde laser op paraffine-kristallen met een laag smeltpunt. Het blijkt dat de paraffine tijdelijk zeer lokaal smelt door de aanwezigheid van de tip, en dat zich een kleine mantel van gesmolten paraffine rondom de tip vormt. Er vindt altijd stofuitwisseling plaats tussen deze mantel en het kristal, wat kan leiden tot groei alswel etsen van de kristallen. Dit mechanisme kan dienst doen om *in situ* het smelt- en stollingsgedrag van deze paraffine kristallen te bestuderen.

In het op één na laatste hoofdstuk wordt dieper ingegaan op het verband tussen kristalstructuur en oppervlaktemorfologie. Hiertoe worden met behulp van AFM de vorm van groeispiralen op vetkristallen bestudeerd. Deze morfologie wordt vergeleken met de morfologie zoals die berekend wordt met verschillende modellen op basis van de kristalstructuur, om zo het voorspellend vermogen van die modellen te testen.

Tenslotte wordt een studie beschreven naar het groeigedrag van insuline kristallen. Deze eiwitten, van belang voor de stofwisseling in het menselijk lichaam, vormen ruitvormige kristallen. Deze zijn tijdens het groeien tot op moleculaire schaal bestudeerd met AFM. Verschillende concurerende groeiwijzen, zoals twee-dimensionale kiemvorming, spiraalgroei en drie-dimensionale kiemvorming zijn waargenomen.

List of publications

1. K. Maiwa, M. Plomp, W.J.P. van Enckevort and P. Bennema, *AFM observation of barium nitrate {111} and {100} faces: spiral growth and two-dimensional nucleation growth*, J. of Crystal Growth **186** (1998), 214-223.

2. M. Plomp, K. Maiwa and W.J.P. van Enckevort, *Atomic force microscopy observations of hollow cores on the {111} and {100} faces of barium nitrate*, J. of Crystal Growth **198/199** (1999), 246-252.

3. M. Plomp, J.G. Buijnsters, G. Bögels, W.J.P van Enkevort and D. Bollen, *Atomic force microscopy studies on the surface morphology of {111} tabular AgBr crystals*, accepted for publication in J. of Crystal Growth, 1999.

4. M. Plomp. A.J. Nijdam and W.J.P. van Enckevort, *The structure of coarse crystal surfaces: the (00) face of $K_2Cr_2O_7$ crystals grown from aqueous solution as an example*, J. of Crystal Growth **193** (1998), 389-401.

5. M. Plomp, W.J.P. van Enckevort and E. Vlieg, *Cleavage asymmetry of $K_2Cr_2O_7$ crystals*, submitted for publication.

6. M. Plomp, W.J.P. van Enckevort and E. Vlieg, *Etching of $K_2Cr_2O_7$ {001} faces observed by* in situ *atomic force microscopy*, to be submitted.

7. M. Plomp, W.J.P. van Enckevort and E. Vlieg, *Observation of a surface water layer on $K_2Cr_2O_7$ crystals by adhesive contrast in atomic force microscopy*, to be submitted.

8. M. Plomp, P.J.C.M. van Hoof, C.J. van de Streek and W.J.P. van Enckevort, *Dislocation movement in n-$C_{40}H_{82}$ paraffin crystals observed by atomic force microscopy*, submitted for publication.

9. M. Plomp, P.J.C.M. van Hoof and W.J.P. van Enckevort, *AFM-induced melt growth on n-paraffin crystals*, submitted for publication.

10. F.F.H. Hollander, M. Plomp, C.J. van de Streek and W.J.P. van Enckevort, *A 2D Hartman-Perdok analysis of polymorphic fat surfaces observed with atomic force microscopy*, submitted for publicaton.

11. K. Waizumi, M. Plomp and W.J.P. van Enckevort, Atomic force microscopy studies of insulin crystal growth, submitted for publication.

List of publications

12. F.K. de Theije, N.J. van der Laag, M. Plomp and W.J.P. van Enckevort, *A surface topographic investigation of {001} diamond surfaces etched in oxygen*, accepted for publication in Phil. Mag. A, 1999.

13. A.R.A. Zauner, J.L. Weyher, M. Plomp, V. Kirilyuk, S. Porowski, W.J.P. van Enckevort, J.J. Schermer, P.R. Hageman and P.K. Larsen, *Homoepitaxial GaN growth on exact and misoriented single crystals: suppression of hillock formation*, to be submitted.

14. C. Sweegers, M. Plomp and W.J.P. van Enckevort, Surface topography of (-Al(OH)$_3$, to be submitted.

Curriculum Vitae

Marco Plomp werd geboren op 24 mei 1969 te Doetinchem. Op de lagere school aldaar leerde hij schrijven zodat hij nu zijn eigen C.V. schrijft. Ik heb in 1987 aan het Ulenhofcollege te Doetinchem mijn Atheneum studie afgerond. Daarna ben ik gaan studeren aan de Universiteit Twente, wat in 1993 leidde tot een diploma in de Technische Natuurkunde. In het kader van deze studie was er een stage bij het ECN in Petten waar ik aan windturbinebladen rekende, en uiteindelijk studeerde ik af in de richting van de Technische Optica. Mijn eindopdracht bestond uit de ontwikkeling van een fiber-interferometrische immuunsensor.

Na mijn afstuderen heb ik in opdracht van het Twentse MESA research-instituut een haalbaarheidsonderzoek uitgevoerd naar de toepassingen van nano-schaal manipulatie met behulp van rastermicroscopie. Dit als invulling van mijn vervangende dienstplicht (die bestond toen nog).

Zo was het in 1995 dat ik bij de vakgroep Vastestofchemie aan de Katholieke Universiteit Nijmegen begon met het door NWO-CW gefinancierde promotie-onderzoek naar kristalgroei met behulp van atomaire kracht microscopie. Dit leidde in 1999 uiteindelijk tot het werkje dat U nu leest.

Crystal growth studied on a micrometer scale

Marco Plomp

1999

Summary

This thesis is a collection of eleven crystal growth studies, which have their subject and the observation technique used in common. All of them deal with crystal faces, which are studied mostly
with the help of atomic force microscopy (AFM).
The basic question that the science of crystal growth tries to answer is: How does a large amount of
separate building blocks (atoms, ions, molecules) evolve into a macroscopic crystal with a number of
specific crystal faces? The research presented in this thesis is addressed to one aspect of this general
question: How does one particular crystal face grow?
In many cases, crystal faces are not roughened en growth proceeds layer by layer, in which every
new layer of growth units spreads over the surface via steps. In situ and ex situ AFM provides a
relatively easy way to image these monomolecular step patterns. The high resolution of AFM even
enables direct imaging of the molecular surface lattice.
Within the general resemblances mentioned above, there is a large diversity of the subjects in this
thesis. Most eye-striking is the difference in investigated crystals: ionic crystals on one hand, and
organic crystals (paraffins, fats and proteins) on the other hand. In addition, the topic of the various
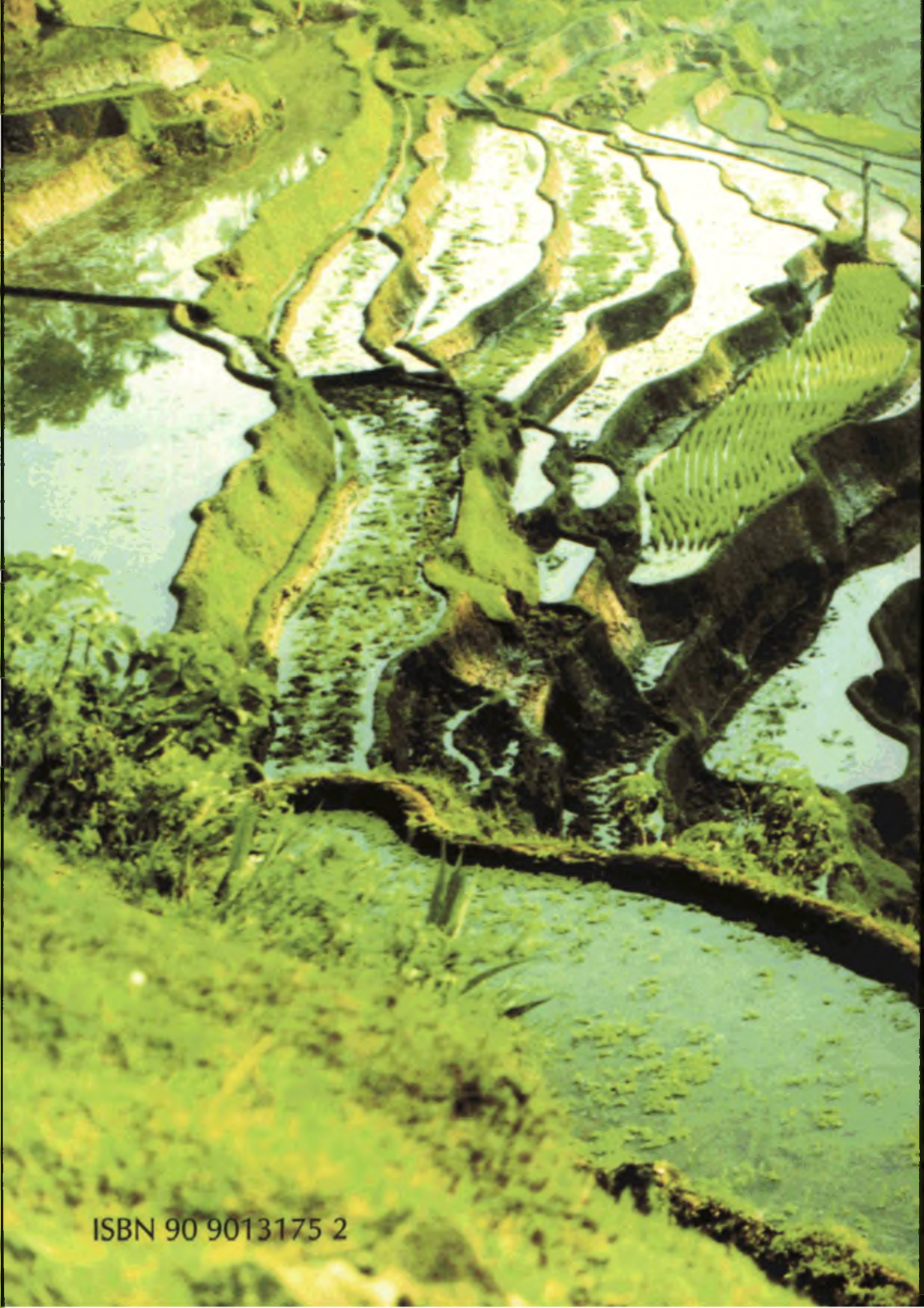crystal surface studies also varies: crystal growth by screw dislocations or 2D nucleation, crystal
dissolution, the influence of the crystal structure on cleavage, the influence of the AFM itself on the
growth of crystals.